UNIVERSITY OF LONDON

Degree PhD Year 2007 Name of Author EFSTATHIOU, Apostolos J, Apostolos

DESIGN CONSIDERATIONS FOR A HYBRID SWING-ARM PROFILOMETER TO MEASURE LARGE ASPHERIC OPTICS

by

Apostolos Efstathiou BSc MSc AMInstP

This thesis is submitted in partial fulfilment of the requirements for the degree of Doctor of Philosophy

Optical Science Laboratory
Department of Physics and Astronomy
University College London

March 2007

ProQuest LLC
789 East Eisenhower Parkway
P.O. Box 1346
Ann Arbor, MI 48106-1346

CONTENTS

LIST OF FIGURES

LIST OF TABLES

ACKNOWLEDGMENTS

First of all I would like to thank my primary supervisor Dr David D Walker for giving me the opportunity to undertake a Ph.D and for his continuing support in all aspects of my research in the last four years.

I would like to thank my supervisor at the National Physical Laboratory, Dr Richard K Leach for his support and guidance since my first day at NPL and for patiently reading myriads of draft reports!

I would like to express my gratitude to the project manager at NPL Dr Andrew J Lewis for his unsurpassable technical advice and for the time he dedicated in technical discussions. I am particularly grateful for the invaluable help he provided in the lab during the evaluation of the SAP and for enabling several defining experiments.

Special thanks to Nigel Cross at NPL for always having a good solution to every problem and for teaching me fundamental metrology skills. Also to all the people at NPL who helped me at one point or another. From UCL I would like to thank Christopher King and Matthew Callender for the endless brainstorming sessions and for all the work we did together.

I am thankful to all my friends and the people close to me for putting up with my systematic grumbling during the last four years... Finally I should thank my parents for their support, financial and otherwise.

DECLARATION

The work presented in this thesis describes a project to design, build and evaluate a new scientific instrument to be housed at the UK national facility for research into the fabrication and metrology of ultra-precision surfaces. A project of this size requires multiple inputs and the project team includes three PhD students and senior scientists and engineers from both University College London (UCL) and the National Physical Laboratory (NPL).

Due to the collaborative nature of this project there has been some overlap on the work carried out. In particular, issues regarding the integration of two separate sensor technologies were evaluated independently by Apostolos Efstathiou and Matthew Callender and there is some overlap in the designs produced. The final design was agreed upon at a meeting of NPL and UCL representatives. Both students had input in the discussion and contributed to the final decision.

Paragraph 6.6 of the thesis presents the author's view on issues regarding the mounting the SAP arm and the hybrid sensor. The mounting method was chosen after several discussions between NPL representatives and three UCL PhD students (Apostolos Efstathiou, Matthew Callender, Christopher King,). The students produced many co-authored internal reports and e-mails.

The final design of the SAP mount and the implementation of the mechanics and peripherals was carried out by Simon Oldfield at NPL. The control software for the SAP was written by Dr Andrew Lewis (NPL).

The thesis is presented in accordance with the guidelines and regulations of the University of London. Parts of the thesis have been used in the following publications:

- Efstathiou A 2004 Profilometry for Support of Large Optical Manufacturing and Testing NPL Report CBTLM (RES) 106

- Euro 50 – Design Study of a 50 m Adaptive Optics Telescope (contributing author) Lund University August 2003

- Callender M J , Efstathiou A, King C W, Walker D D, Gee A E, Lewis A J, Oldfield S and Steel R M 2006 A Swing-Arm Profilometer for Large Telescope Mirror Element Metrology Proc. SPIE 6273 (Poster presentation at the Astronomical Telescope & Instrumentation Conference, 24-31 May 2006, Orlando, Florida, USA)

- Lewis A J, Oldfield S, Callender M J, Efstathiou A, Gee A E, King C W and Walker D D 2006 Arcuate Profilometry-Traceable Metrology for Large Mirrors (Simposio de Metrologia 2006 25-27 October Mexico)

- King C W, Callender M J, Efstathiou A, Walker D D, Gee A E, Lewis A J, Oldfield S and Steel R M 2006 A 1m Swing-Arm Profilometer for Large Telescope Mirror Elements (ASPE 21st Annual Meeting, 15-20 October 2006 Monterey, California USA

The listing of any commercial equipment in this thesis is not to be considered an endorsement by either NPL or UCL.

ABSTRACT

This thesis presents issues regarding the design and implementation of a profilometer based on the swivelling motion of a pivot arm. The main advantage of such a method, over conventional profiling techniques, is that it can be easily adapted to measure a range of optics including both spherics and aspherics, convex and concave as well as a variety of optic diameters and radii of curvature. The initiative for the development of the new aspheric metrology technique comes from the need for fabrication and measurement of hundreds of aspheric segments to enable the future Extremely Large Telescopes (ELTs).

A detailed investigation of currently available aspheric metrology techniques concluded with the proposal of a novel SAP with a hybrid opto-mechanical sensor as a way to tackle issues of ELT segment metrology that remain in doubt. The successful submission of the proposal to the Department of Trade and Industry resulted in the allocation of funding for the development of a functional full scale prototype.

Initially a basic error model was constructed in order to forecast the error of a generic SAP and to estimate allowed sub-component tolerances. Subsequently a first, scaled-down model of an SAP was used as a test platform which guided the construction of a full-scale prototype. The prototype is capable of measuring optics up to 1 m in diameter with a minimum radius of curvature of 1.75 m for concave and 1.25 m for convex surfaces. The SAP performance was evaluated through the measurement of a 680 mm diameter optic and measurements of surface profiles with accuracy better than 20 nm were realised. The thesis describes in detail the design process followed from the conceptual idea to the implementation and evaluation of the instrument.

LIST OF ABBREVIATIONS

AO	Adaptive Optics
API	American Petroleum Institute
BB	Beam Bender
BS	Beam Splitter
CC	Center of Curvature
CCD	Charged Coupled Device
CGH	Computer Generated Hologram
CMM	Coordinate Measurement Machine
CUPE	Cranfield Unit for Precision Engineering
DoF	Degrees of Freedom
DTI	Department of Trade and Industry
DC	Direct Current
DGP	Dual Gauge Profilometer
ELT	Extremely Large Telescope
GUM	Guide to the expression of Uncertainty in Measurement
ISO	International Organisation for Standardisation
LACS	Large Area Curvature Scanning
LVDT	Linear Variable Differential Transformer
LTP	Long Trace Profiler
MWPSI	Multiple-Wavelength Phase-Shifting Interferometry
NIST	National Institute of Standards and Technology
NMS	National Measurement System
NPL	National Physical Laboratory
OMAM	Optical Manipulation And Metrology

OPD	Optical Path Difference
OSL	Optical Science Laboratory
OWL	Overwhelmingly Large Telescope
PV	Peak-to-Valley
PSI	Phase Shifting Interferometry
PTB	Physikalisch-Technische Bundesanstalt
PZT	Piezo-Electric Transducer
PTFE	Polytetrafluoroethylene
PI	Professional Instruments
RoC	Radius of Curvature
RT	Retroreflecting Target
RMS	Root Mean Square
SOML	Steward Observatory Mirror Lab
SPLOT	Stylus Profilometer for Large Optical Testing
SUT	Surface Under Test
SAP	Swing-Arm Profilometer
TWH	Two-Wavelength Holography
TWPSI	Two-Wavelength Phase Shifting Interferometry
UKAS	United Kingdom Accreditation Service
UCL	University College London
VI	Virtual Instrument
VLT	Very Large Telescope

Chapter 1

INTRODUCTION

"We shall not cease from exploration and the end of all our exploring will be to arrive where we started... and know the place for the first time."

T.S.Eliot

The main area of investigation of this thesis is in the design and implementation of a Swing-arm profilometer for the measurement of large aspheric optics. Swing-arm profilometry is a measurement technique which originates from the well established principle of cup-wheel grinding used in optical manufacturing. Currently available aspheric metrology techniques appear to have drawbacks that limit their application. In particular the advent of new astronomical telescopes with aspherical primaries comprising of several hundred segments poses very strict requirements both in terms of speed and accuracy of measurement. The use of a new hybrid opto-mechanical Swing-arm profilometer is proposed as a way to meet the requirements of ELT segment metrology.

1.1 THE NEED FOR LARGE ASTRONOMICAL TELESCOPES

1.1.1 INCREASING THE APERTURE SIZE

The last decade was dominated by optical telescopes with primary mirror diameters in the range of 8 m to 10 m. The advantages of using large reflecting telescopes have been

demonstrated through numerous projects such as the twin Keck telescopes (figure 1.1) which have been in operation since 1993 (Smith 1996). The next generation of telescopes will be 30 m to 100 m in diameter and will make use of adaptive optics.

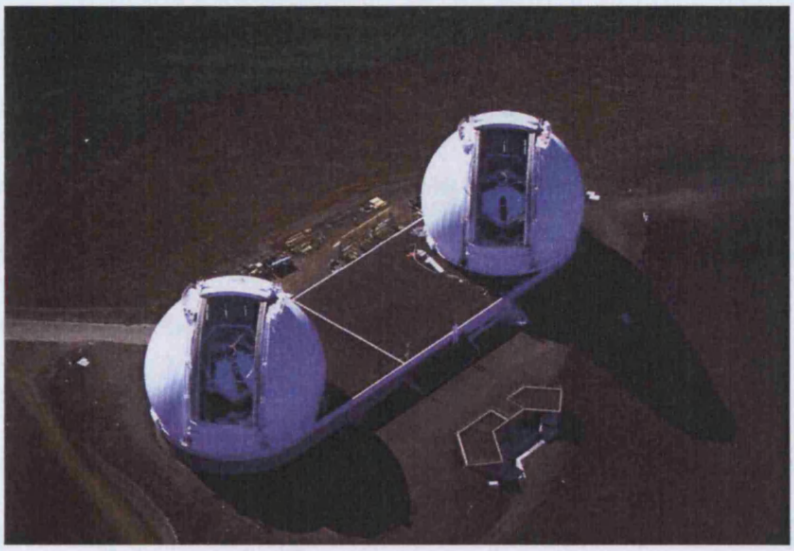

Figure 1.1 The Keck telescopes

One of the advantages of employing large telescopes is the resulting increase in the light collecting area. The light gathering power of a telescope is proportional to D^2, where D is the diameter of the primary mirror. Hence the use of large primary mirrors results in higher brightness and aids the investigation of faint objects.

The other major benefit of large telescopes lies in their resolving power. Every optical system, no matter how well perceived and implemented, will be limited by diffraction which is the physical limit for the resolution of an optical system. With regard to reflecting telescopes, diffraction effects occur when incoming plane waves from a distant object are scattered from the edges of the mirror. The resulting interference with waves incident on other parts of the primary mirror results to a diffraction pattern

known as the Airy disk. The Airy disk consists of a central spot at the focus of the telescope, surrounded by several diffraction rings.

The size of the Airy disk is of particular importance when making observations of self-luminous objects. For example, assume the case of two distant stars of equal irradiance. The stars will appear as two Airy disks when observed with a telescope and the ability to resolve them as two individual objects has to do with the size of their Airy disks. If their Airy disks are too large then the smeared images of the two stars will overlap to a degree that makes them indistinguishable.

The theoretical limit to which such objects can be resolved was calculated by Lord Rayleigh. According to the Rayleigh criterion two point sources can just be resolved if the centre of the Airy disk of one source falls on the first minimum of the Airy disk of the other source. The diameter of the Airy disk is given by $q = 1.22\lambda\, f/\#$ where $f/\#$ is the focal ratio (or f-number) of the optical system given as f/D (where f is the focal length and D is the diameter of the aperture) and λ is the wavelength of the oncoming radiation. For a given focal length the increase in diameter results in a low $f/\#$. In general an optical system is assumed to be "fast" when it has a low f-number (below five). This results in a brighter image and it is more suitable for telescopes used to observe deep sky objects.

The Rayleigh criterion can also be expressed in terms of the angular separation of the two sources. If $\Delta\theta$ is the corresponding angular measure then $\Delta\theta = 1.22\lambda/D$ (since $q/f = \sin\Delta\theta \approx \Delta\theta$ when θ is small) and this corresponds to the minimum resolvable

angular separation of the two objects. It is apparent that increasing the aperture size results to higher angular resolution.

It is important to note that diffraction effects will occur irrespective of the quality of the telescope optics. If the resulting smearing of the image is larger than that produced by the aberrations of the optical system then the imaging process is said to be "diffraction limited". One of the main targets for the new generation of telescopes is to achieve diffraction limited observations at angular resolutions on the scale of milliarcseconds compared to current telescopes where the resolution is on the scale of fractions of arcseconds.

1.1.2 ASTRONOMICAL SEEING

In reality the images produced by a ground based telescope could not be diffraction limited even if the optics were, in theory, perfect. This is due to turbulence in the earth's atmosphere which results in the blurring of the resulting image. The turbulence in the earth's atmosphere is a consequence of temperature and pressure variations at the different layers of the atmosphere. These variations cause non-uniformities in the density of the air which constantly alters the local refractive index. As a result the images of stars appear blurry and their brightness appears to fluctuate. These are some of the main effects of "astronomical seeing". The consequence of astronomical seeing is that the real resolution of ground based telescopes is significantly degraded and diffraction limited imaging cannot be achieved without correction. As an example each of the Keck telescopes, having a primary mirror with a diameter of 10 m, has an angular resolution of about 0.5 arcsec (Gillingham 1997). This is significantly worse than the telescope's diffraction limit which is close to 0.013 arcsec in the visible.

One of the factors used to characterise astronomical seeing is called the Fried parameter (or Fried seeing diameter) r_0 (Fried 1966). The Fried parameter expresses the maximum diameter that a telescope can have before the effects of the atmosphere become dominant. Telescopes with diameters smaller than r_0 have angular resolution that is inversely proportional to the diameter of the telescope's aperture according to the Rayleigh criterion. Nevertheless, for telescopes with apertures larger than r_0 the resolution is independent on the mirror diameter. In fact the maximum attainable resolution corresponds to a value for the diameter of the aperture that is equal to r_0. Bound by this problem the use of larger telescopes does not always reflect an improvement in terms of angular resolution. In this respect a telescope with a larger primary mirror will be most useful in helping to gather more light and produce brighter images. Other parameters that affect seeing are the exposure time and the isoplanatic angle which is described in section 1.1.3.

The Fried parameter is defined with respect to the various observing conditions, the location of the telescope *etc.* For example for city viewing at visible wavelengths the Fried parameter is about 0.05 m while at really good locations such as Mauna Kea it is around 0.2 m. This means that even a very large telescope placed at a good observation site can only offer, without any correction, the same angular resolution as a 20 cm telescope.

1.1.3 ADAPTIVE OPTICS

A way to minimise the problems of seeing is to use adaptive optics (AO), a relatively recent development which was initially used for military purposes. An AO system corrects the wavefront aberrations induced by the atmosphere in real time by reconfiguring the incident wavefront before it reaches the telescope's detectors. The principle of operation relies on the use of curvature sensors, such the Sack-Hartmann sensor (§ 2.8.3). The sensor detects the fluctuations in the wavefront as variations in the local slope and this information is used to create the inverse effect and hence remove the aberrations before the wavefront reaches the detector. This can be achieved with the use of a deformable mirror with the ability to change shape several hundred times every second. Several actuators located at the back surface of the mirror are used for this purpose. The local slope variations on the incident wavefront are corrected by adjusting the tip and tilt at various locations on the deformable mirror.

An AO system requires a reference source of high brightness in order to be effective. Such a source can be, for example, a star of sufficient brightness located close to the object under observation. Part of the wavefront returning from this reference, or guide, star is used in order to evaluate the atmospheric distortion at this part of the sky. Using this information a wavefront coming from a star under observation is reconfigured in order to remove the effects of the atmosphere. Nevertheless this method is not always convenient since sufficiently bright guide stars do not exist at all parts of the sky.

An additional problem has to do with anisoplanatism. This is an effect related to the differences between the light arriving from a guide star and the light arriving from the star under observation. If there is a spatial separation between the two then the light

coming from the star under observation will go through regions of different turbulence from those experienced by the light coming from the guide star (Whiteley 1998). The result is a rapid degradation of the image quality since the AO compensation is not as accurate.

In order to overcome problems associated with natural guide stars, artificial guide stars can be used. Artificial guide stars rely on the use of high-power lasers and they are commonly generated when laser beams tuned at 589.2 nm excite sodium atoms in the mesosphere. When the atoms are excited they emit radiation and in this way they can be used effectively as guide stars. Although artificial guide stars can be used instead of natural guide stars, they still have many limitations such as the fact that variations at the height of the sodium layer in the atmosphere can result to focus errors. Furthermore, there can be variations in the intensity of the photons returning from the sodium layer due to changes in the concentration of sodium atoms in the layer (Devaney 2007). In this case it is still necessary to use a natural guide star in conjunction with the artificial guide star.

The various drawbacks associated with AO limit the overall sky coverage. The field of view to which an AO is effective is defined by the isoplanatic angle (figure 1.2). This is the angular extent after which the two images (from the guide star and the star under observation) become uncorrelated. The isoplanatic angle is proportional to the Fried parameter which in turn varies as $\lambda^{6/5}$ where λ is the wavelength at which observations are made. This implies that AO correction is more effective at longer wavelengths. In visible wavelengths the isoplanatic angle is only a few arcseconds.

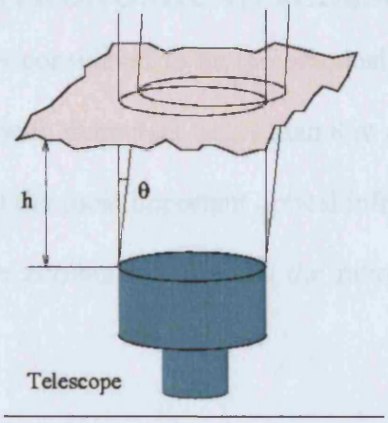

Figure 1.2 The isoplanatic angle θ is the maximum angular separation between a guide star and an object under observation after which the correlation of the two is no longer sustained.

The new generation of large aperture telescopes will have primary mirrors with diameters of at least 30 m, and for example, will enable astronomers to:

- find terrestrial planets in extra-solar systems. The habitable zone close to a star depends on the luminosity of the star (Gilmozzi 2004). In order to search for planets within this zone both very high light gathering power and resolution is required in order to separated the planet from its parent star;
- investigate stellar evolution. A 30 m to 100 m telescope will have sufficient resolution to be used for planet demographics which will provide information for the formation of stars and their planetary systems;
- dark matter investigation. A large telescope will help to observe regions with very large redshift which will provide mass measurement of distant galaxies and offer clues on the evolutionary history of dark matter;

1.2 SUMMARY OF ASTRONOMICAL TELESCOPE PROJECTS

A diameter of 8 m to 9 m is considered to be the practical limit for monolithic mirror manufacture and telescopes with diameters larger than 8 m are classified as Very Large Telescopes (VLTs). Some of the most important optical/infrared telescopes of this class are shown in table 1.1. The number, F# denotes the ratio of the focal length to the diameter of the mirror.

Name	Aperture (m)	Mirror type	Material	F #
Keck I, II	10	Segmented (36 segments 1.8 m diameter each)	Zerodur	1.75
Hobby-Eberly Telescope-HET	9.2	Segmented (91 segments 1 m diameter each)	Zerodur	1.8
Subaru	8.3	Meniscus	ULE	1.8
Antu, Kyeyen, Melipal, Yepun-(Very Large Telescope) VLT	4 telescopes 8.2 m each	Meniscus	Zerodur	1.75
Gemini-South, North	8.1	Meniscus	Zerodur	1.8
South African Astronomical Observatory-SALT	11	Segmented (91 segments 1 m diameter each	Sitall	1.8

Table 1.1 Presently operating very large telescopes

One of the main problems associated with very large monolithic mirrors is the construction of the glass and the transportation from the factory to the telescope site. Grinding and polishing of such large mirrors is also an extremely difficult and expensive process. The way to overcome these difficulties is to introduce segmented primary mirrors. In this case the primary mirror consists of smaller mirror segments which, when assembled together, form the equivalent of a monolithic mirror with the same diameter and optical properties.

The main ELTs under construction, all having segmented mirrors, are presented in table 1.2. Table 1.3 presents a summary of all the future proposals with diameters of primary mirror greater than 30 m.

Name	Aperture (m)	Mirror type	Mirror Material	F #
Gran Telescopio Canarias-GTC	10.4	Segmented (36 segments)	Zerodur	1.65
Twin 8.4 Large Binocular Telescope-LBT	2×8.4	Honeycomb	E6	1.14

Table 1.2 Extremely Large Telescopes under construction

Name	Aperture (m)	Primary mirror segments	Mirror material	F#
OverWhelmingly Large Telescope-OWL	100	2018 segments 1.8-2 m diameter each)	Silicon Carbide, Zerodur	1.42
Euro50	50	618 segments 2 m in diameter	Zerodur	0.85
Thirty Meter Telescope TMT-(previously CELT)	30	1080 segments 1 m diameter each	Zerodur, ULE	1.5
Very Large Optical Telescope-VLOT	20	Segmented	Silicon Carbide	1

Table 1.3 Proposed studies for extremely large telescopes

An interesting case is the initiative for the Euro50 project that is a 50 m[1] class European ELT (figure 1.3) proposed jointly by Finland, Ireland, Spain, Sweden and the United Kingdom. If ever built, the Euro50 primary mirror will be adaptively corrected, and the

[1] In December 11th 2006 a document published by the European Southern Observatory suggested a primary mirror of 42 m in diameter based on the use of 906 segments, 1.45 m in diameter.

resolution will be 2 to 3 milliarcseconds in the visible (Andersen *et. al.* 2003). The adaptive optics will be integrated into the telescope and will be used to correct for the effect of atmospheric blurring. The overall estimated cost for the development of Euro50 is €573 M.

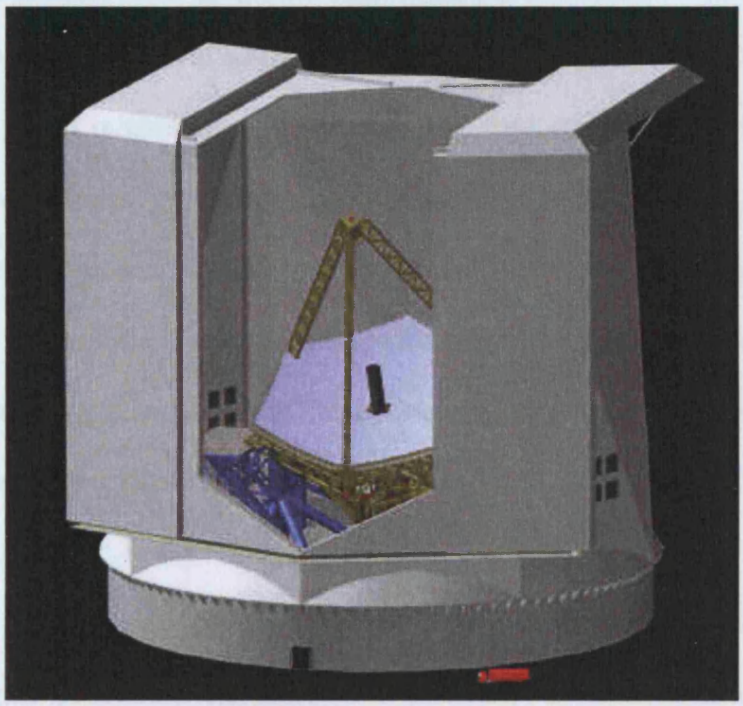

Figure 1.3 The dome and primary mirror of the Euro50 telescope (picture from Euro50 website)

The secondary mirror for the Euro50 will be monolithic and of concave form. The primary mirror will consist of 618 hexagonal segments each with a diameter of 2.3 m across flats and the form of the mirror will be elliptical. The alignment of the segments will be achieved with the aid of actuators. The experience gained by other projects, such as the twin Keck telescopes, will be an essential guide to the construction of the Euro50. The choice of the mirror substrate is an important performance indicator and several options have been considered including Zerodur, metal coated carbon fibre, nickel coated aluminium and silicon carbide (Andersen *et. al.* 2003). The tolerance on the absolute surface form error of the Euro50 primary mirror panels is 36 nm RMS for low

spatial frequencies and 20 nm RMS for high spatial frequencies, with a panel-to-panel reproducibility of ± 0.5 mm for the radius of curvature. The asphericity ranges from 3 μm for the innermost ring of panels to 300 μm for the outermost ring.

1.3 PRODUCTION OF LARGE ASPHERIC OPTICS

The use of aspheric mirrors in a telescope offers significant advantages over spherical mirrors such as the minimisation of spherical and field aberrations, and it implies a simpler telescope design. In a telescope with a spherical primary, several optics would be required to compensate for aberrations, therefore increasing the complexity of the design. As an example the OWL proposal requires two flexible 8 m class active mirrors, a 4.2 m focusing mirror and a 2.35 m flat fast steering adaptive mirror in addition to the primary and secondary mirrors (Dierickx *et. al.* 2000).

The availability of large aspheric mirrors and associated optics is the key to the provision of next generation telescopes for a wide range of applications in the field of cosmology and future space technology and exploration. However, there are relatively few facilities worldwide that are able to manufacture and test such large precision optics. The UK, with its long history of excellence in optical manufacturing and testing could be well placed to secure substantial contracts for many aspects of the design, manufacture, testing and commissioning of these next generation telescopes, providing the necessary metrological underpinning is in place.

A report by Bensammar (2003) into the metrology issues concerning manufacture and testing of large telescope segments stated:

"It is widely regarded in the industry that limitations of metrology are holding back the general take-up of aspherics in a wide range of industrial applications".

Within the next decade there will be several high profile opportunities for the UK optical manufacturing and testing industry. These will involve bidding for work aligned with the manufacture and testing of a variety of large optics. The lack of metrological development in large aperture profilometry, as highlighted by the above cases, could compromise the chances of UK industry securing contracts in these areas or of expensive facilities not achieving their desired goals.

Clearly, with telescope designs considering the use of specialised low expansion materials for optical elements up to several metres in diameter and the overall challenging accuracy requirements of this and similar projects, the requirements on any supporting metrology systems will be equally strict. The development of a method for metrology of large industrial aspheric elements will have a strong influence on the selection of a suitable metrology platform for further consideration and will prove the UK's capability to participate in ELT projects.

Consideration must also be given to the speed of the metrology system. For projects with several hundred panels to be measured, not just at first stage manufacture, but during subsequent cleaning and maintenance operations, the metrology technique used on such multi-panel optics cannot be too slow. If the metrology developed during the project, that is the subject of this thesis, is to be of any use for future customers either with single measurement tasks or those customers with multiple parts for measurement, the system must be capable of metrology of one-off and multiple elements. In the case

of multiple elements, it may be necessary to use one element as a 'master' and then demand good reproducibility of the metrology, rather than absolute accuracy.

1.4 THE NEED FOR NEW ASPHERIC METROLOGY METHODS

The polishing of mirror segments for mass production is one of major challenges in the construction of ELTs. Various techniques for polishing aspheric mirrors are currently available including:

- Continuous (planetary) polishing along with ion figuring. This method was used to construct the segments of the Hobby-Ebberly telescope (Sebring and Ramsey 1996).
- Stressed mirror polishing. The mirror is stressed to the inverse aspheric shape and is polished to a spherical shape. When the mirror is relaxed it obtains the required aspherical shape (Martin *et. al.* 1998).
- Precession polishing. A sub-diameter tool moulds around the local asphere. This is achieved by using a variable area polishing head (Walker *et al* 2001).

Given the constraints on transportation of large optics, it may make better sense for any metrology system to be co-located with the manufacturing capability. Transportation of elements to/from the manufacturing facility at various stages of manufacture in order for interim testing would be very expensive and time consuming. Therefore, consideration must be given to the possibility of on-machine metrology.

Although the methods for grinding and polishing aspheric surfaces are considered to be satisfactory, the measurement techniques are still an area of extensive research. In spite of the fact that spherical surfaces can be easily measured, a universal method, both fast

and accurate enough, to measure aspheric surfaces does not yet exist. Aspheric surfaces are traditionally measured with Fizeau interferometers and the aid of null optics (Burge 1995). The difficulty in this approach is that every asphere requires a matching null lens in order to be tested and the method can only be applied for low-scale production. In addition, null lenses are themselves difficult and expensive to manufacture and to measure.

Other measurement methods include:

- computer generated holograms;
- phase stepping/shifting interferometry;
- two-wavelength holography;
- lateral shear interferometry;
- mechanical/optical profilometry;

Most of the currently available measurement techniques have certain merits with regard to aspheric metrology, however, these are also counterpoised by significant drawbacks.

1.5 OVERVIEW OF THIS THESIS

When in comes to ELT segment metrology several criteria have to be considered including cost effectiveness, high accuracy and fast measurement times.

In order to asses the current state of aspheric metrology most of the available techniques are analysed in detail in chapter 2. The advantages and disadvantages of each technique with regard to ELT segment metrology are analysed. The investigation concludes with

the proposal of a new opto-mechanical measurement method based on the combination of a swing - arm profilometer (SAP) and a wavefront sensor.

The proposal is examined in more detail in chapter 3 where the general principles of swing-arm profilometry are discussed.

In chapter 4 a parametric error model for a generic SAP instrument is presented as a first step towards the design of a functional instrument. The model is consequently used in order to perform sensitivity analysis simulations and to construct a basic error budget.

Chapter 5 presents a first prototype which was constructed using a decommissioned roundness measurement instrument. The prototype was used as a platform where ideas regarding the alignment and adjustability of a generic SAP were tested.

Chapter 6 is an overview of the design of a full-scale SAP prototype. At the beginning of the chapter a design solution for a future hybrid sensing system is presented. Consequently there is a detailed analysis of the evolution of the SAP design including the choice of the mechanical platform, the selection of the subcomponents and the implementation of the instrument.

Chapter 7 presents issues regarding the mechanical probing of the SAP and the traceability of the measurements. A linear scale displacement probe is chosen and a special rig is constructed in order to calibrate the probe against a high accuracy laser interferometer.

The evaluation of the completed instrument is presented in chapter 8 through the measurement of a 640 mm diameter spherical concave optic. The accuracy of the SAP

is evaluated by the comparison to an interferometric measurement. The conclusions from the current work and suggestions for future work are presented in chapter 9.

1.6 AUTHOR'S CONTRIBUTION

The author contributed to various aspects of the project. Initially the successful submission of a project proposal (Efstathiou 2004) supported the case for constructing a prototype Swing-arm profilometer (SAP) to be used to measure the form of large diameter optics in the regime of 1 m as well as a proof-of-concept for metrology of ELT optics. Subsequently a substantial amount of funding was allocated to the National Physical Laboratory, where the author did his placement, by the Department of Trade and Industry (DTI). In January 2004 the project was incorporated into the official National Measurement System Programme for Length, 2002-2005 under the project number 2.3 and title "Profilometry to support large optical manufacturing and testing". The funding was allocated in stages upon the completion of specified project milestones. The successful submission of the project proposal formed the first deliverable of the project 2.3 which according to the DTI was to:

"*Review of the different solutions: Perform a survey of available techniques for profile measurement. Produce report on techniques and identify one technique for further research and prototyping*".

The author subsequently developed a basic mathematical model of a generic SAP and an error budget for the future instrument. Consequently he developed a first scaled-down prototype which was used as a test bed towards the construction of a full scale instrument. He contributed throughout the design of the SAP by providing input on

several design issues regarding sub-component selection and design. Finally he took a major part in the calibration of the SAP contact probe and in the evaluation of the finished instrument through the measurement of a $f/9.5$ spherical concave optic.

Chapter 2

METHODS FOR METROLOGY OF ASPHERIC OPTICS

"La metrologia non é scienza, é un incubo' (Metrology is not a science it's a nightmare)

Giovanni de Sanctis

2.1 DESCRIPTION OF A GEOMETRIC SURFACE

A surface can be defined as the outer boundary of an artefact that separates the artefact from its surroundings. The geometrical characteristics of a surface can be divided into three distinct categories depending on the spatial characteristics one chooses to investigate: surface roughness, surface waviness and surface profile. Surface roughness refers to the smallest wavelength imperfections caused, for example, by machining processes while waviness refers to medium wavelength deviations of the measured surface from the nominal surface. Finally, surface form refers to long wavelength deviations of a surface from its nominal shape. All these descriptions are defined in conjunction with other characteristics of the surface such as the size of the surface and the process used to make it (Whitehouse 1997). The surface form is a descriptor of the overall macroscopic "shape" of a surface and it typically refers to spatial frequencies that are in the regime of under 10 mm^{-1} (Schulz *et. al.* 2000).

2.2 ASPHERIC OPTICS

Aspheric optics are optics with one or both surfaces neither planar or spherical (Hecht 2002). Aspheric optics are commonly employed to reduce spherical aberration as well as distortion and field curvature. Further advantages include the reduction of the optic mass due to smaller surface sag and in certain cases reduction of the overall cost of an optical system (Kumler 2005). A rotationally symmetric aspheric optic can be described through its sag over a chord that is a polynomial

$$Z = \frac{cr^2}{1+\sqrt{1-(1+k)c^2r^2}} + Ar^4 + Br^6 + Cr^8 + Dr^{10} + Er^{12} + \ldots \qquad (2.1)$$

where Z is the sag of the optic and r is the radial distance from the vertex (figure 2.1). The quantity c denotes the curvature on axis and is equal to the reciprocal of the radius of curvature of the optic. The quantity k is the conic constant which is defined as $k = -e^2$ where e is the eccentricity of the corresponding conic section. The first term of equation (2.1) expresses the sag of a conicoid of revolution while the terms A, B, C... represent higher order aspheric coefficients that describe freeform aspheric optics.

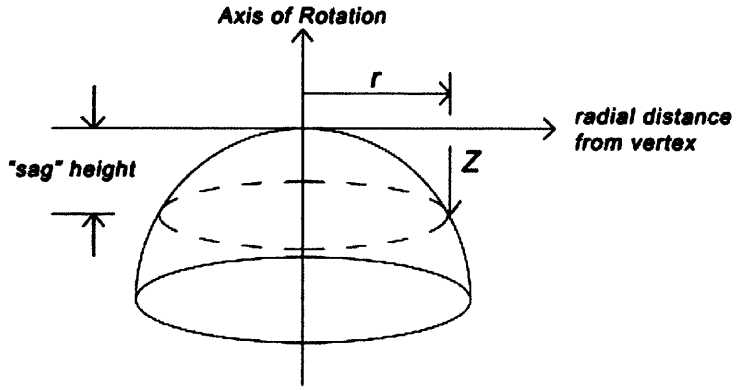

Figure 2.1 An aspheric surface can be described through its sag Z

2.3 SURFACE PROFILE AND SURFACE FORM

The surface profile is a descriptor of surface form and it represents the line generated by the intersection of a surface with a plane perpendicular to it (figure 2.2).

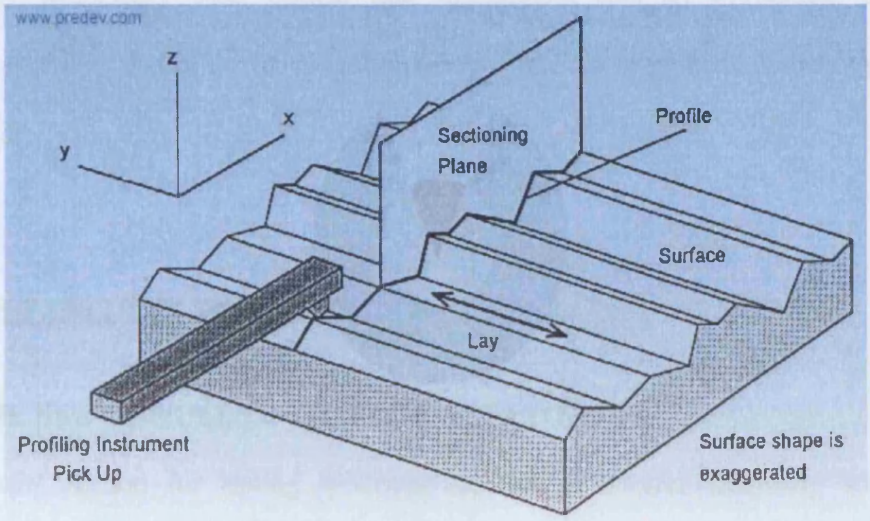

Figure 2.2 The profile of a surface is the line resulting from intersection of the surface with a sectioning plane (picture taken from http://www.predev.com/)

The form of optical surfaces can be measured optically or mechanically. Mechanical measurements are based on the measurement of several line profiles that are then integrated in order to reproduce a 3D map of the form of the surface. These profilometers measure directly height deviations of the actual surface from the nominal reference with the aid of displacement sensor probes. The most well know example of such an instrument is that of the Form Talysurf (Taylor-Hobson website). Optical techniques are based on full-field illumination (Burge 1996) where the whole surface is measured in a single measurement, or sub-aperture illumination (Harasaki 2000) where parts of the surface are scanned and the measurements are integrated to yield the surface shape. Optical methods generally offer faster measurement times since they provide larger surface coverage than mechanical scanning. Both optical and mechanical measurement techniques have advantages and disadvantages with regard to metrology

of conventional spherical optics. However, when it comes to aspheric optic measurements certain problems arise that have to do with the fast changing gradient of the surface. The current chapter is a review of the majority of the available aspheric metrology techniques both optical and mechanical and an evaluation of these techniques. At the end of the investigation a new approach to aspheric metrology will be suggested.

2.4 NULLING TECHNIQUES

2.4.1 THE USE OF NULL OPTIC COMPENSATORS

A common method for testing spherical surfaces is interferometrically where the lens/mirror under test is compared against a corresponding test plate. For example, a convex mirror is measured with a matching concave test plate whose radius of curvature matches the radius of curvature of the test optic. However, in the case where the mirror under test is aspheric, a custom aspheric wavefront needs to be used implying that an aspheric null optic has to be constructed. This constitutes the main drawback of using null compensators since the construction of the null optics is difficult, expensive and time consuming. The construction of aspheric null optics can be as difficult as the construction of the actual test optics. Null compensators have to be tested themselves and flaws on the null will result to an incorrect measurement of the test optic. It is therefore apparent that conventional null testing cannot be appropriate for metrology of mass produced optics (*i.e.* metrology of telescope mirror segments) since a large volume of aspheric nulls would be required.

2.4.2 COMPUTER GENERATED HOLOGRAMS

Another approach to aspherical optical testing is the use of computer-generated holograms (CGH). CGHs are synthetic holograms that are employed in order to compensate for the aspheric departure of the test optic. The major advantage of using CGHs is that the need for aspheric null optics is eliminated. A typical CGH is shown in figure 2.3.

Figure 2.3 A typical CGH

The CGH pattern is found by calculating the theoretical fringe pattern that would emerge if the plane reference wave interfered with a perfect wavefront produced from a hypothetical perfect optic. The method was introduced by Lohmann and Paris (1967) and it has the advantage that no optic has to physically exist in order to produce the CGH as long as the mathematical description of the optic is available. Once the interference pattern is calculated it is plotted by a plotter and in turn is photographically reduced to match the theoretical fringe positions. The next step is to record the calculated fringe pattern in a transparent medium using specialised plotting devices according to the calculated fringe pattern. Finally, in order to perform the null test the CGH is placed in an interferometer as shown in the figure 2.4.

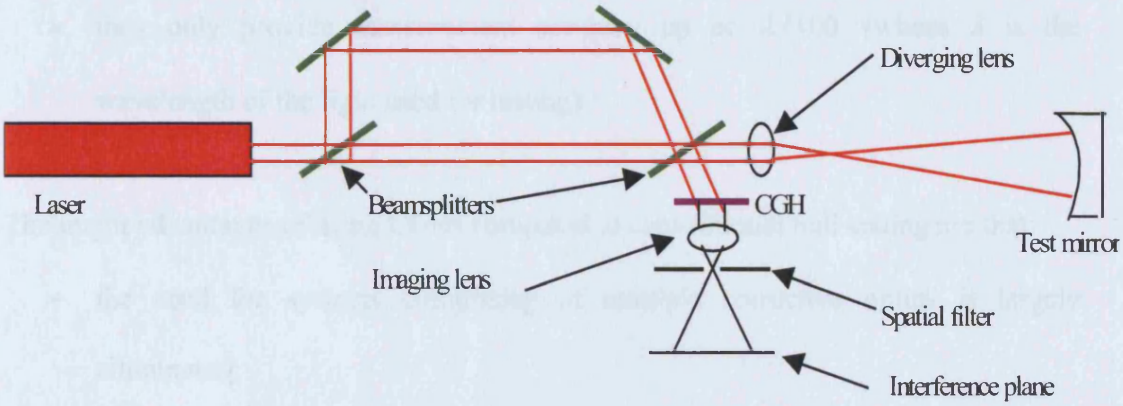

Figure 2.4 CGH testing setup

An incident beam is split into two components one of which travels to the test mirror while the other is reflected around a loop by mirrors. The second beam and the one reflected from the optic recombine at the second beamsplitter and are directed through the CGH. The function of the CGH is to convert the aspheric wavefront from the test mirror into a plane wavefront. Eventually the interference of the two wavefronts is used to measure the departure of the mirror under test from its nominal shape.

CGHs have been extensively used in the past, but have many disadvantages such as:

- the construction of test plates is difficult, expensive and time consuming;
- the alignment of the CGH in the interferometer can be difficult;
- writing the CGH is a process that introduces many errors such as distortion from the plotter or incorrect hologram size during photoreduction;
- in the case of telescope mirror segment fabrication there may be many different families of segments with various shapes. This means that CGHs for all the different shapes have to be constructed;

- they only provide measurement accuracy up of $\lambda/100$ (where λ is the wavelength of the light used for testing).

The major advantages of using CGHs compared to conventional null testing are that:

- the need for systems comprising of multiple corrective optics is largely elliminated;
- they are simpler to construct and less expensive that conventional null optics;

2.4.3 COMBINATION OF CGH AND NULL OPTICS

Another technique for testing aspheric optics is to combine CGHs with spherical null optics. In this case the interference rings of the CGH are made of metal and are imprinted onto the test plate. The rings of the CGH pattern are positioned such as to produce the desired wavefront (Burge 1995). The aspheric optic under test is held a few millimetres away from the spherical reference and is illuminated by laser light as shown in figure 2.5. Since the air gap is small, atmospheric effects, such as turbulence and temperature changes are minimised. The reference wavefront is produced when the incident radiation is diffracted by the CGH and strikes the test mirror. The reflected beam forms the test wavefront that interferes with the incident wavefront to generate a fringe pattern. The resulting interference pattern reveals the errors in the surface of the mirror under test (Pfeifer *et. al.* 1992).

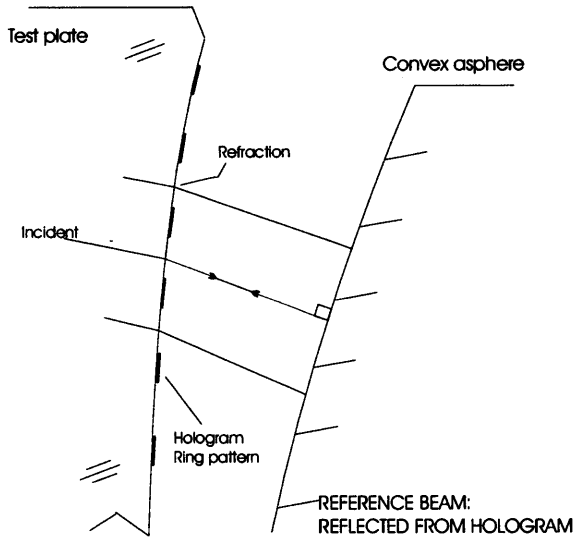

Figure 2.5 The measurement of a convex asphere using a combination of CGH and null optics

As in the case of conventional CGHs the printing of a CGH on a test plate can generate significant errors such as incorrect positioning of the CGH rings. Custom laser writers plot circular rings onto the spherical test surface while the substrate rotates. The hologram is manufactured using thermo-chemical writing (Burge 1996). This process has many sources of error including vibration and misalignment of components in the set-up. In particular misalignment and insufficient control of the laser head According to Liu (2004) the CGHs produced by this method are inferior compared to the ones produced by photolithography. The method still requires the construction of actual test plates and can, therefore, prove inadequate for ELT segment metrology. The method is accurate to $\lambda/100$.

2.4.4 PROJECTION OF CGHS ONTO SPHERICAL TEST PLATES

Another aspheric measurement method involving CGHs proposed by Burge (1999) is based on the projection of the CGH on a spherical test plate. The versatility of the method lies in the fact that several types of segments can be tested using a single test plate and several CGHs. The CGHs are not imprinted on the test plate but are accurately

written onto conventional substrates using e-beam lithography. Since the holograms are not imprinted on the test surface but are projected onto it, various shapes can be tested simply by changing the hologram whilst keeping the same test plate. One of the main disadvantages of projecting CGHs onto spherical test plates is the complexitiy of constructing large test plates from highly transmissive material. Also the accuracy of the method is limited to $\lambda/100$.

2.5 NON-STATIC INTERFEROMETRIC TECHNIQUES

2.5.1 GENERAL PRINCIPLES

In order to increase the precision of optical, interferometric measurements a variety of methods have evolved where consecutive measurements are taken, each measurement having a phase difference with respect to the other. These methods include phase-stepping interferometry (PSI), two-wavelength holography (TWH) and two-wavelength phase-shifting interferometry (TWPSI), which can be used for accurate non-destructive measurement of aspheric optics. The phase difference is achieved by using piezoelectric actuators that move the interferometer optics to predefined intervals.

2.5.2 PHASE STEPPING/SHIFTING INTERFEROMETRY

Phase-stepping interferometry is a method where a step-like phase shift is introduced between the test and reference wavefronts. The shape of a wavefront or a surface under test can be determined from a phase map, which is calculated from the measured intensities (Creath *et. al.* 1985). The set-up can be a Twyman-Green interferometer and the phase shift can be obtained by moving the mirror in the reference arm by means of piezoelectric actuators. The phase can be altered many times and the intensity of the

interferogram is recorded for every phase change. The intensity data are then used to calculate the phase of the test wavefront and consequently the optical path difference between the reference and object wavefront.

Phase-shifting interferometry is the same as phase-stepping interferometry with the only difference that the phase change is continuous and the value of the intensity is integrated over the time needed to produce the phase shift (Creath *et. al.* 1985).

PSI has some serious drawbacks, for example, it is very sensitive to vibration, which can severely distort the interference pattern. Furthermore, conventional phase PSI makes use of a single wavelength under the assumption that the optical path difference between adjacent pixels in the detector is not greater than $\lambda/2$. However, when the surface under test is very steep the phase difference between adjacent pixels becomes larger than 2π and discontinuity problems arise (Cheng *et. al.* 1985). The accuracy of the method is up to $\lambda/100$.

2.5.3 TWO-WAVELENGTH HOLOGRAPHY

Two-wavelength holography (TWH) is a method where a combination of visible wavelengths is used in order to produce long synthetic wavelengths capable of measuring steep surfaces. Two-wavelength holography is divided into two main categories: single and double exposure.

In single exposure TWH, a laser of wavelength, λ_1, is used to record the hologram while the test surface is in place. The hologram is developed and is placed back in the initial position where it is illuminated by light of a different wavelength, λ_2. The interference

pattern is filtered using spatial filters and the resulting fringes are spaced as if they were created by an equivalent wavelength λ_{tot} given by

$$\lambda_{tot} = \frac{\lambda_1 \lambda_2}{|\lambda_1 - \lambda_2|}. \tag{2.2}$$

The sensitivity of the measurement can be adjusted by altering the combination of the wavelengths (Creath *et. al.* 1985). The flexibility of the method relies on the fact that there are many commercially available lasers emitting at various wavelengths, which can be combined in order to obtain the desired equivalent wavelength.

The main problem with single-exposure, two-wavelength, holography has to do with atmospheric variations. The initial fringe pattern is recorded at one instant of time from a wavelength, λ_1. It is then placed back in the interferometer and illuminated by an interference pattern produced by a laser of wavelength λ_2. However, in the time between recording and illumination the atmospheric conditions may change. Air turbulence and may result in small changes in the refractive index around the test area. These changes in the refractive index will consequently alter the effective wavelength of the laser light and distort the fringe pattern. This problem can be minimised by applying double exposure.

Double exposure is similar to single exposure but the hologram is recorded simultaneously at both wavelengths, λ_1, λ_2, and is then illuminated by either λ_1 or λ_2. Again the results are the same as if the optics under test were illuminated by an equivalent wavelength given by equation (2.2). However, since both fringe patterns are recorded simultaneously the effect of atmospheric variations is minimised.

The drawbacks of both single and double exposure TWH are that they are only accurate to $\lambda/100$ and the contrast of the fringes is usually low.

2.5.4 TWO-WAVELENGTH PHASE-SHIFTING INTERFEROMETRY

Two-wavelength phase-shifting interferometry (TWPSI) is a combination of two-wavelength holography and phase-shifting interferometry (PSI). The TWPSI method is fundamentally the same as conventional phase-shifting interferometry but two wavelengths are used in order to achieve sensitivity similar to that of two-wavelength holography. The expression for the OPD is given by

$$OPD = \frac{\phi \lambda_{tot}}{2\pi} \tag{2.3}$$

where

$$\lambda_{tot} = \frac{\lambda_1 \lambda_2}{|\lambda_1 - \lambda_2|}. \tag{2.4}$$

TWPSI combines the accuracy of TWH with the versatility of PSI. In TWPSI there is no need for intermediate holographic recording, in contrast to conventional TWH. In addition, the sensitivity is greater compared to that of conventional PSI since longer equivalent wavelengths are used, therefore, the 2π ambiguities are removed. The accuracy of TWPSI can be $\lambda/100$ (Creath *et. al.* 1985).

2.5.5 MULTIPLE-WAVELENGTH PHASE-SHIFTING INTERFEROMETRY

Multiple-wavelength phase-shifting interferometry (MWPSI) is a further development of two-wavelength phase-shifting interferometry. MWPSI uses three wavelengths in

order to achieve measurements of steep profiles that cannot be performed with TWPSI. According to Cheng and Wyant (1985) the idea behind MWPSI is to use three wavelengths, λ_a, λ_b and λ_c (where $\lambda_a < \lambda_b < \lambda_c$) and combine them in such a way so as to create a longest equivalent wavelength λ_{eql} and a shortest equivalent wavelength λ_{eqs}. The wavelength λ_{eql} can be used in order to correct the 2π phase ambiguities in the phase of λ_{eqs}, and then the corrected phase of λ_{eqs} can be used in order to correct the ambiguities in λ_a, λ_b and λ_c. In this way it is possible to test steep slopes that cannot be tested using TWPSI.

2.6 MECHANICAL PROFILOMETRY TECHNIQUES

2.6.1 STYLUS PROFILOMETRY

Stylus-type profilometry is a common method of measuring the profile of various surfaces including engineered surfaces and mirrors. In mechanical profilometers, the measurement is obtained by a stylus tip that moves at constant speed relative to the SUT and scans across the surface under test (Morrison 1995). In some profilers the SUT moves under a stationary stylus although there are many designs where the SUT if fixed and the stylus is moving. The stylus contacts the SUT directly and the height variations are translated into electrical signals by suitable transducers. The signal is amplified and used in order to convert the tip displacement into real height data. To do this an electrical circuit is required to filter and digitise the signal. The stylus tip itself is usually spherical and made of diamond or ruby.

2.6.2 BRIDGE TYPE PROFILOMETERS

An example of a stylus profilometer is the SPLOT, which stands for Stylus Profilometry for Large Optics Testing. The initiative for the design of the SPLOT was the measurement of the GEMINI telescope twin mirrors (Yang 2000). The SPLOT is a bridge-type proflilometer that follows the well-established method of using three rectilinear *x*-, *y*- and *z*- axes to move a probe across the SUT (William 1990). The *x*-, *y*- *z*- profilometers are usually built around precise aerostatic slideways and are servo-driven. The SPLOT consists of a contact probe system, a laser reference system and an interferometric distance measuring system (Yang 2000). The laser reference system propagates a beam in the air and defines the line of reference for the measurement. The interferometric system is used to maintain constant height between the reference line and the SUT. All the subsystems are mounted on a granite bridge above the SUT as shown in figure 2.6.

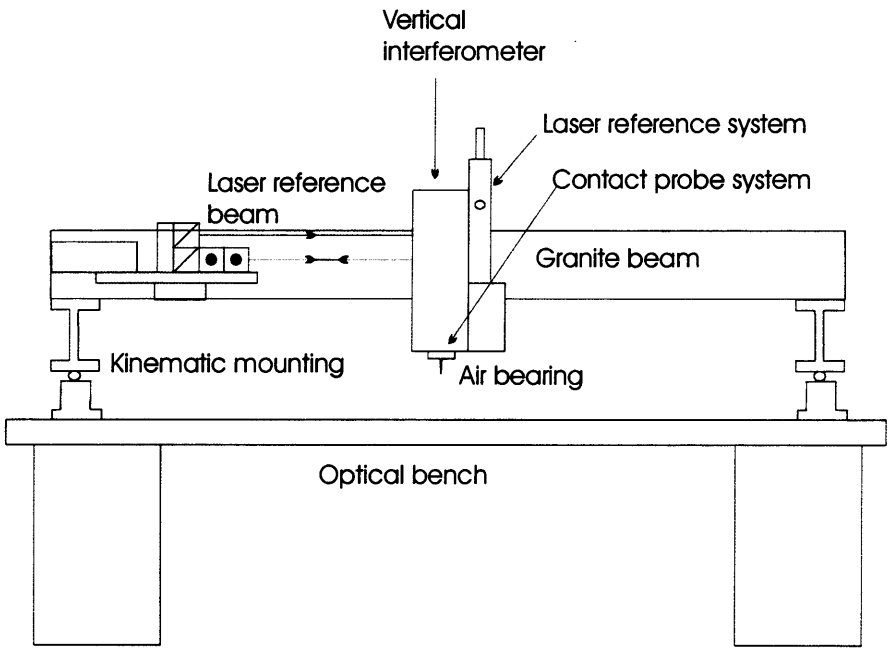

Figure 2.6 The SPLOT profilometer. Figure reproduced from Yang (Yang 2000)

The geometry of SPLOT provides the ability to measure profiles across the diameter of a SUT. Similar to the SPLOT is the Dual Gauge Profilometer (DGP), which measures, in the *x*-, θ- and *z*- directions (Quandou *et. al.* 2000). The profilometer makes use of a straight edge as a reference and is capable of measuring non-symmetric off-axis mirrors of 600 mm in diameter with a reported accuracy of 4 μm peak to valley (PV). The common problem of profilometers such as the SPLOT is the limited dynamical range. When measuring large surface sag the probe deviates from normal incidence as it moves towards the edges of the mirror. This results to a cosine error. Furthermore surfaces of large sag require long probe styli which bend as the probe traverses the SUT. Finally the linear guideways have relatively low motion accuracy in the range of 1 μm.

2.6.3 THE SWING-ARM PROFILOMETER

The swing arm profilometer (SAP) is a measuring instrument, which is designed according to the philosophy of the cup-wheel generators (Angel and Parks 1982). The geometry of a SAP is depicted in figure 2.7. The profilometer has four major subsystems: the probing system, the profilometer arm, a profilometer rotary bearing and a component rotary bearing. The arm is mounted in the profilometer bearing and the probe is positioned to be normal to the SUT. As the bearing rotates, the probe scans across the SUT acquiring arcuate profiles.

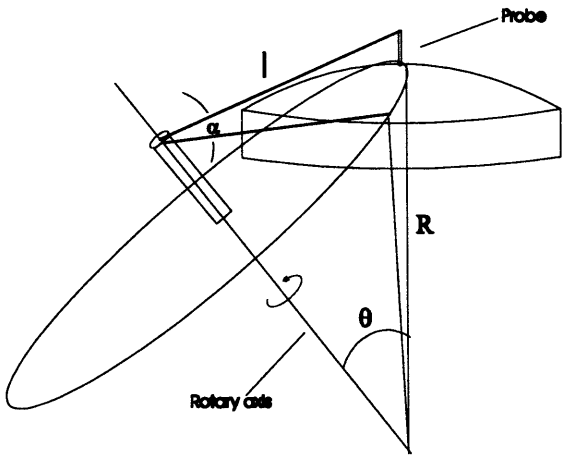

Figure 2.7 The geometry of a swing-arm profilometer (Burge 1995)

If the axis of rotation of the rotary bearing is made to coincide with the centre of curvature of the SUT then the probe follows the curvature of the SUT. The necessary condition for this is given by

$$\theta = \sin^{-1}(l/R) \tag{2.5}$$

where l is the distance between the probe tip and the arm rotation axis and R is the radius of curvature of the surface under test (Anderson and Burge 1995).

One of the main benefits of the SAP method is that when scanning aspheric surfaces the displacement of the probe at the end of the arm provides a direct measure of the asphericity of the surface. The method, however, cannot provide measurements along the diameter of the test surface since the swing-arm geometry only allows arcuate scanning.

The main problems associated with the SAP, some of them common to other contact profilers, are:

- Deflection of the probe during continuous scanning;
- Destructive nature of the measurement. Mechanical contact between the probe and the SUT can cause scratches on the SUT;
- Measurements are slow and can only generate line scans. A surface map can only created by combining multiple line scans.

The disadvantages of the SAP are counterpoised by numerous benefits: a SAP can be easily integrated to a polishing machine for interim profile monitoring while its unique geometry allows the measurement of a variety of surfaces, spherical and aspherical, convex and concave as well as optics of different radii of curvature and size. The versatility of the SAP means that it can measure optics ranging from flats to hemispheres with a single set-up. In addition it has a proven accuracy of 50 nm RMS over 1.8 m diameter surfaces (Burge 1997).

2.6.4 COORDINATE MEASUREMENT MACHINES

A commonly used instrument, based on mechanical probing, is the coordinate measurement machine (CMM), which is an instrument for measuring a variety of three-dimensional structures. A typical CMM is a structure built around three perpendicular *x*-, *y*- and *z*-translational stages which form a Cartesian coordinate system (Bosch 1995). There are several types of CMMs that differ in the mechanical set-up, however, they all provide measurements of three-dimensional objects through the use of a contact, or optical, probe that moves within the reference frame. The most common type of CMM is the moving bridge type that is depicted in figure 2.8.

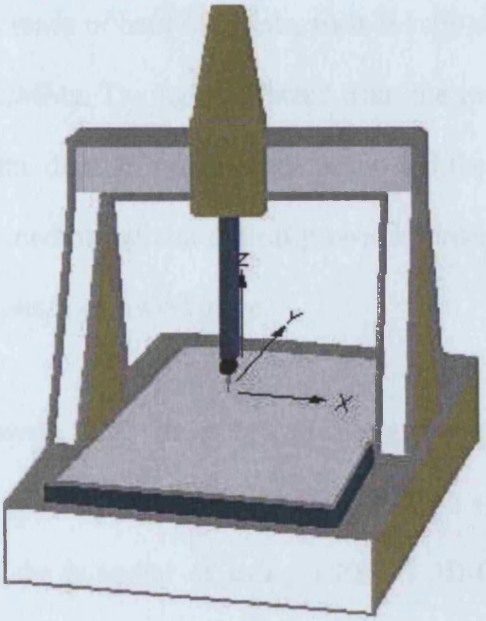

Figure 2.8 Schematic of a CMM

In this moving bridge CMM there are two columns, which form a bridge and provide movement in the *y*-direction, and a probe arm that moves in the *x*-direction. The probe head can also move in the *z*- direction and all the mechanical movements are made using precision air bearing slideways.

The probe contacts the test object to obtain the coordinates of a specific feature and moves to another position to obtain a new measurement. CMMs can also operate in 'scanning' mode, where the probe maintains contact with the SUT, and the CMM is servo controlled during a scan, to nominally move the probe along the features of a given SUT. However, the uncertainty when operating in scanning mode is significantly worse than when performing individual probing operations, due to the kinematic errors of the machine and the difficulty in accurately determining the probing deflection vector.

CMM contact tips are made of hard materials, such as ruby or diamond. Optical probes can also be used on CMMs. The light reflected from the test surface is collected and analysed to measure the distance between the probe and the workpiece. Some CMMs use a combination of mechanical and optical probes in order to obtain complementary information about the shape of a workpiece.

CMMs can in principle be used for surface profiling of optical components and have been employed in the past for the measurement of aspheric surfaces. Otto (*et. al.* 2000) for example reported the potential of using a ZEISS 3D-CMM (figure 2.9) for the measurement of the GEMINI 1 m secondary mirrors. The CMM was used along with a high speed scanning probe and the accuracy of the mid spatial frequency deviations was better than 100 nm rms.

Nevertheless the use of CMMs for large surfaces in the reign of 2 m is not recommended. The commonly used step-and-repeat measurement proves slow, especially when it comes to large volume production of ELT segments and the accuracy cannot be as good as the 20 nm necessary for ELT applications.

Figure 2.9 The UPMC 850 CARAT S-ACC, 3D ZEISS coordinate measurement machine (picture taken from the ZEISS specification booklet)

2.7 OPTICAL PROFILOMETRY

Optical profilometry is based on sub-aperture scanning of the test surface by means of an optical probe. Optical scanning systems can have a field of view at the focus of an optical system and do not need an external reference to operate (Schmidt *et. al.* 2000). The measurement of surface profile is usually achieved using coherent light sources. Laser profilometry is a method that brings together stylus profilometry and interferometric testing techniques.

2.7.1 ANGLE MEASUREMENT TECHNIQUES - AUTOCOLLIMATION

Another optical profiling technique is based on the integration of slope values obtained by autocollimation (Ennos and Virdee 1986) on reflecting surfaces with an accuracy of tenths of seconds of degree. Laser autocollimation is based on the measurement of the

change in the angle of a laser beam that is reflected by the SUT. The values obtained by autocollimation are integrated with respect to the distance to obtain profile height (Virdee 1986).

The autocollimation technique is particularly efficient when a pentaprism is used in order to direct the laser beam onto the SUT. The pentaprism has the advantage of deflecting a beam at right angles and is insensitive to tilt. The method is good for large optics and can be used to test both convex and concave surfaces (Malacara 1992). The use of a pentaprism has been applied in the past for measurement of x-ray microscope reflecting objectives (Ennos and Virdee 1982).

The principle of profile measurement using autocollimation is illustrated in figure 2.10.

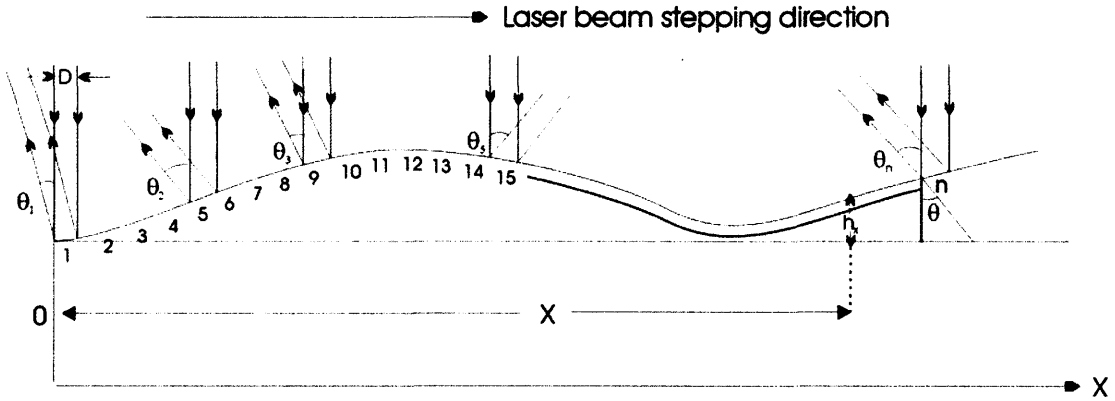

Figure 2.10 Principle of profilometry using autocollimation

A laser beam is stepped along the SUT starting from a position where the horizontal distance, x is assumed to be zero. The angle of the reflected beam changes according to the variations on the slope of the SUT. After the beam has traversed a horizontal distance, x, the profile height at that point is calculated as

$$h_x = \int_0^x \frac{\theta}{2} dx = \sum_{n=0}^{n=X/d} \frac{\theta_n}{2} D \tag{2.6}$$

where θ_n is the angle of reflection, D is the width of the laser beam, n is the number of steps and h_x is the height of the SUT after the laser beam has traversed n steps in the x-direction. According to equation (2.6), the laser beam is stepped along the SUT at equal steps of length equal to the beam diameter, D. The reflected beam is collected by a lens and is focused on a photodetector. A diagram of a typical, commercially available, autocollimator is shown in figure 2.11.

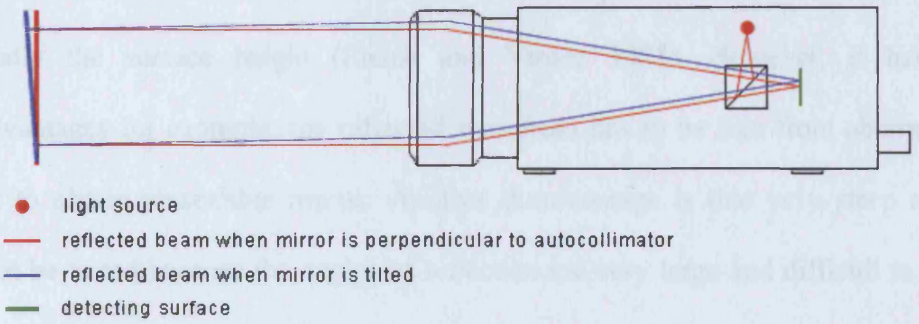

Figure 2.11 Schematic diagram of a typical autocollimator (figure taken from http://www.micro-radian.com/index.html)

The principle of operation of the autocollimator telescope is shown in figure 2.12. A reticule is illuminated by a laser and is focused at infinity by the telescope. The image of the cross lines travels to the surface under test where it is reflected and returns back to the autocollimator telescope. The tilt can be evaluated by the difference between the reflected image and the reticule.

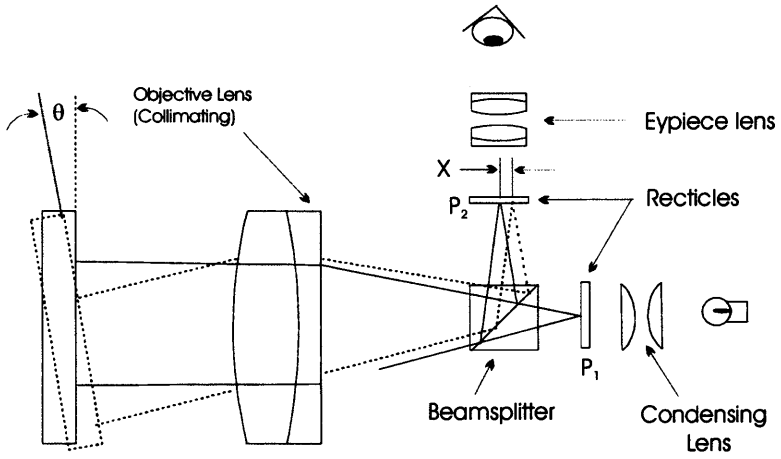

Figure 2.12 Principle of operation of autocollimation telescope

Autocollimation is a measurement technique that provides a means of measuring optically the surface height (Ennos and Virdee 1985). However, it has many disadvantages for example, the reflected wavefront has to be free from aberrations in order to obtain reasonable results. Another disadvantage is that very steep aspheres cannot be tested because the angles of reflection are very large and difficult to pick-up by the detector. Finally, it should be mentioned that the drift of the beam due to environmental fluctuations, such as turbulence and temperature changes, as well as long measurement times can degrade the repeatability of the measurement.

2.7.2 SLOPE MEASUREMENT TECHNIQUES – LONG TRACE PROFILER

The long-trace profiler (LTP) is a slope-measuring instrument that can measure the profile of optical surfaces with nanometre accuracy. The LTP was originally employed for measurement of optical components used in synchrotron radiation systems (Takacs *et. al.* 1988). The LTP measures the local slope differential using two separate laser beams. The method used is also known as pencil beam interferometry (Irick 1992). The two laser beams are reflected from the SUT and are combined to create an interference

pattern. During measurement the SUT remains stationary and the optical head moves across it on a linear air-bearing slide. The interference pattern is focused onto CCD detectors through a lens. The LTP takes many measurements of the slope at several points on the SUT and these values are integrated to obtain the local surface height. A detailed mathematical description of the how the surface height is obtained from the slope data is given elsewhere (Takacs *et. al.* 1988 and Irick 1992). A schematic diagram of the optics in a common LTP is shown in figure 2.13.

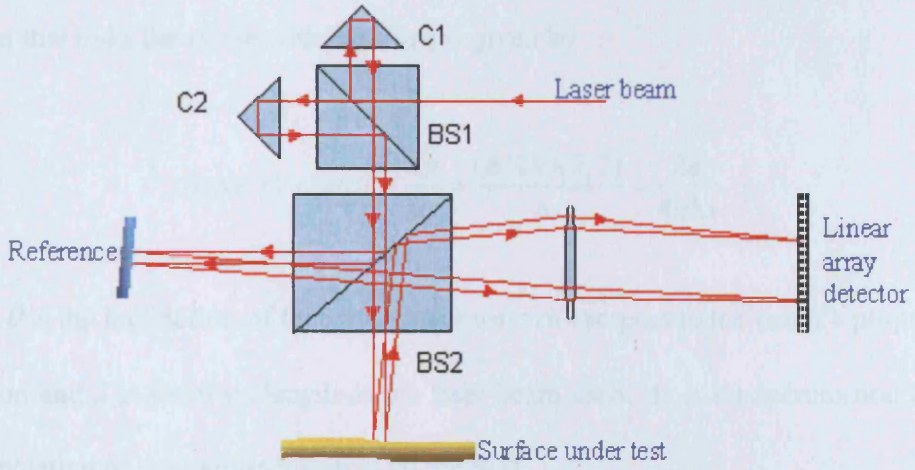

Figure 2.13 Schematic of the set-up of the optical components in the long-trace profiler

With reference to figure 2.13, the laser beam enters the first beam-splitter (BS1) and splits into two component beams. Each beam is reflected by a retroreflector (C1 and C2) and enters the beam splitter again. The passage of the beams through the retroreflectors means that they are collinear and laterally displaced as they emerge from BS1. The beam separation can be altered by altering the position of the retroreflectors and can be varied from $d = 0$ (where the two beams overlap) to several millimetres allowing optimisation of the sampling period. A common beam separation is 1 mm. The spot size can also be altered by introducing a lens before the incident beam enters BS1.

After leaving BS1, the beam pair enters a second beam-splitter (BS2) where it is further divided into a pair of reference and test beams. The components of the test beam-pair scan the SUT, as the profiler moves along, while the reference beam pair is reflected by the reference mirror. Both pairs create interference patterns that are used to investigate height variations on the SUT.

By measuring the intensity, the relative phase between the two interfering beams can be obtained. The phase data in turn can be used to obtain local slope information. The relation that links the phase with the slope is given by

$$slope(x) = \tan\theta = \frac{\Delta y}{\Delta x} = \frac{(\phi/2\pi)(\lambda/2)}{\Delta x} = \frac{\lambda\phi}{4\pi\Delta x} \tag{2.7}$$

where θ is the inclination of the optic under test with respect to the beam's propagation direction and λ is the wavelength of the laser beam used. Δx is the incremental change in the position of the two laser beams on the SUT.

The advantages of the long-trace profiler method rely on the fact that:

- it is a non-contact method so damage to the SUT is eliminated;
- variations in the vertical between the SUT and the probe do not affect the measurement significantly (Schmidt *et. al.* 2000);
- the LTP performs differential slope measurements and is, therefore, insensitive to vibration.

However, the use of the long-trace profiler also has many disadvantages such as:

- it cannot measure the profile of steep aspheres due to the large angles of reflection;

- angular displacements of the optical head about the y-axis can cause large errors;
- its accuracy has a very sensitive dependence on temperature variations. A stable temperature of at least $\pm 0.1\ ^{0}C$ needs to be maintained in order to avoid significant phase errors.

2.7.3 CURVATURE MEASUREMENT TECHNIQUES

Another method for measurement of complex surfaces is based on the measurement of curvature. Measurements of the curvature of a surface are less affected by errors induced by angular or vertical movements of the SUT in relation to an optical head because the curvature is an intrinsic property of the surface (Schmidt *et. al.* 2000). A method based on curvature measurement has been developed at Physikalisch-Technische Bundesanstalt (PTB) and it is called large area curvature scanning (LACS).

In LACS, the measurement is obtained by employing an optical curvature sensor which is scanned across the optic's diameter maintaining a direction normal to the optic. The distance of the optical sensor with respect to the SUT, and the angular position of the probe, are monitored and adjusted in real time in order to ensure that the probe is vertical at all times and that the distance between the SUT and the probe is kept constant.

The sensor scans the SUT at small steps and an interferogram is recorded at every step. The interferograms are used to calculate the topography at the particular point of measurement and the topographies are in turn used to calculate the curvature along a scan line.

The relationship between the curvature *c(x)* and the surface profile *W(x)* (in Cartesian coordinates) is given by

$$c(x) = \frac{W''(x)}{\left[1 + \left(W'(x)^2\right)\right]^{3/2}}. \tag{2.8}$$

Therefore, by measuring the curvature *c(x)* and solving the second order differential equation for *W(x)* the surface profile can be calculated.

The actual curvature sensor is a small phase-shifting interferometer. Such sensors are available commercially and in the LACS technique a FISBA's μPhase® compact Twyman-Green interferometer with an integrated phase shifter and a CCD camera is used. The sensor captures a small area (usually 1 mm to 3 mm) and creates a local topography map. The importance of this is that since the test area is small the number of fringes is not very large as happens with other methods, therefore, steep aspheres can be measured.

One of the obvious advantages of LACS is that the use of a curvature sensor means that the positioning errors due to the vertical movement or angular displacement of the optical head are minimised. Contrary to slope and angle, curvature does not depend on the absolute position of the SUT or the sensor with respect to a defined coordinate system. In other words, small movements of the SUT or the curvature sensor with respect to the coordinate system do not affect the quality of the measurement and nanometre accuracy is realisable.

2.8 OTHER METHODS FOR ASPHERIC METROLOGY

2.8.1 LASER TRACKING

The laser tracker is an optical device that measures the coordinates of a retroreflecting target (RT) positioned on the SUT. Laser tracker systems make use of a fringe counting interferometer in order to measure the lateral movements of the target retroreflector. According to Edgall (1983) the method can provide direct determination of the radius of curvature of a SUT. Laser trackers are extensively used in industry for quality inspection of automotive parts, measurement of aircraft dimensions, *etc.* and can be employed for the measurement of aspheric optics. The operation of a common laser tracker system is shown in figure 2.14.

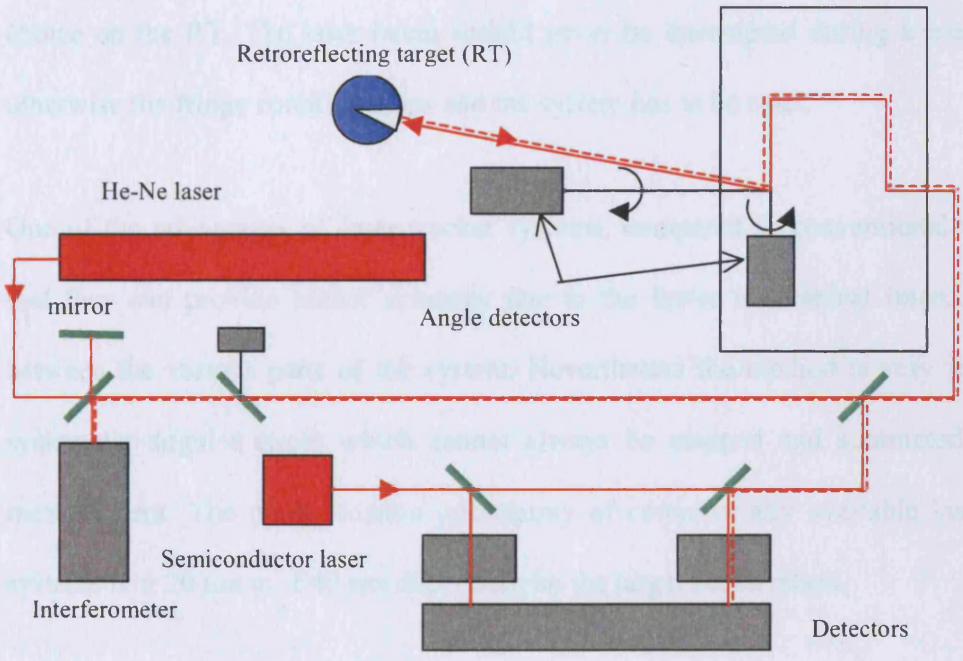

Figure 2.14 The principle of the laser tracker (from www.qualitydiget.com)

With reference to figure 2.14 the beam from a laser is steered on to the retroreflector, where it is reflected and re-enters the tracker at the same point from which it initially emerged. A part of the reflected light enters an interferometer that measures the distance

between the RT and the laser tracker. Furthermore, angular encoders provide information on the angular orientation of the RT and by combining the angular and distance data the coordinates of the RT can be determined. The last step in the measurement process is to subtract the dimensions of the RT from the measurement in order to obtain the real surface shape of the SUT.

In a laser tracker system the beam should be kept centered at a particular point of choice on the RT in order to provide reliable information. If the beam is displaced the measured coordinates will be false. In order to tackle this problem, a portion of the reflected beam is fed to a detector capable of detecting the lateral position of the beam. If the beam is offset the tracker adjusts its position so it is always pointed at the point of choice on the RT. The laser beam should never be interrupted during a measurement otherwise the fringe counting stops and the system has to be reset.

One of the advantages of laser tracker systems, compared to conventional CMMs, is that they can provide higher accuracy due to the fewer mechanical interconnections between the various parts of the system. Nevertheless the method is very sensitive to systematic angular errors which cannot always be mapped and subtracted from the measurement. The point location uncertainty of commercially available laser tracker systems is ± 20 μm to ± 40 μm depending on the target acceleration.

2.8.2 MULTILATERATION

Multilateration is a technique similar to laser tracking and it employed by Greenleaf (1983) for the construction of a self-calibrating measurement machine for the measurement of large aspheric mirrors. In contrast to laser tracking, where a single laser

beam is used, multilateration techniques make use of three or more beams and the measurement of the coordinates is obtained using triangulation. The measuring machine developed by Itek Optical Systems (Edgall 1983) uses four laser beams and is shown in figure 2.15.

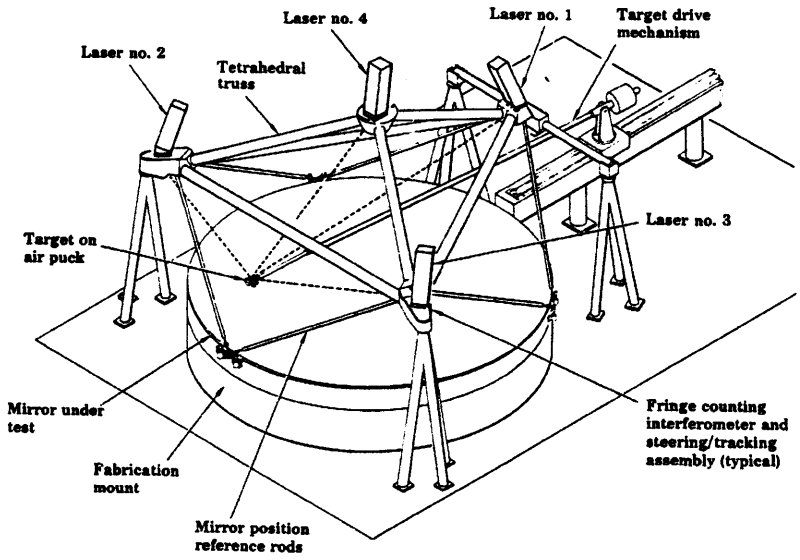

Figure 2.15 The Itek multilateration machine

With reference to figure 2.15, the machine uses four distance-measuring interferometers that are placed at the corners of a tetrahedron. The three interferometers are separated from a retroreflecting target (RT) and form the coordinate reference system for the machine while the fourth interferometer is used for self-calibration. The coordinate reference system is virtual (Estler *et. al.* 2002) and due to self-calibration there is no need for a structure of high accuracy. The retroreflector slides above the SUT on a layer of air without contacting the test surface. The movements of the SUT can be detected using reference rods, which are attached at one end to the SUT and at the other end to transducers that detect small movements.

One of the difficulties associated with multilateration, is that the four laser beams should remain focused on a single point on the retroreflector in order to avoid tracking errors. The beam steering mechanisms, however, introduce many uncertainties and make this difficult. It should also be mentioned that, as in the case of the laser tracker, the measurement should be continuous otherwise the fringe counting is interrupted and the measurement has to be re-started.

To summarise, in multilateration:

- the retroreflector does not touch the SUT, therefore, it is safe to test soft surfaces;
- the machine is self-calibrating and the reference coordinate frame is virtual. This means that there is no need for an ultra-precise mechanical structure;
- multilateration machines can be used during grinding in order to determine surface profile prior to polishing. This reduces significantly the time spent on the polishing machine.

The main disadvantages of multilateration methods are:

- the performance of the retroreflecting targets is limited;
- the mechanism used to steer the beam introduces significant systematic errors.

2.8.3 THE SHACK-HARTMANN WAVEFRONT SENSOR

The Shack-Hartmann wavefront sensor is an optical sensor used mainly in adaptive optics. The operation of the sensor is based on the use of an array of lenslets. The wavefront under investigation is imaged through the array and each lenslet focuses a portion of the wavefront onto a sensor. A perfect wavefront, free from aberrations,

would produce a regular array of focused spots. However, an aberrated wavefront would produce a distorted spot pattern (Greivenkamp *et. al.* 2001). Analysing the spot pattern provides information on the wavefront slope, which is in turn used to reconstruct the wavefront. The displacement of the spots on the detector is given by the product of the wavefront slope and the focal length of the lenslet. The principle of the Shack-Hartmann sensor is illustrated in figure 2.16.

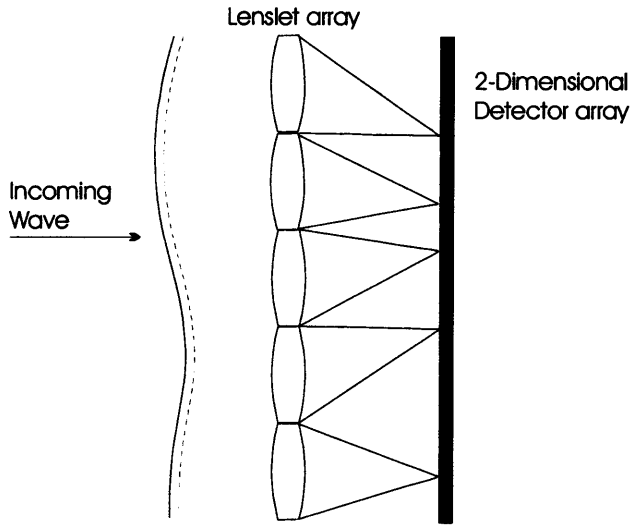

Figure 2.16 The Shack-Hartmann wavefront sensor

The Shack-Hartmann method can be employed directly to test wavefronts produced from aspheric surfaces. It should be noted however that the dynamic range is reduced with increased accuracy and *vice versa.*

2.9 EVALUATION

The advantage and drawbacks of the methods described so far are reviewed in table 2.1.

METHOD	ADVANTAGES	DISADVANTAGES
NULL OPTICS	Accurate and reliable measurement	Difficult and time consuming to built. Inappropriate for ELTs since hundreds of null would be required.
CGH	Relative ease of manufacture	Fabrication process introduces many errors. Low accuracy.
CGH PROJECTION	Same CGH used for a range ofoptics	Complex, low accuracy
PSI	Non-destructive, high accuracy	Very sensitive to environmental disturbances
TWH	Can be used to test steep aspheres	Low fringe contrast, no real-time results
TWPSI/MWPSI	Accurate and versatile	Sensitive to external influences
CMM	Well established method. Has been used for large optics metrology.	Slow/unsuitable for ELT metrology. Insufficient accuracy (100nm)
SAP	-Direct measurement of asphericity -Can measure convex, concave, flat, spherical and aspherical optics in a variety of diameters and RoC with a single set-up. -Can measure large asphericities.	-Slow and destructive measurement. -Cannot measure directly RoC.
AUTOCOLLIMATION	-Fast, non-destructive -Direct measurement of surface height	-Small motions of the test surface cause large measurement errors. -Steep aspheres cannot be tested.
LTP	- Non destructive - Relative insensitivity to vibrations	- Cannot measure steep aspheres - Very sensitive to temperature changes
LACS	- Insensitive to motions of the optical head -Fast and non-destructive -Small size, can be incorporated into existing instruments. -High accuracy	-Errors of the scanner can accumulate when scanning over large areas
LASER TRACKING	-Fast measurement -Can be used for RoC measurement	- The measurement can become discontinuous if the laser beam is interrupted. -Liable to undetectable systematic angular errors
MULTILATERATION	-Self calibrated, no high set-up accuracy required. -Can be used in-situ.	- Low accuracy due to imperfections on the retroreflectors used. -Beam steering causes significant errors.
SHACK-HARTMANN	Reliable method	Dynamic range is reduced with increased accuracy

Table 2.1 Summary of aspheric metrology methods

2.10 RECOMMENDATIONS

This chapter summarised the variety of available methods for the measurement of large optical surfaces with special interest in aspherics. It is clear that there are many methods, optical and non-optical, which have been employed in the past and most of them have many advantages as well as serious disadvantages.

In terms of the requirements which are foreseen in the area of large optical manufacturing, future metrological class profilometers need to satisfy the following requirements:

- measurement uncertainty better than 20 nm;
- measurement apertures up to 1 m diameter (short term)[2];
- measurement apertures up to 2 m to 3 m diameter (long term)[3];
- efficient and robust technology. In other words a technology which can be easily implemented and co-locate in the optical shop for *in-situ* measurements during the fabrication process;
- cost effective, especially for multiple part metrology;
- ability to measure fast and accurately. As an example the measurement of 2 m diameter optics should be made within a few hours;
- capability of measuring steep aspheric surfaces with asphericities of up to 300 μm;
- ability to measure optics of a variety of RoC including optics of very large RoC (for example 85 m in the case of the Euro50).

[2] This refers to a first stage of development for measurement of industrial aspherics up to 1 m in diameter for industrial applications
[3] This refers to the measurement of ELT segments

None of the methods discussed so far can satisfy all of the requirements *per se*.

However, a solution to this problem could be through the combination of some of the available methods in the construction of a hybrid system. The use of an existing mechanical system would provide robustness and the combination with an optical system would provide the ability to measure faster.

A suggestion would be the combination of a swing-arm profilometer with an optical probe. The swing-arm principle has been proven to be efficient, robust and accurate. Furthermore the emerging methods for curvature sensing appear to provide accurate and high-speed measurements. The combination of the two could be a novel way of measuring aspheric surfaces.

The suggested proposal is explained in the chapter 3 and the advantages of the method, for ELT and general large aspheric optic metrology, are discussed in detail.

Chapter 3

PRINCIPLES OF SWING-ARM PROFILOMETRY

"What is not fully understood is not possessed"

Goethe

3.1 INTRODUCTION

After reviewing the majority of the available aspheric metrology methods it was decided to proceed with the proposal of a hybrid optomechanical SAP. The choice of the SAP as the mechanical platform of the new profilometer is justified because the SAP configuration offers great adaptability to different measurement requirements. As it will become apparent in the following sections the distinct geometry of the SAP allows the form measurement of:

- Spherical and aspherical optics;
- Concave and convex optics;
- Optics with large surface slopes;
- Optics with large asphericities;
- Optics of different diameters;
- Optics of different radii of curvature ranging from flats to hemispheres;

As will become apparent in the following sections there is no theoretical limit in the measurable surface slopes and the measurable asphericities can be as large as the travel

range on the contact probe, *i.e.* several millimetres. This is due to the instrument's dinstinct geometry. The measurable diameters and radii of curvature depend only on the dimensions of the SAP arm.

Taking into account the requirements of the current project and the versatility of swing-arm profilometry it was decided that the construction of a SAP would be one of the best options for the current project. The mechanical platform provides the ability to measure a diverse range of optics and the introduction of an optical sensor helps to reduce the overall measurement time. The aim was to take the technology a step further and construct a SAP capable of achieving profile measurements with an accuracy of 20 nm in accordance with the requirements of ELT segment manufacturing. At the time when the current project was investigated the highest measurement accuracy quoted for a SAP was 50 nm. Further to this the new SAP would have to provide the ability to measure significantly faster than any current SAP available.

3.2 OVERVIEW OF A GENERIC SAP

The first SAP was constructed at the Steward Observatory Mirror Lab (SOML) of the University of Arizona by Burge (1996) although the principle was already know and had been applied in the past in optics grinding (Angel and Parks 1982). A SAP obtains data by scanning a probe on the test surface by means of a rotating arm. A typical SAP such as the original SOML instrument (figure 3.1) consists of four major components, namely, the profilometer arm, a rotary bearing that is used to rotate the arm, a second rotary bearing that is used to mount and rotate the optic under test and a probing system. The major part of the probing assembly is a displacement transducer, such as an LVDT, which is mounted at the end of the arm and positioned to be normal to the local

curvature. Additional mechanisms, such as tilting and translational stages, are used to align the probe and the arm to the required positions. An adjustable counterweight is used to balance the arm at its pivot point.

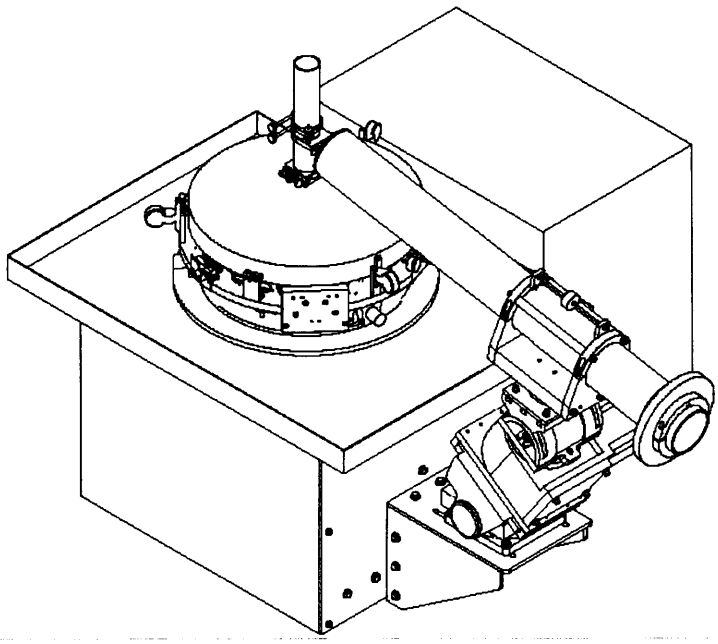

Figure 3.1 The original SOML SAP. It consists of two rotary bearings, a probing assembly and a tiltable arm. The probing assembly maintains the probe at normal incidence to the optic

Compared to other mechanical profilometers, the SAP's adaptability is due to its distinct geometry. Unlike common linear-bridge profilometers that perform linear scans across the diameter of the optic the SAP performs arcuate scans using a tilted arm. If the arm it tilted at a specific angle the trace is made to follow the curvature of the optic at each point of the measurement. Optics ranging from flats to hemispheres can be measured in this way using the same instrument and by simply altering the set-up parameters. The SOML-SAP is a versatile instrument, nevertheless the reported measurement accuracy which is not better than 50 nm and the slow measurement times make it unsuitable for ELT segment metrology.

As is shown in figure 3.2 the rotary motion of the arm ensures that the probe is always normal to the local surface. As a result the dynamic measurement range of the instrument increases dramatically. Furthermore, errors associated with the use of long probe extensions, such as stylus bending, are minimised since a short length stylus can be used universally.

In bridge profilometers the performance of the probe is impaired due to an increasing cosine error towards the edges of the optic as the probe deviates from the normal orientation. Large surface sag results in large cosine error. This problem is minimised in a SAP since the probe is always maintained normal to the SUT when measuring spherical optics. For aspheric optics there will be a small cosine error.

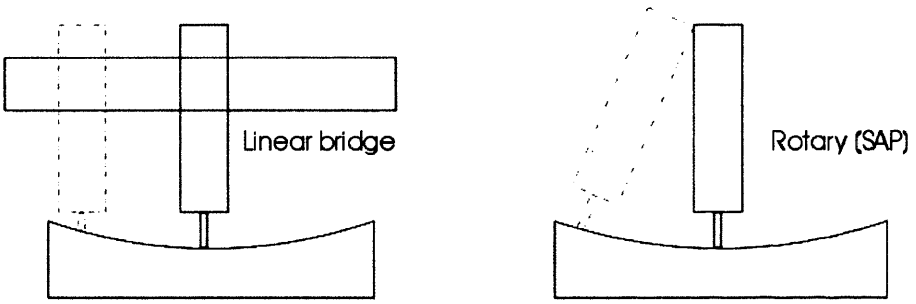

Figure 3.2 Differences between a the SAP and a common bridge-type profilometer

3.3 SAP OPERATING PRINCIPLES

3.3.1 CONDITION FOR SWING-ARM PROFILOMETRY

In order to measure a spherical optic with a SAP, the rotational axis of the SAP arm has to be tilted so that it intersects the extrapolated centre of curvature of the optic (figure 3.3a). This is achieved by tilting the arm rotary bearing by an angle

$$\theta = \sin^{-1}\left(\frac{l}{R}\right) \tag{3.1}$$

where R is the radius of curvature (RoC) of a spherical test optic. The variable, l, is called the "effective arm length" and it represents the perpendicular distance between the probe tip and the axis of rotation of the arm (figure 3.3b). Equation 3.1 constitutes a necessary condition for swing-arm profilometry.

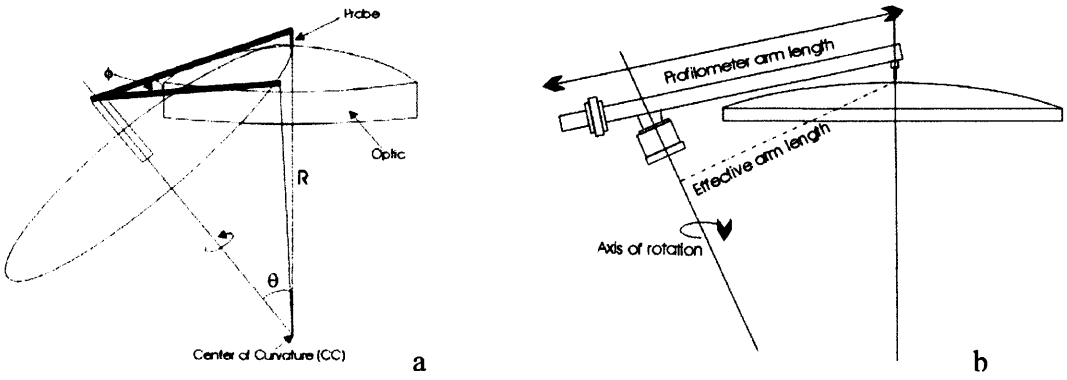

Figure 3.3 Operating principle of the SAP

The rotational movement of the arm means that the probe tip follows a circular path in space during a measuring cycle. If the generated circle is tilted by the angle θ the circular path lies on the surface of the spherical optic and the probe trace matches the shape of the optic. This is better illustrated in figure 3.4. Any deviations from the nominal surface are recorded as a displacement on the measuring probe.

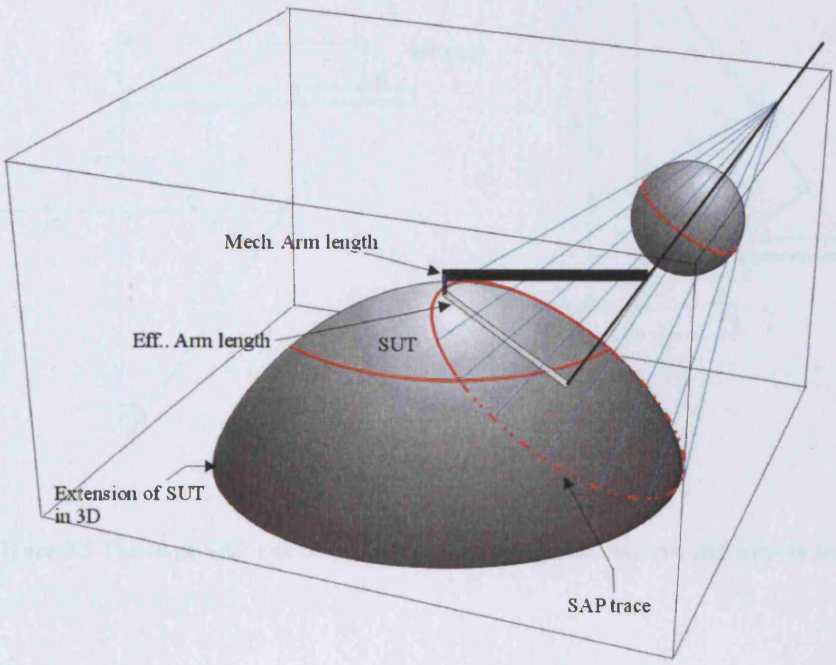

Figure 3.4 When the arm rotation is tilted at the correct angle the SAP trace follows the curvature of the test optic

The SAP condition (equation 3.1) can also be expressed in terms of the physical profilometer arm length, L, and in that case the required tilt angle is given by

$$\theta = \tan^{-1} \frac{L}{R \pm H} \tag{3.2}$$

where L is the physical arm length and H is the vertical distance between the tilt pivot point and the vertex of the mirror. The negative sign for H implies measurement of concave parts while a positive H refers to measurement of convex optics as shown in figures 3.4a and 3.4b. As it becomes apparent from figures 3.4a and 3.4b a SAP can be easily adapted to the measurement of concave optics simply by tilting the rotary axis in the opposite direction.

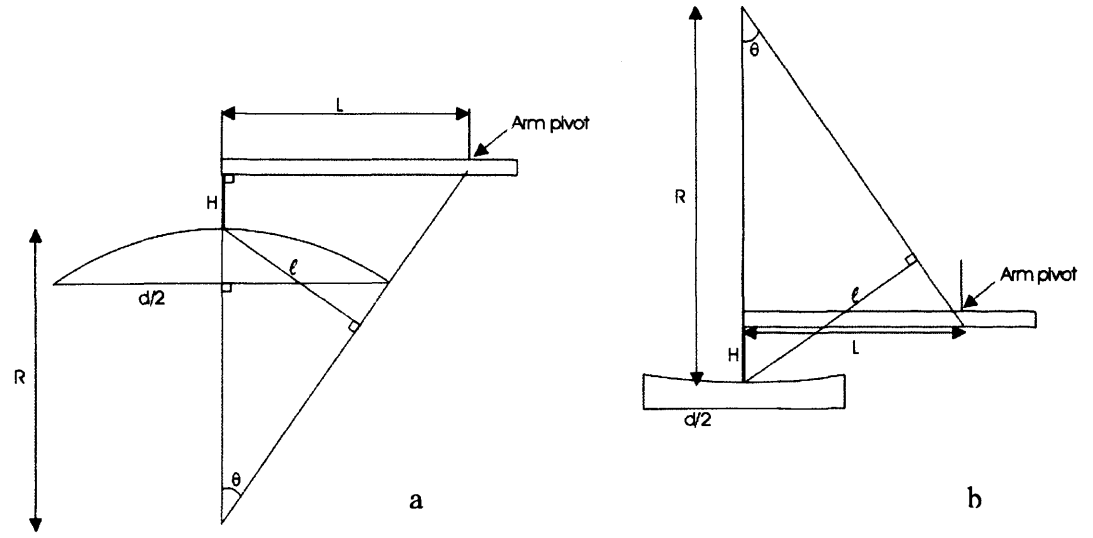

Figure 3.5 The same SAP can be easily adapted to measure concave and convex surfaces

3.3.2 MEASURING ASPHERIC SURFACES WITH A SAP

The SAP can be used equally well for the measurement of convex and concave aspherical optics and the same principle applies as in the case of spherical optics. The main difference is that the variable R in equation 3.1 now refers to the RoC of the aspheric's osculating sphere at the aspheres vertex. The SAP is set to follow the curvature of the osculating sphere but in reality it physically has to follow the surface of the actual aspheric. The resulting height difference between the two is recorded directly by the probe. However, this height difference is actually the radial difference between the osculating sphere and the aspheric SUT, in other words the probe displacement provides a direct measurement of the asphericity of the test optic (figure 3.5).

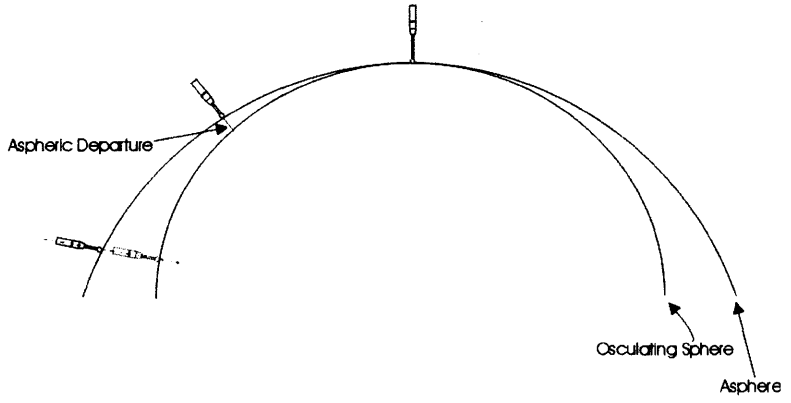

Figure 3.6 When measuring an aspheric optic with the SAP the probe displacement is a direct measure of the optic's asphericity

3.4 MODES OF OPERATION

3.4.1 SCANNING MODES

A SAP can be used in two different scanning modes. In the first mode a number of arcuate scans are performed sequentially at different parts of the optic. After the completion of each scan the optic is rotated to a new angular position with the aid of a rotary air bearing and the process is repeated. In each scan the probe has to pass through the vertex of the optic. The sequential scanning results eventually to a "bicycle wheel" pattern as shown in figure 3.6b. The SAP can be also be used in a spiral scanning mode. In this case the optic is in constant rotation whilst the arm moves slowly from one edge of the optic to the other. This mode of scanning resembles the operation of a record player and results to a spiral trace (figure 3.7a). The data point density depends on the rotation speeds of the arm and the optic.

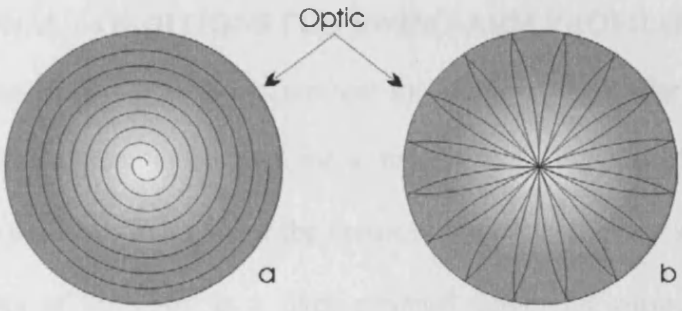

Figure 3.7 The two possible scanning modes of the SAP: (a) spiral scanning, (b) line scanning

During either mode of operation the arm rotates over an angular span that is determined by the size of the optic and the physical length, *L,* of the profilometer arm.

Assuming the simple case of the measurement of a circular flat (figure 3.8), the maximum required swivelling angle can be approximated as

$$\phi \cong 2\tan^{-1}\left(\frac{r}{L}\right) \tag{3.2}$$

where L is the physical arm length and r is the radius of the artefact. The knowledge of the swivelling angle in real time is significant in relating recorded data with physical features on the optic.

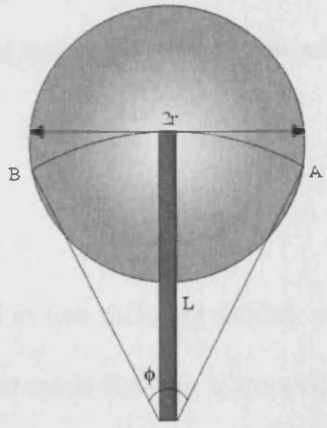

Figure 3.8 The swing angle of the SAP arm is related to the diameter of the optic and the arm length

3.4.2 ADDITIONAL CONDITIONS FOR SWING-ARM PROFILOMETRY

Equation 3.1 describes a necessary proviso for swing-arm profilometry, however, additional conditions have to be met for a functional SAP. One of the conditions requires that the probe passes through the vertex of the optic at every scan. This action assigns the vertex of the optic as a fixed physical datum for correlating data from different scans. Another important reason for having the probe passing through the vertex is that in any other case it would be impossible to measure the central part of the mirror irrespective of the number of line scans (figure 3.9B).

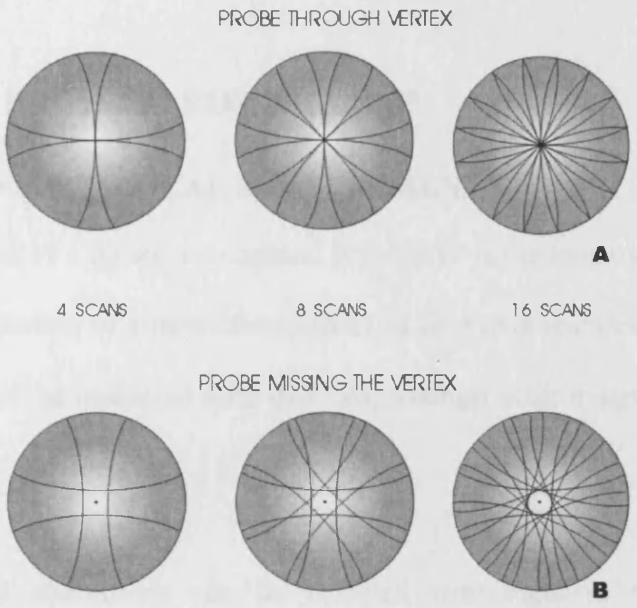

Figure 3.9 Scanning through the vertex (A) and missing the vertex (B)

3.4.3 PROBING MODES

The probing can be performed in two different modes: point-by-point measurements or continuous scanning. In the first mode the arm is stopped at predefined intervals and the probe is lowered onto the surface in order to obtain a measurement. In the second mode

the probe is traversed across the surface performing a continuous scan. Point-by-point probing offers the benefit of minimum impact on polished surfaces contrary to continuous scanning that is more invasive and can result in scratches. The drawback of point-by-point measurement is a significant increase in the overall measurement time. In the design of the SAP both probing methods will be considered since each can be used for a different applications: Continuous scanning is more suitable for interim measurements during grinding where the impact of the probe contact force would be less significant, while point-to-point measurement should be preferred for polished precision surfaces. Both probing modes can be employed for spiral or arcuate scans.

3.5 OPTICAL PROBING FOR THE SAP

3.5.1 THE NEED FOR OPTICAL MEASUREMENT

The main drawback of a typical mechanical probe SAP is the long overall measurement time. The reconstruction of a three-dimensional surface map requires several line scans and the accuracy of the measured form depends, amongst other things, on the density of the scans.

The main optical aberrations can be detected with eight to twelve line scans corresponding to the first few Zernike terms. It is estimated that for large optics over 1 m in diameter each complete line scan could take at least ten minutes with a SAP. A measuring cycle of twelve scans would, therefore, require an estimated two hours to be completed. This would offer sufficient information for interim measurements between grinding cycles since it would provide a good approximation for the overall shape of the optic. However, for polished surfaces shorter wavelength surface irregularities would be missed due to low surface coverage. In order to assess the quality of polished surfaces

tens or hundreds of scans would be required increasing drastically the overall measurement time and making the SAP impractical, especially for multiple segment metrology. As an example in order to measure surface features with wavelengths of 0.5 mm a lateral point spacing of no more than 250 μm is required in order to satisfy the Nyquist criterion. If the SAP is to be used for the verification of hundreds of polished ELT segments, where accuracy and speed are equally important, a different approach has to be adopted.

3.5.2 USING AN OPTICAL SENSOR

In order to reduce the measurement time the incorporation of an optical measurement technique is suggested. The proposed solution integrates an optical sensor and a mechanical probe into a hybrid probing unit. The introduction of the optical sensor can reduce the measurement time by increasing the coverage over a single scan. The mechanical probe can still be used for data redundancy as a way of improving accuracy. As an example, an optical sensor with an aperture of 75 mm would provide an estimated 70% coverage over a 1000 mm parts after sixteen scans, based on consecutive scans that are 22.5^0 apart (figure 3.10). This would reduce the measurement time by orders of magnitude since in order to approach similar levels of surface coverage with a stylus probe, several hundred line scans would be required. Figure 3.11 shows the surface coverage achieved with a contact probe after 160 line scans. Although there is significant overlap between individual line scans the overall surface area coverage is still lower than the corresponding coverage of a SAP with an optical sensor after only sixteen scans.

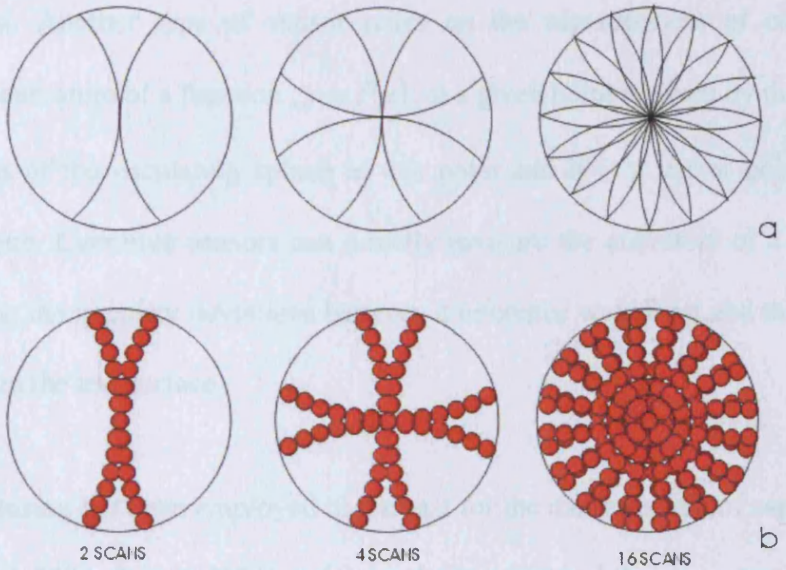

Figure 3.10 Scaled diagram showing a 1000 mm optic scanned by a stylus probe (a) and by a 75 mm aperture optical sensor (b). In the latter case 16 scans result to approximately 70% surface area coverage.

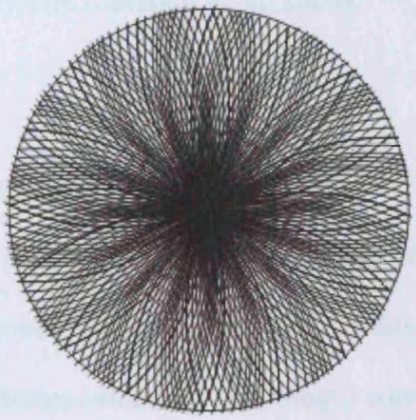

Figure 3.11 Surface coverage after 160 line scans with a stylus probe. The surface coverage is still lower that the corresponding coverage of an optical sensor after sixteen scans (figure 3.10).

3.5.3 OPTICAL SENSORS FOR THE SAP

Several optical sensors could be used to extend the SAP's capabilities. Different classes of sensors include the ones based on differential height measurement and slope

measurement. Another type of sensor relies on the measurement of curvature. In general, the curvature of a function , $y = f(x)$, at a given point is given by the reciprocal of the radius of the osculating sphere at this point and it is a vector pointing at the sphere's centre. Curvature sensors can directly measure the curvature of a test surface by comparing the intensity deviations between a reference wavefront and the wavefront reflected from the test surface.

Curvature sensing has been employed in the past for the measurement of aspheric optics (Schulz *et. al.* 2000, Schulz 2001) and it has been suggested that curvature data can be obtained reliably with nanometric accuracy. Surface profiles can then be reconstructed from these data (Elster 2002). One of the main advantages of using curvature sensors is that curvature measurements are insensitive to small angular and vertical error motions of the SUT or the probing system (Schmidt *et. al.* 2000).

3.5.4 THE OMAM WAVEFRONT SENSOR

Taking into account the benefits of curvature sensing it was decided to use this technology for the optical probing of the SAP. Towards this direction it was decided to use an OMAM (Optical Manipulation and Metrology) wavefront sensor for the SAP. The OMAM is a distinctive type of curvature sensor based on the use of a distorted diffraction grating which allows the imaging of multiple layers onto a single plane (Blanchard 1999).

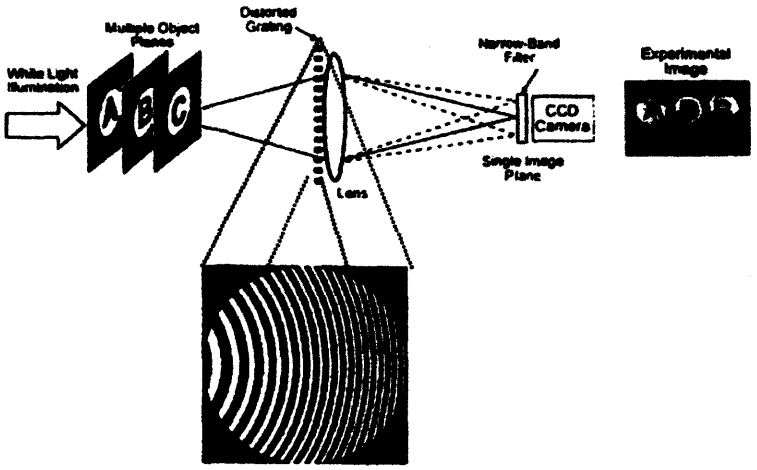

Figure 3.12 The principle of operation of the OMAM wavefront sensor

The operation of the OMAM sensor is described in detail elsewhere (Blanchard *et. al.* 2000, Woods *et. al.* 2002, Roddier *et. al.* 1993). The general principle is based on obtaining three images A,B and C (figure 3.11) one of which is in-focus (B) and the other two (A and C) are slightly defocused. The intensity differences between the two defocused images reveal distortions on the oncoming wavefront. For example if a portion of the wavefront is concave as it travels from A to C, it will propagate towards a focus leading to an increase of the local intensity (Heather *et. al.* 2004). Conversely a convex portion will lead to a decrease in the local intensity. In this way the OMAM sensor is functioning effectively as a curvature sensor.

The OMAM sensor was chosen at the beginning of the project as the default sensor for the hybrid SAP. As a result many SAP design aspects were interrelated to the choice of the particular sensor. Wherever possible the design was such that other sensor technologies could be adapted if necessary. The alternative optical sensors considered include an Arden Photonics AWS-50 wavefront curvature sensor and a Fisba μ-phase interferometer.

The OMAM sensor was incorporated in the SAP project through a collaboration formed under a Smart Optics Faraday partnerships scheme. Faraday partnerships are a UK initiative in order to develop and promote technologies for the benefit of the UK research programmes. This is an attempt to provide maximum exploitation and impact of publicly funded research and development. The OMAM project, operating under the "Smart Optics" Faraday partnership, was aimed at developing commercial applications for wavefront sensing methods. Under this scheme NPL and UCL collaborated with Herriot-Watt University which was the developer of the OMAM sensor in order to incorporate the sensor to the SAP.

From this point of view the SAP project was a commercially orientated project that had to satisfy both the requirements of the Smart Optics partnership as well as the science requirements from the point of view of ELT segment metrology working as a proof-of-concept. In addition the first SAP prototype would have to satisfy further commercial requirements by being capable to be used immediately after completion for measurement of industrial optics. The overlapping of the several requirements often led to confusion especially in terms of the laying of the specifications for the future instrument. Further to this it was necessary to deliver the instrument within a given timeframe in order to be in line with the directives of the SAP funding body.

3.6 SPECIFICATION OF THE SAP

The DTI specification of the project were concise and the aim according to the official DTI document was:

"To produce a prototype profilometer for the measurement of aspheric surfaces up to 600 mm diameter, as a first step towards addressing the needs of manufacturing and testing large components and structures."

The specifications were intentionally left open-ended in order to allow feedback from the industrial collaborators and potential end-users. The project's main industrial partner, through the OMAM collaboration, and final end user is ZEEKO Ltd, manufacturers of precision optic polishing technologies. It was decided that the current project should be the first step in proving UK's capability for large scale ELT mirror production as well as fulfilling part of UK's R&D contribution to the Euro50 project. In order to align with the DTI criteria it was decided that the SAP would be used for measurement of industrial optics up to 600 mm in diameter with the potential of employing the emerging measurement technology to ELT mirror segments.

The measurand of the SAP is the surface form and the target accuracy for this, according to DTI is 20 nm, which is interpreted as 20 nm RMS uncertainty in the measured form. According to DTI the 20 nm accuracy refers to maximum optic diameters of 600 mm. The end user, however, required a maximum diameter of measurable optics of at least 1000 mm. Another requirement had to do with extended range on the measured surface slopes and it was required to measure surface slopes as high as 33^0. As a case study an optic of RoC equal to 532 mm and diameter equal to 600 mm was suggested. It is known, as a rule of thumb that increasing the dynamic range of an instrument results to increased overall measurement uncertainty. In order to

comply with the DTI specification it was decided that the SAP should be designed of be capable of measuring 600 mm parts with 20 nm accuracy whilst investigating ways of extending the measurement range to accommodate 1000 mm diameter parts as well as high surface slopes. The end user agreed to use the SAP at extended range at the expense of reduced measurement accuracy. In that case the SAP would be used primarily for verification of ground surfaces. It was agreed that a maximum form error of 100 nm for polished surfaces and up to 1 μm for ground surfaces would be accepted as a trade-off for increased measurement capabilities.

In order to progress this description into a detailed practical design, there had been consultation between NPL and UCL which resulted in a final provisional specification presented in table 3.1.

PARAMETER	TARGET VALUE
Optic diameter	0.2 m – 1 m
Radius of curvature	532 mm - ∞ (including hemispheres and flats)
Optic types	Convex and concave
Optic shape	Spherical and aspherical (any type)
Optic form	Surfaces of revolution and general aspheres
Surface slope	0^0 to 33^0
Measurement accuracy	20 nm (for polished parts up to 600 mm in diameter) Up to 100 nm (for 1000 mm diameter polished parts, and surface slopes $>15^0$) Up to 1 μm (for 1000 mm diameter ground parts)

Table 3.1 Summary of the specifications for the NPL/UCL profilometer

The specifications of table 3.1 were used throughout the design of the SAP as a guideline.

Chapter 4

ERROR ANALYSIS FOR A GENERIC SAP

"Knowledge rests not upon truth alone, but upon error also"

Carl Gustav Jung

4.1 MACHINE ERRORS

Every measurement machine, no matter how carefully designed and used, will be predisposed to errors. Machine errors can be classified into two main categories: static/quasi-static and dynamic errors. Static/quasi-static errors occur on a stationary machine and are further divided into geometric errors (for example dimensional errors in the machine as a result of manufacturing or assembly variance), load induced deformations, thermal errors, *etc.* Dynamic errors occur as a result of the application of dynamical forces, usually caused by the machine's movement. Such errors include spindle motion errors, dynamical tool deflection, *etc.*

Machine errors can also be classified as systematic (repeatable) errors and random (non-repeatable) errors. Systematic errors are more difficult to detect experimentally but they are deterministic in nature and can in principle be modelled mathematically. Random errors are stochastic errors and although easier to detect by statistical analysis of the measurement data they are difficult to predict and correct.

4.2 ERROR BUDGETING AND UNCERTAINTY ANALYSIS

The two methods, commonly used to account for machine errors, are error analysis and uncertainty analysis. Error analysis (often called error budgeting) is performed prior to the construction of the instrument in order to forecast its future accuracy and it usually involves the creation of a machine error model. In contrast, uncertainty analysis is based on a complete error mapping of the finished instrument either by using prior knowledge such as specifications, estimates based on past experience and calibration reports (Type-B uncertainty evaluation) or by statistical analysis of a series of observations (Type-A uncertainty evaluation). An overview of uncertainty analysis can be found in a technical note published by NIST (Taylor and Kuyatt 1994) as well as in the M300 guide published by the United Kingdom Accreditation Service (UKAS 1997). Finally the "Guide to the Expression of Uncertainty in Measurement" (GUM) (ISO 1994) is the basic document that is used as a guideline by National Measurement Institutions and other institutes in order to evaluate the uncertainty of a system.

Error analysis and uncertainty analysis are often used interchangeably. However, although very similar, they are two distinct procedures. Uncertainty analysis aims to quantify as precisely as possible the real overall machine error of a completed instrument. Error analysis on the other hand is primarily a qualitative design tool used to illustrate the tendency of system to exhibit erratic behaviour as well as to provide an approximation of the projected machine error. Nevertheless the importance of error analysis is immense since it influences the design procedure, it helps to identify where to focus the project's resources and how to distribute error allowances amongst the various subsystems.

4.3 CONSTRUCTING AN ERROR BUDGET

The construction of an error budget depends on the individual designer's background, knowledge and approach. According to Forbes (Forbes and Harris 2000) one of the main requirements for an error budget is the formulation of a parametric error function that describes the machine errors. The selection of an appropriate error function is imperative since it establishes a functional relationship between the machine error and the measurand.

The hierarchy of steps followed on the SAP error budgeting was to:

1. Choose the parameters that describe the operation of a generic SAP.
2. Construct a suitable parametric equation that describes the SAP error.
3. Establish a relationship between the measurand and the error function.
4. Use a simulation spreadsheet where the tolerances across the chosen parameters are estimated.

4.4 PHYSICAL INTERPRETATION OF MACHINE ERRORS

A common way of physically interpreting a machine error is through its final effect which is ultimately the misplacement of the tool, or probe, away from its nominal position. A typical example of such a machine error is that of a robot grabber with nominal position P (x, y, z) and real position $P'(x+\delta x, y+\delta y, z+\delta z)$. The difference between the expected position P and the actual position P' of the grabber expresses the volumetric error of the machine. Nowadays with the advancement of new technologies and compensation techniques the linear x, y and z machine errors can be reduced dramatically and the definition of volumetric error is extended to include rotational errors.

It is known that an unconstrained object has six degrees of freedom (DoF). Three of the object's DoFs consign to the linear motion along the *x*-, *y*- and *z*-axes. The remaining DoFs refer to the rotational motion of the object about the *x*-, *y*- and *z*- axes. The rotation about the *x*-axis is referred to as roll, the rotation about the *y*- axis as pitch and the rotation about the *z*-axis as yaw (Smith 1992). Since an unconstrained object has six DoF it can potentially have six motion errors. These errors express departures of the tool from the prescribed path and are called parametric kinematic errors. Kinematic errors can be the dominant sources of errors in many measurement machines.

4.5 VOLUMETRIC ERROR OF CMMS

The most common measurement machines, used extensively in industry and research, are Cartesian three-axis machines and in particular CMMs. The volumetric error of a CMM is primarily attributed to its parametric motion errors. There are six such errors for each CMM axis, three linear and three rotational (figure 4.1), resulting in a total of eighteen motion errors. In addition there are three squareness errors, denoting the non-perpendicularity between the three axes of the machine and leading in a total of twenty one geometric parametric errors.

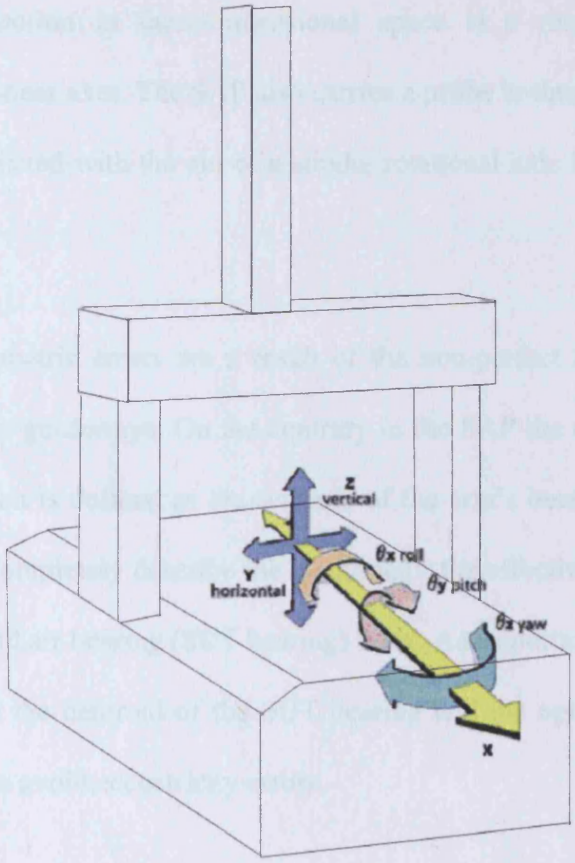

Figure 4.1 Rotational errors of the *x*-axis of a typical CMM

It is common practice to apply principles of CMM error analysis to other machines. An example of this approach is the work of Tong (2005) where the error model of a rapid prototyping machine is constructed using CMM error modelling principles. A comparison between the CMM and the SAP will also be attempted in the current investigation in order to provide a better insight into the function of the SAP.

4.6 SAP PARAMETRIC MOTION ERRORS

4.6.1 DEFINING THE SAP AXES

When comparing the operation of the SAP to that of a conventional CMM the first thing that becomes apparent is the different way in which the probe motion is achieved. In a

CMM the probe motion in three-dimensional space is a result of simultaneous movement of three linear axes. The SAP also carries a probe in three-dimensional paths, however, this is achieved with the aid of a single, rotational axis that is the arm rotary bearing axis.

In a CMM the parametric errors are a result of the non-perfect motion of the CMM frame along its linear guideways. On the contrary in the SAP the only axis responsible for the probe's motion is defined as the centroid of the arm's bearing rotor. Two more axes are needed to completely describe the instrument: the effective arm length and the centroid of the second air bearing (SUT bearing) rotor. An important requirement is that during measurement the centroid of the SUT bearing and the optical axis of the SUT must be coincident to avoid eccentricity errors.

Of the three axes that describe the SAP, the effective arm length has no independent motion and, therefore, cannot generate independent motion errors. The SUT bearing can potentially generate errors but this depends on the scanning mode. For spiral scans the SUT bearing is in constant rotation and hence it produces dynamical motion errors which affect directly the measurement result. For "bicycle wheel" scans the bearing only rotates in between scans resulting merely in static misalignment errors. It is likely that the SAP will be used in both scanning modes hence the worst case scenario will be considered where both bearings are in motion during measurement. As a result the SAP will be treated as a two-axis measuring instrument where the two axes are defined by the centroids of the two rotary bearings.

4.6.2 ROTARY BEARING ERRORS

Air bearings produce both linear and rotational errors. The linear errors are referred to as "radial runout" when the result is linear displacements in the *x*-*y* plane and "axial runout" when the result is an error in the *z*-axis. The rotational error of a bearing is referred to as "coning" and is a combination of pitch and roll errors (figure 4.2).

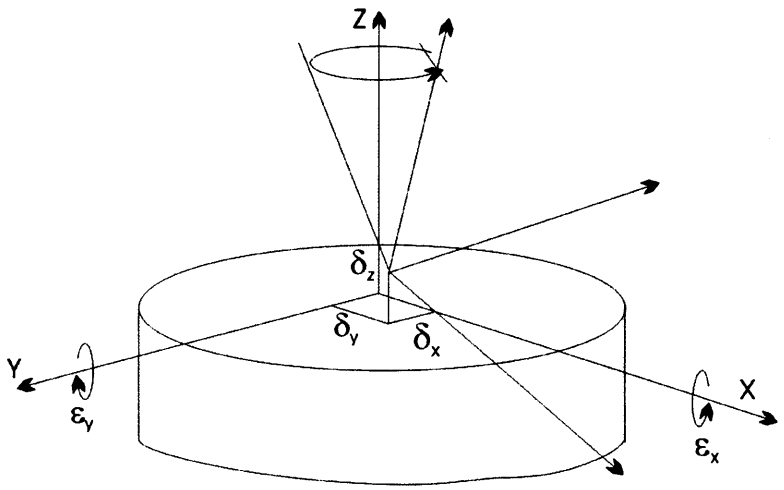

Figure 4.2 Errors present on a rotary bearing

It is apparent from figure 4.2 that a rotary bearing also has six motion errors, three of which are linear and three rotational. One of the three rotational errors is along the direction of motion and is an offset "scaling" error. Since the primary bearing motion is rotational it is inherently more accurate than the motion of linear bearings present on linear three-axis machines. It is known for example that the accuracy of CMM linear guideways is scarcely better than 1 μm (Yang 2003) but the error motion of rotary air bearings can be better than a few tenths of nanometres.

The same linear and rotational errors are present on both SAP bearings and due to symmetry they will have a similar effect on the overall machine accuracy. Nevertheless the SAP is inherently more accurate than linear instruments due to its natural, rotational

motion. Furthermore it has fewer motion errors than linear three-axes instruments since it only employs two motion axes. Due to its distinct geometry it is preferred to model the SAP by describing its spherical measurement envelope rather than modifying existing parametric error models. In order to do this is it necessary to construct a mathematical description tailored to the SAP operation.

4.7 MATHEMATICAL MODELLING AND SIMULATION

4.7.1 MATHEMATICAL DESCRIPTION OF THE SAP OPERATION

In order to describe the function of the SAP it is first necessary to understand the principles governing cup-wheel grinding (Storz and Dow 1994) from which the SAP principle originated. Given a parent sphere of radius of curvature (RoC), R a circle of radius, l where $0 < l < R$, can be orientated such that its periphery lies on the surface of the sphere. The circle[4] will lie on the surface of the parent sphere as long as the axis of the circle (figure 4.3) intersects the centre of curvature of the sphere (Angel and Parks 1982). In order to achieve the required orientation the specific circle should be tilted at an angle

$$\theta = \sin^{-1}(l/R) \tag{4.1}$$

with respect to the y-z plane.

[4] This circle will be referred to as "specific circle".

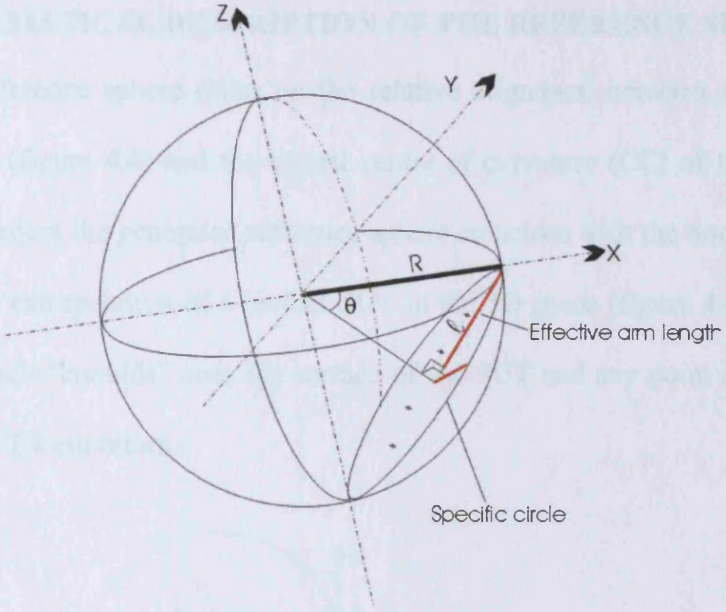

Figure 4.3 Representation of the specific circle and parent sphere

In cup-wheel grinders the specific circle is a circular saw which will cut concave or convex spherical optics of RoC, *R*, as the work rotates about the *z*-axis. A SAP is based on the same principle, however, in place of the saw there is now a probe. The specific circle in this case represents the path of the probe in space as it is scanned across a spherical optic of RoC, *R*.

On a SAP, the parent sphere plays the role of a virtual measurement reference which corresponds to the nominal spherical test surface. This spherical reference is determined by the relative alignment of the instrument's axes and an ideal SAP with perfectly aligned axes would result in a perfect measurement reference. It is, however, a fundamental reality that no instrument can be perfect. An actual SAP will generate an imperfect measurement reference leading to errors that are indistinguishable from the actual surface errors of the SUT. In order to investigate the effect of the SAP errors on the measurement it is first necessary to describe mathematically the reference sphere.

4.7.2 MATHEMATICAL DESCRIPTION OF THE REFERENCE SPHERE

The virtual reference sphere relies on the relative alignment between the axis of the specific circle (figure 4.4) and the virtual centre of curvature (CC) of the SUT. In an optimum alignment the generated reference sphere coincides with the nominal sphere as defined by the extrapolation of a perfect SUT in the 3D space (figure 4.4). In this case the specific circle "moulds" onto the surface of the SUT and any point at its periphery follows the SUT's curvature.

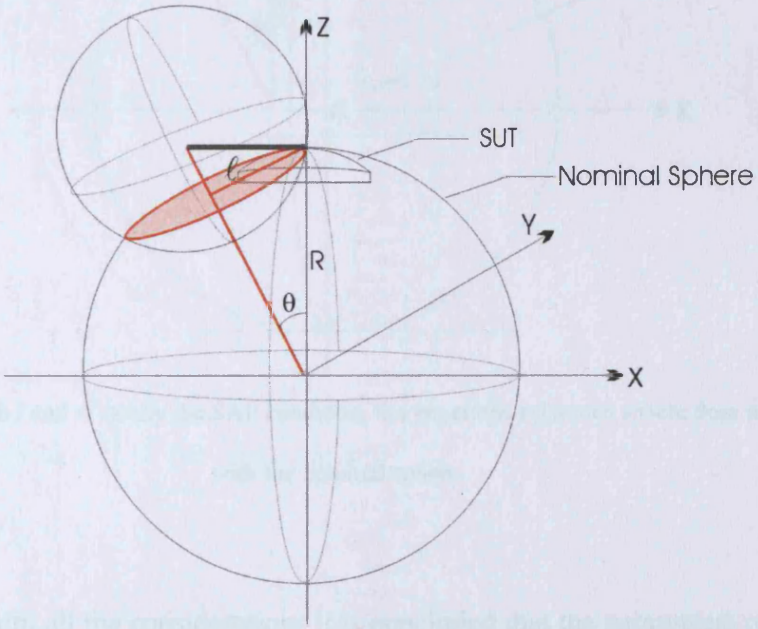

Figure 4.4 Representation of the virtual spherical reference. The specific circle is shown as a red disk

It is apparent from figure 4.4 that the generated reference sphere depends on the dimensions and the orientation of the specific circle. It should, therefore, depend on the descriptors of these features which are the effective arm length, l, and the tilting angle, θ. However, the parameters, θ and l, alone do not offer a complete description of the reference sphere. As is shown in figure 4.5, although l and θ have their nominal values which verify the SAP condition, $\sin\theta = l/R$, the generated reference sphere does not

coincide with the nominal sphere. The reason for this is that the axis of the specific circle does not cross the extrapolated CC of the optic (point A in figure 4.5). It is, therefore, also necessary to account for the linear position of the specific circle in the *x*, *y* and *z* directions.

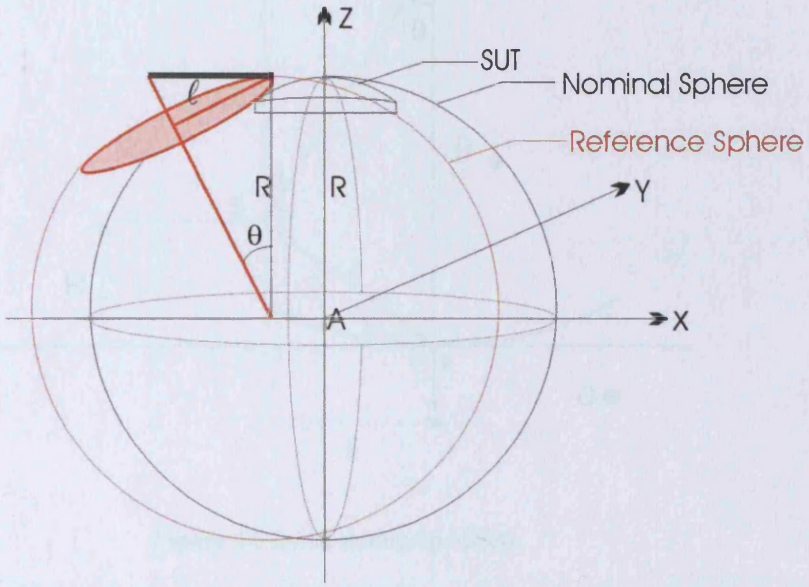

Figure 4.5 Although l and θ satisfy the SAP condition, the generated reference sphere does not coincide with the nominal sphere

Taking into account all the considerations it is concluded that the parameters required to describe completely the specific circle and, hence the spherical reference are *x, y, z, l* and θ. Any SAP errors can then be expressed as perturbations of these parameters which will lead to a perturbed reference sphere. The next step is to establish a mathematical relationship for the reference sphere that includes the parameters x, y, z, l and θ.

Starting with the description of the reference sphere we assume a concave spherical SUT (the same principles apply for convex surfaces) that is part of a perfect parent sphere of RoC, *R*. Assuming a Cartesian *x-y-z* coordinate reference frame located at the

pivot B (figure 4.6), F, G and H are the 3D offsets of the probe's tip position with respect to the pivot B. G is in-plane and is assumed to be zero.

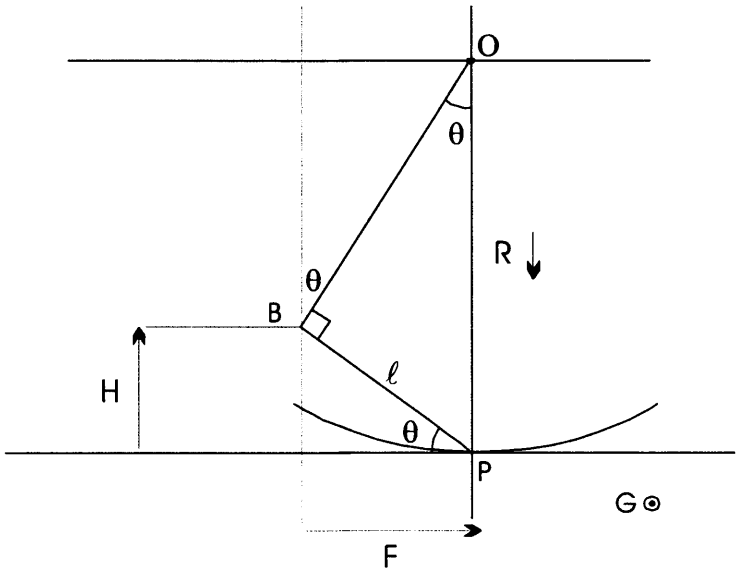

Figure 4.6 Initial setting-up offsets

The values of the offsets F, G and H are given by

$$F = x_P = l\cos\theta \tag{4.2}$$
$$G = y_P = 0 \tag{4.3}$$
$$H = z_P = -l\sin\theta . \tag{4.4}$$

When the arm swings about the pivot B the 3D path of the probe tip (which is the specific circle trace) is described by the following set of parametric equations

$$x = l\cos\theta\cos\phi \tag{4.5}$$
$$y = l\sin\phi \tag{4.6}$$
$$z = -l\sin\theta\cos\phi \tag{4.7}$$

where ϕ is the swivelling angle (figure 4.7).

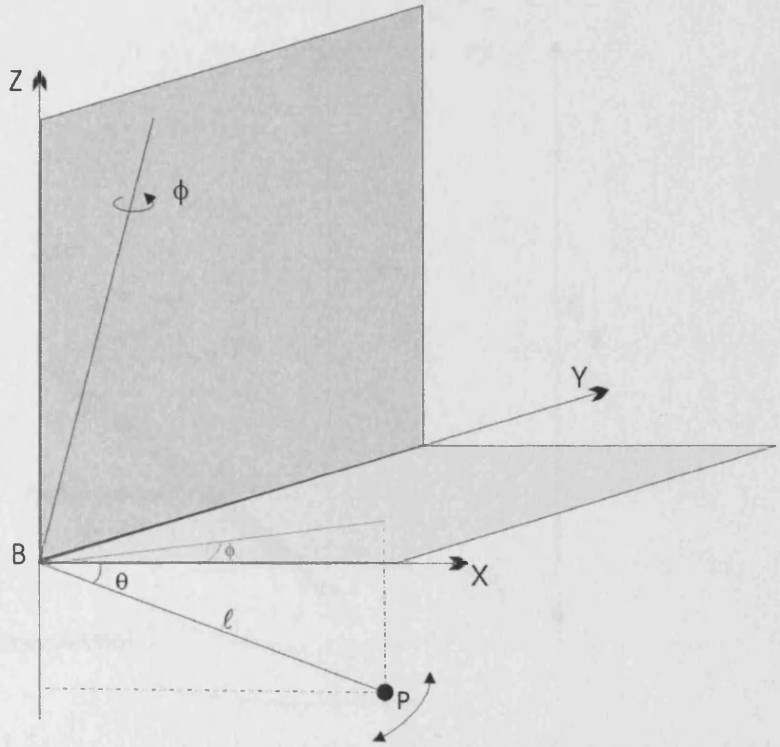

Figure 4.7 Description of the probe travel with respect to the pivot. The *y*-axis is orthogonal to the measurement plane as defined by the axis of rotation and the arm, *l*

With reference to figure 4.8, the CC of the SUT is fixed by the position vector

$$\hat{r}_0 = (x_0, y_0, z_0) \tag{4.8}$$

which coincides with the axis of rotation of the arm.

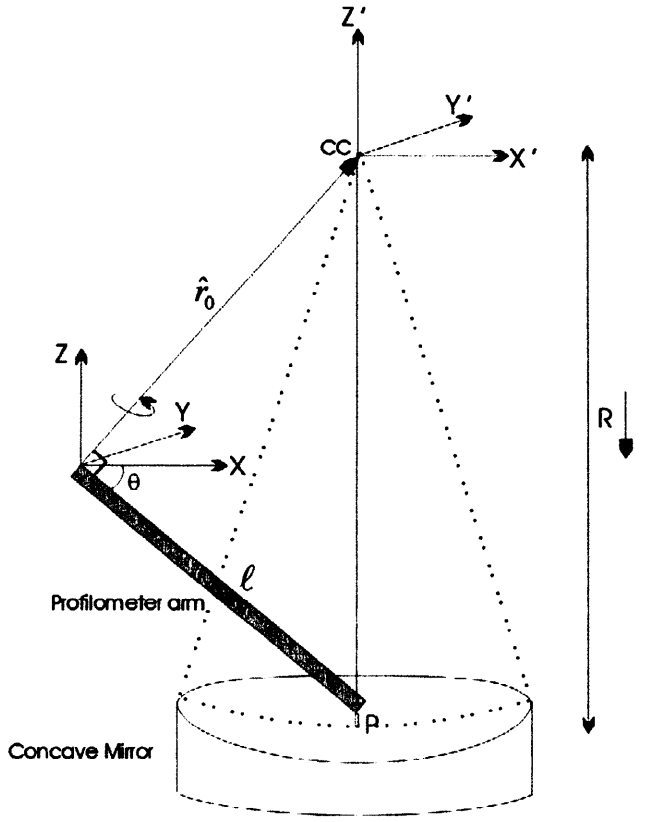

Figure 4.8 A coordinate system *x, y* and *z* is located at the pivot and a coordinate system *x',y'* and *z'* is located at the CC of the SUT

If it is assumed that a second coordinate frame *x'-y'-z'* is located at the CC of the SUT (figure 4.8) we can obtain an expression that includes the parameters x, y, z, l, θ and R. This is achieved by shifting the coordinates of the first frame *x-y-z* by the vector $\hat{r}_0$. The position of the new frame with respect to the pivot B is given by

$$x' = l\cos\theta \tag{4.9}$$

$$y' = 0 \tag{4.10}$$

$$z' = R - l\sin\theta\,. \tag{4.11}$$

Hence the co-ordinates of the probe tip (P_1, P_2, P_3) now lie on a sphere with centre (*x'*, *y'*, *z'*) and radius of curvature:

$$R = \sqrt{(x - l\cos\theta)^2 + y^2 + (z - R + l\sin\theta)^2} \tag{4.12}$$

where x, y and z are given by equations (4.5), (4.6) and (4.7) respectively.

4.7.3 PERTURBATION OF THE REFERENCE SPHERE

The sphere described by equation (4.12) represents the nominal reference sphere. Any perturbations in the position of the probe tip would result in a perturbed sphere of RoC, R'. In order to investigate this independent linear perturbations of $\delta x, \delta y$ and δz can be introduced which result in a new probe position P' (figure 4.9). The RoC of the resulting, perturbed, sphere can now be found by calculating the magnitude of the vector OP'.

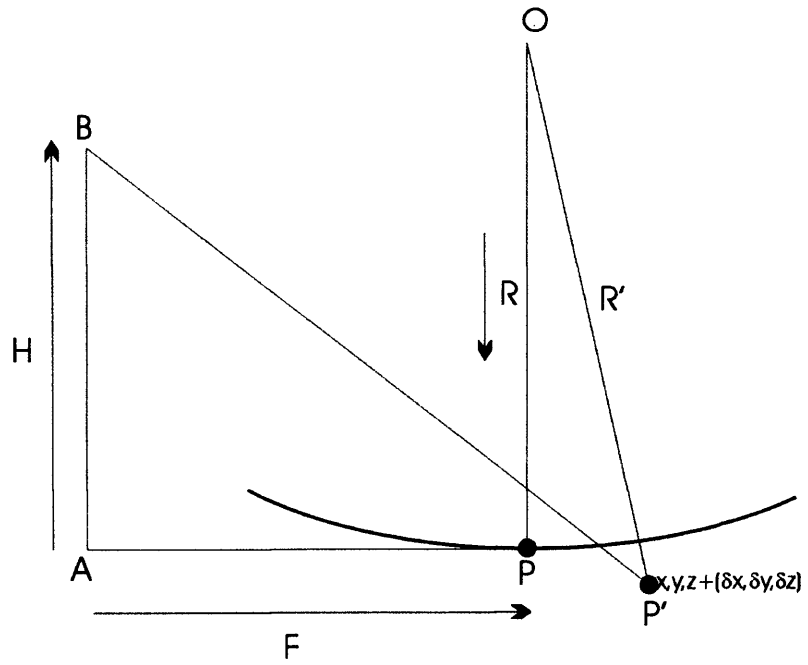

Figure 4.9 The effect of translational error on the RoC of the reference sphere

The distance from O to P' can be expressed as

$$\overline{OP'} = \overline{OP} + \overline{PA} + \overline{AB} + \overline{BP'}$$

or

$$\overline{OP'} = \overline{R} - \overline{F} + \overline{H} + \left(\overline{x} + \overline{y} + \overline{z}\right) + \overline{G} + (\overline{\delta x} + \overline{\delta y} + \overline{\delta z}) . \tag{4.13}$$

Separating into coordinate components gives

$$\overline{OP'} = \left[-\overline{F} + \overline{x} + \overline{\delta x}\right] + \left[\overline{G} + \overline{y} + \overline{\delta y}\right] + \left[\overline{R} + \overline{H} + \overline{z} + \overline{\delta z}\right]$$

or

$$\overline{OP'} = \overline{R'} = \overbrace{-\overline{F} + \overline{x} + \overline{\delta x}}^{X'} + \overbrace{\overline{G} + \overline{y} + \overline{\delta y}}^{Y'} + \overbrace{\overline{R} + \overline{H} + \overline{z} + \overline{\delta z}}^{Z'} . \tag{4.14}$$

The quantity of interest is R', therefore,

$$|R'| = \sqrt{(-F + x + \delta x)^2 + (G + y + \delta y)^2 + (R + H + z + \delta z)^2} . \tag{4.15}$$

Substituting the values for F, G and H from equations (4.3), (4.4) and (4.5)

$$|R'| = \sqrt{(-l\cos\theta + x + \delta x)^2 + (y + \delta y)^2 + (R - l\sin\theta + z + \delta z)^2} . \tag{4.16}$$

Substituting the values for x, y and z from equations (4.5), (4,6), and (4.7) results in

$$|R'| = \sqrt{(-l\cos\theta + l\cos\theta\cos\phi + \delta x)^2 + (l\sin\phi + \delta y)^2 + (R - l\sin\theta + l\sin\theta\cos\phi + \delta z)^2} . \tag{4.17}$$

Equation (4.17) expresses the modified RoC of the reference sphere due to independent linear perturbations of the probe tip position with respect to the vertex of the SUT.

4.7.4 CORRELATED TERMS

It is important to note that equation (4.17) takes into account only the linear perturbations in x, y and z. Nevertheless, a complete description should also account for perturbations in l and θ. These perturbations, however, correlate with linear errors across x, y and z. As an example we assume a change in the arm length due to thermal expansion (figure 4.10). This error can be considered as a direct perturbation δl, however, the final effect is equivalent to a translation of the probe by δx and δz.

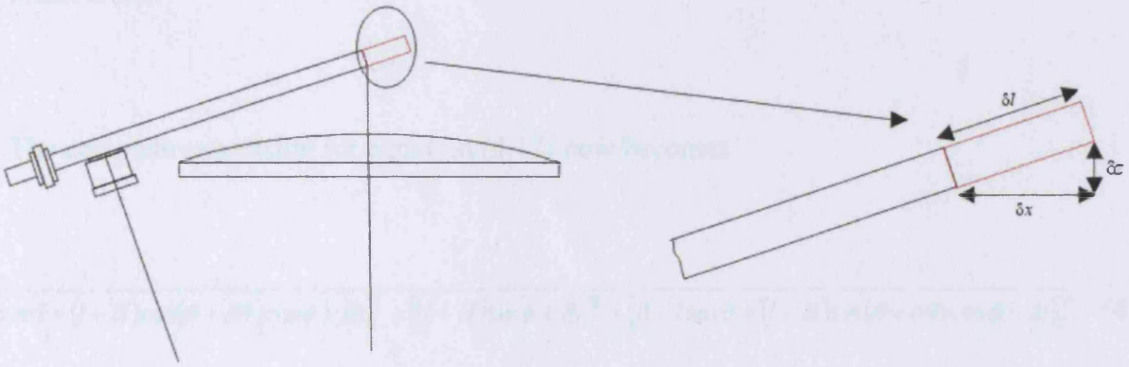

Figure 4.10 The thermal expansion δl of the arm is the equivalent of an error in δz and δx

If the arm was horizontal there would be no δz error which indicates an additional complication where different set-ups of the SAP result in different correlations. Similar correlations that occur for l also occur for errors in the tilt angle θ. A way to overcome this problem would be to express θ and l as functions of x, y and z. It is, however, preferred to maintain l and θ as independent variables in order to relate them to physical errors of the SAP. The correlation can be accounted for if the terms x, y and z in equation (4.13) are expressed as

$$x = (l + \delta l)\cos(\theta + \delta\theta)\cos\phi \tag{4.18}$$

$$y = (l + \delta l)\sin\phi \tag{4.19}$$

$$z = (l + \delta l)\sin(\theta + \delta\theta)\cos\phi . \tag{4.20}$$

In this way the effect of δl and $\delta\theta$ on x, y and z is taken into account and $\delta l, \delta\theta$ are maintained in the equation as independent variables. It is important to note that the perturbations δl and $\delta\theta$, are not included in the terms $-l\cos\theta$ and $-l\sin\theta$ of equation (4.17) since these terms define the original geometrical relationship between the probe tip and the CC where the SAP is assumed to be perfectly set-up and there are no initial offset errors.

The complete expression for equation (4.17) now becomes

$$|R'| = \sqrt{[-l\cos\theta + (l+\delta l)\cos(\theta+\delta\theta)\cos\phi + \delta x]^2 + [(l+\delta l)\sin\phi + \delta y]^2 + [R - l\sin\theta + (l+\delta l)\sin(\theta+\delta\theta)\cos\phi - \delta z)]^2} \tag{4.21}$$

If $\delta x, \delta y, \delta z, \delta l$ and $\delta\theta$, in equation 4.21, are set to zero then the equation results to $|R'| = |R|$ (APPENDIX A). This implies that the RoC of the modified reference sphere is the same as the RoC of the nominal sphere. This is exactly what would be expected if no perturbations were present.

Summarising, an equation that expresses the machine error as a change in the RoC of the reference sphere has been established. This parametric equation can be related to real machine errors as well as to the actual measurand that is the surface form error. In order to do this it is first required to define mathematically the surface form as the latter is measured by a SAP.

4.8 DEFINING THE MEASURAND

The quality of an optical surface is usually described by two types of errors, the peak-to-valley (PV) error and the root-mean-square (RMS) error. The PV error describes the difference between the highest and lowest departures of a surface with respect to the absolute design form. However, small imperfections such as a scratch or pit on the surface of an, otherwise good, optic can result in a very large PV error which does not reflect the overall surface quality.

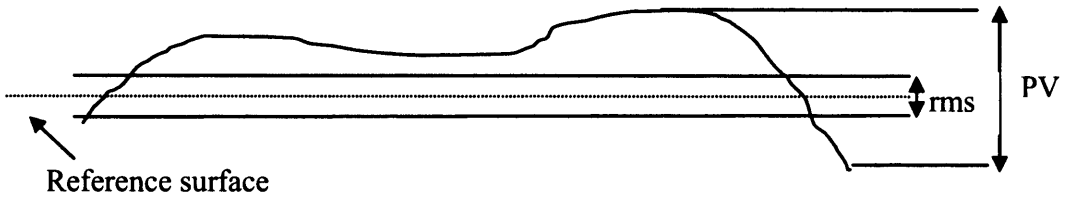

Figure 4.11 RMS and PV errors

A better measure of the surface's quality is the RMS error. The RMS error is a weighted error that expresses the standard deviation of the height of the test surface relative to a reference surface across the measurement range (figure 4.11).

In the case where we measure the surface profile deviations from a nominally flat profile the RMS error is easily realised as the standard deviation of the height of the measured surface relative to the design form. However, in the case of the SAP the profile measurement expresses deviations from a nominal spherical reference. In this case two possible definitions could be used to describe the surface profile error. The first definition considers the difference in sag between the nominal and the measured sphere (figure 4.12). This description interprets the surface error as the axial height difference between the nominal sphere and the measured sphere.

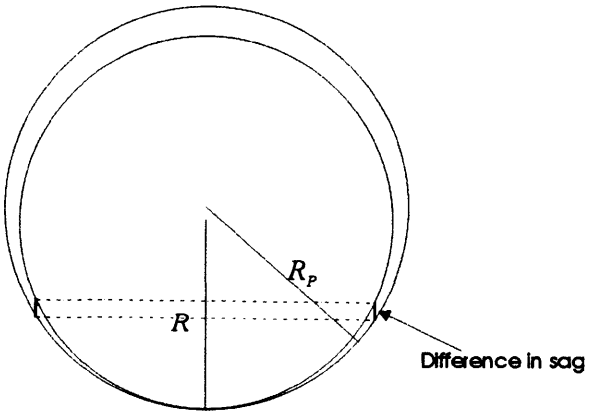

Figure 4.12 Difference in sag between perfect (R) and perturbed (R_P) reference spheres

In a SAP, however, the probe is maintained normal to the SUT during scans. It would, therefore, be more accurate to describe the profile error as the radial difference, $R-R'$, between the nominal and the measured sphere. This is demonstrated in figure 4.13 where an error due to an incorrect tilt angle is presented. The nominal probe tip vector with respect to the origin O is $R=\overline{OP}$. The actual tip vector with respect to the origin is $R'=\overline{OP'}$. The vector, $\overline{PP'}$, represents the probe tip displacement and, since the probe axis is aligned with the radius vector, R, the change in length is measured directly by the probe as an apparent change in the radius of curvature of $R-R'$. As a conclusion, the error $R-R'$ is manifested as a form error and can be used to represent the instantaneous form error, at a particular point.

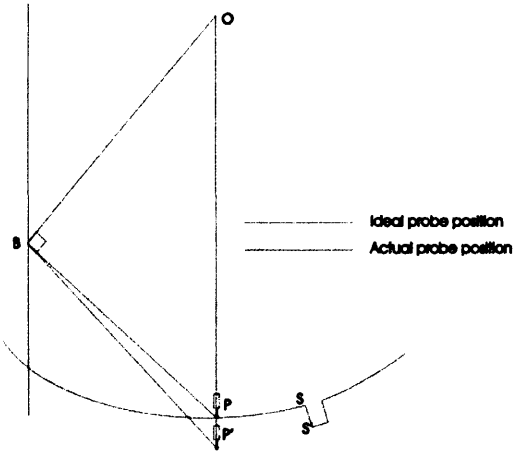

Figure 4.13 The difference in radii of curvature as a description of the form error

4.9 SENSITIVITY ANALYSIS AND SIMULATION

4.9.1 DETERMINATION OF THE SENSITIVE PARAMETERS

Sensitivity analysis is a crucial step towards the construction of an error budget since it can be used both as a qualitative and a quantitative error analysis tool. Qualitatively, sensitivity analysis helps to establish how the variation on the output of a model is apportioned to the variation of the input parameters and, therefore, helps identify the sensitive parameters of the system. Sensitivity analysis can also be used quantitatively to provide the order of magnitude of the allowed tolerances in chosen parameters. Having an estimate of the tolerance in certain directions is of great significance since it can be used to establish sub-component conformability to the overall design.

In order to perform sensitivity analysis equation (4.21) was set up in a simulation spreadsheet where the parameters l, θ and R were the user defined constants. The choice of these parameters simulates different optics and different SAPs. The error terms $\delta\theta, \delta l, \delta x, \delta y$ and δz are used as the input variables and the surface error, $R - R'$, is the output. The sensitive parameters were identified by observing the change in the output for given changes in the input variables.

4.9.2 ESTIMATION OF TOLERANCES

In order to estimate the tolerances in the system's parameters, perturbations were introduced and were varied until a threshold of maximum surface error was reached. The value of each perturbation when the threshold is reached corresponds to the error tolerance in the perturbed parameter. For the estimation of the order of magnitude for the errors of a generic SAP three different cases were investigated. The first case is with regard to the Euro50 specifications (table 4.1). The second case (table 4.2) refers the

extended measurement range according to the proposed case study optic (described in section 3.5). The third case (table 4.3) represents a generic optic and the simulation and the threshold surface form accuracy reflects the DTI specifications.

INPUT CONSTANTS		
Effective arm length	(l)	1.4 m
Tilt angle	(θ)	0.94373^0
Swing-angle range	(ϕ)	-45^0 to 45^0
RoC of best fit sphere	(R)	85 m
Optic diameter	(d)	2.3 m
TARGET OUTPUT		
Max. allowed form error	(R'-R)	36 nm
VARIABLES		
Tolerance in x	(δx_{max})	2.2 μm
Tolerance in y	(δy_{max})	2 μm
Tolerance in z	(δz_{max})	36 nm
Tolerance in θ	($\delta\theta_{max}$)	5.3 marc sec
Tolerance in l	(δl_{max})	1 μm

Table 4.1 SAP tolerances corresponding to the measurement of the Euro50 segments

INPUT CONSTANTS		
Effective arm length	(l)	0.350 m
Tilt angle	(θ)	41.1395^0
Swing-angle range	(ϕ)	-45^0 to 45^0
RoC	(R)	532 mm
Optic diameter	(d)	600 mm
Surface slope	(α)	33^0
TARGET OUTPUT		
Max. allowed form error	(R'-R)	350 nm
VARIABLES		
Tolerance in x	(δx_{max})	0.705 μm
Tolerance in y	(δy_{max})	0.532 μm
Tolerance in z	(δz_{max})	0.35 μm
Tolerance in θ	($\delta\theta_{max}$)	0.2739^0
Tolerance in l	(δl_{max})	0.530 μm

Table 4.2 SAP tolerances corresponding to the case study optic of 33^0 surface slope

INPUT CONSTANTS		
Effective arm length	(l)	0.350 m
Tilt angle	(θ)	5.01980^0
Swing-angle range	(ϕ)	-45^0 to 45^0
RoC	(R)	4000 mm
Optic diameter	(d)	600 mm
Surface slope	(α)	4.3^0
TARGET OUTPUT		
Max. allowed form error	(R'-R)	20 nm
VARIABLES		
Tolerance in x	(δx_{max})	0.23 μm
Tolerance in y	(δy_{max})	0.23 μm
Tolerance in z	(δz_{max})	20 nm
Tolerance in θ	($\delta\theta_{max}$)	0.01184^0
Tolerance in l	(δl_{max})	0.229 μm

Table 4.3 SAP tolerances corresponding to a typical optic of low surface slope. The target output for the surface form is 20 nm according to the DTI specifications

In order to obtain the error tolerances a simulated scan was performed for a swing angle of $\phi = \pm 45^0$ at steps of 1^0 leading to ninety simulated data points. The form error was calculated at every point and the results were averaged.

The calculation of the various tolerances was based on a significant simplifying assumption: it was assumed that that when one parameter is perturbed the perturbations in the rest of the parameters are all constant and equal to zero. As a result the calculated tolerances can only provide an approximate value for the projected error. This is still useful in guiding sub-component selection which was the objective at this stage of the design.

The sensitivity analysis showed very high sensitivity in θ for small tilt angles which resulted in large form errors. The sensitivity in θ decreases dramatically as the tilt angle is increased. This points out that optics with small curvature would require a SAP with

very good tilt control. The system proved less sensitive to changes in x, y and l. The sensitivity in z- is also very high since there is a one-to-one correspondence with the form error.

4.10 SUB COMPONENT CONFORMITY TO THE DESIGN

4.10.1 STATIC ERRORS

If the SAP is not aligned properly at the start of the measurement the probe will not follow the nominal scan path. This will be manifested as an effective form error. This may be the result of static, quasi-static or dynamic errors. An incorrect alignment of the SAP generates a perturbed reference sphere and hence an apparent SUT form error. Misalignment errors can be regarded as static offset errors and need to be corrected prior to the start of a measurement. Hence the SAP alignment mechanisms should have a resolution that is better than the corresponding error tolerance value. For example, according to table 4.3, the tolerance in θ is 0.01184^0. Therefore the angular adjustment mechanism for the SAP should have a resolution of at least 0.01184^0.

The calculated linear tolerances in table 4.3 calls for the use of nanopositioning alignment stages for the probe assembly. These results will be used to aid the evaluation of the future choice of alignment stages.

4.10.2 DYNAMIC AND QUASI-STATIC ERRORS

The calculated tolerances can also be used to evaluate the tolerances of other SAP sub-components which can generate quasi-static or dynamic errors. These errors are more difficult to deal with since it is difficult to predict how contributions from

different sources combine to yield a total error. Adopting a deterministic approach, it is assumed that all these errors obey to cause-and-effect and that individual error components have physical causes that can be identified and quantified. Following the approach of Sartori (1995) the SAP is approximated as a linear system where dynamical errors due to different causes are studied independently and their effects added to yield an overall error in a chosen parameter. The overall variance of each parameter is calculated as the root-sum-of-squares (RSS) of each of the sub-variances. Under this approach is assumed that the overall accuracy requirement of the SAP flows down to the accuracy of it's subassemblies. Assuming, for example, that a generic SAP consists of n components that generate m angular errors, $\Delta\theta_i$, the overall angular tilt error will be

$$\Delta\theta = \sqrt{(a_1\Delta\theta_1)^2 + (a_2\Delta\theta_2)^2 + ... + (a_m\Delta\theta_m)^2} \tag{4.22}$$

where $a_1, a_2 ... a_m$ are coefficients which denote the weight of each term. The coefficients $a_1, a_2 ... a_m$ can be calculated experimentally when the instrument is built. At this stage, however, it was assumed that all coefficients were unity and that each error term had equal weight. It should be noted that the overall variance in the rest of the parameters x, y, z and l is also calculated as the RSS of the corresponding sub-variances. The next step was to estimate the number of subvariances in each error term. In order to do this the main components of a generic SAP were considered and their error contributions were analysed separately.

4.10.3 ALLOCATING ERRORS TO DIFFERENT COMPONENTS

The error of each SAP sub-component has to be expressed through its effect on the parameters x, y, z, l and θ. As an example we consider the errors of the arm air bearing

(figure 4.14). The linear errors are runout errors which correspond to independent perturbations δx, δy and δz .The coning results in perturbations $\delta\theta$ and $\delta\psi$. Since the parametric error function does not include the parameter, ψ, the error, $\delta\psi$, has to be expressed through its effect on any of the defining parameters *x, y, z, l* and θ. As is shown in figure 4.15, the effect of $\delta\psi$ is a cosine error of $\delta y = a\sin\delta\psi$. The correlated error, $\delta\theta$, results in equivalent errors δz_c and δx_c but these have been taken into account in equation (4.21) as $\delta z_c = z = l\sin(\theta+\delta\theta)\cos\phi$ and $\delta x_c = x = l\cos(\theta+\delta\theta)\cos\phi$, therefore, these correlated terms will not be considered here. As a result the air bearing error contributions can be summarised in table 4.4.

Arm air bearing	δx	δy	δz	$\delta\theta$	δl
Wobble	0	+	+	+	0
Radial Runout	+	+	0	0	0
Axial Runout	0	0	+	0	0

Table 4.4 Summary of error contribution for the arm air bearing

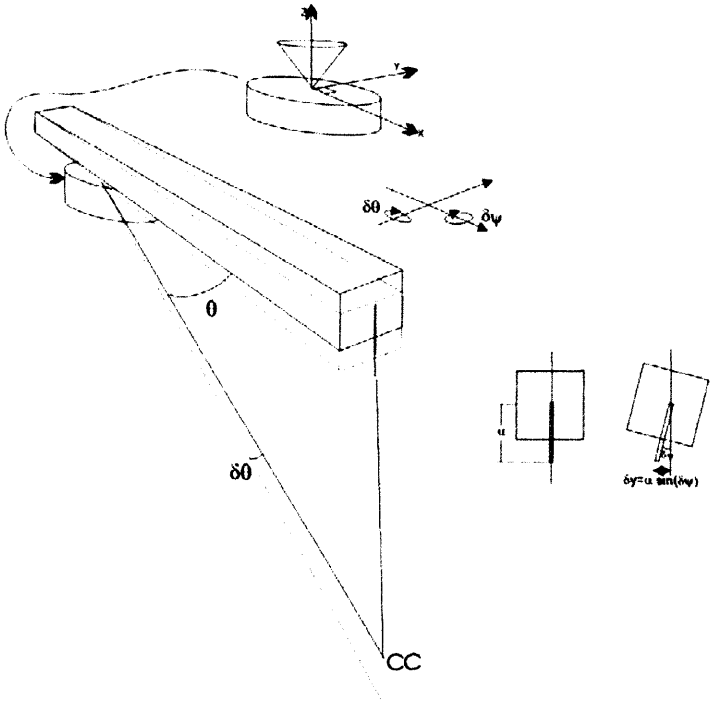

Figure 4.14 Coning results in a correlated error $\delta\theta$ and an independent error $\delta y = a\sin\delta\psi$

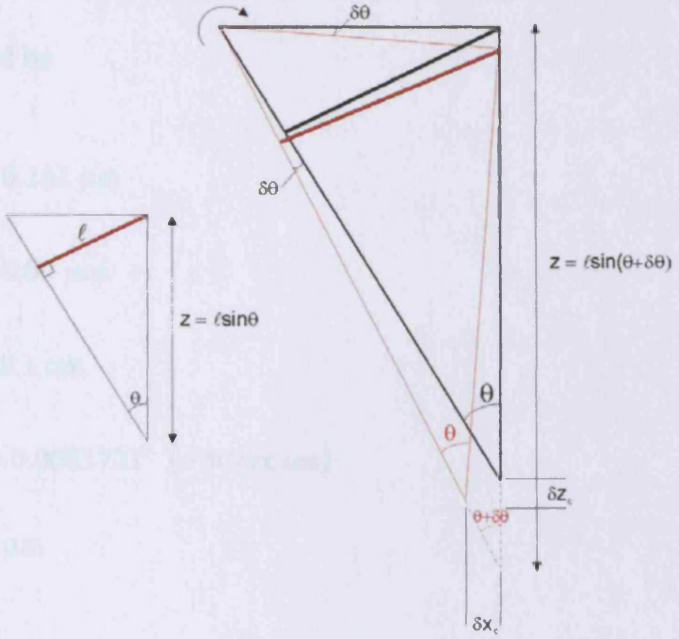

Figure 4.15 The equivalent effect of $\delta\theta$ is an error δz_c and an error δx_c

Following a similar reasoning for other sub-components all SAP errors can be expressed as error contributions of $\delta x, \delta y, \delta z, \delta\theta$ and δl. The summary of the main SAP quasi-static and dynamic errors is shown in table 4.7.

Component	Main independent, dynamic, perturbations				
	Translation			Rotation	Eff.Arm length
	δx	δy	δz	$\delta\theta$	δl
Arm air bearing					
Wobble	0	+	+	+	0
Radial Runout	+	+	0	0	0
Axial Runout	0	0	+	0	0
Component air bearing					
Wobble	0	+	0	+	0
Radial Runout	+	+	0	0	0
Axial Runout	0	0	+	0	0
Arm beam					
Thermal expansion during measurement.	0	0	0	0	+
Vibration intrinsic	0	+	+	0	0
Vibration extrinsic	0	+	+	0	0
Displacement Transducer					
Non-linearity	0	0	+	0	0
RSS Total	$\sqrt{2\delta x^2}$	$\sqrt{6\delta y^2}$	$\sqrt{6\delta z^2}$	$\sqrt{2\delta\theta^2}$	δl

Table 4.5 Error contributions of the main SAP sub-components

Using the results of table 4.5 the maximum allowed error contribution of each sub-component would be

$$\delta x = \sqrt{\delta x_{\max}^2 / 2} = 0.162 \ \mu\text{m}$$

$$\delta y = \sqrt{\delta y_{\max}^2 / 6} = 0.09 \ \mu\text{m}$$

$$\delta z = \sqrt{\delta z_{\max}^2 / 6} = 8.1 \ \text{nm}$$

$$\delta\theta = \sqrt{\delta\theta_{\max}^2 / 2} = 0.0083721^0 \ \ (\approx 30 arc\,\text{sec})$$

$$\delta l = \delta l_{\max} = 0.29 \ \mu\text{m}$$

The result of the error budget is likely to underestimate the overall tolerances for each component. For example a good quality air-bearing is not expected to have radial runout larger than a few tenths of nanometres. This would allow the remaining allowance to be allocated to a different component. Most importantly, some errors will combine in a way so as to cancel out. In order to investigate the SAP model in detail a numerical simulation would be required, however, this is beyond the scope of the current thesis. The main goal is the establishment of the order of magnitude of the projected error in order to guide the component selection.

4.10 CONCLUSIONS

The operation of a generic SAP was analysed from first principles and a parametric error function was constructed. The function was based on five defining parameters which describe completely the spherical envelope of the SAP. A definition of the measurand was adopted that takes into account the SAP measuring principle and the definition was related to the parametric function. The machine errors were then expressed as perturbations of the defining parameters. Any correlated error terms were

taken into account in the expression of the parametric error function. Using the error function a sensitivity analysis was performed in order to identity the system's sensitive parameters and to estimate the error tolerances in each parameter. Each major SAP component was analysed separately in order to find its error contributions. These errors were decoupled and used as independent subvariances to yield a total error. The total perturbation in each parameter was then approximated as the RSS sum of the different sub-variances. In setting the total error equal to the tolerance it was possible to estimate an upper limit for the error contribution of each individual SAP component.

Chapter 5

A FIRST SAP PROTOTYPE

"If we knew what it was we were doing it would not be called research, would it?"

Albert Einstein

5.1 USING A FAG TALYTRON R300 AS A SAP

As part of the SAP design process a scaled-down prototype was constructed in order to gain practical experience on general issues concerning swing-arm profilometry. The prototype was built using a decommissioned FAG-Talytron R300 roundness measuring instrument. According to the manufacturer's specifications, the R300 was capable of measuring the roundness of artefacts of up to 300 mm in diameter. The main sub-components of the R300 are a spindle with a quoted radial runout better than 0.2 μm at 6 rpm and a swivelling gauge holder. The Talytron R300 is shown in figure 5.1.

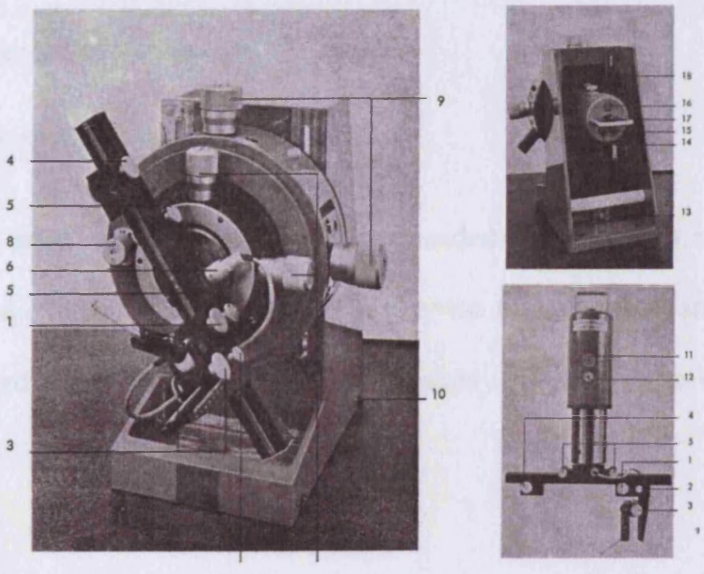

Figure 5.1 The main operating elements of the Talytron R300

With reference to figure 5.1 the sub-components and adjustments of the R300 are explained below.

1. Knob for radially displacing the gauging assembly.
2. Locking screw for the gauging assembly.
3. Knob for axially displacing a swivelling gauge holder.
4. Knob for displacing the counter-weight.
5. The small counter-weight which runs in the transverse support can be displaced from one side to the other by means of the two small knobs.
6. Gauge connection.
7. Tip-tilt screws for the spindle (maximum $\pm 3^0$).
8. Knob for adjusting the tilting and centering unit to the working position of the roundness measuring spindle.
9. X-Y centering screw for the measuring spindle (maximum ± 5 mm).
11. Knob for uncoupling of the spindle drive to turn the unit by hand.
12. Knob for clamping the spindle in four 90^0 positions.
13. Compressed air connection.
14. Electric motor connection.

The R300 has most of the necessary features needed to function as a basic SAP. The swivelling gauge holder can be modified to play the role of a SAP arm and an LVDT can be mounted at the end of the gauging assembly (figure 5.2) in order to perform measurements.

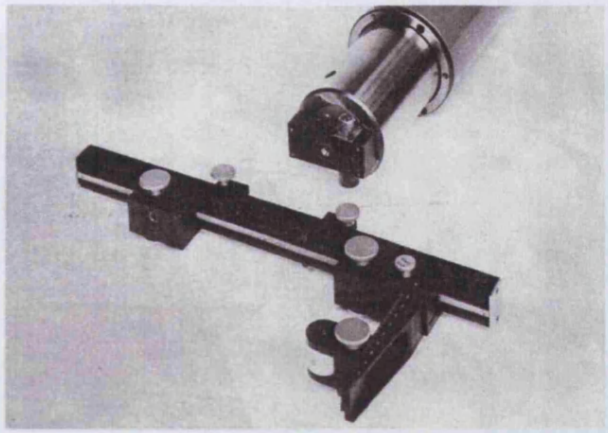

Figure 5.2 The arm and gauging assembly of the Talytron R300

On the arm assembly there is a gauge holder which is axially adjustable by 65 mm. The gauge holder has also a swivelling probe mount (figure 5.3) which allows tilting adjustment of the probe. Both probe linear and angular adjustments prove to be necessary for a generic SAP in order to maintain the probe in contact with the SUT. If for example the arm it tilted clockwise about the y-axis this will result in an equal amount of tilt on the probe stylus as well as a displacement along the positive z-direction. These and similar misalignments can be compensated using the swivelling and axial adjustment of the gauge holder. The re-adjustment of the probe is necessary since, as it was mentioned in earlier chapters, the probe has to be normal to the SUT and aligned to pass through the SUT's vertex at the start of any SAP measurement.

In the R300 the gauging assembly is also adjustable along the x-axis. With an appropriate modification this can be exploited in order to allow an adjustable SAP arm length. On one end of the arm there is a movable counterweight which, as in the SOML SAP, can be used to balance the arm in its pivot. The two tilting adjustment screws allow tip and tilt adjustment of the bearing axis by $\pm 3^0$. The tip/tilt adjustment can be used in order to adjust the arm rotation axis according to the RoC of the test optic. Finally the two x-y centering screws allow for linear adjustment of the bearing.

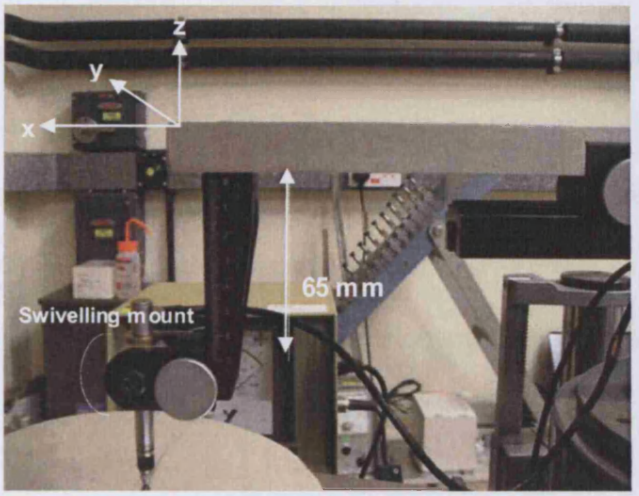

Figure 5.3 The probe mount allows axial adjustment of the probe along the *z*-axis and angular adjustment about the *y*-axis

The main dimensions and travel ranges of the R300 are illustrated in figure 5.4.

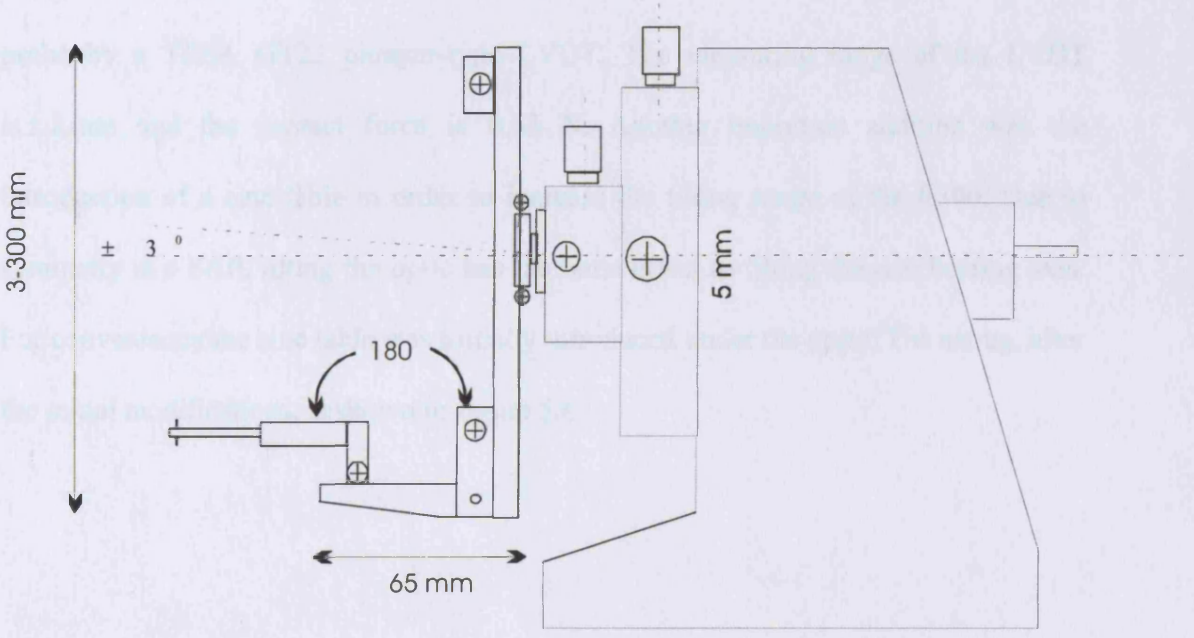

Figure 5.4 Dimensions and adjustability of the TALYTON R300

5.2 MODIFICATIONS OF THE R300 AND INITIAL SET-UP

In order to perform basic experiments with the R300 the instrument had to be modified so that it mimics the operation of a SAP. In order to do this the R300 was placed in a metal enclosure that allowed upright position of the bearing. This resulted in the arm being nominally horizontal as in the case of a typical SAP. Further modifications on the arm included the addition of an aluminium extension and the repositioning of the probe mount under the arm extension (figures 5.3 and 5.5).

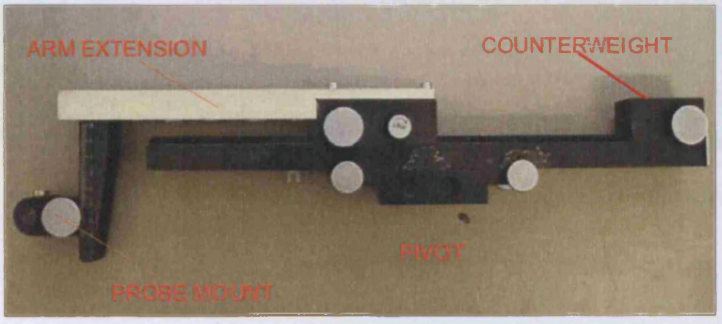

Figure 5.5 Modifying the swivelling arm

Further modifications of the R300 included the replacement of the original cantilever probe by a TESA GT22 plunger-type LVDT. The measuring range of the LVDT is ± 2 mm and the contact force is 0.63 N. Another important addition was the introduction of a sine table in order to increase the tilting range of the R300. Due to symmetry in a SAP, tilting the optic has the same effect as tilting the arm bearing axis. For convenience the sine table was initially introduced under the optic. The set-up, after the initial modifications, is shown in figure 5.6.

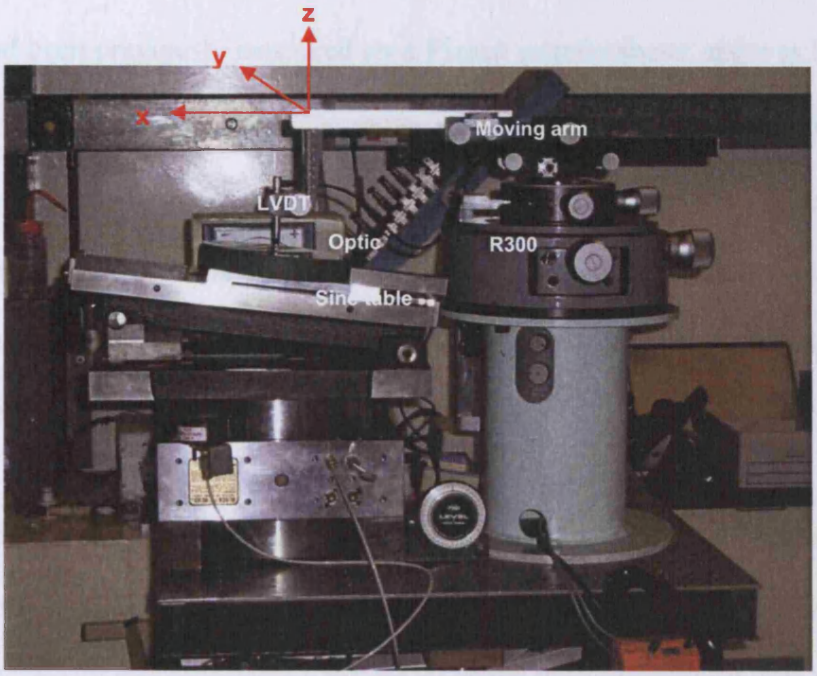

Figure 5.6 The initial set-up. The R300 is shown on the right in upright position. A sine table is introduced in order to increase the tilting range

5.3 PRELIMINARY INVESTIGATIONS

5.3.1 SCANNING A FLAT SURFACE

According to the SAP defining equation, $\sin\theta = l/R$, when the tilt angle of a SAP is set to zero the corresponding measurable RoC becomes infinite. In other words for a zero tilt angle the SAP is set to measure flat surfaces. The zero tilt position will be considered to be the null position of a generic SAP. In order to practically set a SAP to measure a flat surface it is necessary to ensure that the tilt angle of the arm bearing is set to zero with respect to the plane defined by the flat surface.

One of the first experiments with the R300 was to try to set it to its null position. This was attempted initially by setting both tilting knobs on the spindle as well as the sine

table to zero degrees. A circular 15 cm diameter steel flat was used as a test artefact. The flat had been previously measured on a Fizeau interferometer and was found to be nominally flat to better than $\lambda/4$. The motor of the bearing was not operational and in order to perform the measurement it was disengaged and the arm was turned manually. Prior to the measurement the arm was moved so that the LVDT probe was positioned close to the centre of the circular flat. At this position the probe was nulled to zero displacement and consequently the arm was swung across.

A perfect alignment would mean zero probe displacement for the duration of the scan. However, when the circular flat was scanned with the R300 it was observed that the probe displacement was only zero in the centre of the flat and was gradually compressed at the edges. Furthermore it was observed that the amount of deflection was different for the right hand side and the left hand side edge of the flat. A plot of the probe deflection at different positions across the flat is shown in figure 5.7.

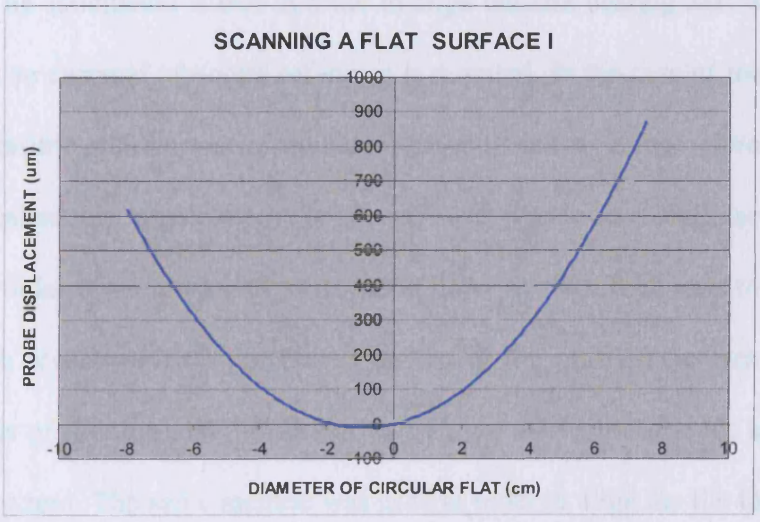

Figure 5.7 Probe displacement against optic diameter

If the R300 was perfectly aligned the plot in figure 5.7 would be a straight line coincident with the *x*-axis. Instead the result of the experiment shows a graph which is

curved and non-symmetrical about the y-axis. The features of the graph can be justified if two angular misalignments are present. The curvature of the graph is an indication that the tilting angle, θ, of the bearing is set incorrectly. As a result the reference surface and the actual surface do not coincide and an apparent curvature is measured by the probe. The asymmetry of the graph about the y-axis can be justified if there is a lateral tilt term present (roll). This means one edge of the SUT is at an elevation with respect to the x-y plane, hence resulting in an additional amount of displacement of the probe on that side. This is shown as a different in height between the ends of the graph.

5.3.2 THE NEED FOR AN EXTERNAL REFERENCE

From this preliminary investigation it is apparent that although both the bearing and the flat were set to zero roll/tilt, according to the null positions of their alignment stages, there were still effective roll/tilt terms present. These angular errors can only be explained as a result of internal misalignments within the metrology loop of the instrument. The conclusion is that in order to align the arm bearing axis with respect to the SUT axis an external, absolute reference is required. In the case of the R300 one of the most accessible options was to use the direction of gravity as the reference direction. In order to realise this, an electronic level was used. The level makes use of a damped pendulum in order to obtain a null position. In order to align both axes to the direction of gravity the level was first positioned on top of the profilometer arm (figure 5.8) above the axis of rotation and the tilting knobs were used to set the tilt and the roll to approximately zero. The same method was used in order to align the flat to the direction of gravity. In order to gain better control over alignment a tip-tilt stage was introduced under the flat.

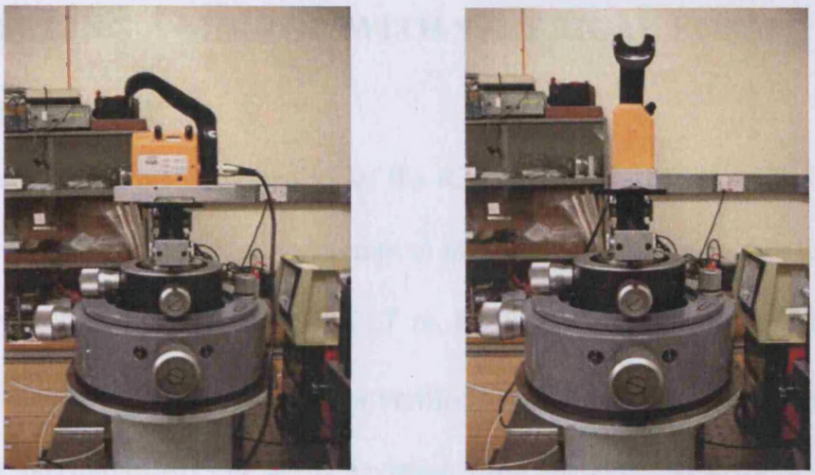

Figure 5.8 Using an electronic level in order to reset the angle in two axes

The measurement of the mirror was repeated and the plot of the result is shown in figure 5.9. It is apparent from figure 5.9 that both angular errors are still present but they are reduced by nearly an order of magnitude. The dominant error is a tilting error and it is probably a result of the level not being positioned at exact coincidence with the bearing axis during alignment. This was difficult to achieve in practise and it is likely that the bearing was aligned to gravity at a slightly offset position. This resulted to an Abbe error which was manifested as a tilt error.

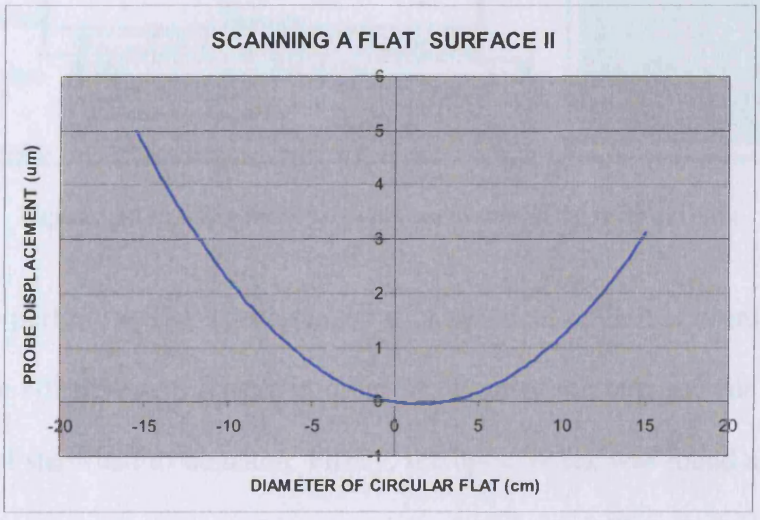

Figure 5.9 Plot of probe displacement against diameter after alignment

5.4 MEASURING A MIRROR WITH SPHERICAL FORM

5.4.1 INITIAL SET-UP

Having demonstrated the functionality of the R300 as a rudimentary SAP with the aid of the steel flat the next step was to attempt to measure an actual optic. For this purpose a concave mirror of focal length, $f = 1.27$ m, RoC, $R = 2.54$ m and estimated surface sag of 1.7 mm was used. The mirror was verified to be nominally spherical with the aid of a ZYGO interferometer. The RMS deviation from the spherical shape was found to be to 0.087λ. The measurement results are shown in figure 5.10.

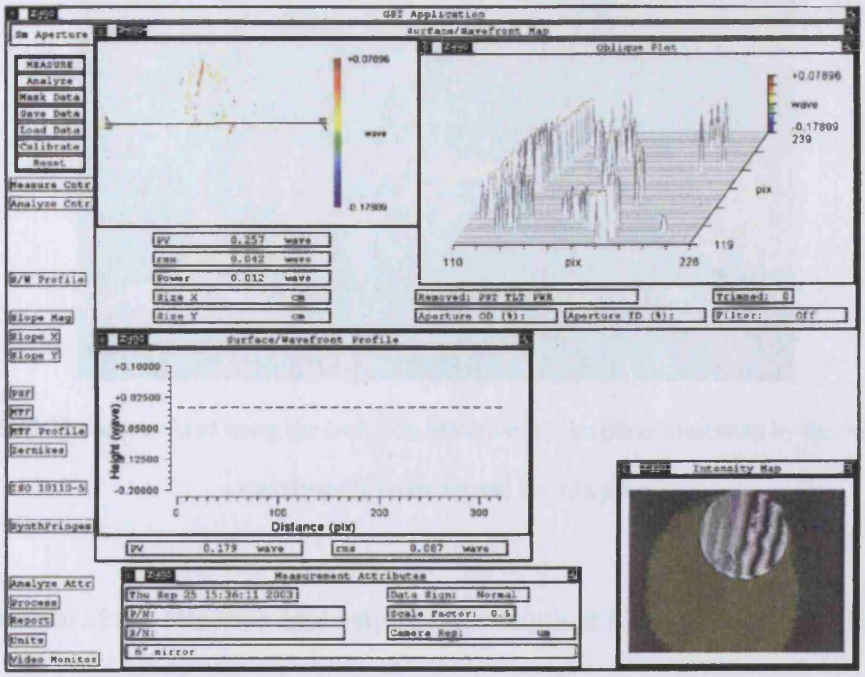

Figure 5.10 Interferometric measurement results of the spherical optic

In general, to perform a SAP measurement of a spherical optic it is necessary to know accurately the effective arm length in order to calculate the required tilt angle. To do this a series of steps had to be taken. Firstly, the optic vertex was found approximately by taking a chord on the optic and its perpendicular bisector. The centre of the optic is then found by locating the midpoint of the perpendicular bisector. After locating the

optic vertex, the arm was extended until the probe tip coincided with the vertex. Consequently the locking screw was applied to hold the arm extension in place and the whole arm structure, along with the gauging assembly and the LDVT, was removed from its pivot and was placed on a CMM. In this way the effective arm length (figure 5.11) could be measured with high precision and was found to be 292.6442 mm $\pm$0.0005 mm.

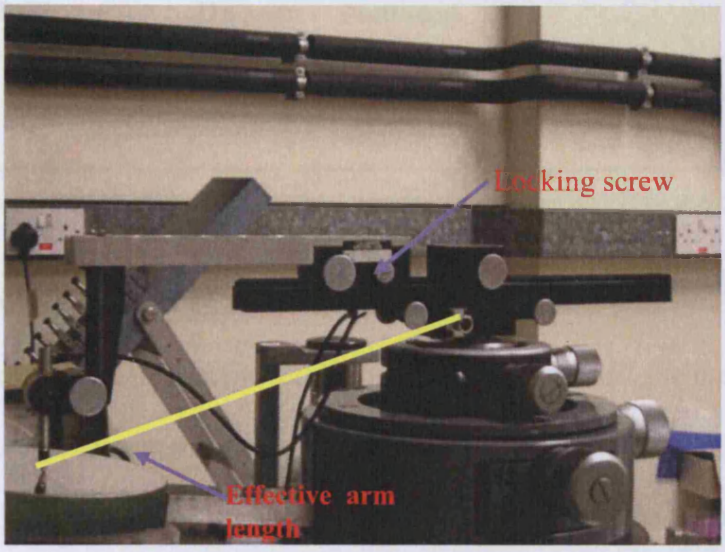

Figure 5.11 The arm is fixed using the lock. The effective arm length is illustrated by the yellow line connecting the probe tip and the arm pivot

Having measured the effective arm length, *l*, the required tilt angle was calculated using $\theta = \sin^{-1}(l/R)$. For $l = 292.6442$ mm and $R = 2.54$ m the resulting tilt is 6.61598^0. Since the tilting range of the R300 is only $\pm 3^0$ the sine table was used to generate the remaining tilt. The sine table has a length of 300 mm and the highest resolution offered by gauge blocks is about is 0.1 μm. As a result the sine table can provide an angular resolution of 6.84 milliarcseconds. In order to assess if this resolution is sufficient for the current epxeriment the simulation spreadsheet was used. For the demonstration

purposes of the current experiment the target accuracy was set to 1 μm. The corresponding tolerances are shown in table 5.1.

Specifications		*Sensitivity*		
Arm Length	292.6442 mm	**Positional**	δx	8.7 μm
Tilt angle	6.61598^0	**Positional**	δy	8.7 μm
Nominal RoC	2540 mm	**Positional**	δz	1 μm
		Angular	$\Delta\theta$	7 arcsec

Table 5.1 Calculated tolerances for the measurement of an R = 2540 mm optic

It is apparent from table 5.1 that the resolution of the sine table is an order of magnitude higher that the required alignment resolution hence it was used for the alignment. In order to perform the measurements the tilt angle of the R300 was set-up using the full 3^0 range of the R300 while the remaining tilt was generated by the sine table.

5.4.2 MEASUREMENT RESULTS

After setting the tilt angle, the arm was swung across the spherical optic. Initially the LVDT meter was set at the lowest sensitivity setting ($\pm$ 2 mm range) and as the arm was moved across the mirror the reading on the meter showed zero displacement as expected. However, when the sensitivity was increased it was realised that alignment errors were still present (figure 5.12).

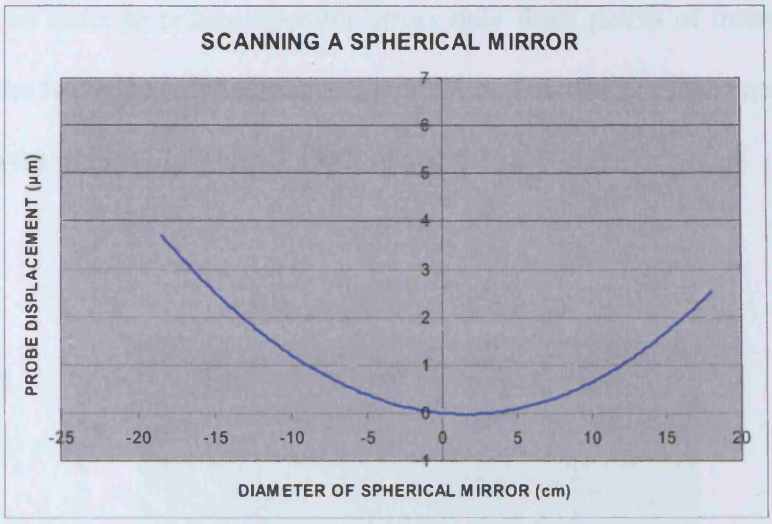

Figure 5.12 The measurement of a concave spherical optic

The graph of figure 5.12 resembles the graph of figure 5.9 in the sense that the resulting plot is a curved trace, asymmetric about the *y*-axis. As in the case of the flat measurement, the asymmetry of the graph can be justified as a tip alignment error. For the curvature of the graph, however, there could be two reasons: either the tilt angle, θ, is incorrectly set or the probe tip is misaligned with respect to the vertex of the mirror. If the probe is not passing through the vertex the result is that the trace of the SAP does not match the form of the SUT and an effective curvature is measured by the probe. The resulting error could also be a combination of both angular and positional errors. It should be noted that when measuring a flat, the curvature of the graph can only be attributed to tilting errors. The displacement error according to figures 5.12 is 3.5 µm and no further modifications were made to improve the accuracy as the current experiment was merely a proof-of-concept exercise.

In order to verify the operation of the R300 as a SAP some basic repeatability tests were performed. The same spherical optic was measured but the measurement was repeated ten times. Due to the fact that an analogue meter was used for the measurement it was

decided that in order to reduce operator errors only three points of interest would be considered: the two edges of the optic and the vertex. The results of the repeatability test are shown in the graphs of figures 5.13, 5.14 and 5.15.

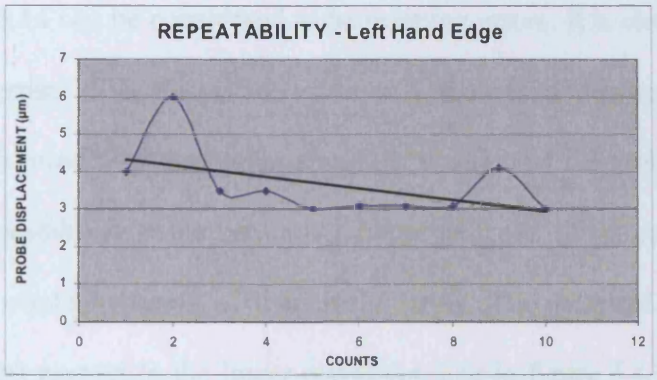

Figure 5.13 Repeatability on the left hand edge of the mirror for ten measurements

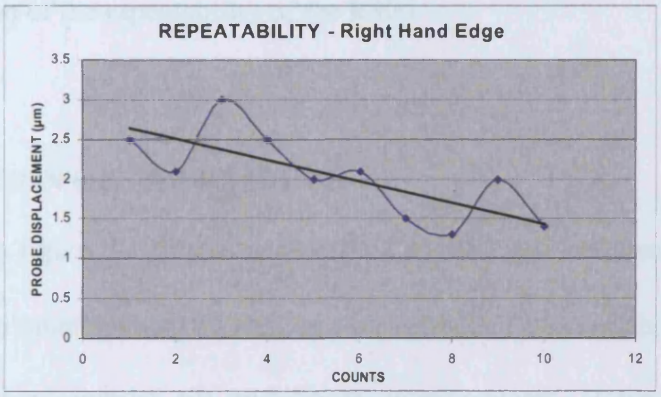

Figure 5.14 Repeatability on the right hand edge of the mirror for ten measurements

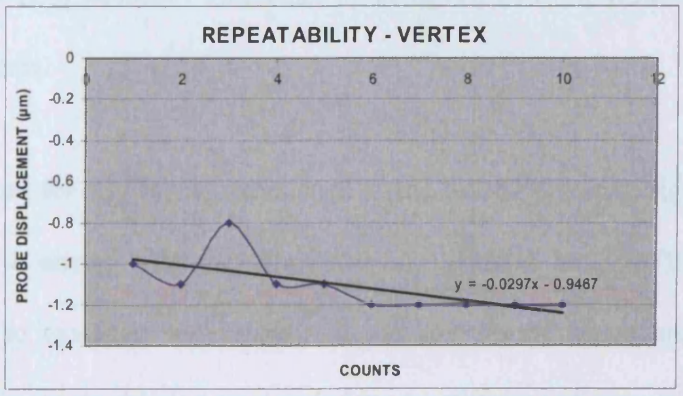

Figure 5.15 Repeatability on the vertex of the mirror for ten measurements

A qualitative check on the graphs of figures 5.11, 5.12 and 5.13 reveals that the repeatability is significantly better through the vertex than at the edges of the mirror. This can be justified by the fact that the arm was swung manually and as a result it was repositioned at slightly different positions on the mirror. Hence the errors shown in figures 5.13 and 5.14 can be considered to be resetting errors. It is clear that in order to avoid resetting errors it is necessary to have a motorised bearing and a tracking mechanism which provides information about the position of the probe with respect to the optic. The repeatability at the centre is a better indicator of the repeatability of the instrument as a whole in terms of dynamical errors. The standard deviation of the measured data with respect to the linear regression line in figure 5.13 was found to be 133 nm. This number represents the repeatability of the measurement at the vertex and gives an indication of the repeatability of the R300.

5.4.3 EVALUATION OF THE RESULTS

With reference to figure 5.12 there is an estimated measurement error of 1 μm which corresponds to tip misalignment as well as a measurement error of about 3.5 μm which is a combination of angular tilt and linear misalignments. However, the required measurement accuracy for optical surfaces is usually in the range between 50 nm and 100 nm. This level of accuracy could not be achieved with the R300 primarily due to alignment problems.

In order to account for alignment errors such as the roll-tilt errors of figure 5.12 it is not only necessary to ensure that the alignment mechanisms have sufficient range and resolution. It also essential to ensure that the sources of errors are identified and separated. In order to do this it was decided to use different alignment strategies and a

more accurate set-up. The introduction of additional alignment mechanisms could also function as a redundancy check.

5.5 FURTHER MODIFICATIONS TO THE R300

Further modifications were made to the R300 in order to improve the alignment and measurement accuracy and to expand the instrument's functionality. One of the changes was the introduction of an indexing table in order to allow precise rotation of the optic and the performance of "bicycle wheel" or spiral scans. The position of the sine table was changed and it was now placed under the R300 in an attempt to reduce the complexity of the alignment set-up and the potential for internal misalignments.

In order to improve the alignment procedure an optical alignment system (figure 5.16) was built and a frame was constructed around the R300 in order to mount the alignment optics. The optical system was based on a combination of a movable beam splitter and a fixed beam bender. The system makes use of an incident laser beam that is separated into two component beams, one of which is directed onto the arm pivot and the other on the vertex of the mirror *via* the beam bender, BB.

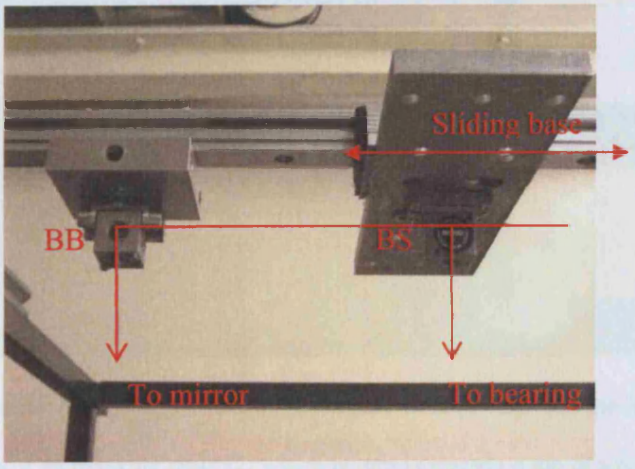

Figure 5.16 A beam splitter (BS) splits the incident beam into two component beams. The first beam is directed to the axis of the bearing and the other to the vertex of the mirror *via* a beam bender (BB)

The idea behind the optical set-up was to utilise the spots reflected from the SUT and the bearing as an alignment aid. Regrettably the system was not completed and no further progress was made with the R300 because the whole prototype had to be removed and disassembled due to space occupancy problems. The final set-up of the system prior to removal is shown in figure 5.17.

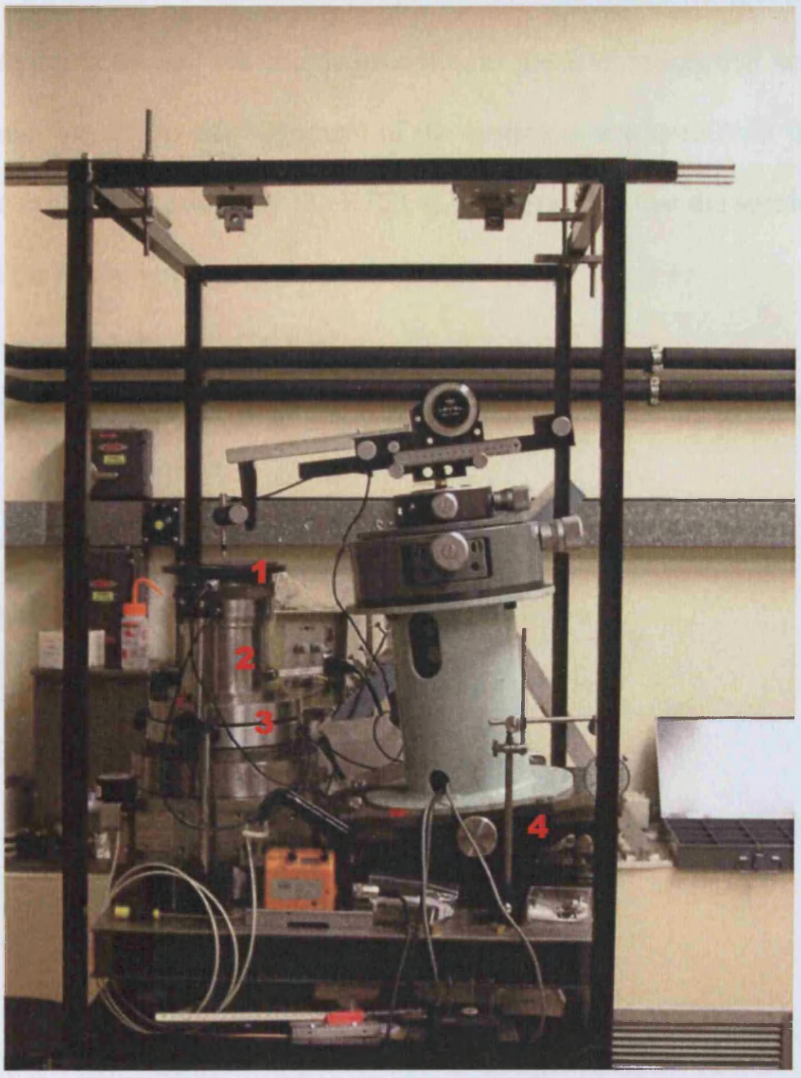

Figure 5.17 The final set-up prior to deconstruction. The sine table (4) has been moved under the R300. The optic (1) sits on top of an indexing table (2) which in turn is placed on top of a tip/tilt stage (3). The overhanging frame holds the alignment optics

5.6 CONCLUSIONS

A first SAP prototype was used as a proof-of-principle in order to investigate ideas of swing-arm profilometry. The SAP was built by modifying a FAG R300 roundness measurement instrument. The prototype had most of the basic functions that a generic SAP would have and provided some insight and directives concerning the design of a full-scale prototype. In particular it became apparent that in a SAP the incorrect alignment constitutes the main source of static error. The alignment of a SAP is not a straightforward process and the unique geometry of the SAP means that any change in any one parameter affects the alignment of the system as a whole. With this in mind, and with the experience gained by the R300, it was suggested that the second prototype should have the following alignment mechanisms:

1. Adjustable arm length. This will be used in order to reposition the arm to the vertex of optics of different diameters.
2. Tilt adjustment of sufficient resolution and range for the arm air bearing.
3. Tip adjustment for the optic and/or the arm air bearing.
4. Linear *x-y* adjustment for the optic and/or the SAP bearing.
5. Axial *z* adjustment and tip/tilt adjustment for the probe.
6. A motor for the arm air bearing and an encoder to provide positional information for the arm (and hence the probe).

Chapter 6

THE DESIGN OF THE SAP

"Knowledge is of no value unless you put it into practice."

Anton Chekhov

6.1 INTRODUCTION

This chapter is an overview of the design of the SAP. The design process starts by considering different options for the construction of the hybrid sensor and the effect on other SAP design aspects. After proposing a provisional hybrid sensor design, the implementation of the mechanical platform of the SAP is discussed. The SAP had to be built on an existing platform to reduce manufacturing costs. This placed significant design constraints which had to be overcome in order to realise the project specifications. The following sections describe in detail the evolution of the design towards the construction of a large-scale prototype SAP.

6.2 HYBRID SENSOR DESIGN CONSIDERATIONS

6.2.1 INTRODUCTION

The significance of the NPL-UCL SAP proposal lies on the prospective of obtaining simultaneous measurements from an optical and a mechanical sensor, namely the OMAM wavefront sensor and a contact displacement transducer, such as an LVDT. The hybridisation of the two sensors has a direct impact on the design and selection of other SAP components and had to be investigated at an early stage of the design.

On a functional SAP the measurement axis has to coincide with the optical axis of the test surface. This means that the contact probe has to be mounted so that it contacts directly the SUT at normal incidence. However, this is not necessary for the OMAM sensor because the output beam can be steered to be at normal incidence even if the sensor is mounted at an angle. The following sections investigate the advantages and disadvantages of various mounting configurations for the two sensors, and conclude with a provisional hybrid sensor design.

6.2.2 OMAM SENSOR MOUNTED VERTICALLY

6.2.2.1 DESCRIPTION OF CONCEPTUAL DESIGN

One of the obvious options for the hybrid sensor design is based on mounting the OMAM at normal incidence to the SUT as shown in figure 6.1. In the suggested design the OMAM is placed within an enclosure and the contact probe is mounted on an external bracket. The whole hybrid device is mounted onto a custom gimbal mount, as in the case of the SOML SAP, to provide independent and uncoupled rotation about two orthogonal axes allowing the hybrid sensor to align to the axis of gravity.

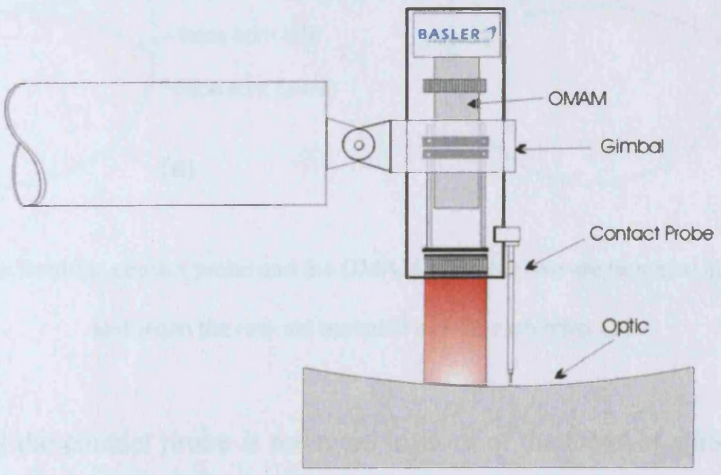

Figure 6.1 Concept design of a hybrid sensor where the OMAM is mounted vertically

The main concern with the proposal shown in figure 6.1 has to do with the focal length of the OMAM sensor. The aperture of the sensor will have to be mounted at a vertical separation of 350 mm from the SUT in order to focus the image of the SUT onto the sensor grating. This would require an equally long stylus for the probe in order to maintain contact with the SUT. Nevertheless, using very long probes between a sensor and a moving point is considered poor practise when high precision measurements are required (Chetwynd 1992). According to Flack (2001) the stylus bending increases with the cube of the stylus length, for constant stylus cross-section, and in the SAP it could cause significant errors during continuous scans.

6.2.2.2 PROBING CONSIDERATIONS

If the OMAM is mounted vertically there are two main mounting options for the contact probe: on the side or on the front (or back) of the sensor housing. The resulting traces in each case and for each sensor are shown in figures 6.2(a) and 6.2(b).

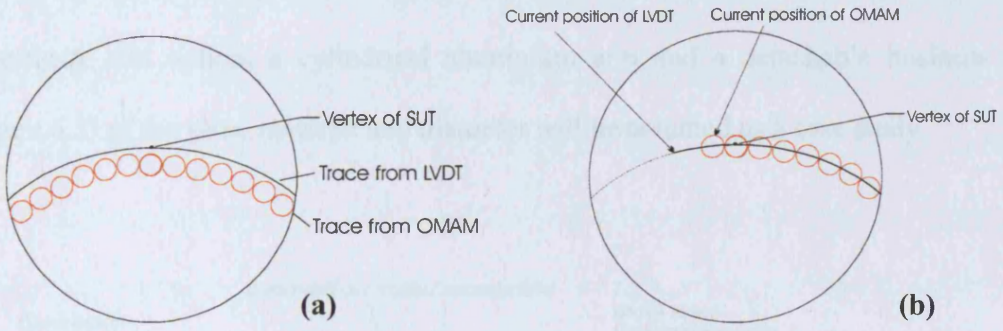

Figure 6.2 Traces from the contact probe and the OMAM when the two are mounted after each other (a) and when the two are mounted next to each other (b)

In figure 6.2(a) the contact probe is mounted in front of the OMAM sensor. Two traces are shown, a line trace corresponding to the contact probe and a sequence of circular

patches denoting the trace from the OMAM. The problem with the configuration of figure 6.2(a) is that the trace of at least one of the sensors will not pass through the optic vertex negating the SAP principle. This could be resolved if the contact probe was mounted at the side of the OMAM as shown in figure 6.2(b). In this case both traces pass through the optic vertex and the SAP principle is maintained for both sensors. In this case the main problem is that at a given time each sensor would be scanning a different part of the optic making the correlation of the two measurement datasets difficult.

6.2.3 OMAM SENSOR MOUNTED HORIZONTALLY

6.2.3.1 THE USE OF A DETACHABLE END PART

One of the choices for horizontal mounting of the OMAM sensor is based on the use of a detachable end part. The employment of a detachable business end would allow the use of extensions of different lengths, hence increasing the adaptability of the SAP to measuring optics of a greater range of diameters and radii of curvature. In order to investigate this option, a cylindrical aluminium arm and a detachable business end (figure 6.3) of the same material and diameter will be assumed as a case study.

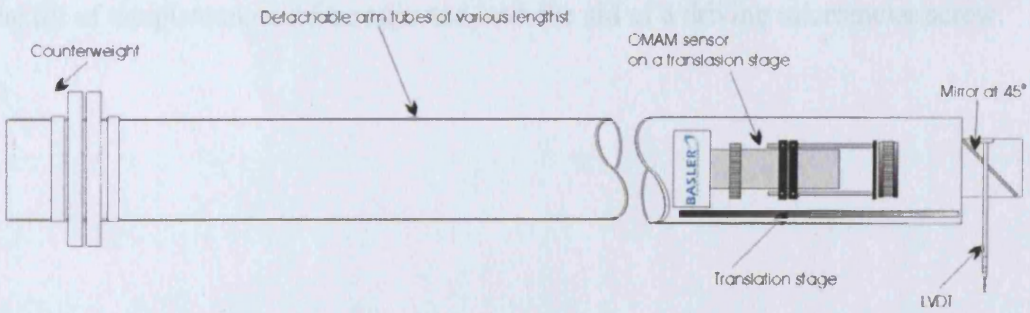

Figure 6.3 Case study design for the SAP arm and hybrid sensor. The arm tube consists a detachable business end containing the components of the hybrid sensor

If the OMAM is fitted inside the arm, the inner diameter of the tube will be defined by the largest OMAM component (the CCD camera). The square enclosure of the CCD camera has a diagonal of 85 mm and if an additional clearance of 25 mm is allowed for service lines the inner diameter of the tube should be at least 110 mm.

With the OMAM sensor placed horizontally inside the business end, the output beam can be directed onto the SUT with the help of a common, square, front-silvered mirror positioned at 45^0 with respect to the centroid of the tube. The contact probe can be passed through a central hole in the mirror to ensure that both sensors scan the same part of the mirror simultaneously and that both traces pass through the optic vertex. The shadow of the probe is likely to result to some obscuration on the CCD detector ,however, the effect should not be significant (Matt Callender personal communication).

The use of a mirror at 45^0 can ensure that both sensors meet the SUT at normal incidence only if the arm is held horizontal at all times. In many cases, however, the arm will be tilted and the probing system will have to be adjusted independently in order to maintain normal incidence. Both sensors have to be tilted by the same amount to maintain a fixed correlation between their datasets. This could be achieved by mounting the mirror and the contact probe onto a plateau pivoted at a hinge (figure 6.4). The tilt of the plateau could be adjusted with the aid of a driving micrometer screw.

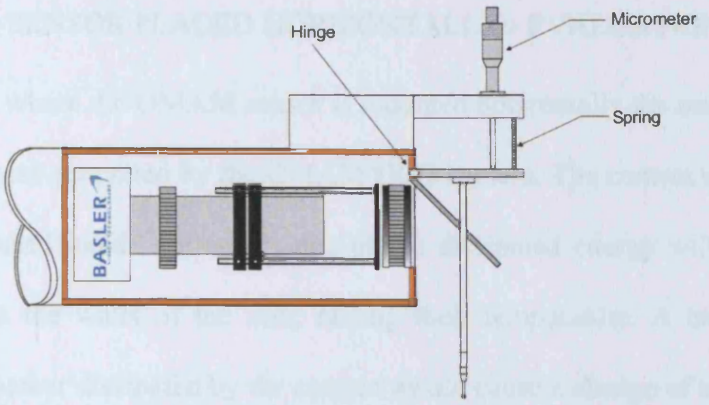

Figure 6.4 Concept design for a hybrid sensor and associated tilting mechanism. Tilting can be achieved with the aid of hinged plateau driven by a micrometer screw

The configuration shown in figure 6.4 allows simultaneous tilt adjustment for both sensors although the OMAM is not physically tilted. The main problem with the suggested tilting mechanism is that it would be difficult to incorporate a linear *z*-axis adjustment which is necessary for positioning the contact probe onto the optic surface.

6.2.3.2 THE USE OF A MONOLITHIC ARM

The alternative of using a monolithic tube for the profilometer arm is an option that requires similar mounting requirements for the sensing equipment as in the case of the detachable business end. The main difference is that the OMAM sensor is now fixed within the main section of the arm. The advantage of this is increased arm stiffness since a uniform tube section is used.

The OMAM can be mounted with its axial centre 300 mm away from the end face of the arm tube maintaining an optical path length of 350 mm whilst reducing the vertical separation to 50 mm. For fine focus adjustment the OMAM can be placed onto a custom built displacement stage located at the bottom of the tube.

6.2.3.3 OMAM SENSOR PLACED HORIZONTALLY - EVALUATION

In both designs where the OMAM sensor is mounted horizontally the main problem has to do with the heat generated by the OMAM CCD camera. The camera operates at 6 W and, if it is housed inside the arm, some of the dissipated energy will eventually be transferred onto the walls of the arm, raising their temperature. A basic calculation shows that the power dissipated by the camera would cause a change of temperature of

$$\frac{\Delta\theta}{\Delta t} = \frac{P}{mc} = 0.2\ \text{mKs}^{-1} \tag{6.1}$$

on an aluminium tube, where P is the thermal energy transferred to the tube per second, c is the specific heat capacity of the tube and m is its mass. For a 1 m long aluminium tube with a mass of 35 kg, two hours of continuous operation would cause an estimated rise in temperature of 0.3 ^{0}C. The resulting error in the effective arm length due to linear expansion would be

$$\Delta l = \alpha l_o \Delta\theta \approx 7\ \mu\text{m} \tag{6.2}$$

where α is the coefficient of thermal expansion of aluminium. Consequently the linear expansion error would result in a measurement error of 612 nm whilst the target form accuracy is 20 nm. This rudimentary calculation indicates the significance of thermal errors and calls for a design where the OMAM sensor is mounted externally. If the sensor has to be mounted inside the arm it would be necessary to provide sufficient cooling. Passive radiators (for example copper plates or cables) could be used to draw thermal energy out of the structure but an unknown heat would still be transferred to the walls of the tube after continuous operation Another option could be forced ventilation by means of a fan but this would cause vibration on the arm.

6.2.4 USING AN OPTICAL BREADBOARD

6.2.4.1 DESCRIPION OF THE CONCEPT DESIGN

In order to overcome problems associated with the heat generated by the OMAM, it was proposed by D. D. Walker (UCL) to use an optical breadboard as the interface for the hybrid sensor. Under this concept all the sensor subcomponents are mounted directly onto a breadboard which then attached to the SAP arm. The use of a breadboard can also allow the incorporation of other optical and mechanical sensors, increasing the SAP adaptability with minimum impact on other instrument parameters. Under the suggested concept both the OMAM sensor and the contact probe could be attached onto the breadboard as shown in figure 6.5. In the suggested design the OMAM sensor is mounted vertically and the optical path is folded with the aid of mirrors. There are four mirrors, three of which are used to divert the OMAM output beam around the breadboard. The use of the mirrors results in a compacted optical path length, hence, reducing vertical separation between the breadboard and the SUT. Drawing on the conclusions from the previous design proposals, a fourth mirror is used to direct the beam onto the SUT and the contact probe is mounted through a central hole in the mirror.

For fine focus adjustments the OMAM sensor could rest on a linear translation stage. The number of mirrors and their relative separations could be adjusted in order to achieve optimum path length.

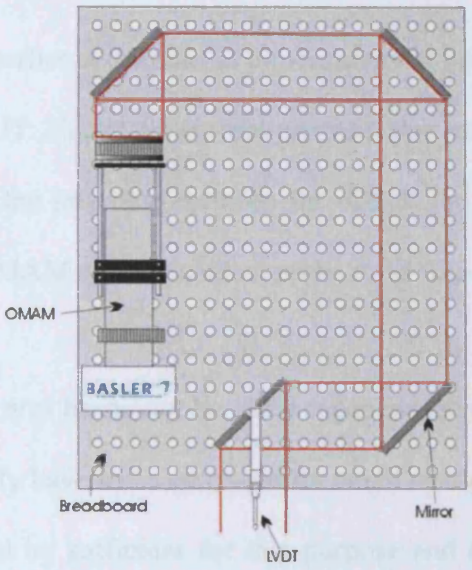

Figure 6.5 Suggested design for hybrid probing system based on the use of an optical breadboard. The output beam from the OMAM is diverted around the breadboard in order to reduce the vertical optical path length

An important advantage of the current proposal is that it increases the adaptability of the SAP to different measurement conditions. Since the hybrid sensor is separated from the rest of the SAP structure it can be removed in order to be used with arm sections of different length. According to the project specifications the SAP should be capable of measuring optics with maximum diameters of 1000 mm. This would require an effective arm length (and hence a physical arm length) of at least 500 mm to 600 mm. In theory a fixed arm length of 600 mm could be used universally but this would severely limit the measurable radii of curvature in optics of smaller diameters. Using as an example the case study optic of table 4.2, where R = 532 mm, the use of an arm length of 600 mm would make $\sin\theta = l/R$ undefined. Hence, in order to simultaneously satisfy the requirements for measurement of optics with diameters up to 1000 mm and RoC as low as 532 mm it is necessary to alter the effective arm length. The use of a breadboard means that beams of various lengths can be used without the need for altering the hybrid sensor.

6.2.4.2 ANGULAR ADJUSTMENT FOR THE BREADBOARD

As was discussed earlier at the start of a measurement both sensors have to be at normal incidence to the SUT. Under the current proposal this could be achieved by introducing a flexure hinge at the interface between the end of the arm and the breadboard. This would allow the OMAM and the contact probe to be tilted in unison.

Assuming that the arm beam can be tilted independently from the am bearing then the breadboard will only have to be corrected for small residual tilt errors. An angular travel range of $\pm 2^0$ would be sufficient for this purpose and the resolution should be better than 0.012^0 in order to comply with the specifications. Flexures offer theoretically infinite resolution which is practically limited only by the driving mechanism. Assuming that the pivot of the flexure is at a distance 200 mm away from the SUT (figure 6.6) angular resolution as low as 1 arc second could be achieved by the use of a common micrometer screw located at the bottom of the flexure.

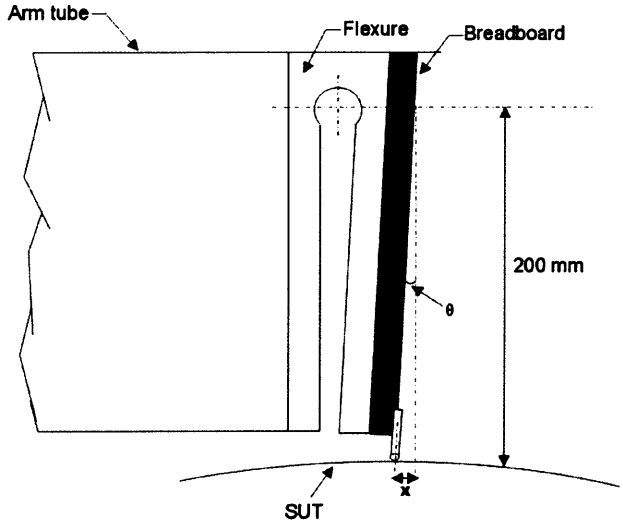

Figure 6.6 A flexure attached at the end of the arm with its pivot 200 mm away from the probe tip can offer angular resolution of 1 arc second

6.3 CHOOSING A MECHANICAL PLATFORM FOR THE SAP

6.3.1 THE FAG COORDINATE MEASUREMENT MACHINE

The next step of the design involved the choice of a mechanical platform for the SAP. Taking into account the financial constraints and time limitations it was decided to pursue a design based on an existing mechanical platform. For this reason a decommissioned CMM was used. The particular CMM was built by Cranfield Unit for Precision Engineering (CUPE) using FAG components and it was employed for the measurement of American Petroleum Institute (API) thread gauges at NPL. It consists of a main *x-y* air bearing translation platform and a vertical stage for translating a probing assembly across the *z* axis. The FAG CMM was used in conjunction with a large rotary air bearing manufactured by Horstmann Gauge and Metrology Ltd. The whole CMM, including the Horstmann bearing, lies on a Granitan base supported by three girders. The girders are adjustable in height, hence, allowing tilt and roll adjustment of the whole Granitan base. Figure 6.7 shows the FAG machine along with the original thermal enclosure and control unit.

Figure 6.7 The original FAG CMM within its thermal enclosure

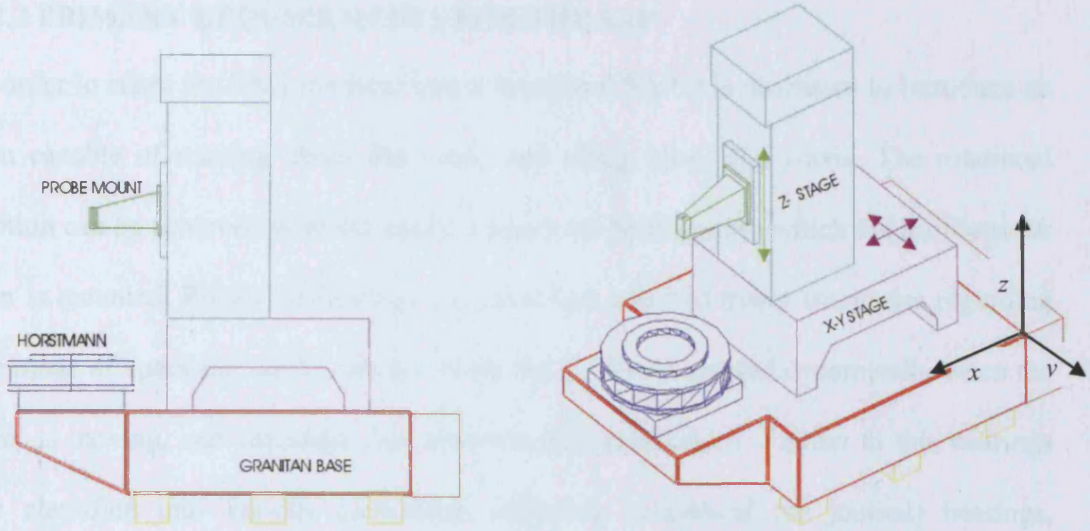

Figure 6.8 CAD drawings of the FAG machine (drawings produced by C. W. King, UCL)

Figure 6.8 shows CAD drawings of the FAG CMM illustrating the motion axes of the instrument.

The motion of the *x-y* stage is achieved with the aid of two leadscrews driven by servomotors while a third leadscrew is used to move the probe mount in the *z*-axis. The resolution of motion in all axes is 100 nm. The *x-y* platform sits on twelve air-bearing pads and is operated by mains pressurised air supply. The Horstmann has a separate linear *x-y* alignment table which can be adjusted using built-in micrometer screws (figure 6.9). The axial load capacity of the Horstmann bearing is 450 kg.

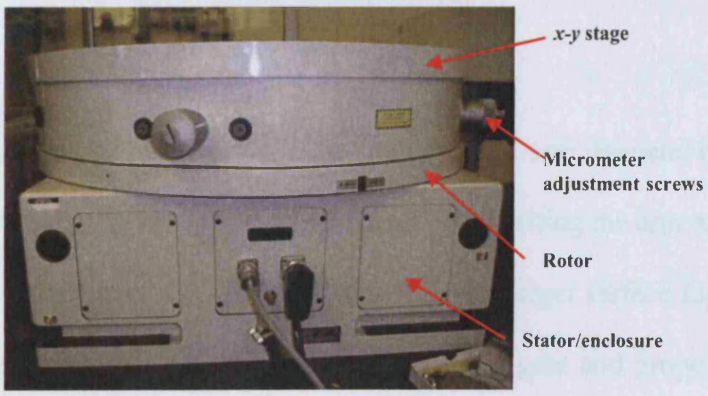

Figure 6.9 The Horstmann rotary air bearing

6.3.2 PRIMARY REQUIREMENTS FOR THE SAP

In order to adapt the FAG machine into a functional SAP it is necessary to introduce an arm capable of rotating about the *z*-axis and tilting about the *y*-axis. The rotational motion can be achieved with the use of a rotary air bearing onto which the profilometer arm is mounted. Rotary air-bearings are classified into two major categories regarding the mode of operation: aerodynamic, where the air film is created dynamically when the rotor is moving, and aerostatic that are externally pressurised. Further to this bearings are classified into various geometries including cylindrical (or journal) bearings, spherical bearings and hemispherical (figure 6.10) bearings.

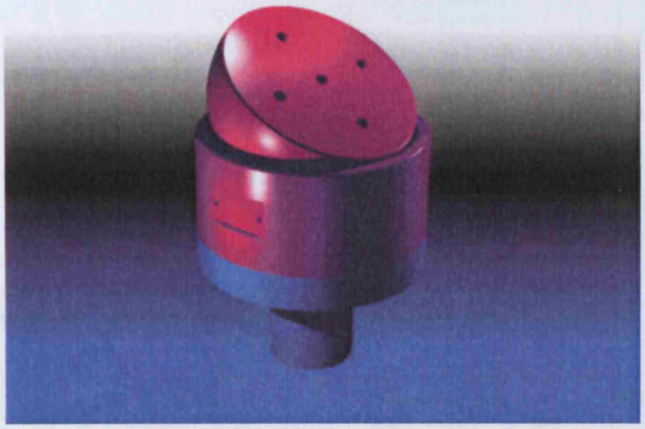

Figure 6.10 Schematic of a typical hemispherical air-bearing (figure taken from www.specialtycomponents.com)

According to the project specifications the case study of a 600 mm diameter optic with a 33^0 surface slope would require a SAP with the capability of tilting the arm rotation axis by an angle of 41^0 (based on an arm length of 0.35 m and a target surface form error of 350 nm). At this stage of the design the goal was to investigate and propose ways of modifying the existing FAG platform in order to incorporate a profilometer arm with the necessary tilting capacity to cover the specification optics.

6.3.3 THE USE OF COUPLED BEARINGS

6.3.3.1 USING COUPLED JOURNAL BEARINGS

A way of modifying the FAG into a functional SAP is be by employing two coupled journal bearings as shown in the concept drawing of figure 6.11. The two journal bearings are coupled with a rigid link onto which the profilometer arm is mounted. The necessary tilt is achieved by transforming the linear motion the FAG stage into angular motion of the arm through a custom made rotary coupling. The whole hyperstructure is mounted on a heavy-duty tilting table capable of providing a tilt of at least 41^0.

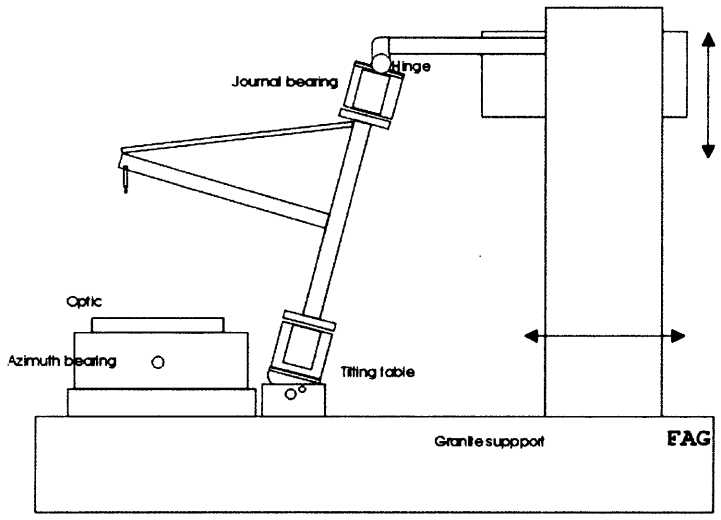

Figure 6.11 A concept SAP based on two, coupled journal rotary bearings

The suggested design was discussed with a representative from MotionLink Ltd, manufacturers of Precision air bearings, in 2003. The company suggested a custom system based on two 350 mm diameter journal bearings. Under the proposal the compliance of the bearings would be approximately 1 μm at 41^0 tilt which is close to specifications but it refers to unloaded bearings. The main problem with using journal bearing has to do with lateral loads when the bearings are tilted which can cause

eccentricity error and bearing failure. Also taking into account the overall cost, in excess of £70000, the idea of using coupled journal rotary bearings was dismissed.

6.3.3.2 USING COUPLED SPHERICAL BEARINGS

In order to overcome the radial lateral loading problems associated with the coupled journal bearings, coupled spherical bearings ware proposed. Under this proposal the problem of non-uniform loading is minimised since the spherical geometry means that the load is distributed evenly at any tilt angle. Commercially available spherical and hemispherical air bearings offer typical load capacities between 0.250 kg and 375 kg (Nelson Air). The use of coupled spherical bearings means that the tilting of the arm can be achieved without the need for an external coupling since the spherical cups are employed for this reason (figure 6.12).

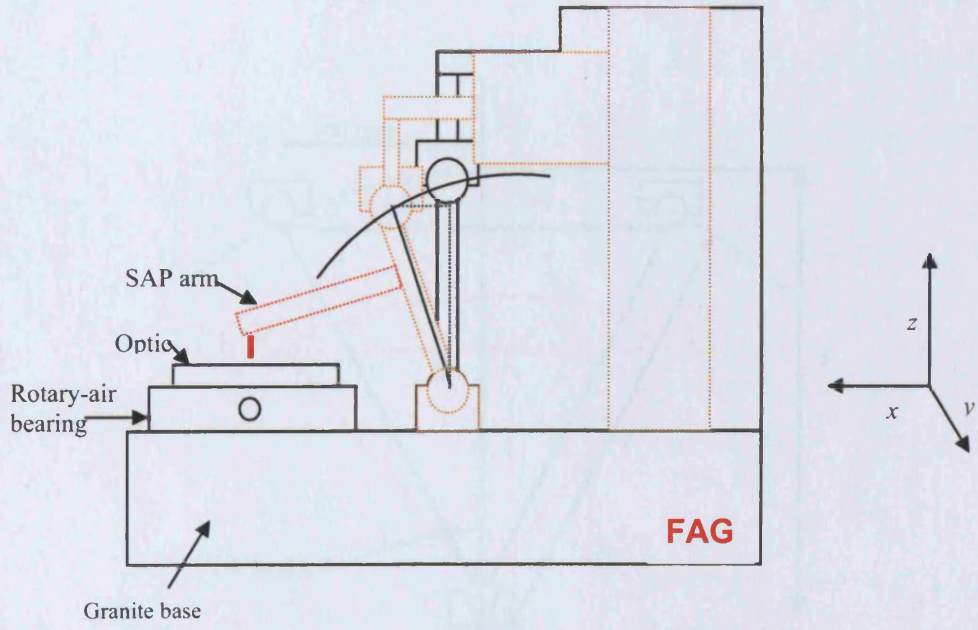

Figure 6.12 Concept design of a SAP based on the use of two coupled hemispherical bearings

According to the suggested design the tilt range of the arm depends on the available extension/retraction range of the FAG stage along the *x*-axis and on the separation between the two bearings (figures 6.13, 6.14)

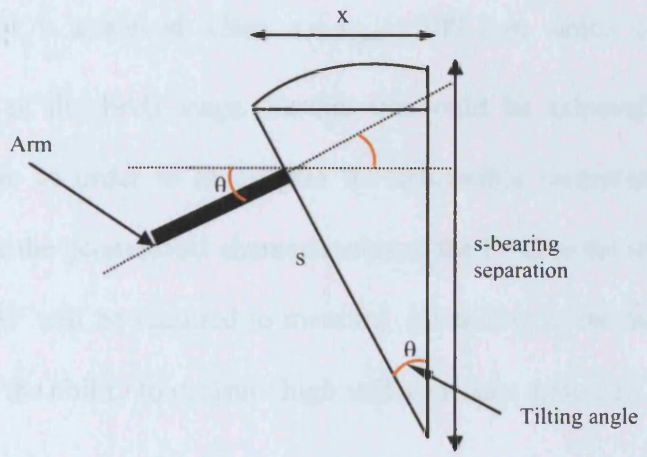

Figure 6.13 Geometrical relationship between the FAG *x*- axis travel range and the tilt of the SAP arm

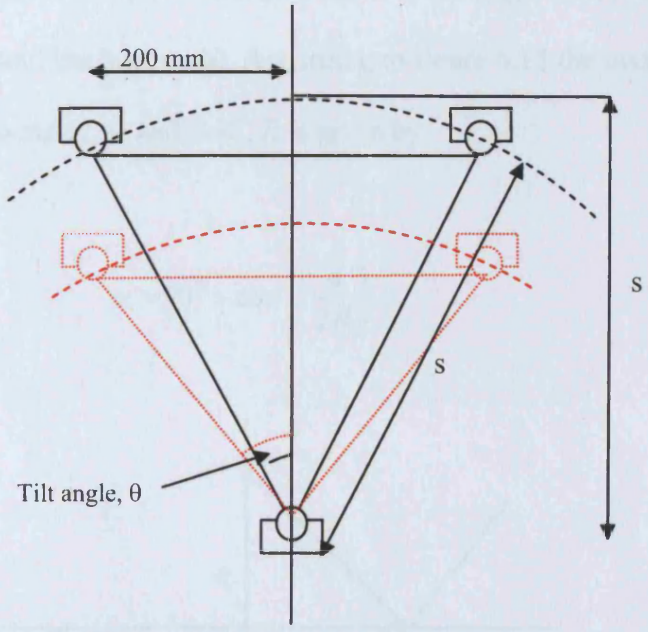

Figure 6.14 The tilting range of the SAP arm as related to the bearing separation *s* and the *x*-axis travel range of the FAG

According to figure 6.14 the tilt of the arm can be expressed as

$$\theta = \sin^{-1}(x/s) \tag{6.4}$$

where θ is the tilt angle, x is the x-axis displacement and s is the bearing separation. The maximum tilt is achieved when $x = x_{max} = 200$ mm which corresponds to the maximum travel of the FAG stage. Further tilt could be achieved by reducing the bearing separation. In order to investigate the achievable measurement range it was necessary to relate the geometrical characteristics of the FAG to the specifications of the optics that the SAP will be required to measure. According to the end user, one of the main requisites is the ability to measure high surface slopes up to 33^0.

The surface slope at any given point of an optic can be found by calculating the first derivative of the equation that describes the profile of the optic. Geometrically the maximum surface slope of an optic could be defined as the angle between the tangent at the edge of the optic and the horizontal. According to figure 6.15 the maximum surface slope of an optic of diameter, d, and RoC, R is given by

$$\alpha = 90^0 - \cos^{-1}\left(\frac{d}{2R}\right). \tag{6.5}$$

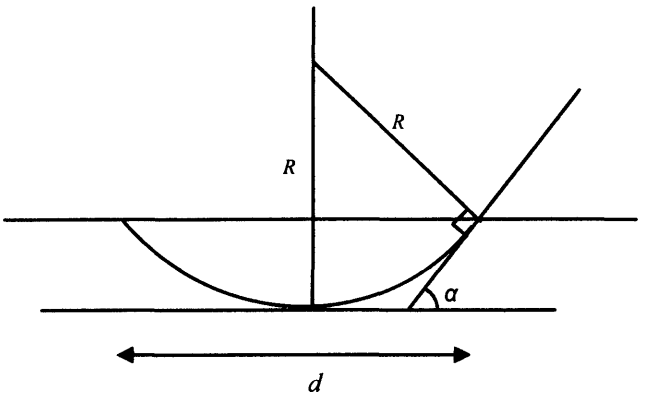

Figure 6.15 Representation of the surface slope, α, of a concave optic of RoC, R

However, according to the SAP condition, $R = l/\sin\theta$, hence equation (6.5) can be rewritten as

$$\alpha = 90^0 - \cos^{-1}\left(\frac{d\sin\theta}{2l}\right). \tag{6.6}$$

Combining equations (6.4) and (6.6) we obtain:

$$s = \frac{dx}{2\cos(90-a)l}. \tag{6.7}$$

Equation (6.7) relates the physical characteristics of the FAG machine, such as the travel range along the x-axis, to characteristics of the SUT, such as the surface slope and the diameter. Using the limiting case of 33^0 surface slope on a 600 mm diameter optic the necessary bearing separation for three different arm lengths is shown in figure 6.16.

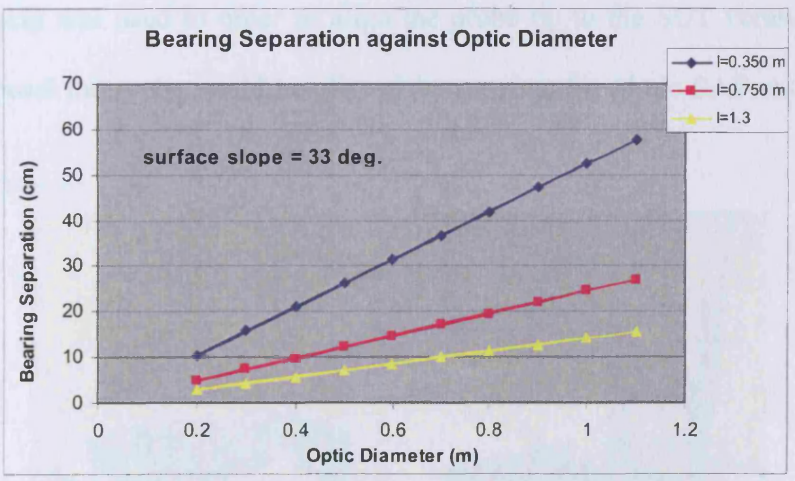

Figure 6.16 Graph of bearing separation against optic diameter for a fixed surface slope of 33^0 and for three different arm lengths

As shown from in figure 6.16 the measurement of 600 mm diameter optics requires a bearing separation no greater than 320 mm. Taking into account the finite size of the

spherical bearing and the arm, a 320 mm separation would require very small clearances that would be very difficult to achieve. Taking this into account as well as the very limited number of companies offering customised spherical bearing solutions it was decided to pursue a different design.

6.3.4 USING A SINGLE JOURNAL BEARING

6.3.4.1 DESCRIPTION OF THE CONCEPT

After investigating the viability of a coupled bearing design it was decided to proceed with a SAP design based on the use of a single journal bearing. This required significant modifications, of the FAG platform, such as the removal of the *z*-axis granitan column, in order to create space for the SAP frame (figure 6.17). It was decided to retain the main *x*-*y* stage as a means of linear adjustment of the SAP position. In chapter 5 an extendable arm was used in order to align the probe tip to the SUT vertex. Under the current proposal the probe could be aligned by moving the whole SAP with respect to the SUT.

Figure 6.17 The FAG machine after the removal the *z*-column

A key issue for any SAP is the capability to adjust the tilt and the roll of both the arm rotation axis and of the SUT bearing axis. In the FAG machine the Horstmann can be used as the SUT bearing but there is no tilt/roll adjustment available. Nevertheless, the *x-y* stage has a built in tilt/roll stage that can be used as a mount for the SAP main frame (figure 6.18).

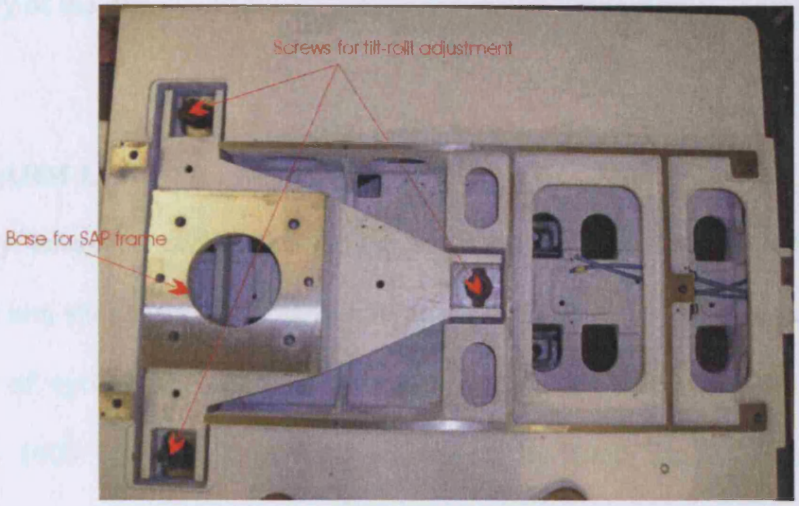

Figure 6.18 Plan view of the FAG *x-y* stage. Independent tilt/roll adjustment can be achieved by adjusting the three screws on the triangular base

6.4 THE PROFILOMETER ARM

6.4.1 INTRODUCTION

At the initial stages of the design of a machine component attention must be given to the geometry and the choice of material. The compliance of a particular component can be assessed by evaluating its conformity to the various design constraints. The primary constraints regarding the design of the arm are:

1. The ability to measure optics with diameters between 0.2 m and 1 m.
2. The ability to measure surface form with accuracy between 350 nm and 20 nm.
3. The minimisation of manufacturing related costs.

4. The ability of incorporating a hybrid sensor platform.

In order to satisfy these requirements many considerations had to be taken into account. The SAP arm represents a typical example of a load-carrying mechanism and was treated as such. One of the first design considerations had to do with the dimensions and the geometry of the arm.

6.4.2 THE ARM LENGTH

The primary design concern regarding the arm's geometry, has to do with its overall length. The arm should be sufficiently long in order to allow scans across the diameter of a range of optics. According to the specifications the maximum desirable optic diameter is 1000 mm. Therefore, the effective arm length should be an absolute minimum of $d/2$, where d is the optic diameter. In reality the actual arm should be much larger than $d/2$ in order to accommodate the necessary clearances between the optic and the SAP frame. Since the proposed SAP will rely on a balanced cantilever it is also important to allow extra length for counterbalancing purposes. Taking these considerations into account it was decided that the overall length of the arm should be in excess of 1 m.

6.4.3 THE SHAPE OF THE ARM

The shape of the arm can have an effect on various performance characteristics including stiffness and vibration behaviour. For the current design solid beams are not considered since they would add unnecessary mass to the structure whilst hollow beams are preferred because they offer higher stiffness at lower mass. The choice of the

optimum shape of the arm relies on a variety of performance indicators such as the shape factor, ϕ. The shape factor characterises the cross sectional shape of a beam (Cebon and Ashby 1994) and can be defined for a range of requirements and applications. In the current design where stiffness is important we use the shape factor for a stiffness limited design which is given by

$$\phi = \frac{4\pi I}{A^2} \tag{6.8}$$

where I is the second moment of area and A is the cross-sectional area of the beam. Three commonly used shapes will be considered, a cylindrical, rectangular and square beam. These configurations are readily available for a range of materials and can often be obtained as off-the-shelve components.

The corresponding areas and second moments of area of the suggested shapes are shown in figure 6.19.

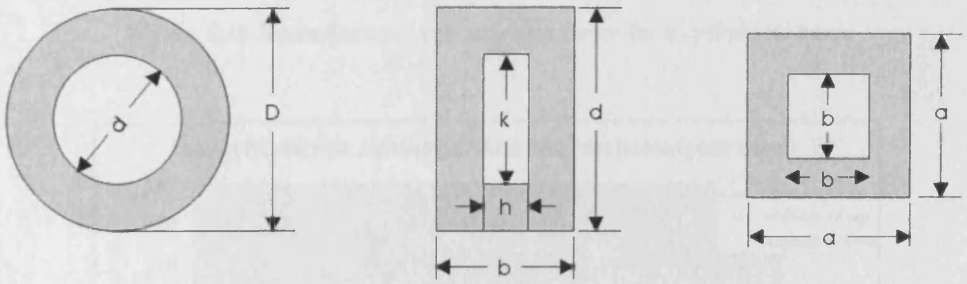

$$A = \frac{\pi\left(D^2 - d^2\right)}{4} \qquad A = bd - hk \qquad A = a^2 - b^2$$

$$I = \frac{\pi\left(D^4 - d^4\right)}{64} \qquad I = \frac{bd^3 - hk^3}{12} \qquad I = \frac{a^4 - b^4}{12}$$

Figure 6.19 Areas and second moments of area for various hollow beam geometries

In order to assess the stiffness characteristics for each of the three geometries the stiffness shape factor is plotted against the beam's outer diameter for a range of tube diameters and thicknesses (figures 6.20, 6.21 and 6.22). As it becomes apparent thin-walled tubes offer higher stiffness than thick-walled structures for a given weight and as a typical example, beams of outer diameters approximately equal to 300 mm and wall thickness of 3 mm can offer a high stiffness shape factor close to 50. When employing thin walled structures care should be taken to avoid buckling. It is apparent from figures 6.20, 6.21 and 6.22 that all three considered geometries offer similar stiffness shape factors. As a result the final selection for the beam shape should depend upon other parameters such as availability and cost.

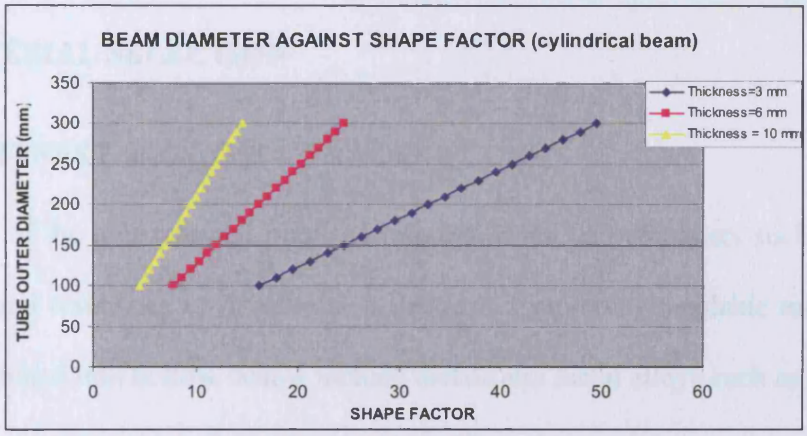

Figure 6.20 Beam diameter against shape factor for a cylindrical beam

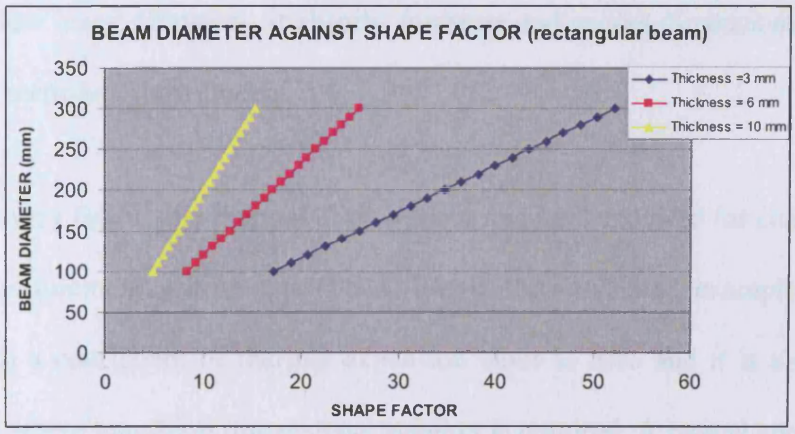

Figure 6.21 Beam diameter against shape factor for a rectangular beam

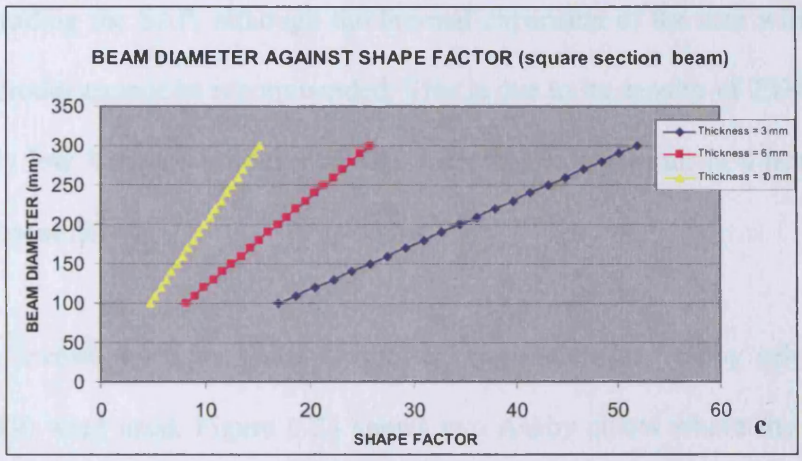

Figure 6.22 Beam diameter against shape factor for a square section beam

6.4.4 MATERIAL SELECTION

6.4.4.1 STIFFNESS AND COST CONSIDERATIONS

The choice of the arm material plays an important role on parameters such as thermal expansion and resistance to dynamical deflections. Commonly available materials that can be machined into hollow beams include metals and metal alloys such as aluminium, steels and iron, and composites such as carbon fibre, glasses and ceramics. Carbon fibre is an excellent material that has a Young's modulus of up to 350 GPa and offers high stiffness at low mass. However, it absorbs moisture and causes dimensional instability in precision metrology instruments.

Zerodur has very favourable thermal characteristis and has been used for construction of precision measurement instruments (Leach 2000). Zerodur is an example of a glass ceramic with a coefficient of thermal expansion close to zero and it is also ideal for applications where long-term dimensional stability is required. A typical application for

Zerodur is in mirror panels for Extremely Large Telescopes (Hartmann and Morian 2004). Regarding the SAP, although the thermal expansion of the arm will be a major concern, Zerodur cannot be recommended. This is due to its density of 2530 kg m^{-3} and its relatively low Young's modulus of 90.3 GPa that would result in a heavy beam of relatively low stiffness.

In order to investigate other material options, two-parameter, Ashby selection charts (Ashby 1999) were used. Figure 6.23 shows two Ashby charts where the stiffness-to-weight ratio against specific strength is plotted for a range of common materials. Strength is interpreted as a measure of ductility and it describes the tensile force required to pull the material to its breaking point. Although the strength-to-weight ratio is not so important in the current application the stiffness-to-weight ratio is crucial because it forecasts the arm's ability to withstand dynamical deflections during measuring. It is important to note that the mass of the arm should be kept low since it affects other SAP design aspects such as the choice of the arm rotary bearing. It is desirable to maintain a low arm mass since this would allow the use of a smaller bearing with a relatively low load capacity, hence reducing the overall cost.

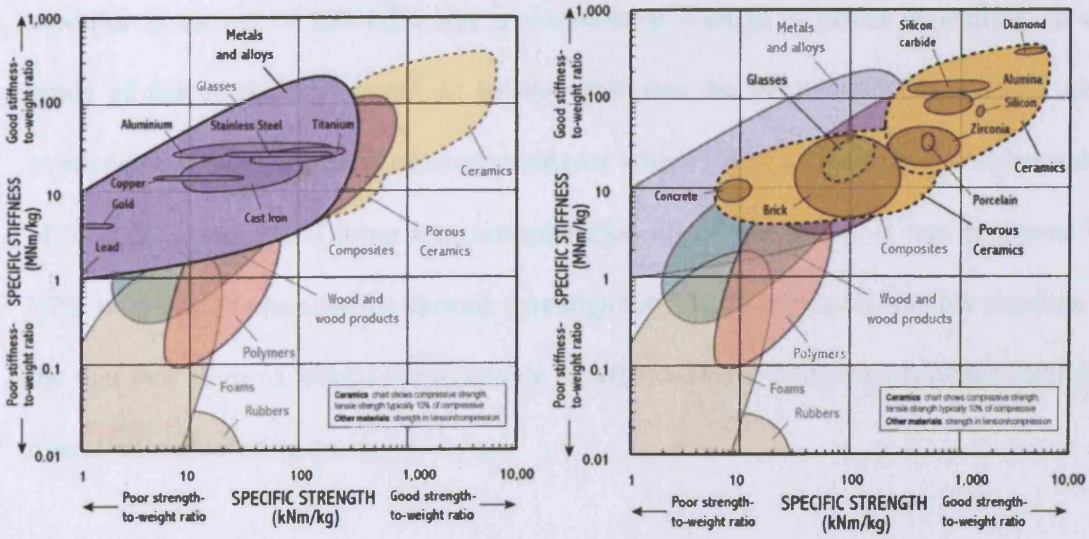

Figure 6.23 Ashby charts for specific stiffness against specific strength for metals and ceramics

The graphs of figure 6.23 suggest that certain ceramics have a much better stiffness-to-weight ratio compared to ordinary metals such as aluminium and stainless steel. Ceramics, however, are in general more expensive than metals and this has to be taken into account since cost is a major constraint on the current project. Material selection graphs relating the cost and the Young's modulus of various metals and ceramics are shown in figure 6.24.

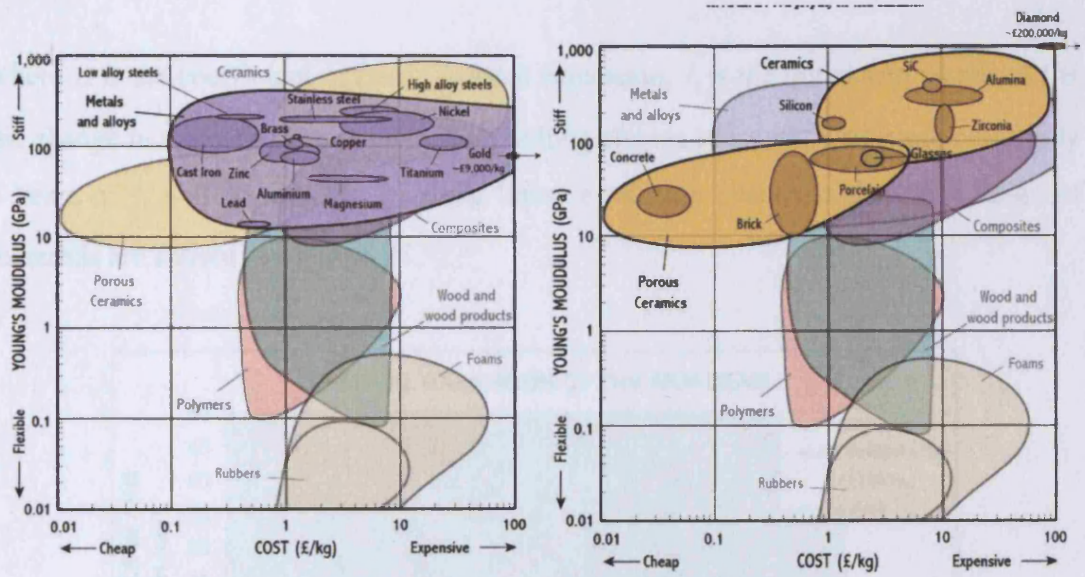

Figure 6.24 Ashby charts for Young's modulus against cost for metals and ceramics

Figure 6.24 shows that the commonly available aluminium is a relatively cheap material but it has a comparatively low Young's modulus. Stainless steel has a value of Young's modulus in excess of 200 GPa and is available at a range of prices depending on the grade of the steel. It is important to note that that the price band for stainless steel overlaps with the price band of some ceramics which offers a significantly higher value of Young's modulus. Taking into consideration all of the above, it was proposed by NPL to consider alumina for further investigation. Another reason for this decision is the fact that alumina beams are available as off-the-shelve components hence reducing overall manufacturing costs.

6.4.4.2 THERMAL EXPANSION

An important factor that can potentially introduce significant measurement errors has to do with the thermal expansion of the arm. The expansion of the profilometer arm beam can be approximated using the linear expansion law

$$\Delta l = \alpha l_0 \Delta T \tag{6.9}$$

where α is the coefficient of linear thermal expansion, l_0 is the initial arm length, ΔT is the change in temperature and Δl is the resulting change in length. Using as a case study a beam of l_0 = 1000 mm the resulting linear expansion characteristics for a range of materials are shown in figure 6.25.

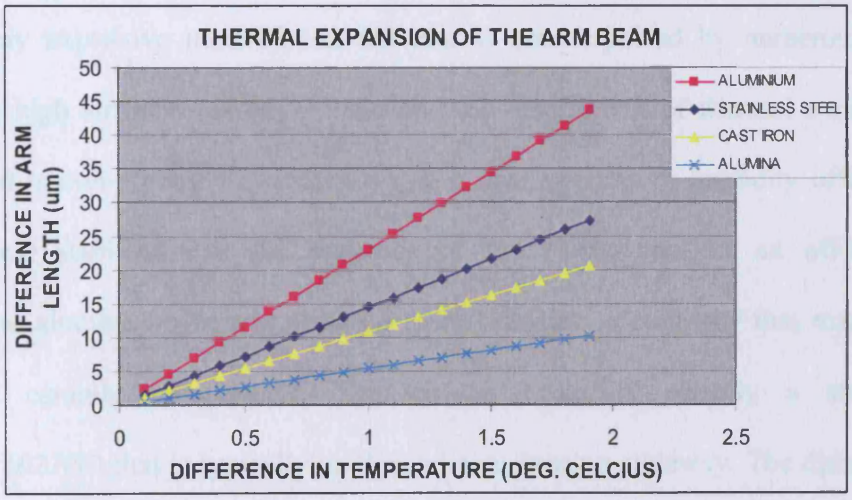

Figure 6.25 Graphs of linear arm expansion against temperature for different arm materials

According to figure 6.26 the material with the largest thermal expansion is aluminium while alumina exhibits the best thermal expansion characteristics. In order to evaluate each material it is necessary to take into account real environmental factors. The SAP will be located in a temperature controlled room where the maximum variation in temperature is expected to be no more than $\pm 0.5\,^{0}$C. Assuming an average temperature

change of $\Delta T = 0.3\,^{0}\mathrm{C}$ the corresponding change in beam length would be 7 μm for aluminium, 4.32 μm for stainless steel, 3.24 μm for cast iron and 1.62 μm for alumina. Changes in the arm length are manifested as linear δl errors. According to the error analysis of chapter 4 the maximum allowed tolerance δl_{max} is approximately 0.3 μm. From the materials investigated, the material that is closer to this specification is alumina.

6.4.4.3 USING A RECTANGULAR ALUMINA BEAM

Taking into consideration the available materials and configurations as well as the various design constraints it was decided to use an alumina arm for the SAP. Alumina is a relatively expensive material but the cost is counterpoised by numerous benefits including high stiffness-to-weight ratio and low coefficient of thermal expansion. In addition it is non-porous which means that it does not absorb humidity offering high dimensional stability. For the purposes of the current project an off-the-shelve rectangular alumina beam was obtained from Coorstek, a company that manufactures precision ceramic components. The chosen beam is actually a straightedge (part no. *102280*) that is typically used as a linear bearing slideway. The dimensions of the beam are approximately $1220\ mm \times 203\ mm \times 76\ mm$ and the cost was 2825 USD. The mass of the beam i 40 kg and the beam thickness is 20 mm. The grade of the alumina beam is AD-99.5 which corresponds to a Young's modulus of 370 GPa. Some other typical properties of alumina AD-99.5 are presented in table 6.1.

		CoorsTek Advanced Materials:				Traditional Materials:		
Properties	Units	Al_2O_3 Ceramic AD-96	Al_2O_3 Ceramic FG-99.5	Al_2O_3 Ceramic AD-99.5	SiC Ceramic SC-DS	Steel 1020	Aluminum 6061-T6	Granite
Density	g/cc	3.72	3.80	3.90	3.15	7.88	2.69	2.6 - 3.1
	lb/cu in	0.134	0.136	0.141	0.11	0.284	0.097	0.09 - 0.11
Modulus of Elasticity	GPa	303	350	370	410	207	69	28 - 110
	x10^6 psi	44	51	54	59	30	10	4 - 16
Specific Stiffness	$\frac{GPa}{g/cc}$	81	91	95	131	26.5	25.6	24
Flexural Strength MOR	MPa	358	375	397	480	*483	*483	9.6 - 38
	x10^3 psi	52	54	57	70	*70	*45	1.4 - 5.5
Coefficient of Thermal Expansion at 25° C	10^-6/ °C	6.1	6.1	6.1	2.1	11.9	22.5	6.5 - 8.3
	10^-6/ °F	3.4	3.4	3.4	1.1	6.6	12.5	3.6 - 4.6
Thermal Conductivity	w/m °C	24.7	27.5	30	175	47	204	35 - 61
	btu/hr.ft.F	14.3	15.9	17.33	102	27	118	20 - 35
Specific Heat	J/kg. °C	880	880	880	658	962	418	840
	btu/lb °F	0.21	0.21	0.21	0.16	0.23	0.10	0.20
Water Absorption 48 hr soak	% by weight	none	none	none	none	none	none	0.02 - 0.58

Table 6.1 Comparative table of mechanical properties of various materials (graph Taken from the Coorstek product catalogue)

6.4.4.4 VIBRATIONAL CHARACTERISTICS OF THE ARM

The vibration of the arm beam during measurement can be a significant source of measurement error. In general the vibrations in an instrument are caused by intrinsic sources, such as moving parts within the system, or due to external influences (for example traffic, seismic vibration, noise from adjacent machines, *etc.*). The profilometer arm will be one of the components most susceptible to vibration since it is, in effect, a long moving cantilever.

During a pick-and-poke measurement cycle the arm will be moving, stopped and restarted several times. These sudden disturbances can result in significant vibration in the arm, and consequently the probe tip. When the arm is stopped its kinetic energy is transformed into elastic potential energy. If the arm is approximated as a typical spring-

mass system the total energy stored can be described by simple energy conservation principles as

$$\varepsilon = \frac{1}{2}m\left(\frac{dy}{dt}\right)^2 + \frac{1}{2}\lambda y^2 \tag{6.10}$$

where ε is the total energy stored, m is the mass of the equivalent spring-mass system and y is the displacement at the free end. The quantity, λ, is the stiffness of the beam and it is equal to $\lambda = \frac{EI}{3L^3}$ where E is the Young's modulus, L is the length of the beam and I is the second moment of area of the rectangular beam (figure 6.20). Using the manufacturer's specifications it can be found that $I \approx 4\times10^{-5}$ m^4 and $\lambda \approx 24$ GPa m for the chosen beam.

At instants of zero velocity all the energy of the system is stored in the arm as elastic potential energy and the beam attains maximum displacement at the free end. When the velocity is zero the elastic potential energy of the arm is

$$U = \frac{1}{2}\lambda {y_{\max}}^2 = \varepsilon_{\max}^{kin}. \tag{6.11}$$

Hence the maximum amplitude of the resulting oscillation at the free end would be

$$y_{\max} = \sqrt{2\varepsilon_{\max}^{kin}/\lambda}. \tag{6.12}$$

The oscillation will occur along the y-axis and the end effect will be the movement of the probe tip in and out at different zones on the optic. This will appear as noise in the measured data.

The amplitude of the oscillation can be found by estimating the maximum kinetic energy of the arm as

$$\varepsilon^{kin} = \frac{1}{2}mu^2 \tag{6.13}$$

where u is the maximum scanning speed, that is not expected to exceed 10 mm s^{-1} in real measurement conditions, and m is the mass of the equivalent spring mass system. In applying equation (6.13) it is important to note that the mass of the alumina beam cannot be regarded to be the same as the mass of the equivalent spring mass system. This is because different parts of the beam oscillate at different velocities and the parts closer to the free end oscillate faster than those at the fixed end. In order to find the equivalent mass (modal mass) the whole beam can be approximated as a series of point masses. The calculation of the modal mass follows a standard procedure which can be found in lecture notes published by the University of Colorado (Axerlad *et. al.* 2006) and is summarised in appendix B. The modal mass for a beam is given by

$$m \approx 0.23657 m_{beam} \tag{6.14}$$

where m_{beam} is the overall mass of the beam. In the case of the alumina beam where $m_{beam} = 40\,\text{kg}$ the modal mass is $m = 9.46$ kg. Substituting this into equation (6.13) the maximum attainable kinetic energy is found to be 4.7×10^{-4} J and the amplitude of the oscillation is about 200 nm. The oscillation will be manifested primarily as a perturbation along the y-direction where the calculated tolerance is 0.23 μm. The estimated error is, therefore, within the tolerance.

6.4.4.5 NATURAL FREQUENCY OF THE BEAM

Extrinsic vibrations caused by environmental factors can also excite vibration of the arm. The way the arm is affected has to do with its resonant frequency. In order to obtain a description for the resonant frequency, the arm is approximated as an equivalent spring-mass system. The resonant frequency of such a system is given by

$$f_0 = \frac{1}{2\pi}\sqrt{\frac{k_s}{m}} \tag{6.15}$$

where k_s is the spring constant and m is the mass. In the case of the arm beam (6.14) can be modified into

$$f_0 = \frac{1}{2\pi}\sqrt{\frac{\lambda}{m}} \tag{6.16}$$

where $m = 0.2357 m_{beam} + M$ and M is the mass at the free end corresponding to the mass of the probing system along with the mass of the breadboard and the probe mounts.

By substituting the value for the stiffness, λ, the equation for the natural frequency can be rewritten as

$$f_0 = \frac{1}{2\pi}\sqrt{\frac{EI}{ML^3 + 0.2357\rho AL^4}} \tag{6.17}$$

where E is the Young's modulus, I is the second moment of area, ρ is the density and A is the cross sectional area of the beam. Substituting the value for I and A results in

$$f_0 = \frac{1}{4\pi}\sqrt{\frac{E(bd^3 - hk^3)}{3[ML^3 - 0.2357\rho(bd - hk)L^4]}} \tag{6.18}$$

Using the beam specifications equation (6.18) yields a natural frequency of 7.46 kHz for the arm (including the probing system).

The high natural frequency means that the beam is less likely to be sensitive to common external sources of vibration. In a typical laboratory the frequency content ranges from 4 Hz to 100 Hz (table 6.2). The high natural frequency of the alumina beam means that the arm is unlikely to be affected by environmental noise at its resonant frequency.

Common Vibrational Sources

Source	Frequency (Hz)	Amplitude (in.)
Air Compressors	4–20	10^{-2}
Handling Equipment	5–40	10^{-3}
Pumps	5–25	10^{-3}
Building Services	7–40	10^{-4}
Foot Traffic	0.55–6	10^{-5}
Acoustics	100–10,000	10^{-2} to 10^{-4}
Air Currents	Labs can vary depending on class	Not applicable
Punch Presses	Up to 20	10^{-2} to 10^{-5}
Transformers	50–400	10^{-4} to 10^{-5}
Elevators	Up to 40	10^{-3} to 10^{-5}
Building Motion	46/height in meters, horizontal	10^{-1}
Building Pressure Waves	1–5	10^{-5}
Railroads	5–20	±0.15g
Highway Traffic	5–100	±0.001g

Table 6.2 Common sources of vibration and their respective frequency range (source: Melles Griot)

6.4.4.6 STATIC ARM DEFLECTIONS

A significant source of error can occur in the form of static arm deflections. Different types of beams attain different deflections and the SAP arm will be approximated as a cantilever beam, fixed at one end and with a load at the free end (figure 6.26).

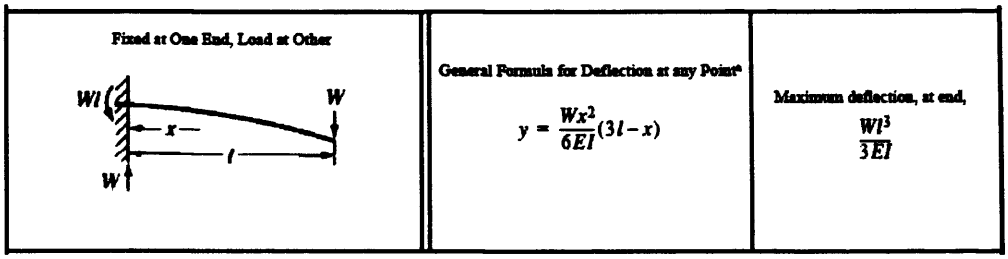

Figure 6.26 Deflection of a cantilever beam, fixed at one end, and loaded at the free end

The deflection at the free end of such a beam, due to the load applied at the free end, is given by

$$z_{load} = \frac{W_M L^3}{3EI} \tag{6.19}$$

where W_M is the load at the free end. The arm will also experience a deflection due to its own weight and this is described by

$$z_{sw} = \frac{W_{beam} L^3}{8EI} \tag{6.20}$$

where W, is the weight of the beam, which is assumed to be uniform (Oberg *et. al.* 2000). In the current approximation the weight, W_{beam}, refers to the part of the arm overhanging from the pivot. This will have a length of at least 600 mm to 900 mm which means that for the calculation of the self-weight deflection the effective mass of the cantilever would be between 20 kg and 30 kg.

The overall deflection of the arm would, therefore, be given by

$$z_{total} = \frac{W_{beam} L^3}{3EI} + \frac{W_M L^3}{8EI} \tag{6.21}$$

which results to a maximum static deflection of 5.4 μm. This is a comparatively large error and it occurs in the *z* direction where there is a one-to-one correlation with the form error. However, due the nature of the SAP geometry a static variance in the shape of the arm does directly affect the measurement. This is because the SAP principle is defined according to the effective arm that is the distance between the probe tip and the arm rotation axis. A static deflection would result into a change in the value of the effective arm length leading to a systematic error but this can be compensated before the start of the measurement. Static deflections can, therefore, be regarded as misalignment errors. It is important to note however that the arm is likely to undergo dynamic deflection during measurement due to torsion when scanning at large tilt angles. The higher deflection due to gravity loading will occur at the extremities of the scan (*i.e.* at large sweep angles).

6.5 THE ARM ROTARY AIR-BEARING

6.5.1 CHOOSING AN AIR BEARING

The air bearing that enables the rotary motion of the arm is the most important component of the SAP. As was discussed in chapter 4, the arm rotary bearing defines the main motion axis[5] of the whole SAP instrument and the overall measurement accuracy of the SAP relies primarily on the bearing's performance.

In terms of technical characteristics the bearing should have sufficient load capacity in order to carry the weight of the overhead arm structure, including the arm beam, the probing assembly and the counterweights. Some weight allowance should also be

[5] The SAP has also another motion axis that is the rotary axis of the SUT bearing but this is not used during single bespoke scans.

allowed in order to account for the arm mounting mechanism. The bearing axial load capacity should be at least 1000 N to 1500 N in order to accommodate comfortably the weight of the alumina beam, the probing system, the counterweights and the mountings. Air rotary bearings are supplied in different sizes and load capacities. For the UCL/NPL SAP, where the accuracy is of prime concern, a PI BLOCK-HEAD® 10R (figure 6.27) bearing was obtained from Professional Instruments (PI). The particular bearing offers very high accuracy and high stiffness necessary for the current application. The analytic specifications of the 10R bearing are shown in table 6.3.

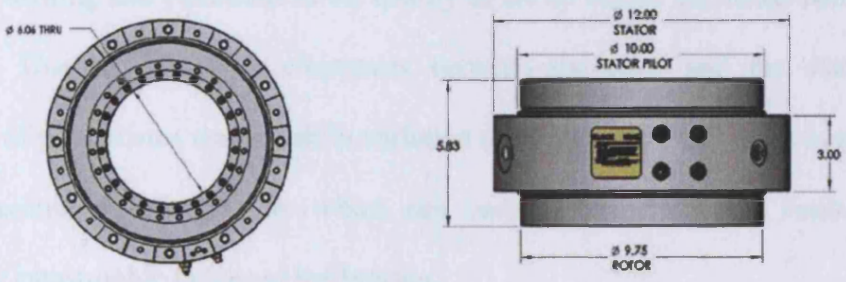

Figure 6.27 The PI 10R BLOCK-HEAD® air bearing (figure taken from PI catalogues)

LOAD CAPACITY		ULTIMATE	WORKING
	RADIAL	1780 N	890 N
	AXIAL	10700 N	5350 N
	TILT	680 Nm	340 Nm
STIFNESS	RADIAL	350 N/µm	
	AXIAL	1750 N/µm	
	TILT	11.3 Nm/µm	
ERROR MOTION	RADIAL	< 25 nm	
	AXIAL	< 25 nm	
	TILT	< 0.1 nm	
TOTAL WEIGHT		680 N	
ROTOR WEIGHT		350 N	
ROTOR INERTIA		0.254 kgm^2	
MAXIMUM SPEED		1800 rpm	
AIR CONSUMPTION		< 85 L/min	

Table 6.3 Manufacturer's specifications for the PI 10R BLOCK-HEAD® bearing

According to PI, the ultimate load capacities refer to metal-to-metal contact across the bearing surfaces and represent the ultimate loading limit for the bearing. The working load capacity is the usable loading capacity and is equal to 50% of the ultimate load capacity. The radial and axial runout of the 10R bearing is less than 25 nm which is well below the projected tolerance in the x- and y-axes.

6.5.2 PRESSURISED AIR SUPPLY CONSIDERATIONS

The gas supply plays a critical role in the performance and life expectancy of a precision air bearing and variations in the quality of the air supply can cause damage to the bearing. Due to the small clearances between the rotor and the stator the introduction of particulates may result in variation of the air gap. This can in turn cause miniscule decentering of the rotor which can cause surface-to-surface contact and consequently catastrophic failure of the bearing.

A similar problem can be caused by variations in the air pressure. In laboratories where pressurised air is provided by a mains supply the simultaneous use of the supply line by different users can create pressure pulses that are propagated through the line and eventually into the bearing. The pressure pulses can impinge on the stability of the bearing causing contact between the bearing surfaces.

Another potential problem has to do with the upsurge of moisture in the system. It is known that relative humidity of air produced by compressors can often cause condensation (Conely *et. al.* 1983). Condensation can also occur as a result of cooling and compression and can cause corrosion in the ferrous components of the 10R bearing.

In order to address the issues regarding the air supply two solutions were suggested. The first solution involved the use of a dedicated supply, such as a bank of static high pressure rechargeable bottles, or even a portable supply tank. The second solution was to rely on the use of an accumulator to provide air supply of constant pressure. The solution of the bottle bank was rejected on the grounds of operational efficiency and cost, the continuous operation of the PI bearing would require a set of six bottles of air, pressurised to 2500 psi, for every two hours of continuous operation. It was hence decided to use the mains air supply along with an accumulator. For this purpose the existing accumulator of the original FAG machine was used and a separate line was set-up in order to provide pressurised air to the PI bearing.

The cleanliness of the air supply can maintained to acceptable levels through the use of filters in the accumulator unit. The mains air supply at NPL is classified as "medical grade" which means that it contains less than 0.5 mg of particulates per cubic meter of air (Jacob 2001) and is virtually free of moisture. However, the NPL classification refers to air produced at the pressurisation station. The air that reaches the laboratory where the SAP is located passes through a few hundred metres of external piping that is exposed to weather conditions. The steep changes in temperature between the external piping and the lines inside the temperature controlled laboratories can introduce humidity to the system. In order to resolve this problem the air passes through a separate unit that monitors and regulates the temperature of the compressed air before it enters the accumulator. The accumulator and the temperature control unit are shown in figures 6.28(a) and 6.28(b) respectively.

Figure 6.28 (a) The accumulator and (b) temperature control units of the FAG

A significant drawback regarding the use of the mains air supply is that the SAP has to be operated at a relatively low pressure of 7.5 bar. The PI load capacities quoted in table 6.1 refer to a feed air pressure of 150 psi (approximately 10 bar). Using the NPL mains air supply means that the axial load capacity of the PI bearing is reduced to 410 N for axial loading and 667 N for radial loading. Nevertheless, even at reduced pressure, the axial loading capacity of the bearing is sufficient. Problems arise with the reduction in radial load capacity since the bearing will have to be operated at tilt angles of up to 40^0. The effects of this are discussed in more detail in section 6.6.2.

6.6 ADJUSTABILITY OF THE SAP ARM

6.6.1 INTRODUCTION

As was mentioned in section 6.1.4.1, that in order to comply with the project specifications, it is necessary to be able to alter the effective arm length. The measurement of the case study optic with diameter of 600 mm and RoC of 535 mm would require an effective arm length of at least 350 mm which corresponds to a tilt

angle of 41.13^0. Longer arm lengths could be used in order to cover the whole range of specified optic diameters up to 1000 mm but this would result in very large tilting angles as shown in figure 6.29. The following sections address these issues and present the design options considered in an attempt to increase the SAPs measurement range to adhere to the project specifications.

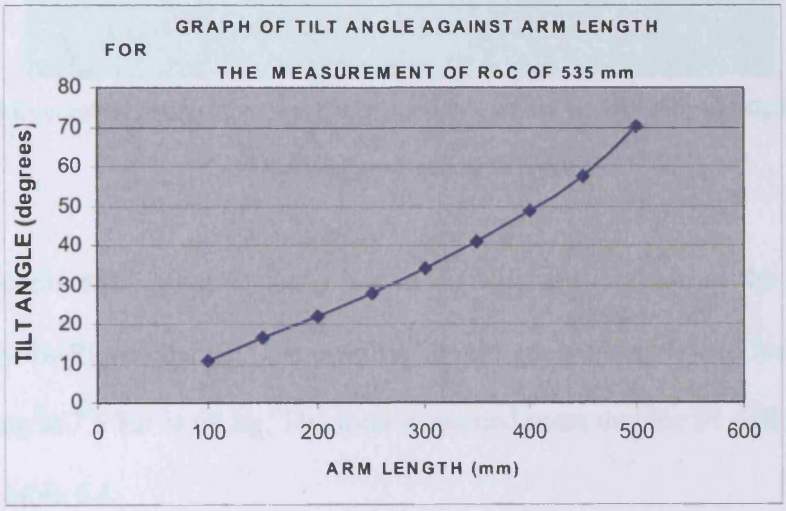

Figure 6.29 A graph of tilt angle against arm length shows that the use of very long arm lengths for measurement of short RoCs results to unrealistically large tilting angles

6.6.2 USING A MOVEABLE ARM

A way of altering the arm length would be by accommodating the arm within a custom made clamp located at the PI tilting pivot. Common friction clamps are not recommended since they would induce undesirable band stress that could cause fractures to a brittle ceramic material like alumina. An alternative design could be based on the use of spring loaded clamping pads as shown in figure 6.30.

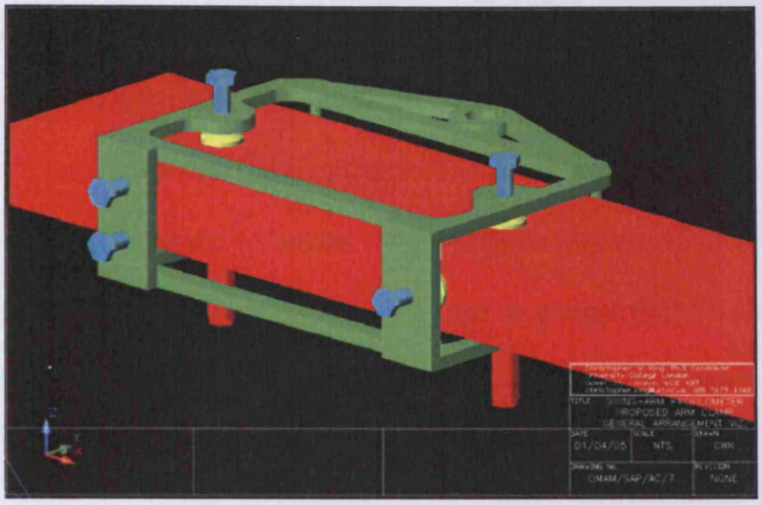

Figure 6.30 Conceptual design of an arm clamp, used to alter the mechanical arm length (design and CAD drawing produced by C W King)

One of concerns with using a clamp has to do with the increase in the overall mass supported by the PI air bearing. The absolute maximum working lateral load capacity of the PI bearing at 7.5 bar is 68 kg. The total estimated mass that the PI will have to carry is shown in table 6.4.

Item	Mass (kg)	Source
Ceramic beam	40	From CoorsTek®
Sensor package	8	Estimate based on OMAM
Sensor mounting plate	5	Estimate
Additional metalwork	48	Estimate
Total	**101**	

Table 6.4 Mass budget for the SAP arm

For an arm structure of 101 kg the corresponding radial load on the PI bearing at a tilt angle of $\theta = 41^0$ is $m_{rad} = m_{total} \sin\theta = 66.26kg$ which is marginally close to the bearing's absolute tilt load capacity and it leaves a mass allowance of only 1.73 kg for a clamp. Assuming that the clamp is made of steel and using volumetric data from the

CAD drawings of figure 6.33 the calculated clamp mass is approximately 8.7 kg. This significantly exceeds the mass allowance of 1.73 kg. In theory the mass could be reduced if the clamp was made out of thinner sections. However, this would be likely to distort the clamp at large sweep angles. An alternative way would be to construct the clamp out of lightweight, yet strong, materials such as carbon fibre. Nevertheless, this idea was discarded on the grounds of cost and complexity of manufacture.

6.6.3 TILTING THE HORSTMANN BEARING

Maintaining a long arm length comes at the expense of increased tilt angle. Assuming a theoretical absolute minimum effective arm length of 500 mm (to cover the whole range of quoted diameters) the measurement of an optic with RoC, R=532 mm would require a tilt of 69^0. The PI bearing cannot be tilted beyond 41^0, however, due to symmetry, the remaining tilt of 28^0 could be generated by the Horstmann bearing. According to figure 6.31 if the PI is tilted clockwise by θ_1 and the Horstmann tilted anticlockwise by θ_2 the overall effective tilt of the SAP measurement will be $\theta = \theta_1 + \theta_2$.

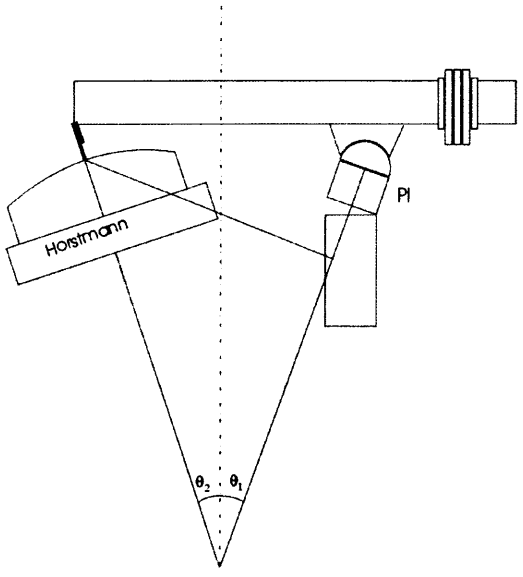

Figure 6.31 Tilting both the Horstmann and the PI bearing results to a compound SAP tilting angle

In order to investigate the feasibility of tilting the Horstmann the bearing's radial load capacity was examined by applying lateral loads onto the bearing table. An LVDT placed in contact with the side of the table was used to measure the resulting displacement (figure 6.32).

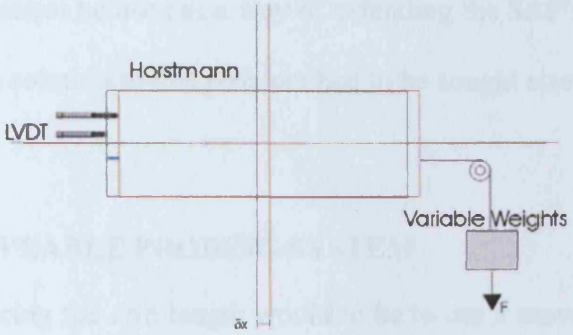

Figure 6.32 Experimental set-up used for measuring bearing motion under lateral loading

The application of a lateral load of approximately 22.7 kg resulted to a displacement of 256 μm. This displacement is interpreted as an effective, δx, misalignment between the SUT optical axis and the Horstmann rotor axis and results in 212 nm of surface form error. The resulting error cannot be justified as rotor movement since the average gap between the rotor and the stator in most commercially available bearings is no more than 10 μm (Nigel Cross NPL - personal communication). The understandable conclusion is that the error is a result of independent movement of the *x-y* table with respect to the rotor (figure 6.33).

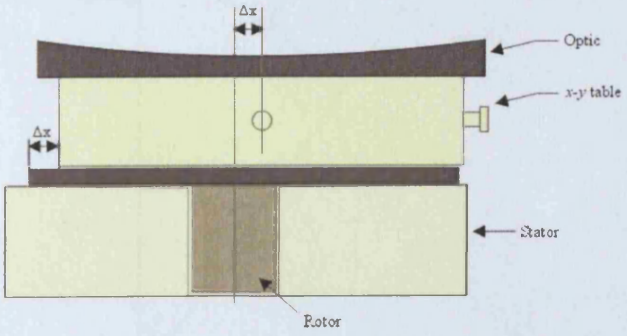

Figure 6.33 The application of lateral loads can lead to significant misalignment between the optical axis of the SUT and the bearing rotor axis

The result of the experiment suggests that the bearing is unsuitable for radial loading and hence tilting. A typical 1 m diameter spherical mirror made of Zerodur, including its mirror mount, could have a mass between 50 kg and 80 kg resulting in a lateral load between 23 kg and 41 kg at a tilt angle of 28^0. It is, therefore, obvious that tilting the Horstmann bearing cannot be used as a way of extending the SAP's measurement range to lower RoC and the solution to this problem had to be sought elsewhere.

6.6.4 USING A MOVEABLE PROBING SYSTEM

Another way of reducing the arm length would to be to use a moveable probing system that slides along the alumina beam. Since the effective arm length is defined as the distance between the probe tip and the arm rotary axis a sliding "saddle" would allow the effective arm length to be altered without altering the physical length of the beam (figure 6.34). According to the concept of figure 6.34, bringing the saddle closer to the tilt pivot reduces the arm length allowing the measurement of smaller RoC.

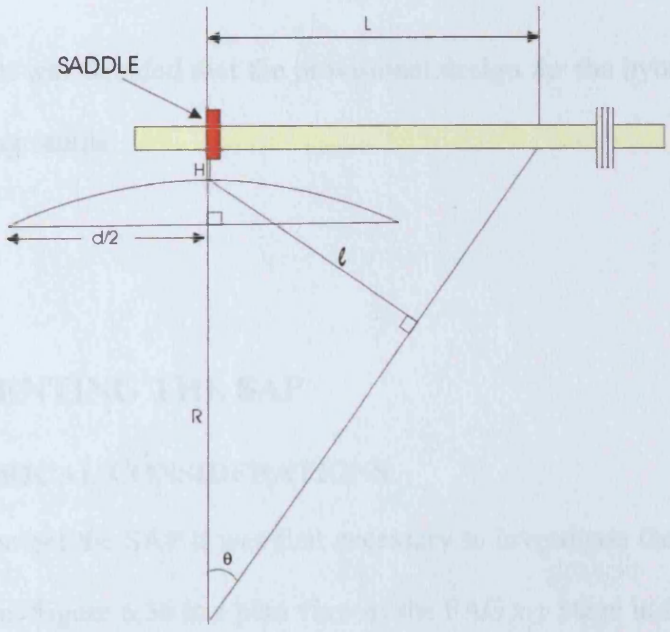

Figure 6.34 Principle of employing a moving saddle to modify the mechanical arm length

In order to comply with the hybrid sensor design shown in figure 6.35 the saddle could be made into a rectangular, ring-shaped breadboard onto which the probing components are mounted such as in figure 6.35. High-stiffness spring-loaded pads and restrainers could be used to lock the saddle into position.

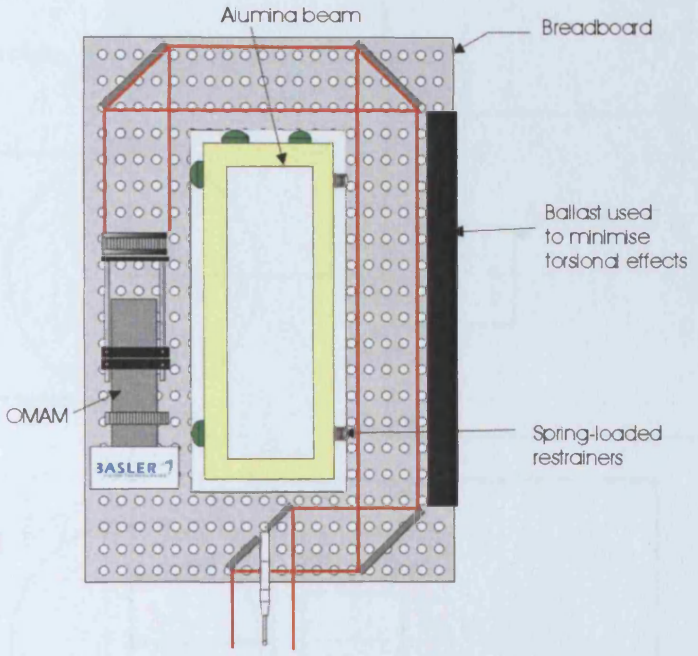

Figure 6.35 Conceptual design of a saddle structure and mounting configuration for the hybrid probe

As a conclusion it was decided that the provisional design for the hybrid sensor will be based on a moving saddle.

6.7 IMPLEMENTING THE SAP

6.7.1 GEOMETRICAL CONSIDERATIONS

In order to implement the SAP it was first necessary to investigate the configuration of the FAG platform. Figure 6.36 is a plan view of the FAG *x-y* stage in full extension and retraction, showing the distance between the centre of the face A and the centre of the

Horstmann bearing. Face A is the square metal casting where the granite column of the original CMM was located. It was decided that the SAP hyperstructure should be mounted onto Face A for improved rigidity and stability.

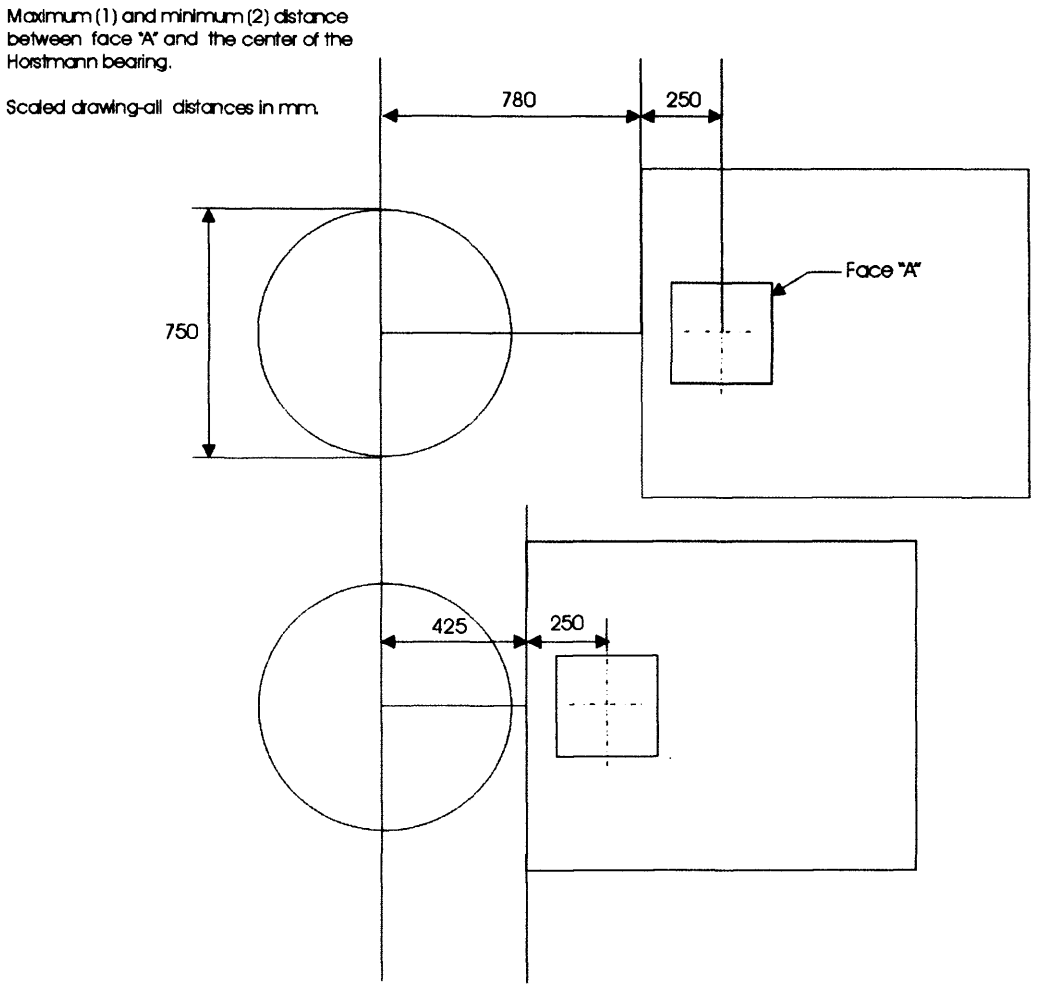

Figure 6.36 Maximum and minimum separation between the centre of the Horstmann bearing and the proposed, PI bearing tilt pivot

According to figure 6.39, if the PI is mounted with its axis coincident with the centre of Face A the minimum achievable arm length would be 675 mm. The measurable RoC can then be calculated using $R = L/\tan\theta \pm H$. For a maximum tilt of 41^0 and a minimum arm length of 675 mm, the measurable RoC would depend on the separation,

H, between the probe tip and the tilt pivot. A plot of achievable concave RoC against *H* is shown in figure 6.37.

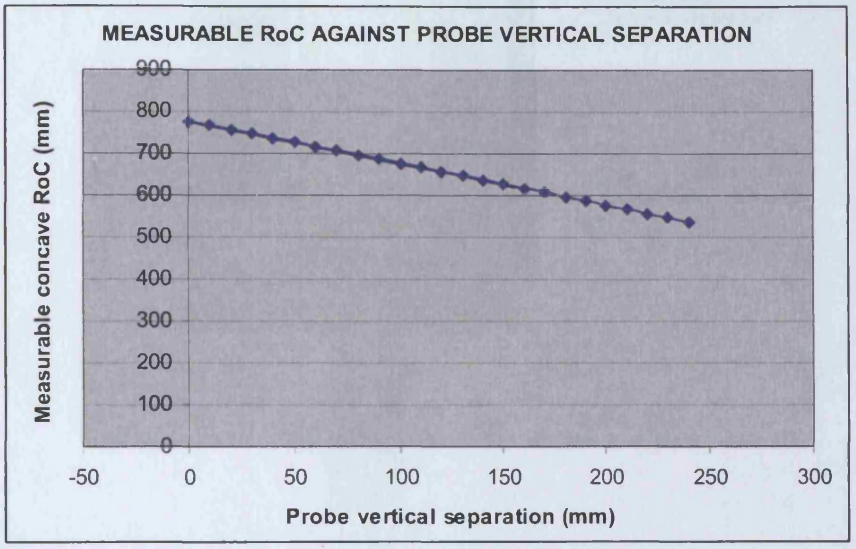

Figure 6.37 Measurable RoCs for concave optics against vertical probe separation with an arm length of 675 mm

It is apparent from figure 6.40 that that measurement of concave optics of RoC as low as 536 mm can be achieved only if H = 240 mm. This, however, would require the use of a very long probe extension which is considered bad practise for precision instruments. In order to maintain a large value for H without compromising the accuracy of the instrument the concept hybrid sensor design of figure 6.35 could be modified as shown in figure 6.38 where the breadboard has an annexe where the contact probe is mounted. Mounting the contact probe at the annexe means that the use of long styli can be avoided. The annexe can also be made adjustable in height in order to allow positioning of the probe along the *z*-axis.

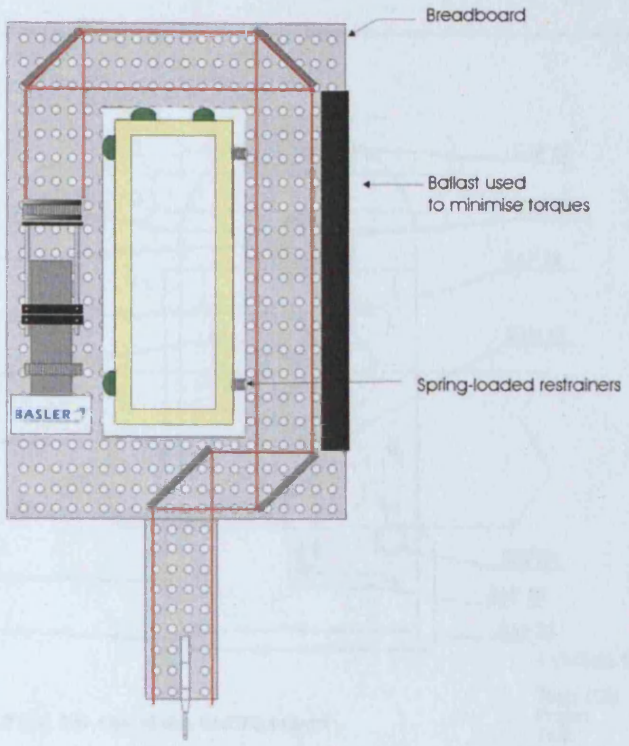

Figure 6.38 Concept design of an annexed saddle. The contact probe is mounted on the annexe which is adjustable in height

6.7.2 THE ARM AND PI BEARING SUPPORT FRAME

The design of the main PI bearing and arm mount was the result of a collaborative effort between the author, PhD students and colleagues from both UCL and NPL. The final implementation of the frame and support structures was performed by Simon Oldfield at NPL with constant input from the involved parties.

The final design is based on an inverted bearing configuration where the arm is suspended from the rotary bearing rather than being mounted on top of it. The support frame is shown in the CAD drawings of figures 6.39, 6.40 and 6.41.

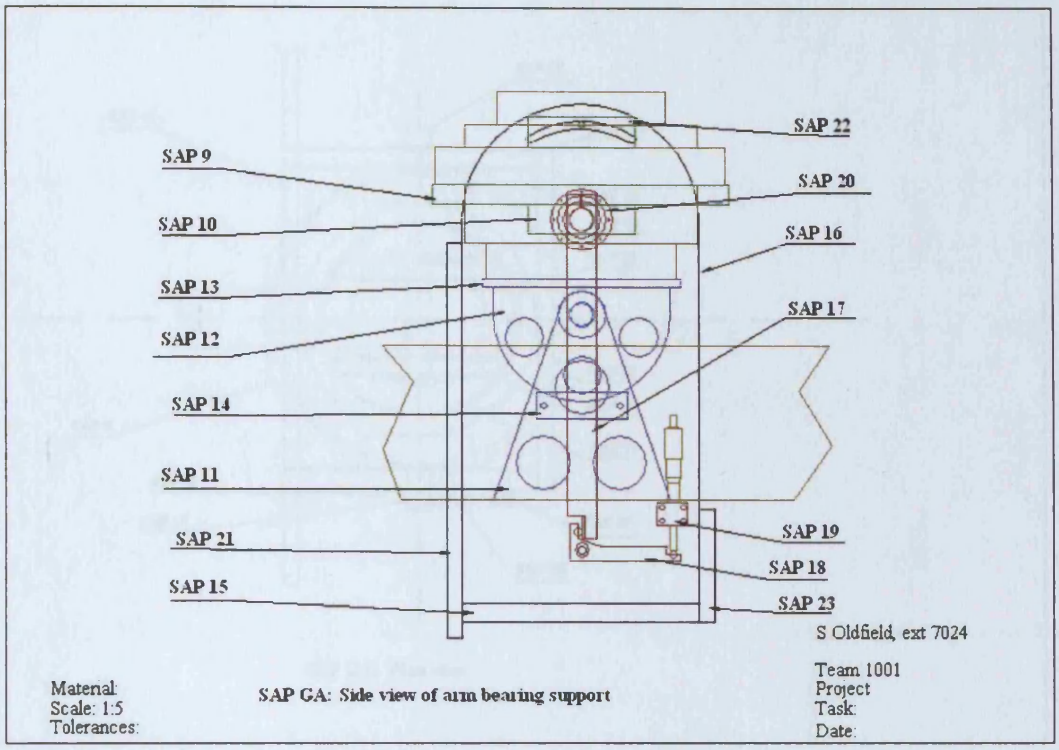

Figure 6.39 Side view of the arm bearing support

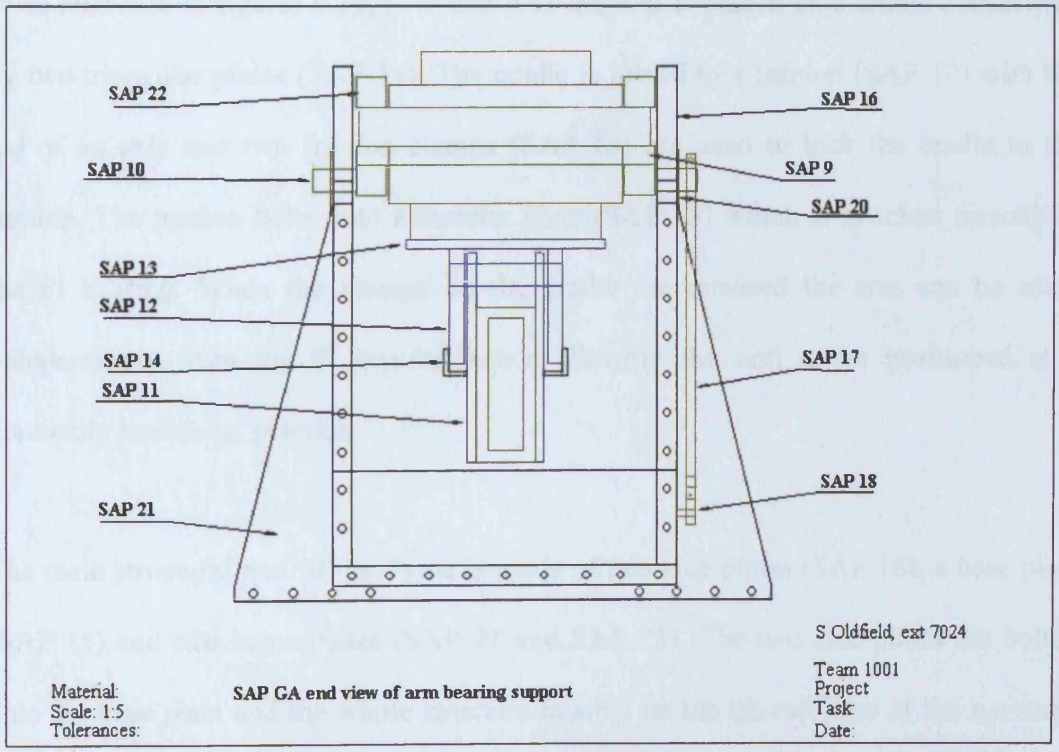

Figure 6.40 End view of the arm bearing support

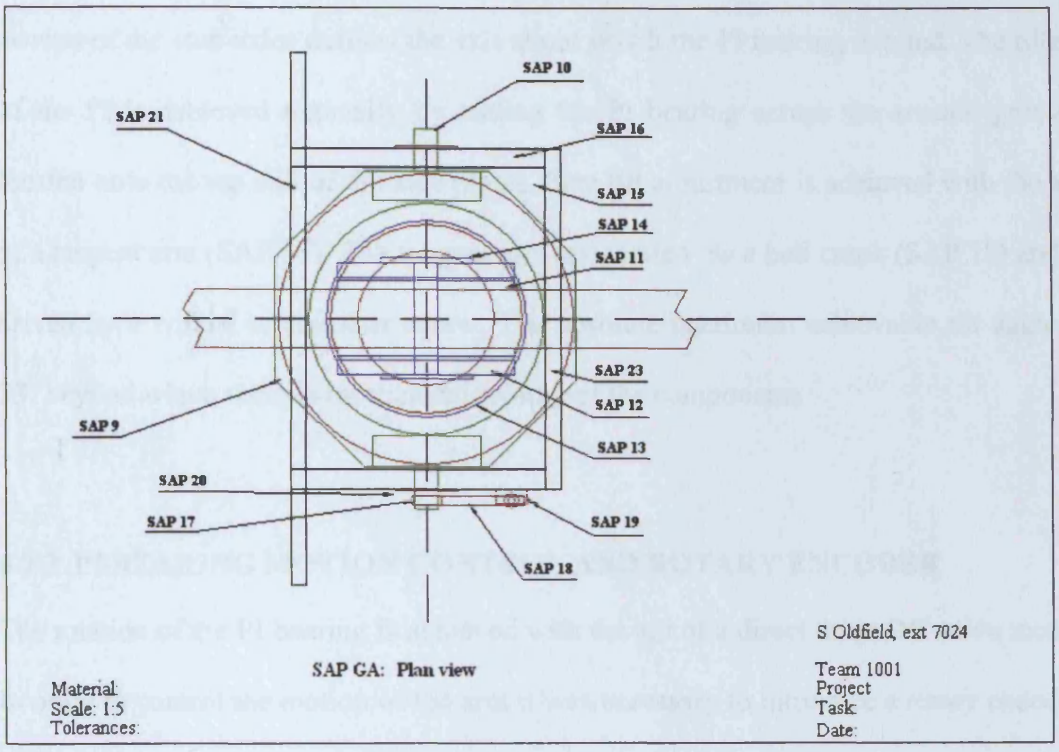

Figure 6.41 Plan view of the arm bearing support

With reference to figures 6.39, 6.40 and 6.41 the arm is placed on a cradle constructed by two triangular plates (SAP 11). The cradle is joined to a trunion (SAP 12) with the aid of an axle and two friction clamps (SAP 14) are used to lock the cradle to the trunion. The trunion bolts onto a circular plate (SAP 13) which is attached directly to the PI bearing. When the clamps on the cradle are released the arm can be tilted independently from the PI bearing hence allowing the arm to be positioned at a nominally horizontal position.

The main structural part of the frame is made of two side plates (SAP 16), a base plate (SAP 15) and two brace plates (SAP 21 and SAP 23). The two side plates are bolted onto the base plate and the whole structure mounts on the tilt-roll base of the *x-y* stage shown in figure 6.19. The PI bearing is placed inside a ring shaped interface plate (SAP

9) which is supported by two symmetrical stub axles (SAP 10). The line joining the centres of the stub axles defines the axis about which the PI bearing is tilted. The tilting of the PI is achieved manually by sliding the PI bearing across the arcuate grooves located onto the top end of the side plates. Fine tilt adjustment is achieved with the aid of a tangent arm (SAP 17). The tangent arm is operated *via* a bell crank (SAP 18) and is driven by a typical micrometer screw. The absolute maximum achievable tilt angle is 33^0 beyond which there is mechanical fouling of the components.

6.7.3 PI BEARING MOTION CONTROL AND ROTARY ENCODER

The rotation of the PI bearing is achieved with the aid of a direct drive DC servo motor. In order to control the motion of the arm it was necessary to introduce a rotary encoder. The encoder used for the SAP is a Heidenhain ERP 880 which is based on a radial grating installed into a hollow shaft (figure 6.42(a)). The principle of operation is based on the photoelectric scanning of the grating. The resolution of the encoder is 0.00001^0 and the accuracy is ± 1 arc-sec.

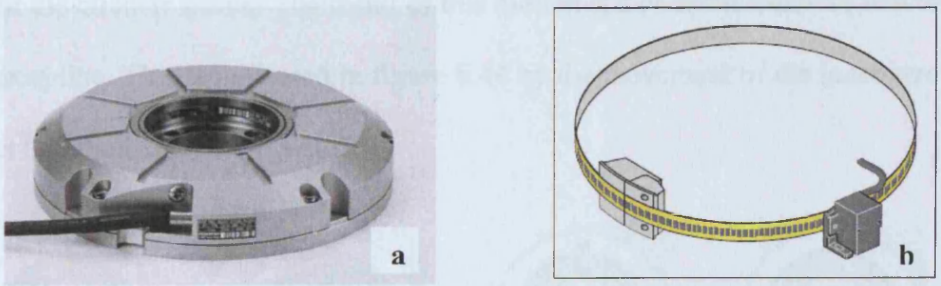

Figure 6.42 Photograph of the ERP 880 encoder (a) and schematic of its principle of operation (b) (pictures taken from Heidenhain catalogues)

6.7.4 HARMONIC DRIVE GEAR

The motion of the DC motor is transmitted onto the PI bearing through a harmonic drive gearing system. The harmonic drive consists of three elements, a circular spline, a flexible spline (flexspline) and a wave generator (figure 6.43).

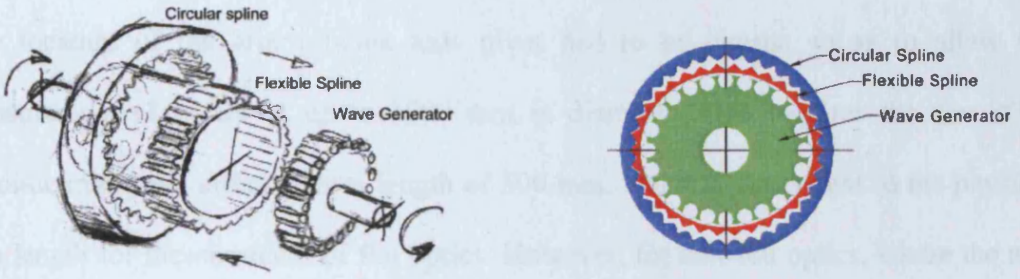

Figure 6.43 Schema of the components of a typical harmonic drive

The flexispline is smaller in diameter than the circular spline and usually has two fewer teeth. The wave generator is an elliptical cam onto which the DC motor is connected. When the wave generator is rotated it transfers its elliptical shape onto the flexispline which engages the circular spline across the major axis of the resulting ellipse. As shown in figure 6.44 as the cam rotates the flexipline engages and disengages different parts of the circular spline. The result of this motion is a counterclockwise movement of the flexispline. This is indicated in figure 6.44 by the movement of the inner arrow with respect to the outside, fixed arrow.

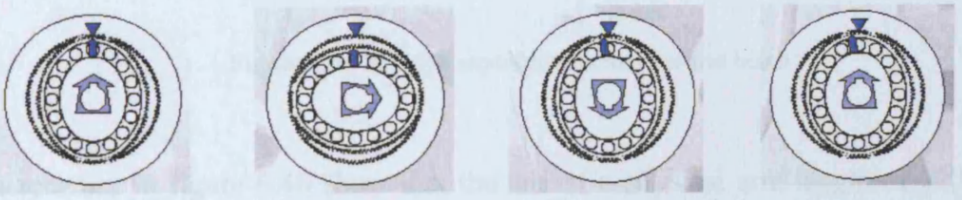

Figure 6.44 Principle of operation of a typical harmonic drive

At the end of a complete 180^0 rotation, the inside arrow has moved two teeth counterclockwise. The chosen AG harmonic drive offers high output torque and a reduction ratio of 200:1.

6.8 MEASUREMENT RANGE OF THE SAP

The location of the arm rotation axis pivot had to be chosen so as to allow the measurement of optics of up to 1000 mm in diameter. This requires the use of an absolute minimum effective arm length of 500 mm, which is equivalent to the physical arm length for measurement of flat optics. However, for non-flat optics, where the arm axis is tilted (figure 6.34), a physical arm length that is much larger than the effective arm length is needed. In order to account for this it was decided to allow a physical arm length of $L = 720$ mm. This allows 500 mm of beam section to be used for counterbalancing purposes (figure 6.45).

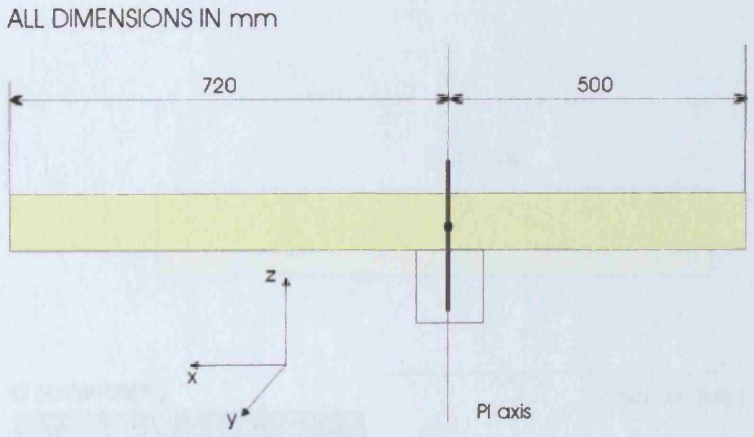

Figure 6.45 Relative separations across the arm beam

The schemas in figure 6.46 show that the use of a physical arm length of 720 mm is adequate even at a maximum tilt angle of 33^0 where the beam is fully retracted.

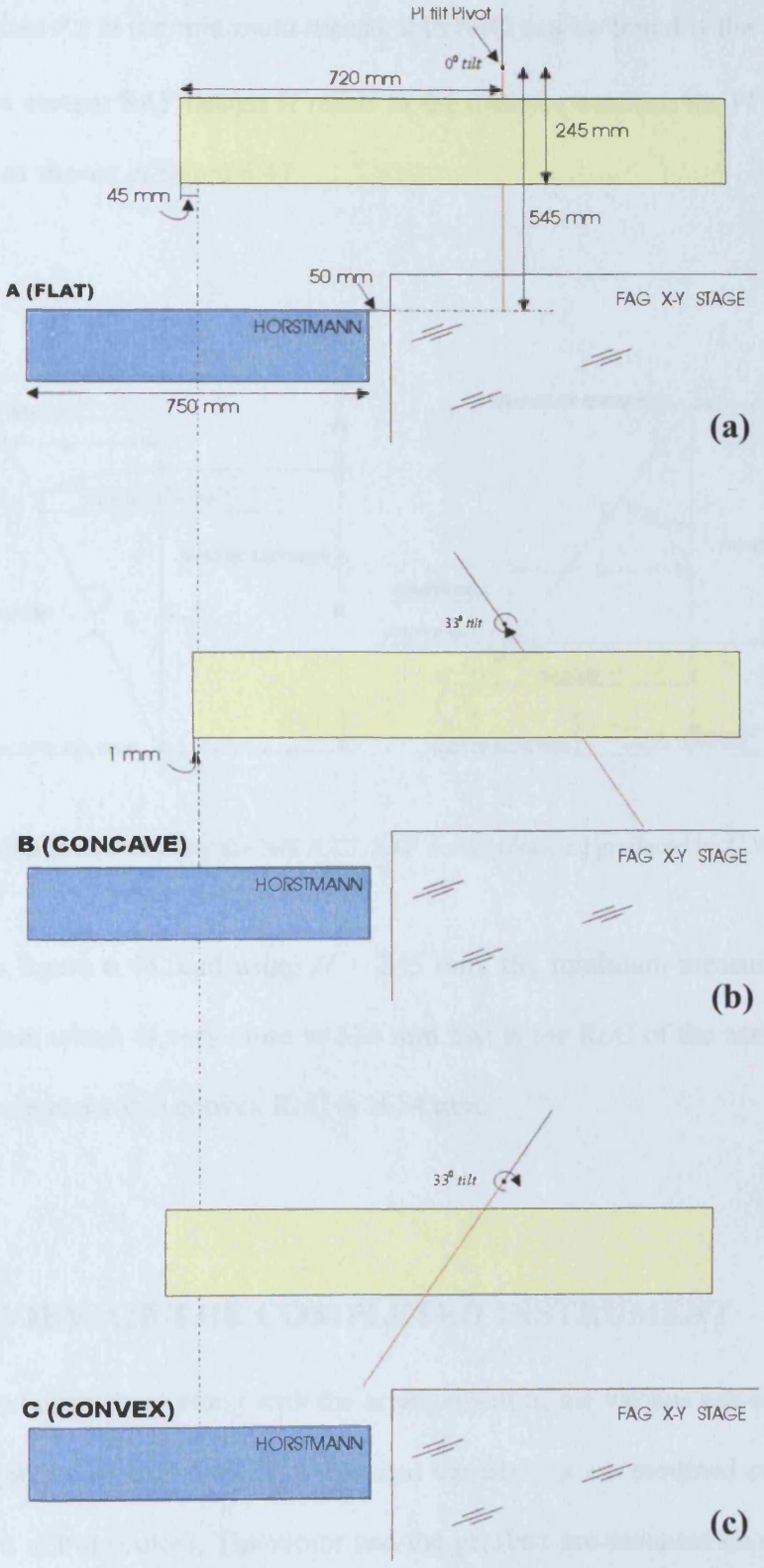

Figure 6.46 Scaled diagram showing the relative separations between the SAP arm, the FAG *x-y* stage and the Horstmann bearing when measuring flat (a), concave (b) and convex (c) optics. The figures show the *x-y* stage at maximum extension as in figure 6.39 (2)

Using $R = L/\tan\theta \pm H$ the minimum measurable RoC can be found if the distance H is known. In the current SAP design H refers to the distance between the PI tilt pivot and the probe tip as shown in figure 6.47.

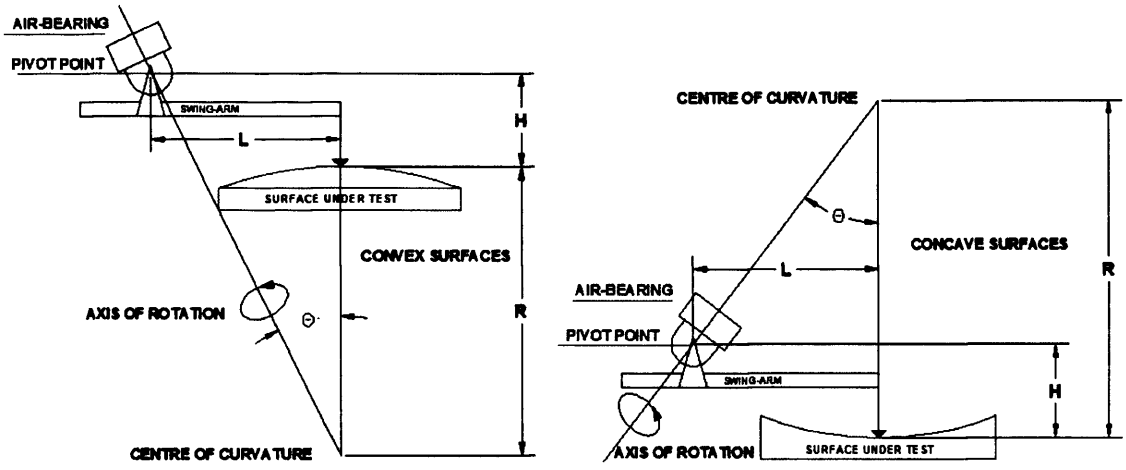

Figure 6.47 Description of H for the NPL/UCL SAP design (drawing produced by C.W.King UCL)

According to figure 6.46, and using H = 245 mm, the minimum measurable concave RoC is 564 mm which is very close to 536 mm that is the RoC of the case study optic. The minimum measurable convex RoC is 1654 mm.

6.9 OVERVIEW OF THE COMPLETED INSTRUMENT

The completed instrument along with the arrangement of the various sub-components is shown in figures 6.48 and 6.49. The arm and the bearing are mounted on the support frame (shown in blue color). The motor and the gearbox are mounted on a table which is supported by six pegs that are bolted onto the PI bearing. A custom coupling transmits the motion of the motor to the PI bearing. There are two hand wheels on the back and on the side of the main x-y stage that are used in order to translate the stage

linearly across the *y*- and *x*-axes. The hand wheels have built in micrometers to allow fine adjustment.

Figure 6.48 Sub-component configuration of the completed SAP

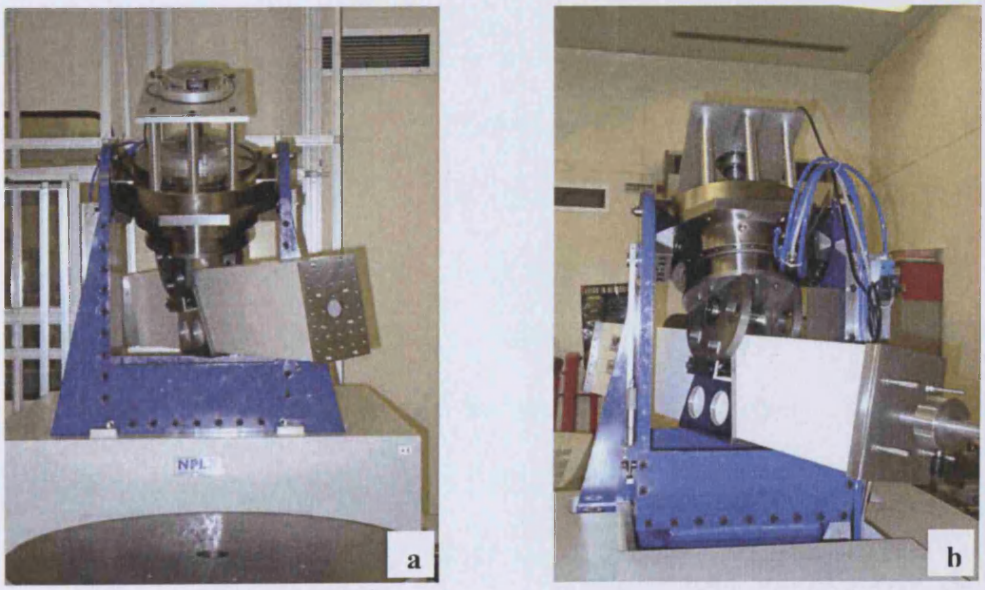

Figure 6.49 Front (a) and rear (b) view of the SAP when the PI bearing is tilted by 33^0

6.10 SUMMARY

A SAP prototype has been constructed by modifying a decommissioned FAG CMM. The prototype is based on the rotary motion of a high quality PI air bearing and uses a stiff alumina beam to move a hybrid probing system. A provisional design for the hybrid opto-mechanical sensor has also been proposed. The hybrid sensor will be based on a sliding optical breadboard onto which a contact probe and a wavefront sensor will be mounted. The whole of the SAP frame is mounted on an existing *x*-*y* stage which can be used to position the probe onto the optic to within 100 nm.

Chapter 7

MECHANICAL PROBING AND TRACEABILITY

"Fast is fine, but accuracy is everything."

Xenophon

7.1 INTRODUCTION

The contact probe will form an important part of the hybrid sensor and it has to be chosen carefully to reflect the project requirements. There is a large selection of commercially available displacement sensors including the Linear Variable Differential Transformer (LVDT) type which uses an electromechanical sensor based on the phenomenon of mutual induction. The linearity range of common LVDTs is usually 80% of the total displacement range (Novacek 1999). Another popular type of contact displacement sensor is the linear scale sensor that employs a linear grating to convey information about the displacement of the stylus. For the SAP it was decided to use the Solartron LE12/IP65 linear scale sensor (figure 7.1). The chosen sensor has a range of 13 mm, therefore, it can be used in theory for measurement of asphericities up to 13 mm. The probe's resolution is 12.5 nm which is sufficient for resolving surface profile irregularities of 20 nm as required by the DTI specifications. The measurement principle in the case of the Solartron LE12/IP65 is based on photoelectric scanning of two graduated scales situtated inside the transducer (figure 7.2).

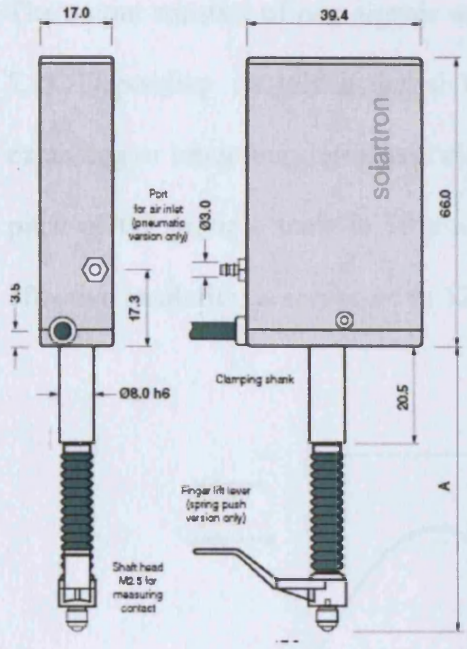

Model	LT12
Size	95 x 30 x 12 mm
Weight	30 g (approx.)
Supply Voltage	5V DC, 225 mA
Suppply current	180 mA
Operating Temperature	0 C^0-60 C^0
Gauging speed	0.2 ms^{-1}
Max Stroke Length	13 mm
Resolution	0.0125 µm
Accuracy over full range	± 0.5 µm
Reference temp	20 C^0
Gauging force	0.5 N
Max side load	0.1 N

Figure 7.1 Schema of the Solartron probe and main specifications

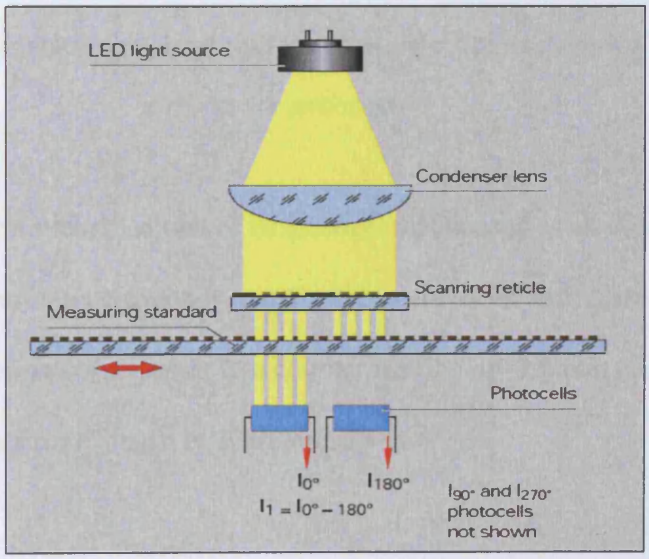

Figure 7.2 The principle of photoelectric scanning: Two scales of equal pitch are illuminated by collimated light producing light and dark bands that are detected by photocells (picture reproduced from Heidenhain catalogues)

The output consists of two signals with a phase difference of 90^0 between them (figure 7.3). Depending on which signal leads it is possible to determine if the probe is extending or retracting. Integrated electronics are used for digitisation of the signal. The pitch of the probe's scale is 10 µm, however, interpolation of ×800 ensures that the effective resolution is increased to 12.5 nm.

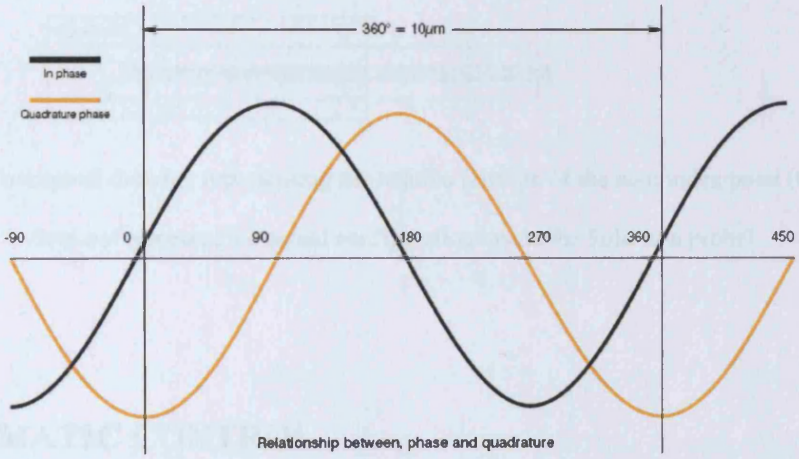

Figure 7.3 The quadrature output signal on the Solarton probe. The wavelength of the signal is equal to the grating pitch

The probe has a zero mark on one of its gratings that is used as an absolute reference point. A full extension corresponds to a displacement of 9.5 mm from the index point while a full retraction corresponds to a counter reading of -3.5 mm (figure 7.4). The overall maximum stroke length is, therefore, 13 mm.

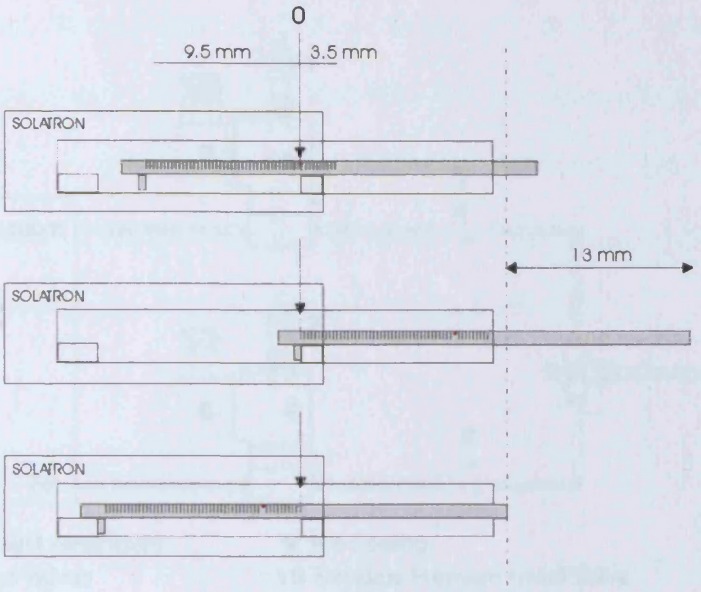

Figure 7.4 Conceptual drawing representing the relative position of the zero index point (the drawing does not represent the actual configuration inside the Solartron probe)

7.2 PNEUMATIC CONTROL

The Solartron LE12/IP65 is a pneumatic probe chosen because the pneumatic control can allow easy pick-and-poke measurements. With no air supply the probe can be loaded onto the surface under its own weight. In this case, however, there is no effective spring constant and this can cause unwanted skidding of the stylus within its housing leading to measurement errors. In order to overcome this problem and allow for extension and retraction of the probe, a basic, prototype, pneumatic control system was built.

The extension/retraction circuit (figure 7.5) was constructed using catalogue components. A dual air/vacuum pump was used to provide the necessary suction and air flow. With respect to figure 7.5 the two outlets of the pump are each connected to a solenoid Excel valve which is actuated electrically by a 24 V supply.

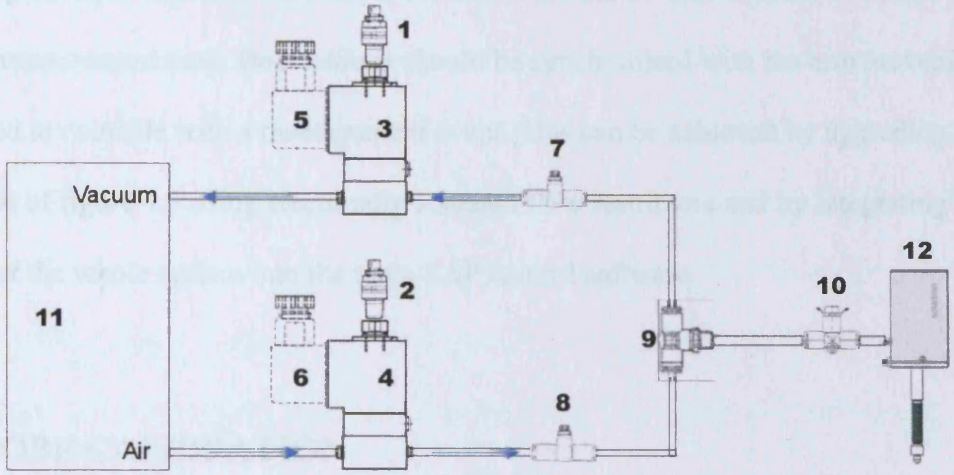

1,2 Exhaust Restrictors
3,4 Excel Valves
5,6 Cable Sockets
7,8 Flow Regulators
9 Tee Feeting
10 Residual Pressure Relief Valve
11 Vaccum Pick-Up
12 Solartron Probe

Figure 7.5 Pneumatic control system

When valve 3 is switched off, compressed air is flowing through valve 4 reaching the Solartron probe after being diverted by a "Tee" connector. The compressed air extends the probe and generates an effective spring force. When valve 4 is switched off, the air flows only towards the pump in the upper part of the circuit, generating a vacuum which allows the retraction of the stylus. In order to maintain continuous pump operation when valve 4 is switched off the air drawn into the valve escapes to the environment *via* exhaust 2 leaving the rest of the system unaffected.

Flow restrictors introduced at the outputs of the Excel valves can be used to control the speed of extension and retraction. For the purposes of the current investigation it is only necessary to supply the probe with air of constant pressure. However, when the pneumatic circuit forms part of an integrated probe control system it will be necessary to control the direction and the speed of the probe's movement during pick-and poke measurements. The extension speed should be low (0.5 mm/s to 1 mm/s), in order avoid

damaging the optical test surface while retraction should be fast in order to reduce the overall measurement time. Both actions should be synchronised with the arm movement and timed to coincide with a measurement event. This can be achieved by upgrading the prototype of figure 7.5 using electrically actuated flow restrictors and by integrating the control of the whole system into the main SAP control software.

7.3 PROBE CALIBRATION

7.3.1 THE NEED FOR INTERFEROMETRIC LENGTH MEASUREMENT

A common way of calibrating displacement sensors, such as LVDTs, is with the aid of a gauge block comparator. To perform the calibration, gauge blocks of chosen steps are inserted between the anvil of the comparator and the probe tip. The displacement of the probe is then plotted against the corresponding gauge block step lengths in order to verify its linearity. This method, however, cannot be used for the current calibration because the Solartron probe is intended to measure discrepancies of 20 nm on the optical surface and it should calibrated to at least this level of accuracy. Gauge blocks can only provide a minimum step length of 100 nm. This step length is not always realisable since even high grade optical gauges can introduce uncertainties of up to 100 nm (Decker and Pekelsky 1997). The main uncertainties arise from thermal expansion of the gauge blocks and an it has been observed that an uncertainty of 1 mK in the gauge block temperature measurement can give rise to a length uncertainty of 12 nm (Hamid, Sendoglu and Edogan 2005). It was, therefore, decided that an interferometric technique had to be used in the current calibration.

7.3.2 THE INTERFEROMETRIC SET-UP

For the purposes of the current calibration a differential plane mirror interferometer was used. The type of interferometer used has been employed in the past for calibration of displacement transducers (Downs and Nunn 1998, Yacoot and Cross 2002). The linearity of the particular interferometer has been discussed elsewhere (Yacoot and Downs 2000). One of the main components of the interferometer is a Jamin beamsplitter which is a glass plate with opposed alternating half silvered areas (Born and Wolf 1999) as shown in figure 7.6. An incident laser beam at 45^0 gives rise to two beams, one transmitted through the front surface and the other reflected from the rear surface of the Jamin beamplitter. The coating of the Jamin beamsplitter introduces a phase difference of 90^0 between the two output beams.

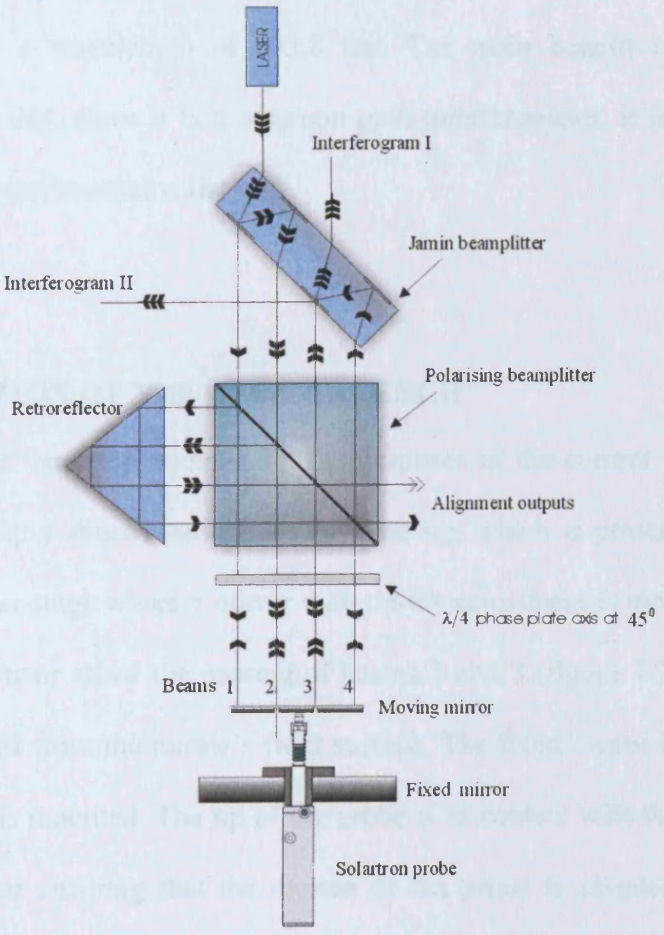

Figure 7.6 The interferometric set-up

When the two beams emerge from the Jamin beamplitter they are parallel but laterally displaced. Both beams travel onto a polarising beamsplitter cube where they are transmitted and continue through a quarter-wave ($\lambda/4$) plate positioned at 45^0. The combination of the polarising beamsplitter and the $\lambda/4$ plate ensures that the beams are subsequently transmitted and reflected by the beamsplitter after every passage. After passing through the $\lambda/4$ plate the first beam is reflected by the moving mirror and the second by a stationary mirror. After reflection the beams re-enter the $\lambda/4$ plate and are directed once more round the interferometer *via* a cube corner retroreflector until they finally recombine at the Jamin beamplitter producing two interferograms. The two output signals have equal amplitudes and are in phase quadrature allowing bi-directional fringe counting. The interferometric measurement was based on the use of a Helium-Neon laser with a wavelength of 632.8 nm. The main benefit of using a Jamin interferometer is that, since it is a common path interferometer, it is less sensitive to vibrations and environmental variations.

7.3.3 DESCRIPTION OF THE OPTICAL BENCH

In order to utilise the interferometer for the purposes of the current calibration it was necessary to set-up a special calibration rig. The rig, which is presented in figure 7.7 consists of a linear stage where a mirror with tip-tilt adjustment is mounted. Two holes on the moving mirror allow the passing of beams 2 and 3 (figure 7.7) whilst beams 1 and 4 are reflected from the mirror's front surface. The fixed mirror has a central hole where the probe is mounted. The tip of the probe is in contact with the back surface of the moving mirror ensuring that the motion of the probe is coupled to the mirror's motion.

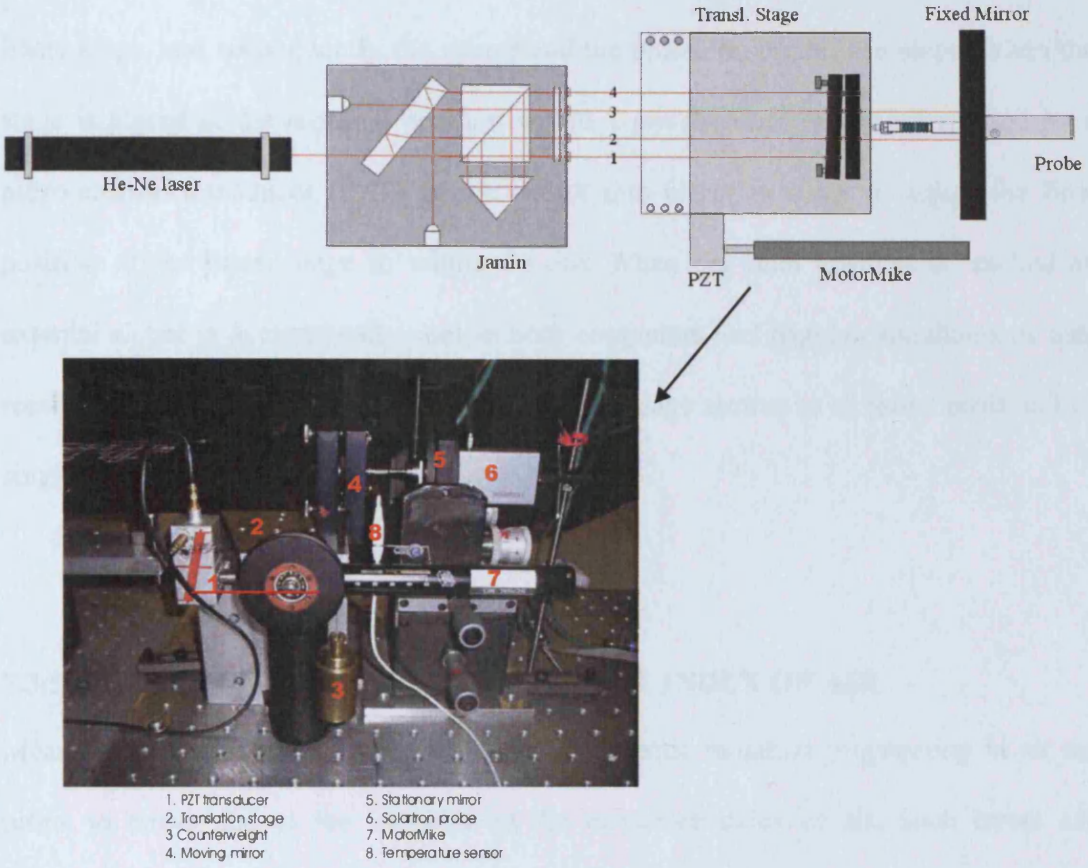

Figure 7.7 The main components of the calibration rig

7.3.4 MEASUREMENT PROCESS

The calibration system employs two computers, one for control of the rig and data acquisition from the interferometer and the other for data acquisition from the probe. Both computers use dedicated LabVIEW virtual instruments (VIs) for data acquisition and processing. The software used for the interferometer has been used in the past for similar experiments while a new VI was created for data acquisition from the counter. The calibration process is fully automated and the parameters of each calibration are user defined. The procedure requires inputting the calibration parameters, including initial and final position, step size and speed, onto the front panel of the

interferometerer's VI. The VI then energises a motorised micrometer which moves the linear stage, and consequently the mirror and the probe, on predefined steps. When the stage is placed at the required position within 1 μm the micrometer is bypassed by a piezo-electric transducer (PZT) which comes into effect in order to adjust the final position of the linear stage to within 10 nm. When the final position is reached an external signal is automatically sent to both computers and triggers simultaneous data recording. After the end of the calibration run the stage returns to its initial position in a single step (fly-back).

7.3.5 CORRECTION FOR THE REFRACTIVE INDEX OF AIR

Measurements that require the use of electromagnetic radiation propagating in air are prone to errors due to the variation in the refractive index of air. Such errors can contribute several nanometres of displacement error and it is necessary to be accounted for in measurements where high accuracy is required. A correction for the refractive index can be achieved by applying Edlén's equation (Edlén 1966) which calculates a value for the refractive index based on the measurement of the ambient temperature, pressure and humidity. In order to apply the correction in the current experiment a high accuracy temperature sensor along with a digital pressure sensor were employed for the measurement of the ambient air pressure and temperature.

Edlén's equation as revised by Birch and Downs (1993) is given by

$$(n-1)_{tp} = \frac{p(n-1)_s}{96095.43} \times \frac{\left[1+10^{-8}(0.601-0.00972\,t)p\right]}{(1+0.0036610\,t)} \qquad (7.1)$$

where p is the atmospheric pressure in Pa, t is the temperature in ${}^0C$ and $(n-1)_s$ is the refractivity of standard air and it is given by

$$(n-1)_s \times 10^8 = 8343{,}05 + 2406294\left[130-\sigma^2\right]^{-1} + 15999\left[38.9-\sigma^2\right]^{-1} \qquad (7.2)$$

where σ is the vacuum wavenumber in μm^{-1}.

The data from the sensors were used for software optimisation based on the modified Edlén equation before each calibration. In addition, a cover was used to shield the air path between the interferometer and the mirrors.

7.3.6 CORRECTION FOR QUADRATURE ERRORS

Quadrature encoding is achieved by combining two output intensity signals $u_1 = R\cos\omega t$ and $u_2 = R\cos(\omega t + \pi/2)$ that describe a vector (u_1, u_2) from the origin. For an ideal encoder the signals u_1 and u_2 are 90^0 out of phase and have the same magnitude which means that the vector tip traces a circle of radius R. In a real encoder, however, owing to differences in amplitude and phase, the corresponding Lissajou figure is an ellipse.

Quadrature errors can be corrected by performing a least square fit of the ellipse on the experimental data. The correction, which is described by Heydemann (1981) was already incorporated in the original interferometer data analysis software and ensures that the quadrature error is reduced to 10^{-8} m.

7.4 RESULTS

A number of experiments were carried out in order to assess the performance of the probe. The probe was tested for various performance indicators including linearity, repeatability, accuracy, static noise, scaling error, drift and hysteresis. In the current calibration the overall probe accuracy is realised as the degree to which the probe displacement, as measured by the probe counter, corresponds to the same displacement as measured by the interferometer. Under this approach we assume that the overall interferometer uncertainty is lower that the overall counter uncertainty.

The first measurement involved displacing the probe through the majority of its measurement range, starting from the point of near maximum extension (9 mm with respect to the index point) and ending at the point of near maximum compression (- 3 mm). The results of this measurement are shown in figure 7.8.

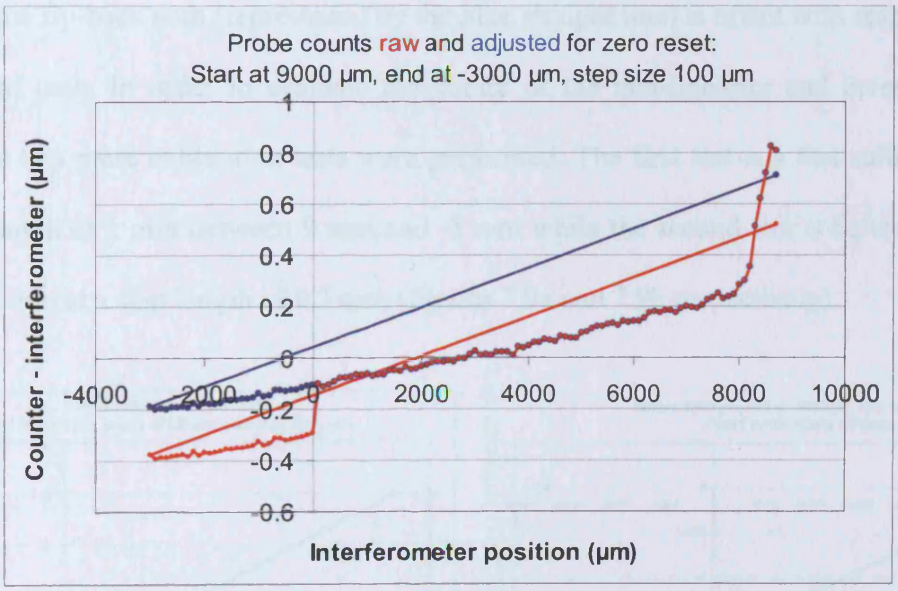

Figure 7.8 First calibration run between 9 mm and -3 mm. The red curve shows the acquired data and the blue curve represents the data corrected for thermal drift

Figure 7.8 shows that the response of probe is linear over most of its range. Significant non-linearity behaviour appears between 9 mm and 8 mm which indicates that the probe might have a mechanical fault in this region, such as an incorrectly laid scale. At the point of zero displacement there is a sudden drop which offsets the calibration curve by approximately 0.2 μm. This difference between two adjacent data points is too large to be attributed to inherent probe error. The offset can, however, be explained as a thermal drift that displaced the absolute position of the index point. The probe stylus might have been warmed up as a result of handling prior to calibration which resulted in a slow thermal drift. The extent of the drift becomes apparent at the zero point where the probe counter resets. In figure 7.8 the graph plotted in red represents the raw data while the graph plotted in blue shows the data corrected of the thermal drift between 0 mm and 3000 mm.

Another important feature of graph 7.8 is that there appears to be a hysteresis effect since the fly-back path (represented by the blue straight line) is offset with respect to the forward path. In order to evaluate the nature of the non-linearity and investigate its origins two more calibration tests were performed. The first test is a fast calibration of step length of 1 mm between 9 mm and -3 mm while the second test is between 6 mm and -3 mm at a step length of 0.3 mm (figures 7.9a and 7.9b respectively).

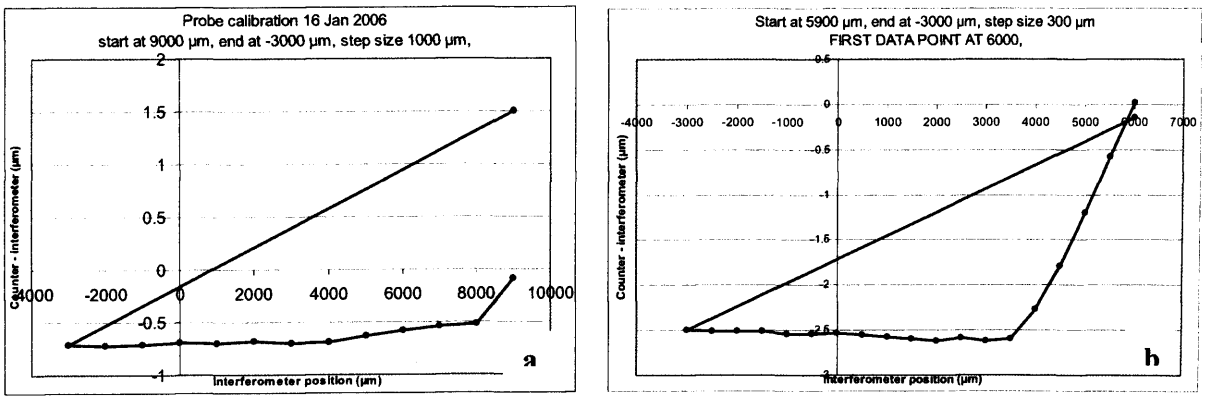

Figure 7.9 Probe calibration over a 12 mm range with a step size of 1000 μm (a), and 300 μm (b)

Figure 7.9(a) verifies the non-linear tendency of the probe between 9 mm and 8 mm. It also suggests that the effect is not a time related drift: the same effect appears between 9 mm and 8 mm on both the calibrations of figures 7.8 and 7.9(a) although the two calibrations were performed on different days and at different speeds. The distance between 9 mm and 8 mm was covered in 3 minutes in the first case contrary to 1 minute in the second case. Figure 7.9(b) shows that a similar effect is observed even when the calibration starts at 6 mm. The effect now appears in the, previously linear, region between 6 mm and 3.5 mm which suggests that the apparent non-linearity may be a measurement or alignment error rather than an intrinsic probe error.

Further evidence for the suggestion that alignment errors are responsible for the apparent non-linearity was provided by the calibration tests of figures 7.10(a) and 7.10(b) where the calibration range is again 12 mm but the starting and ending points have been reversed. The large peak of graph 7.10(b) at 6450 mm is probably the effect of vibration due to demolition which was being carried out in a nearby building or "stick and slip" effects between the probe tip and the moving mirror.

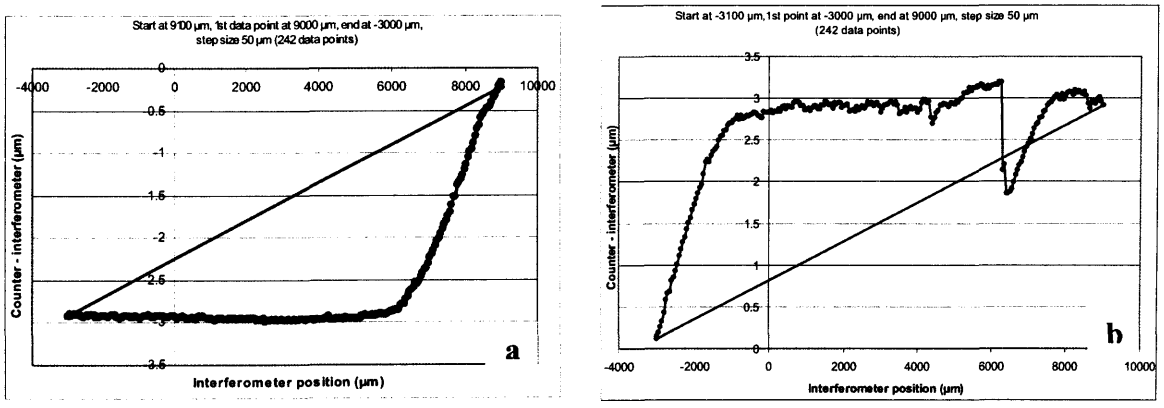

Figure 7.10 Probe calibration over a 12 mm range with a step size of 1000 µm (a). The direction of the calibration is reversed in (b)

As is shown in figures 7.10(a) and 7.10(b), reversing the direction of the calibration sequence reverses the non-linearity, hence, indicating that the effect must be related to the experimental set-up. After inspecting the alignment of the moving mirror with a quad photocell it became apparent that the mirror was misaligned with respect to the probe axis. This, results in an offset force applied on the probe forcing the stylus to move laterally inside the shaft. Although the mirror remains sufficiently aligned during the whole 12 mm travel to maintain the fringes and provide interferometric displacement data, a varying cosine error is introduced on the counter data. Once the stylus is forced onto the side of the shaft the lateral movement ceases and only a constant error remains. The point where the lateral movement stops appears as a steep slope change in the graph. When the direction of travel reverses the stylus is moved towards the opposite wall of the shaft hence reversing the non-linear effect. After aligning the stage the experiment was repeated and the results of three subsequent calibration tests are presented in figures 7.11(a), 7.11(b) and 7.11(c).

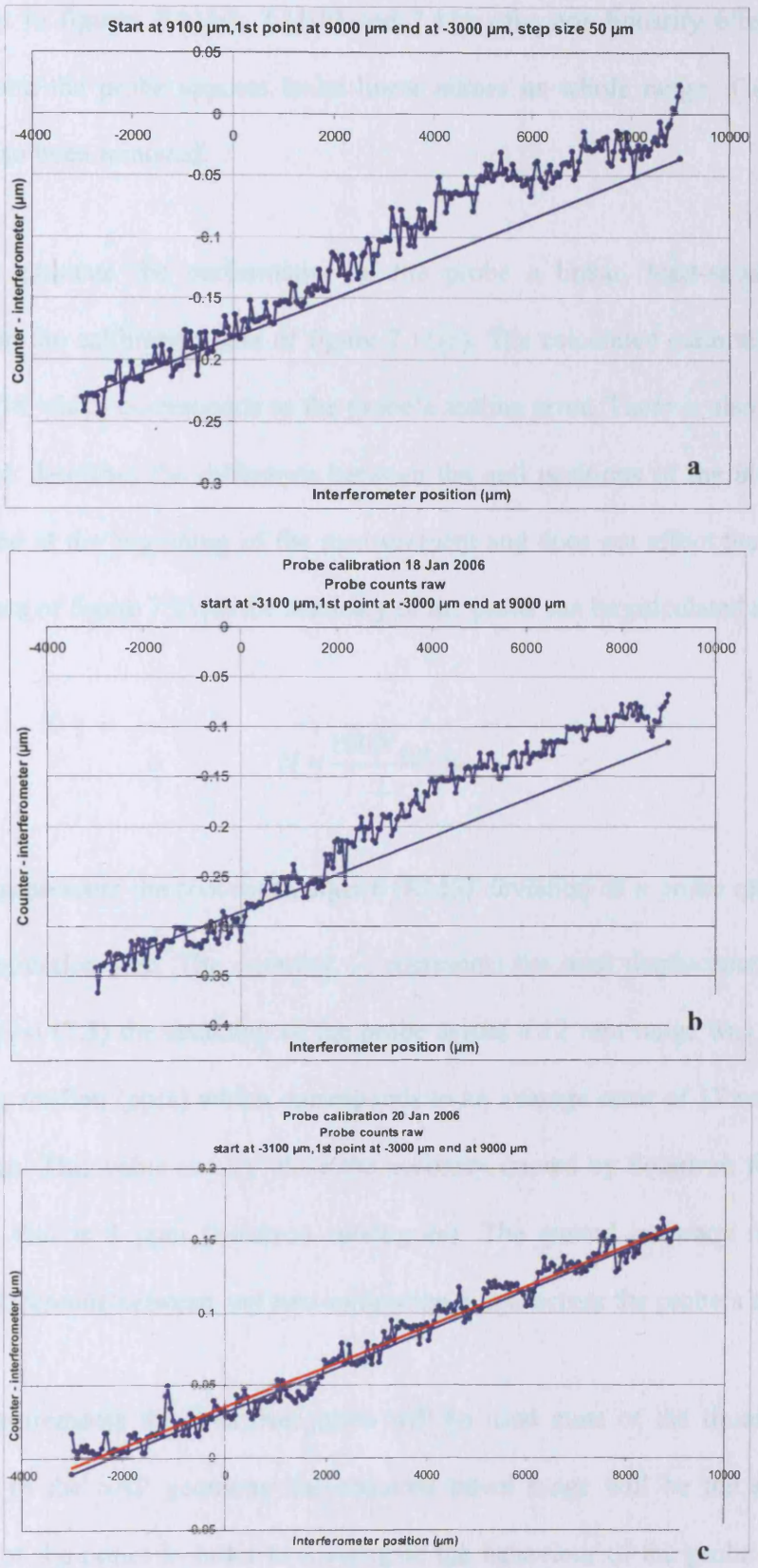

Figure 7.11 Calibration tests after the stage had been aligned

As is shown in figures 7.11(a), 7.11(b) and 7.11(c) the non-linearity effect has been eliminated and the probe appears to be linear across its whole range. The hysteresis effect has also been removed.

In order to estimate the performance of the probe a linear, least-squares fit was performed on the calibration data of figure 7.11(c). The calculated calibration factor is 0.9999861118 which corresponds to the probe's scaling error. There is also an offset of 35 nm which describes the difference between the null positions of the interferometer and the probe at the beginning of the measurement and does not affect the calibration. Using the data of figure 7.11(c) the accuracy of the probe can be calculated as

$$N = \frac{100 N_{RMS}}{L}\% \tag{7.3}$$

where N_{RMS} represents the root mean square (RMS) deviation of n probe measurements from the regression line. The quantity, L, represents the total displacement travelled. Using equation (7.3) the accuracy of the probe across a 12 mm range was found to be 1.4 parts per million (ppm) which corresponds to an average error of 17 nm across the 12 mm range. This value is very close the accuracy quoted by Solartron for the LE12 type probe, that is 1 ppm (Solatron catalogues). The quoted accuracy refers to the maximum difference between any two calibration points across the probe's range.

During measurements the Solartron probe will be used most of the times at a small range. Due to the SAP geometry the required travel range will be the same as the asphericity of the optic. In order to investigate the behaviour of the probe at a shorter range further experiments were conducted. Figures 7.12(a), 7.12(b) and 7.12(c) present

three calibrations with subsequently decreasing range and step length. The smallest range tested was 20 μm with a step length of 100 nm (figure 7.12(c)).

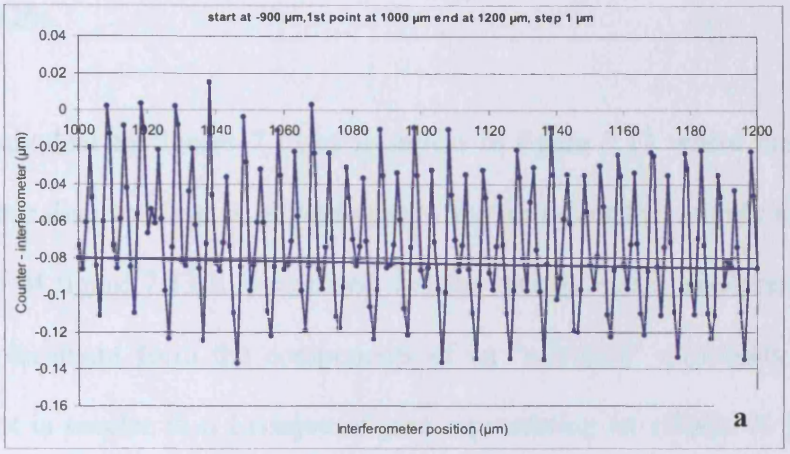

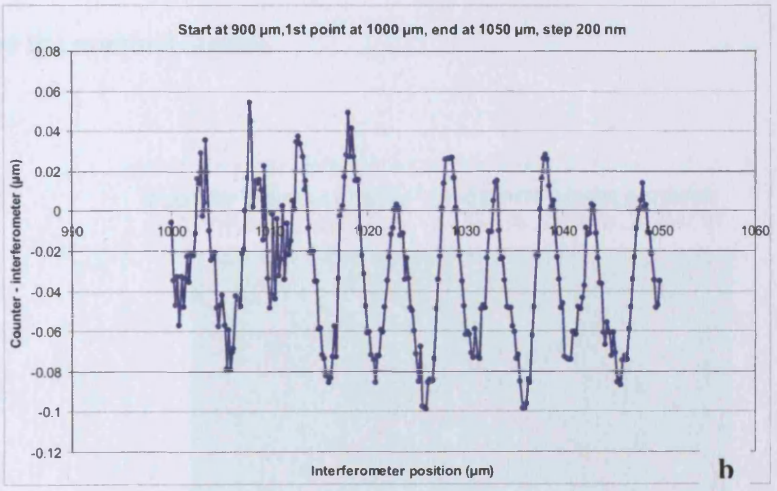

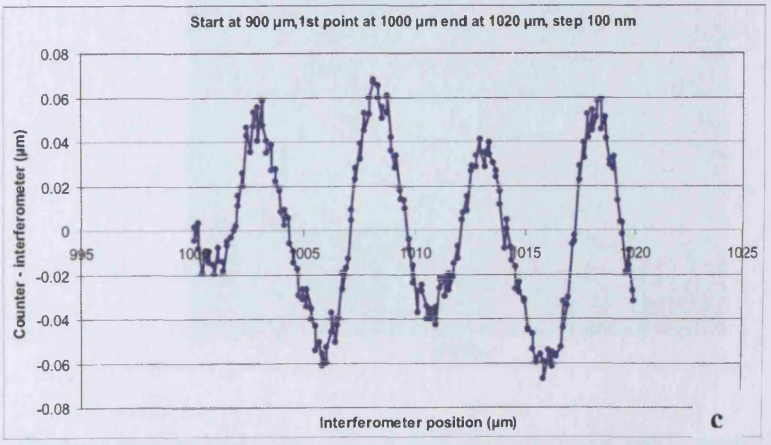

Figure 7.12 Probe calibrations for decreasing range and step size

It is evident from figure 7.12 that the dominant error is a periodic non-linearity error with an approximate amplitude of 60 nm and a periodicity of 5 μm. The calculated non-linearity is 0.2%.

A graph equivalent to figures 7.12(c) is shown in figure 7.13 where the sine of the interferometric displacement is plotted against the cosine of the counter displacement. In the graph of figure 7.13 it is assumed that the interferometer displacement and the counter displacement form the components of an "effective" quadrature signal. The resulting plot is similar to a Lissajous figure representing an ellipse. A circle is also plotted to represent the two components of the interferometer quadrature signal which is assumed to be the nominal signal.

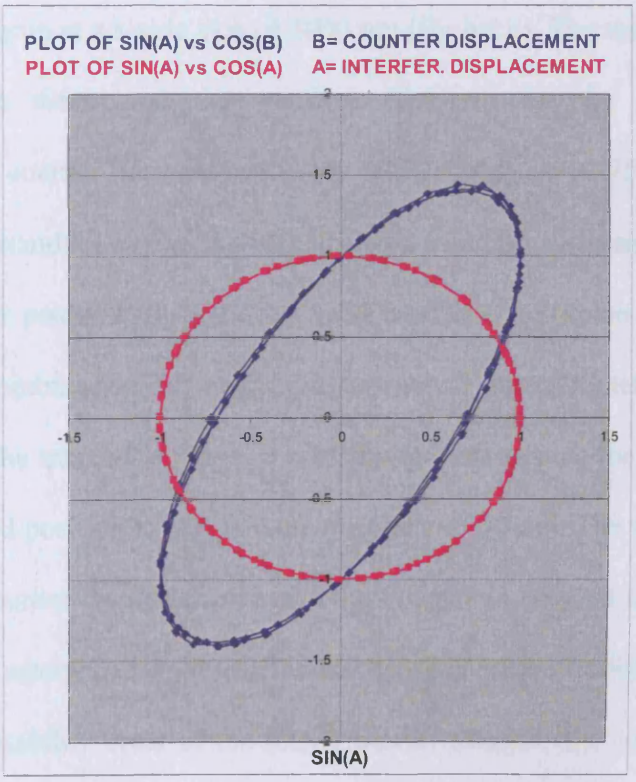

Figure 7.13 Effective Lissajous plot of the counter displacement against interferometer displacement (ellipse). The circle represents the interferometer quadrature signal

Combining the information from figures 7.12(c) and 7.13 we can say that the observed cyclic error has the characteristics of a typical quadrature encoding error. The four points where the ellipse is crossing the circle represent the four peaks of the sinusoidal graph in figure 7.12(c). The quadrature error for the interferometer had been corrected using the Heydemann correction, therefore, the observed effective quadrature error can only be attributed to the counter. This can be verified by the fact that the period of the error is equal to 5 μm which is half the period of the counter's grating pitch.

Finally the repeatability and the noise of the counter were measured. The repeatability was measured by displacing the probe back and forth at a range of 2000 μm (±1000 mm about the index point). The probe was initially placed at -1000 μm with respect to the index point and moved to 1000 μm at a single step of 2000 μm. Then the probe returned to its initial position again at a single step of 2000 μm (fly-back). The measurement was repeated twenty five times and the standard deviation for the interferometric measurement and the counter measurement were calculated to be 30.75 nm and 27.13 nm respectively. The standard deviation was calculated using the difference between the initial and the fly-back position. It should be noted that the error on the interferometric measurement is a combination of errors on the actual interferometer as well as positioning errors of the translation stage. It is also important to note the stage can only be placed to a required position to a maximum accuracy of 50 nm. The stage errors are also present in the counter displacement since the counter is coupled to the stage. In order to remove these errors we take the difference between the repeatability error of the counter and the repeatability error of the interferometer at each data point. Using the result the standard deviation was calculated to be 25 nm. This error is the overall repeatability error and corresponds to around two counts on the 12.5 nm resolution Solartron scale. The resulting error is very low and could possibly be attributed to

problems with the pressure pump. It has been observed that the pressure pump that provides pressurised air to the probe occasionally operates abnormally sending pressure waves that displace the probe by several nanometers. In future a different pressure pump is likely to be used.

7.5 CONCLUSIONS

The Solatron LE12/IP65 linear displacement sensor was calibrated against a plane mirror differential interferometer. The calibration verified the nanometric capability of the probe and the linearity was calculated to be 1.4 ppm. The scaling error of the probe over its full range is expressed as the slope of the calibration curve and was found to be 0.9999861118. An important finding was that the probe is prone to a variable cosine error when a lateral force is applied to the stylus. This effect can cause measurement errors when the probe is measuring large aspheric departures. The main source of error in the probe is a quadrature error which can be corrected by applying the Heydemann correction in the probe data acquisition software.

The work presented in this chapter was undertaken to verify the performance of the probe. If the laser that was used in the probe calibration is calibrated against a higher standard then it will be possible to realise the traceability of the SAP measurement to the realisation of the definition of the metre. The calibration of the laser will be part of future work on the SAP project.

Chapter 8

RESULTS AND EVALUATION

"Door meten tot weten" (To knowledge by measurement)

Heike Kamerlingh Onnes

8.1 INTRODUCTION

The operation and performance of the SAP was verified in a series of experiments, using a spherical $f/9.5$ concave mirror, which was immediately available at NPL. The mirror shape was verified to be spherical to within $\lambda/6$ RMS using a *WYKO*, laser interferometer operating at 632.8 nm. The mirror has a diameter of 640 mm and a RoC of 6098 mm corresponding to a maximum surface slope of 3^0. It is made of Pyrex glass and has a nominally flat back surface. In order to conduct the experiments a temporary mount was used. The mount allows the motion of the probe along the z-axis and has tilt and roll adjustments (figure 8.1).

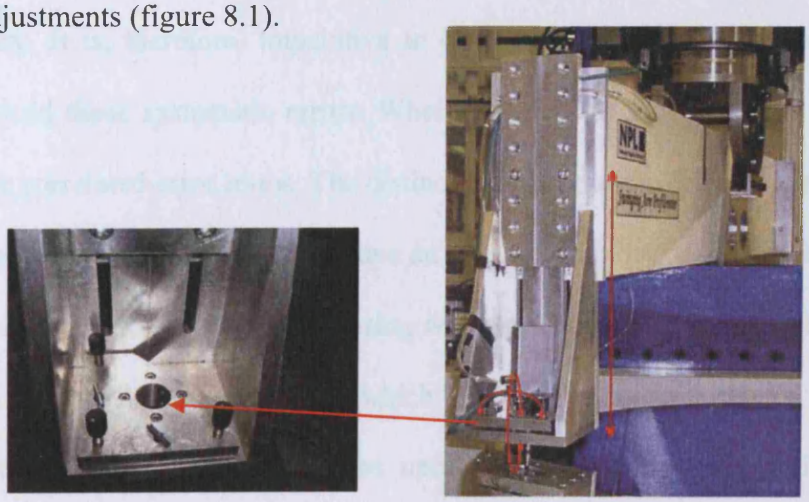

Figure 8.1 Provisional mount for the Solartron probe, designed by Matthew Callender (UCL)

Initially, trial scans revealed that the steel tip of the Solartron probe was damaging the aluminium coating. In order to avoid possible damage of the glass substrate the original steel tip was replaced by one made of polytetrafluoroethylene (PTFE) which was chosen for its low coefficient of friction. The probe tip was custom made at NPL and has a diameter of 1.3 mm. It important to note that using PTFE will result to compression of the tip when the latter is loaded onto the test surface. Nevertheless due to nature of the SAP measurement the tip always meets the SUT at normal incidence. This means that the resulting error from the probe compression will remain the same across the scan. A cosine error might appear as a result of the probe being dragged along the SUT in continuous scans. This should be of low magnitude taking into account the fact that the PTFE probe has low coefficient of friction.

8.2 ALIGNING THE SAP

8.2.1 INTRODUCTION

As was discussed in chapter 4, a SAP measurement can be affected by dynamical and static errors. Static SAP errors are mainly attributed to incorrect alignment and can result in an incorrect reference sphere, negating the principle of swing-arm profilometry. It is, therefore, imperative to establish a rigorous alignment process in order to avoid these systematic errors. When aligning the SAP it is also important to account for correlated error terms. The distinct geometry of the SAP means that in most cases a change in one parameter will have an effect on another parameter. For example, a change in the tilt angle of the PI bearing will also result in a change in the probe tip position along the instrument's x-axis which will have to be compensated for. In order to avoid cross-correlated errors it was necessary to establish a specific alignment sequence which is described in detail in the following sections.

Throughout the alignment of the SAP, reversal techniques were extensively applied. Reversal is an error separation technique where one component is rotated in between measurements such that the sign of the error under investigation is reversed. There are different types of reversal including the Donaldson Ball Reversal (Donaldson 1972) which is used to separate radial errors between a spindle and a round artefact. Donaldson reversal can also be used to provide information regarding alignment between two round artefacts (Hales 1999) and it was used extensively throughout the alignment of the SAP.

8.2.2 CENTERING THE OPTIC

Before a measurement the rotation axis of the SAP arm must be made to intersect with the interpolated centre of curvature of the optic. In practise this implies that the probe tip has to coincide with the optic vertex at the start of the measurement. This alone, however, is not sufficient since in a complete measurement cycle the optic is rotated in between scans. In order to ensure that all scans will pass through the optic vertex, the optic has to be centered with respect to the Horstmann bearing.

In order to centre the optic, it was initially placed, by eye, to be approximately concentric with the Horstmann bearing table. An accurate way to examine residual concentricity errors could be by placing an LVDT in contact with the side of the optic and rotating the Horstmann (figure 8.2). As the bearing rotates any residual eccentricity can be detected directly as a displacement on the LVDT. The chosen test mirror, however, had very large waviness on its side and for this reason the LVDT test was rejected as unreliable.

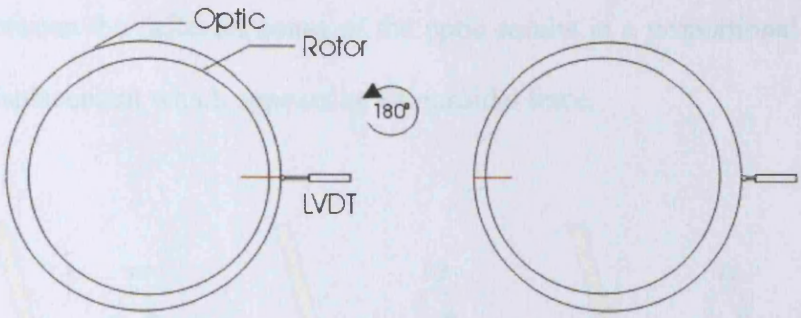

Figure 8.2 Using an LVDT to detect concentricity errors

The method that was finally employed involved the use of the Solartron probe. The arm was swung at an angle of $+20^0$ and the probe was lowered onto the optic. Subsequently the Horstmann was rotated and the displacement of the probe was recorded throughout the rotation of the bearing. The resulting trace after four complete rotations is shown in figure 8.3.

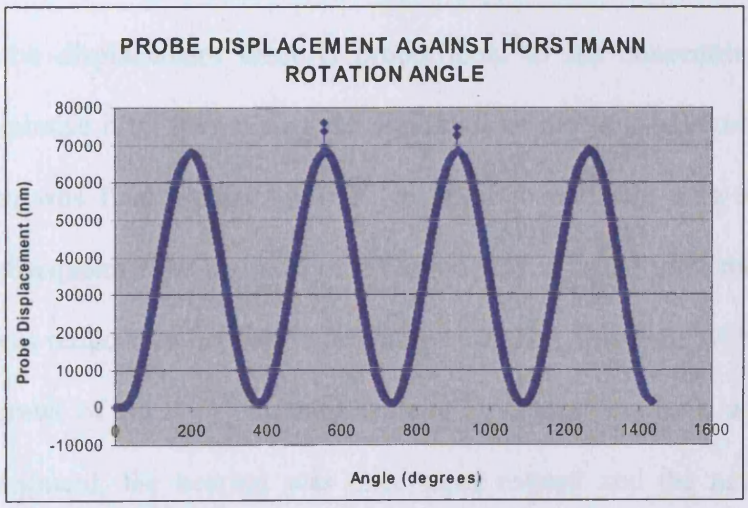

Figure 8.3 Trace of the Solartron probe after four complete rotations of the Horstmann

As shown in figure 8.3, the trace of the probe displacement is a sinusoidal variation with an approximate PV error of 70 μm. The sinusoidal nature of the graph indicates a concentricity error between the axis of the optic and the centroid of the Horstmann rotor. As the bearing rotates the optic follows an elliptical path and as a result the probe tip appears to be moving in and out at different zones of the optic (figure 8.4). The slope

variation between the different zones of the optic results in a proportional variation in the probe displacement which appears as a sinusoidal trace.

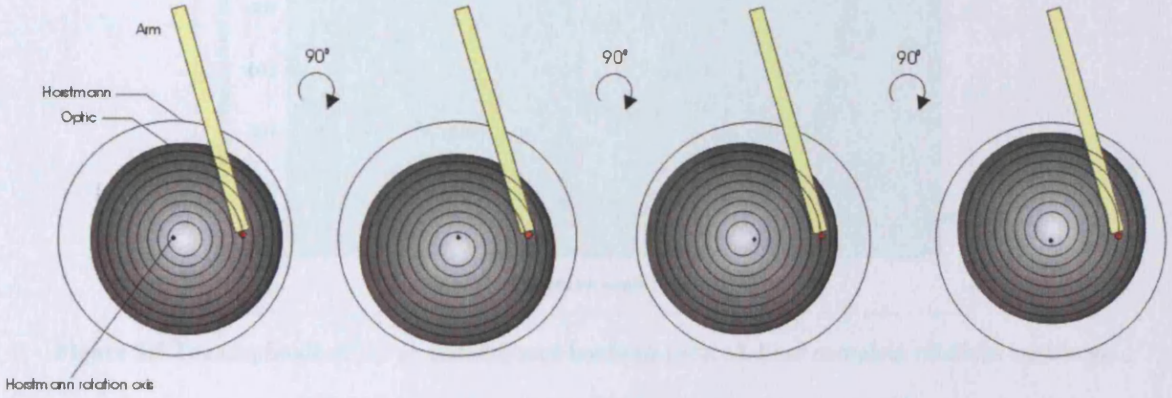

Figure 8 4. A decentering error between the Horstmann and the optic means that the probe tip is moving in and out at different zones of the optic.

Since the probe displacement error is proportional to the concentricity error it is possible to minimise it by minimising the amplitude of the sinusoidal trace. To do this the Horstmann was first rotated by 180^0, in order to coincide with a displacement maximum. Subsequently the position of the optic was adjusted until the amplitude of the sinusoid was reduced to half of its original value. This was done with the aid of the micrometer screws of the *x-y* Horstmann table or by tapping the optic when necessary. After the adjustment, the bearing was once more rotated and the new trace of the Solartron probe displacement is shown in figure 8.5.

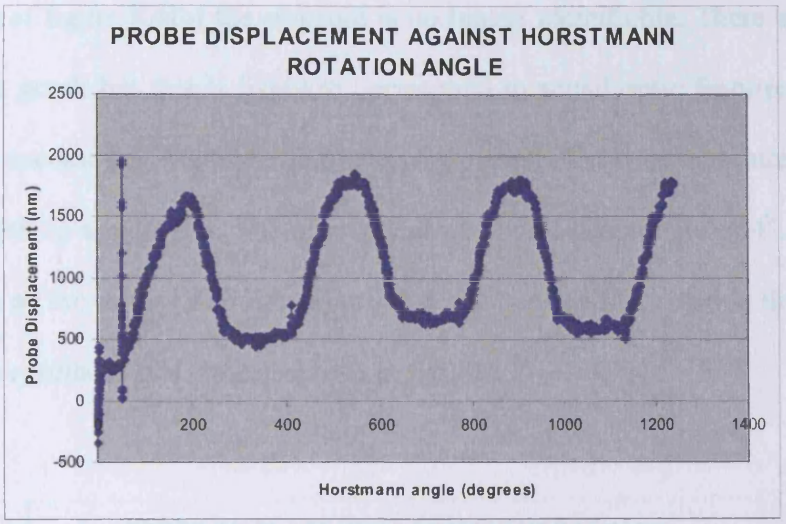

Figure 8.5 The amplitude of the sinusoidal trace has been reduced. Four complete rotations are shown

It is apparent from figure 8.5 that the PV error has been reduced significantly, even though the sinusoidal pattern is still present. The PV error is now approximately 1.25 μm (ignoring the initial drift) and at this scale the effects of noise become apparent. Subsequent adjustments resulted in the traces of figures 8.6(a) and 8.6(b).

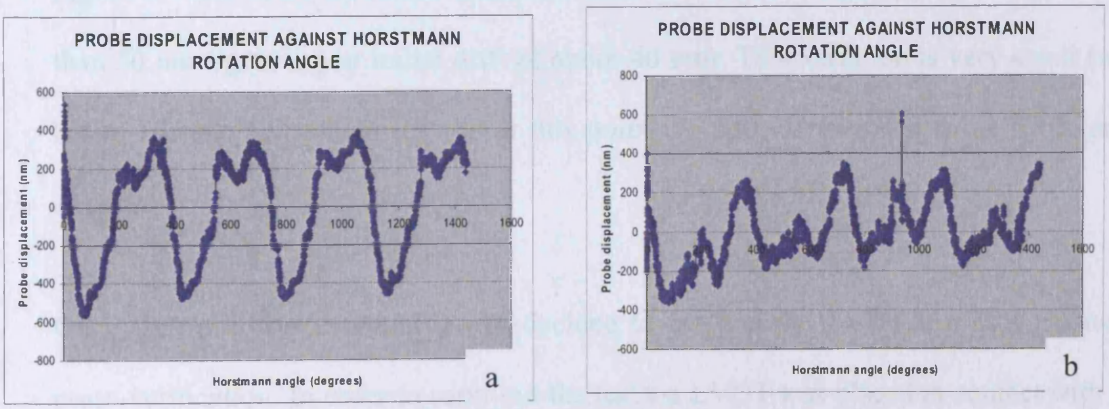

Figure 8.6 Traces from the Solartron probe after subsequent adjustments

In the graph of figure 8.6(b) the sinusoid is no longer identifiable. There are still some peaks on the graph but this is likely to correspond to actual optic features. In order to improve the accuracy of the test, the probe was moved closer to the centre of the optic where the optic is almost flat. The arm was placed at a sweep angle of 4^0, with respect to the centre of the mirror, and the experiment was repeated by rotating the Horstmann bearing. The results of this test are shown in figure 8.7.

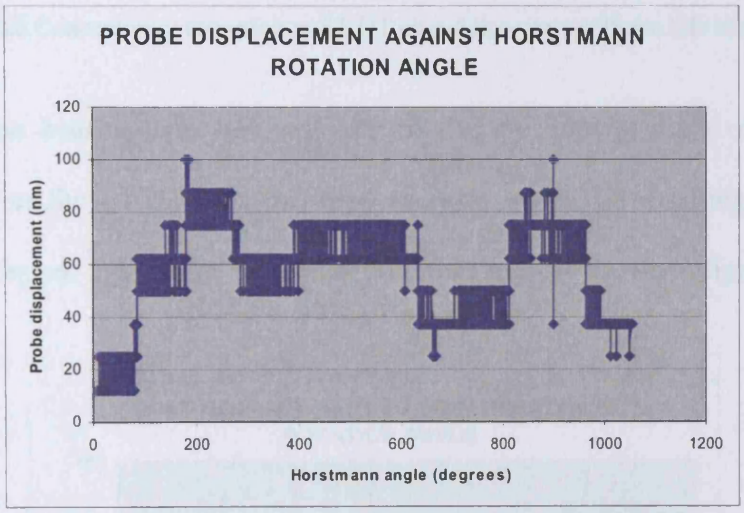

Figure 8.7 Trace from the Solartron probe at a swing angle of 4^0

Figure 8.7 shows a very small sinusoidal variation where the estimated PV error is less than 50 nm (ignoring an initial drift of about 40 nm). This variation is very small (well below the allowed tolerance) and at this point the optic is assumed to be sufficiently centered.

Once the optic was centered it was decided to perform the LVDT test as a means of cross-verification. In order to carry out the test the LVDT was placed in contact with the side of the optic as shown in figure 8.8.

Figure 8.8 Concentricity test using an LVDT placed in contact with the side of the optic

The Horstmann bearing was consequently rotated by 360° at steps of 10° and the displacement on the LVDT was recorded at every step. The resulting graph of the LVDT displacement against the Horstmann rotation angle is shown in figure 8.9.

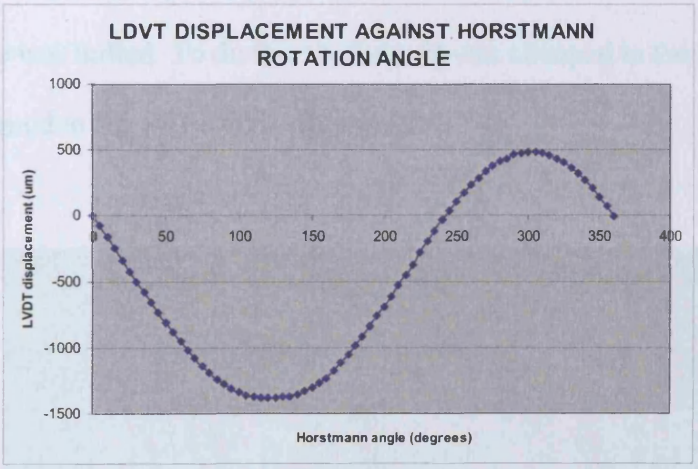

Figure 8.9 A graph of the LVDT displacement against Horstmann rotation angle

As shown in figure 8.9, the resulting trace is an asymmetric sinusoidal curve. The observed variation in the amplitude denotes an effective ovality which cannot be justified as a decentering error since the maximum departure is two orders of magnitude larger that error measured using the Solartron probe. The conclusion from this test is that the actual glass substrate has an oval shape instead of the nominal circular shape.

8.2.3 NULLING THE SAP

8.2.3.1 LEVELLING THE SAP AXES

The next step in the alignment process involved nulling the SAP axes. This can be done either by using a calibrated flat or spherical artefact, or by using a traceable external reference. Since suitable calibrated artefacts were not readily available at the time of the test, it was decided to use an external reference. An electronic level (Talyvel) was used to level the axes of the SAP with respect to the direction of gravity. The Talyvel employs a pendulum and electronic amplification to give angular resolution of 1 arc second.

To null the SAP it was necessary to null the tilt and the roll of both the optical axis and the PI bearing axis. Nulling the tilt of the optic was difficult to do in practise because there was no independent tilt adjustment for this purpose. Instead, the tilt of the Horstmann table was nulled. To do this the Talyvel was clamped to the edge of the table with its axis aligned to the SAP *x*-axis (figure 8.10).

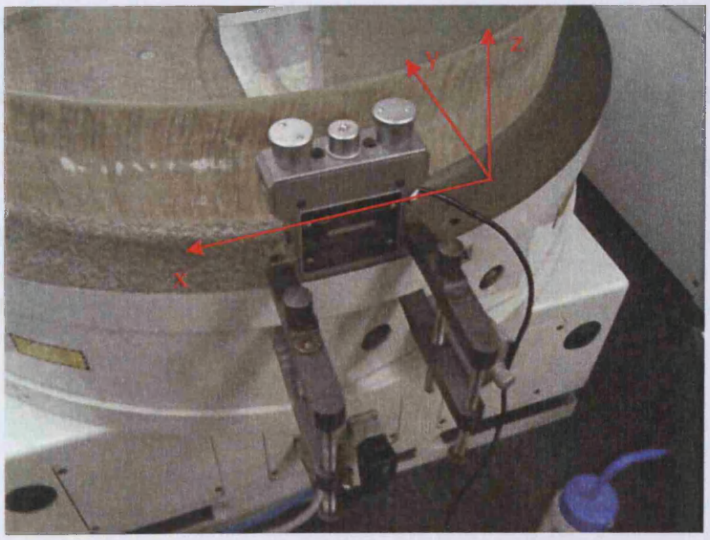

Figure 8.10 The Talyvel is clamped onto the side of the *x-y* bearing table

In order to correct the residual tilt of the table, reversal was applied by rotating the table by 180^0 degrees. As the table rotates the Talyvel also rotates by the same angle and the difference between the reading at 0^0 and the one at 180^0 provides the value of the residual tilt.

The reversal showed 6 arc seconds of residual tilt which was corrected to within 1 arc second. Since the Horstmann bearing does not have independent angular adjustments the correction can be performed by tilting the whole SAP granitan base. The roll of the bearing was adjusted in the same way to within 1 arc sec. In this case reversal was applied between 90^0 and -90^0.

The next alignment step involved levelling the rotation axis of the arm. This is done by levelling the PI bearing which defines the arm rotation axis. In order to null the tilt of the PI the Talyvel was placed on top of one of the arm clamps with its axis coincident with the *x*-axis of the SAP. Then reversal was applied by rotating the Talyvel by 180^0 and in this way the tilt of the PI bearing was corrected to within 1.5 arc second. The tilt was corrected by sliding the bearing along the grooves situated on the side plates of the SAP support frame. Fine tuning was achieved using the tangent arm. Subsequently the roll of the bearing was nulled. The PI bearing does not have roll adjustment and the residual roll error was corrected by adjusting the angle of the whole SAP frame using the large tilt-roll stage onto which the SAP frame is mounted (figure 6.18).

8.2.3.2 PROBE AND ARM ADJSUSTMENTS

Prior to any measurement the arm has to be balanced at its pivot point. Balancing the arm is not critical for the SAP operation but it helps reduce unnecessary stresses due to

unbalanced forces and ensures smooth operation of the PI servo motor. The arm beam can be balanced using the counterweights at the back of the beam and it can be set at equilibrium horizontally or at an angle. For the current experiments the arm beam was balanced at a horizontal position. The tilt of the beam was monitored with a lightweight plastic bubble level placed on top of the arm beam. Fine tuning was achieved using the movable counterweight at the back of the arm. When the arm was sufficiently balanced to within 3 arc seconds to 5 arc seconds the arm cradle was clamped onto the trunnion.

The final step involved levelling the probe. This was done using a small bi-directional bubble level which was placed on top of the probe enclosure. The tilt and roll residuals were removed with the aid of the tilt/roll platform which is located on the probe mount.

8.2.4 PREPARING THE SAP FOR MEASUREMENTS

8.2.4.1 ESTIMATING THE NECESSARY TILT ANGLE

In order to set up the SAP to measure an optic it is necessary to have knowledge of the RoC, R, of the optic as well as of the effective arm length, l. If these two quantities are known then the necessary tilt angle can be calculated from the SAP condition using $\theta = \sin^{-1}(l/R)$. The main problem with calculating the required tilt angle is that the effective arm length is an unknown variable which attains different values for different tilt angles. Nevertheless when the arm rotation axis is at its null position of zero tilt, the effective arm length coincides with the mechanical arm length[6]. In this case it is easier to calculate the necessary tilt angle using the equation

[6] The mechanical arm length is defined as the arm beam section overhanging from the pivot and overlooking the optic.

$$\theta = \tan^{-1}\frac{L}{R+H} \tag{8.1}$$

which relates the tilt angle to the mechanical arm length, L and the separation, H between the probe tip and the SUT. The value of L can be found by directly measuring the separation between the probe tip and the arm pivot (figure 8.11).

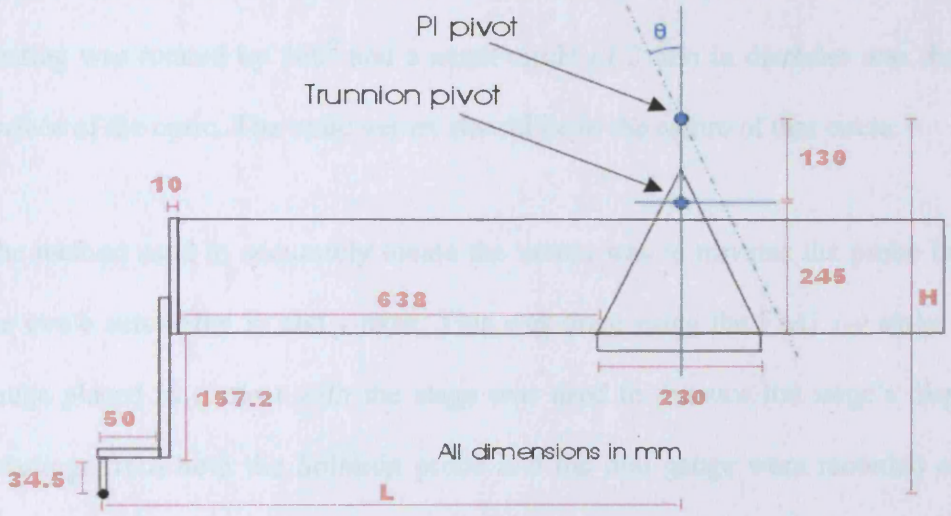

Figure 8.11 Measuring the mechanical arm length of the SAP at zero tilt

With the arm beam, the PI bearing and the probe set to zero tilt the mechanical arm length was found to be approximately 823 mm which when substituted to equation (8.1) results into a tilt angle of 7.0396^0. The tilt of the PI bearing was set to this angle. This was done with the aid of a sine bar which was set to 7.0396^0 using a stack of 10.0 mm, 1.5 mm, 2.06 mm and 2.004 mm gauge blocks. The sine bar was then placed on top of one of the pivot clamps and a bubble level was placed on top of the sine bar. Subsequently the PI bearing was tilted until the bubble level was balanced. Using this simple technique the tilt of the sine bar is transferred to the PI bearing.

8.2.4.2 LOCATING THE VERTEX OF THE MIRROR

Before performing measurement on the $f/9.5$ optic it was necessary to position the probe tip at the optic vertex. Some optics are supplied with a small dimple ground onto the vertex but the $f/9.5$ mirror did not have a central dimple and a series of steps had to be taken to locate its vertex. First a ruler was used to approximately establish the centre of the optical surface. Then the arm was brought close to the centre of the mirror and a non-permanent felt pen was attached at the side of the probe mount. The Horstmann bearing was rotated by 360^0 and a small circle of 2 mm in diameter was drawn at the surface of the optic. The optic vertex should lie in the centre of that circle.

The method used to accurately locate the vertex was to traverse the probe in an out of the circle across the x- and y-axes. This was done using the FAG x-y stage and a dial gauge placed in contact with the stage was used to monitor the stage's displacement. Readings from both the Solatron probe and the dial gauge were recorded and plotted against each other for both the x- and y- axes (figure 8.12). The resulting graphs correspond to the shape of the optic at the vicinity of the vertex The latter should lie at positions of zero slope which coincide with the graph minima. In order to exactly determine the positions of zero slope second order polynomials were fitted to the data and were in turn differentiated. The values for which the first derivatives are zero yield the coordinates of the vertex with respect to the null position of the dial gauge.

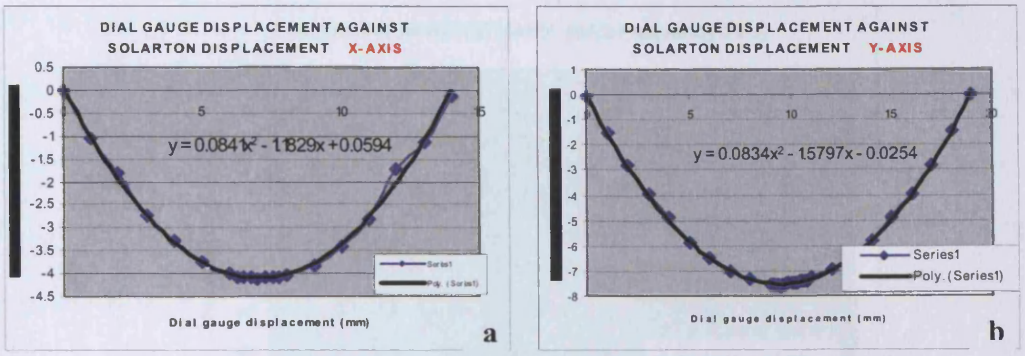

Figure 8.12 Second order polynomials are fitted in the data in order to help locate the positions of zero slope

Following the method described, the coordinates of the vertex were found to be x = 7.032699 mm and y = 9.470623 mm. The FAG x-y stage was consequently moved to the calculated positions hence locating the probe tip directly at the vertex to within 100 nm (which is the resolution of the FAG x-y stage).

8.3 STATIC NOISE MEASUREMENTS

The static noise levels of the SAP were assessed in a number of experiments. It was anticipated that most of the static noise would be the result of the air flow in the various SAP bearings. Since all the SAP bearings operate through separate supply lines it was possible to measure independently the noise contribution from the SAP x-y stage, the PI bearing and the Horstmann bearing. The results of the static noise measurements are shown in figures 8.13, 8.14 and 8.15.

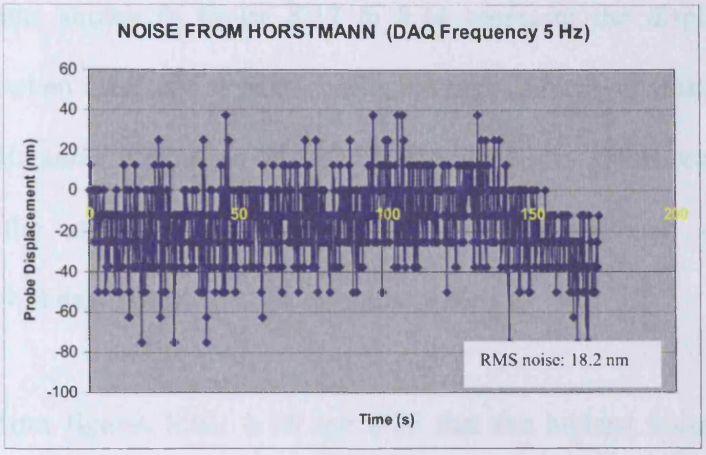

Figure 8.13 Noise generated by the Horstmann bearing

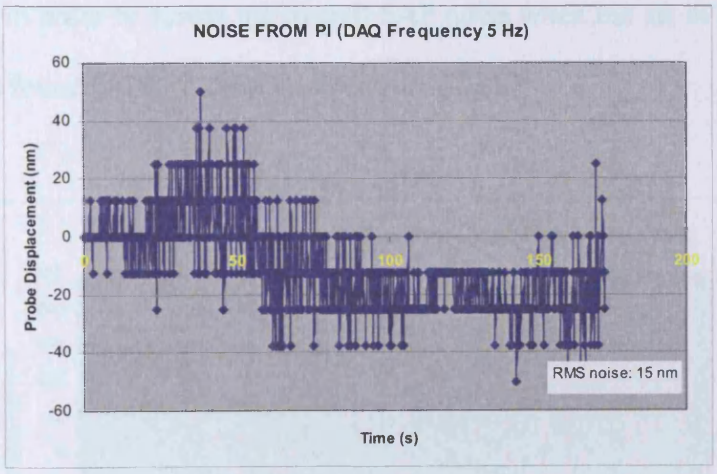

Figure 8.14 Noise generated by the PI bearing

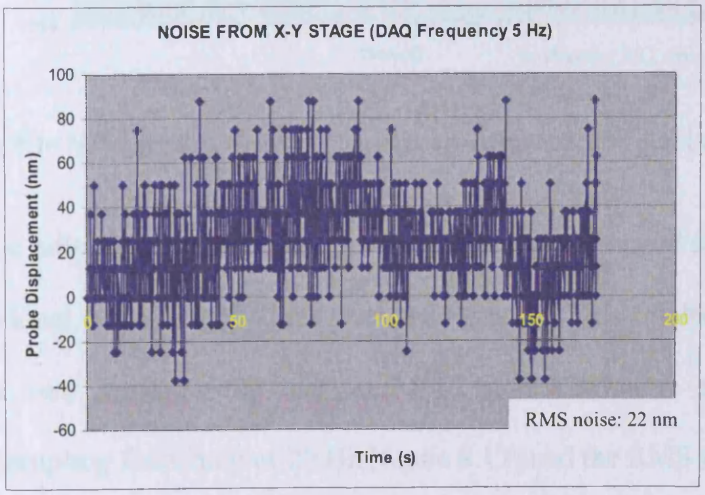

Figure 8.15 Noise generated by the x-y stage

The measurements shown in figure 8.12 to 8.14 represent the displacement of the Solartron probe when the probe is contact with the optic. They were taken at a sampling frequency of 5 Hz and the duration of each measurement was 3 minutes. The noise was calculated as the standard deviation of all the displacement values acquired (approximately 900 data points) for the duration of the test.

It is apparent from figures 8.13, 8.14 and 8.15 that the highest noise levels (22 nm RMS) originate from the FAG *x-y* stage. The Horstmann bearing produces 18.2 nm (RMS) of static noise and the PI bearing produces an RMS value of 15 nm. Another test was performed in order to assess the overall SAP noise when the air in all the bearings is on and it was found to be 37.2 nm RMS (figure 8.16).

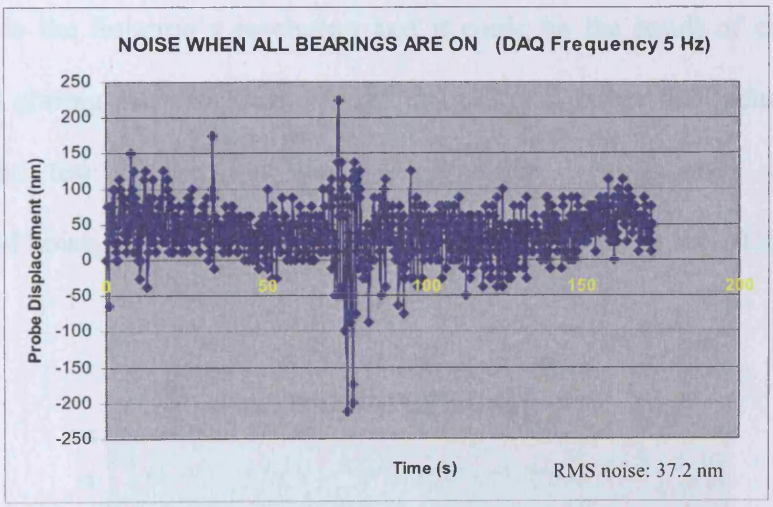

Figure 8.16 Noise generated when all bearings are on (sampling frequency 5 Hz)

The overall static noise when all bearing are on can be also calculated as the quadrature sum of the individual noise contributions from each bearing. This results to 32 nm RMS noise which is very close to the measured 37.2 nm. The same experiment was performed at a sampling frequency of 20 Hz (figure 8.17) and the RMS noise was found to be 37 nm (measurement duration 3 minutes).

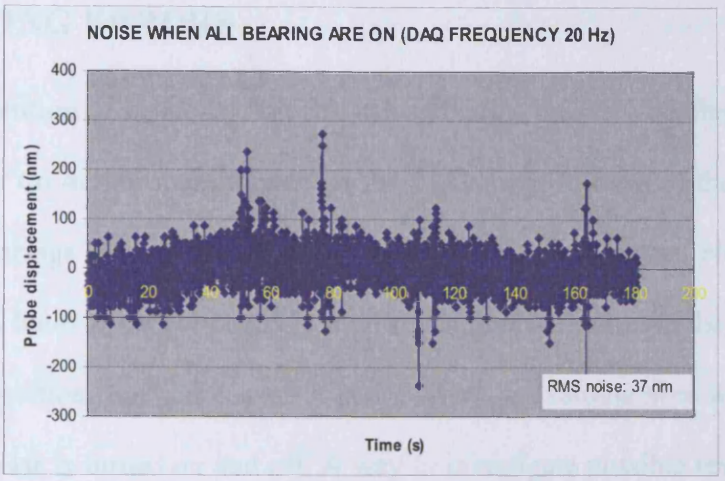

Figure 8.17 Noise when all bearings are on (sampling frequency 20 Hz)

The final test involved turning off the air in all bearings in order to measure the ambient noise. The results of this measurement are shown in figure 8.18. It is apparent from figure 8.18 that the ambient noise is very low with a PV value of 12.5 nm. This corresponds to the Solatron's resolution and it could be the result of stylus slippage between two grating lines or even a small thermal drift rather than actual noise. The results of the test suggest that the SAP structure is sufficiently isolated from environmental noise since the ambient noise levels are well below the 20 nm threshold.

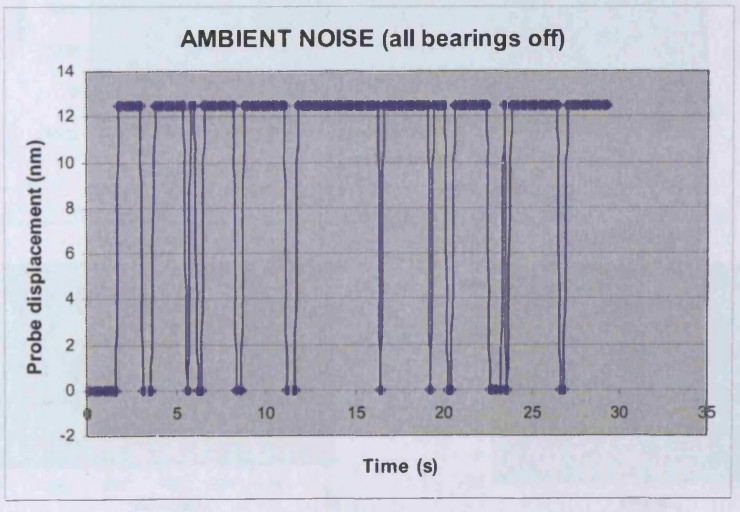

Figure 8.18 Ambient noise (all bearings off)

8.4 RESSETING ERRORS

During the execution of bespoke, "bicycle-wheel" scans the only bearing that needs to be continuously on during measurement is the PI bearing. In most of the cases the rest of the SAP bearings can be turned off to reduce the overall noise. Nevertheless the Horstmann will have to be switched on amid scans in order to rotate the optic to a new measurement position. For this reason it is necessary to examine how well the bearing resets when the air is turned on and off. A way to investigate possible resetting errors is to turn the air supply to the Horstmann bearing on and off and record the resulting displacement on the Solatron probe when the probe contacts the optic. The results of such a test are shown in figure 8.19 where a graph of the probe displacement against time for five consecutive resetting tests is recorded. At the start of the test the air to the Horstmann was off and the Solartron probe was nulled.

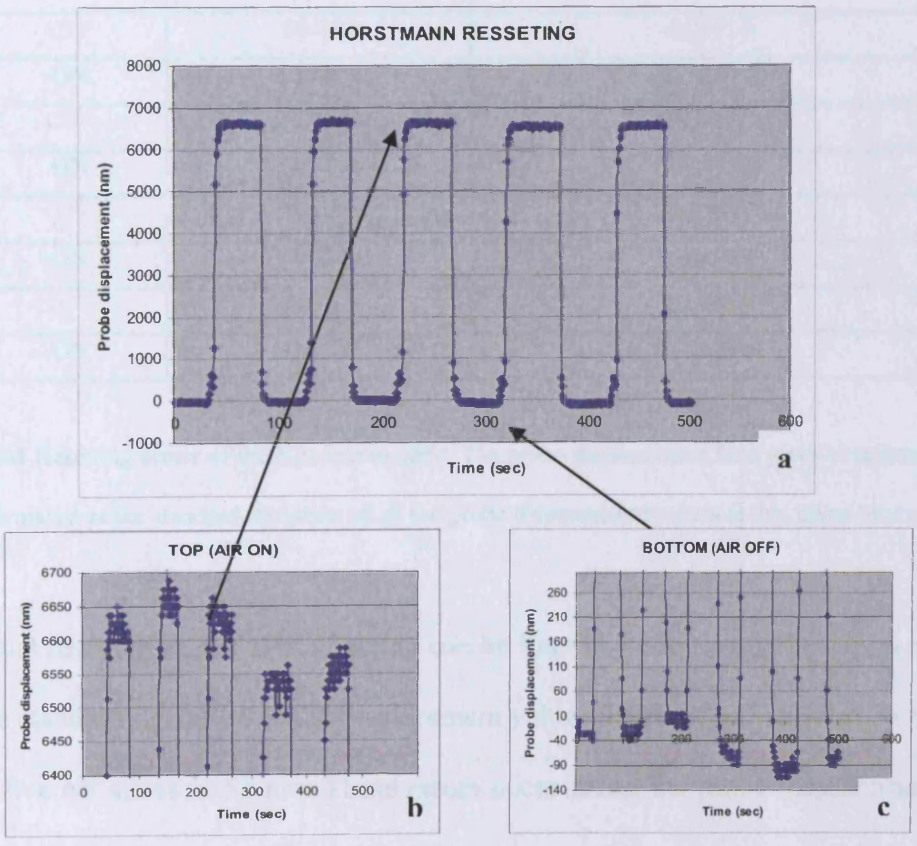

Figure 8.19 Probe displacement when the air on the Horstmann bearing is switched on and off. The inset graphs (b) and (c) represent magnified regions of graph (a)

From figure 8.19(a) it is understood that the air gap between the rotor and the stator of the Horstmann bearing is approximately 6.6 μm. Figures 8.19(b) and 8.19(c) are magnified regions of graph 8.19(a) and show clearly the resetting errors for the on state (8.19(b)) and the off state (8.19(c)). The probe remains at each state for several seconds and as is shown in the inset graphs, during this time, there is significant variation in the probe displacement. The standard deviations of the probe displacement for each state, and for each different time interval are shown in table 8.1.

When switching from one state to the other some relaxation time is required. The displacement data referring to this time are disregarded from the calculation in order to improve accuracy.

STATE	INTERVAL (s)	PROBE DISPLACEMENT (nm)
OFF	0-25	-23.557
ON	43-75	6613.672
OFF	80-117	-21.0714
ON	130-162	6657.407
OFF	168-204	2.027
ON	215-259	6624.653
OFF	264-305	-58.631
ON	315-364	6534.239
OFF	368-414	-91.4894
ON	428-467	6554.063

Table 8.1 Resetting errors of the Horstmann table. The probe displacement for a given time interval is calculated as the standard deviation of all the probe displacement values at that given interval

The actual resetting errors of the bearing can be found by comparing the values in table 8.1. The standard deviation of the displacement values the five "on" states is 36 nm and for the five off states is 51 nm. These errors occur along the probe measurement axis

and hence they are regarded as form errors. It is also important to note these errors are not repeatable.

The experiment, the results of which are shown in figure 8.19(a) was performed with the probe placed at the vertex of the optic which coincides with the Horstmann bearing centroid. This means that the experiment was mainly useful for investigating linear errors in the *z*-axis. Nevertheless it is likely that the error of the bearing is a combination of linear and rotational motion as shown in figure 8.20.

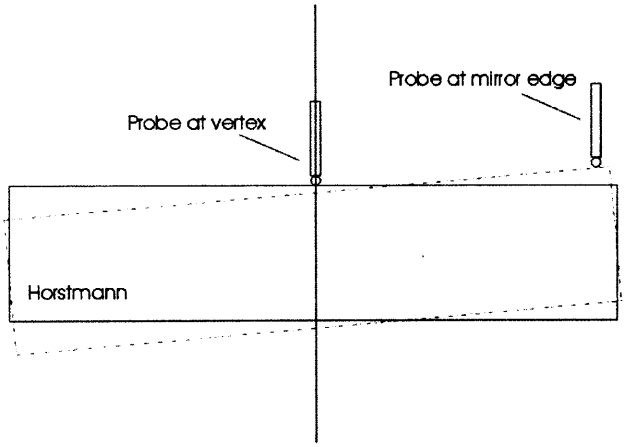

Figure 8.20 The probe needs to be placed at the edge of the optic in order to detect possible angular errors of the Horstmann bearing

In order to investigate possible angular errors of the bearing another experiment was performed where the Solartron probe was in contact with the outer edges of the optic. Two tests were carried out with the probe placed at sweep angles of $+20^0$ and -20^0. The results of the tests for both cases are shown in figure 8.21. The blue curve represents the probe displacement at $+20^0$ and the purple curve represents the displacement recorded at -20^0.

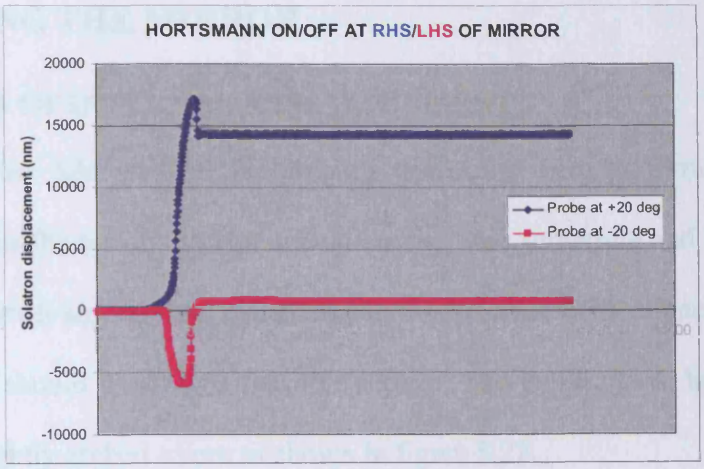

Figure 8.21 Graph of the Solartron displacement when the air is turned on. The blue curve shows the displacement a sweep angle of $+20^0$ and the purple shows the displacement at -20^0

In both cases the tests start with the air turned off and the probe nulled. When the air is turned on, the blue curve exhibits a peak and the purple curve shows a trough. Both curves eventually settle approximately 13 μm apart. The experimental result suggests that when the air on the bearing is switched on the right-hand side (RHS) of the bearing overshoots while the left-hand side (LHS) of the bearing is being compressed. This behaviour could be explained if there was an offset load on the Horstmann table. As the bearing is switched on, the sudden flow of compressed air forces the lighter RHS upwards and as a result the bearing rotor is tilted on one side forcing the LHS downwards. The overall behaviour exhibits poor bearing stiffness and the resulting bearing motion is manifested as an effective roll error in the measured data. This error can be corrected by re-aligning the bearing before conducting a measurement. Nevertheless the low bearing stiffness is also likely to generate random roll errors that are difficult to correct. As a conclusion it is suggested that the Horstmann bearing should be replaced by one with higher stiffness. For the time being the Horstmann was retained in order to complete the initial experimentation.

8.5 SCANNING THE MIRROR

8.5.1 EFFECTS OF INTERNAL MISSALIGNMENTS

After aligning the SAP several preliminary test scans were performed. In order to execute the scans the air on the Horstmann bearing was turned on and the bearing was re-aligned to correct any residual roll errors. In theory, a perfectly aligned SAP scanning a perfect optic, should result to a flat, linear trace. The initial scans, however, showed inclined and slightly arched traces as shown in figure 8.22.

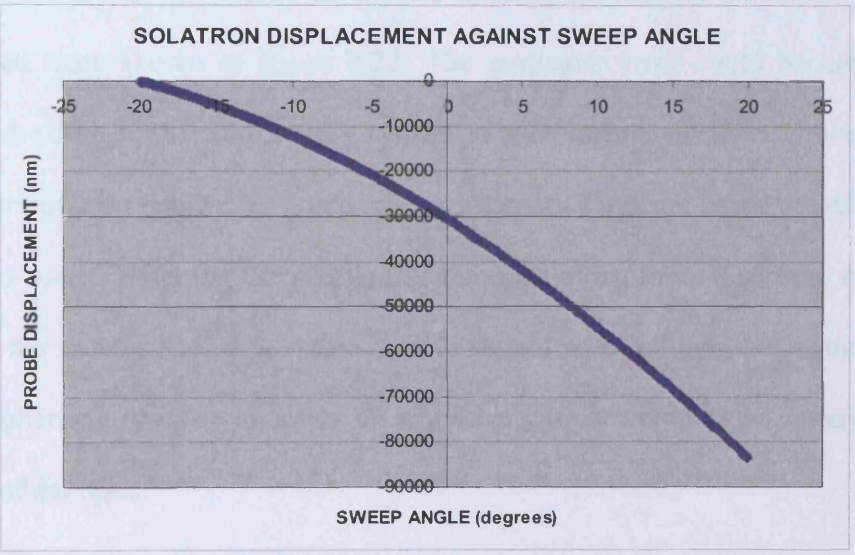

Figure 8.22 Initial scan showing the displacement of the Solartron probe against the arm sweep angle

The scan shown in figure 8.22 was performed by sweeping the arm between -20^0 and $+20^0$ starting from the LHS of the mirror (-20^0). The null position for the sweep was set to zero to coincide with the mirror vertex. The inclination on the graph in figure 8.22 indicates that the RHS of the optic is lower than the LHS by 80 μm and as mentioned in section 8.4 this height difference indicates a roll error.

Since both the Horstmann and the PI bearings were aligned to the direction of gravity to within 1 arc second to 2 arc seconds, the large roll error could not be justified as a SAP misalignment error. It could not be justified as an error in the optical surface since, according to the interferometric results, the RMS surface deviation from the nominal sphere is no more than 105 nm and the maximum PV deviation between any two parts of the mirror is no more than 720 nm. The resulting roll error, however, could be explained if there was an internal misalignment between the mirror and the top of the Horstmann table. If the mirror is slightly rolled towards the RHS of the bearing table then the probe stylus will extend as it scans towards the RHS of the mirror leading to the inclined trace shown in figure 8.22. The particular error could be corrected by adjusting the roll of the mirror with respect to the Horstmann table. However, since there is currently no facility for doing this, an alternative method based on offsetting the mirror was used. Offsetting the position of the optic along the *x*-direction, effectively, levels out the scan as shown in figure 8.23. It should be noted that this method is valid only for spherical, symmetric optics. In any other case it would be necessary to adjust the angle of the optic.

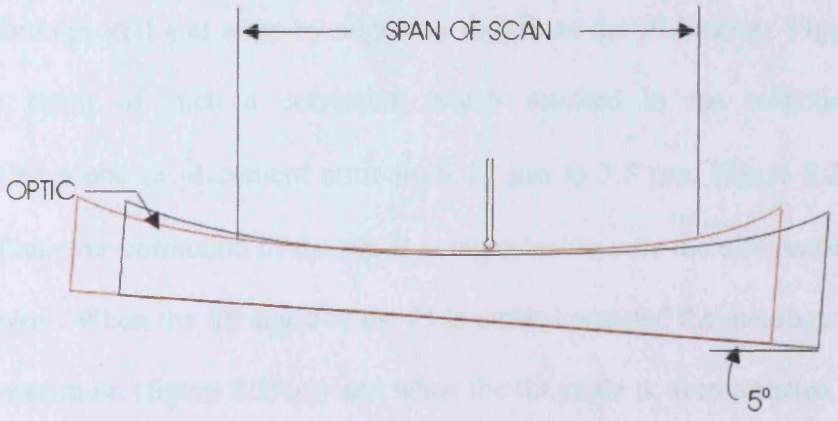

Figure 8.23 Internal roll errors between the mirror and the bearing table can be corrected by offsetting the optic across the *x*-axis. As a result the scan is levelled. The figure shows an optic tilted by 5^0 and the ghost image (red) shows the optic displaced towards the left

In order to correct the roll error the optic was moved until the reading on the probe, at the RHS of the mirror was -40 μm. The mirror was then re-scanned and the resulting trace (figure 8.23(a)) shows that the effective roll error has been significantly reduced. The curvature of the trace denotes a tilt error which is a result of mismatch between the reference sphere and the curvature of the actual optic. Further adjustment of the roll resulted in the levelled scan of figure 8.24(b) where the prominent error is tilt.

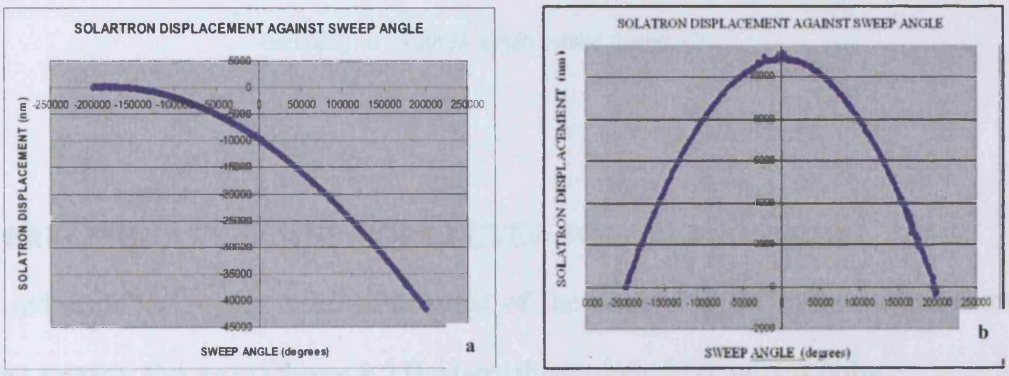

Figure 8.24 Subsequent adjustments result to a levelled trace where the roll error is corrected (a). As the roll error is corrected the tilt error becomes apparent (b)

The residual tilt error is once more the result of internal misalignments. This can be corrected through trial and error by adjusting the tilt of the PI bearing. Figure 8.25(a) shows the result of such a correction which resulted in the reduction of the corresponding probe displacement error from 11 μm to 3.5 μm. Figure 8.25(b) is an example of an over-correction of the tilt. It is important to note the differences between the two figures. When the tilt angle of the PI is under-corrected the measurement curve exhibits a maximum (figure 8.25(a)) and when the tilt angle is overcorrected it exhibits a minimum (figure 8.25(b)). This can be used as guide to the correction of the tilt angle.

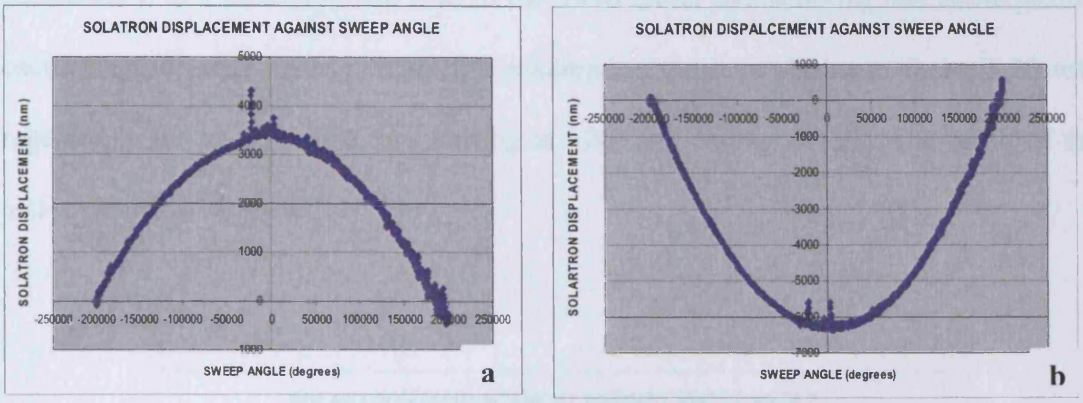

Figure 8.25 When the tilt is over corrected the curve exhibits a positive peak (a) and when is it over corrected it exhibits a minimised trough (b)

8.5.2 PRELIMINARY SCANS CORRECTED FOR TILT AND ROLL

Trial and error led to the removal of most of the remaining tilt and subsequent tests showed a nearly flat trace (figure 8.25) where the prominent error was noise.

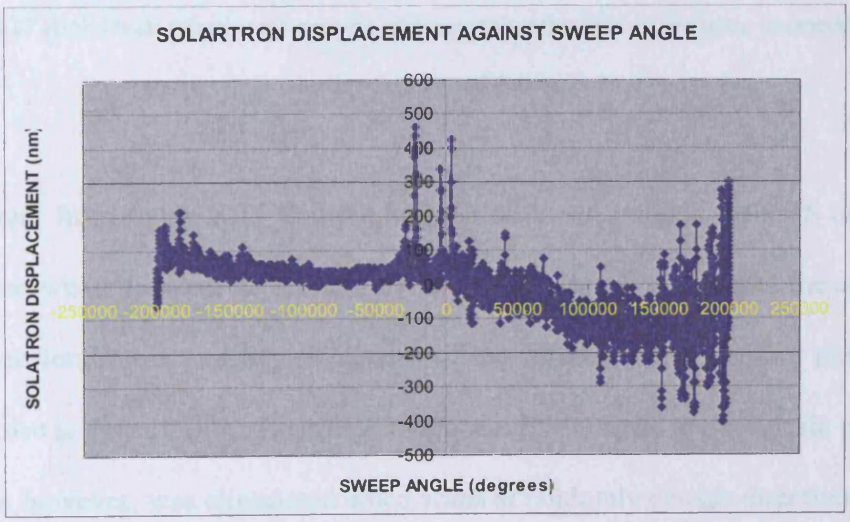

Figure 8.26 Plot of arcuate scan between -20^0 and 20^0 with both tilt and roll error minimised

Figure 8.26 shows that the noise increases towards the RHS of the mirror. The increase in the noise was initially thought to be a result of servo motor oscillation, the arm acquires significant momentum towards the end of the scan and the attempt to

decelerate it to a stand-still can lead to the servo motor overshooting and consequently oscillating. In order to investigate this assumption the scan shown in figure 8.26 was repeated in the reverse direction starting at $+20^0$ and ending at -20^0. The result of the test is shown in figure 8.27.

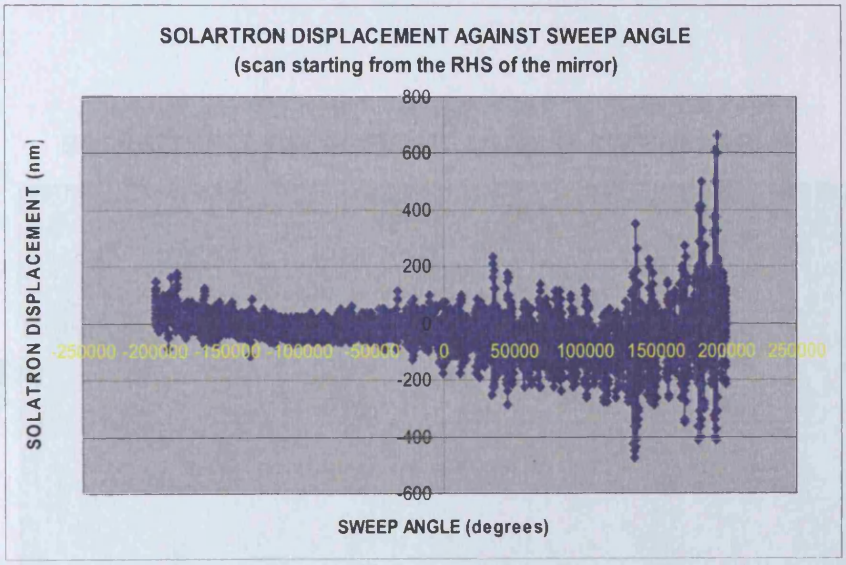

Figure 8.27 High levels of noise are present when scanning the RHS of the optic irrespective of the starting position of the scan

It is apparent from figure 8.26 that the high noise levels towards the RHS of the optic remain even when the scan direction is reversed. This result invalidates the assumption that the deceleration is causing oscillation of the servo motor. Another possibility is that the noise is a result of high surface roughness of the optic at the certain point. This possibility, however, was eliminated when scans at randomly chosen directions revealed similar behaviour. The conclusion from the experiments is that a slight asymmetry on the structure of the SAP frame, is likely to be exciting vibration on the arm as the latter moves in the vicinity of positive sweep angles.

8.5.3 COMPARISON WITH INTERFEROMETRIC MEASUREMENT

Subsequent adjustments and fine tuning of the SAP resulted in the graph of figure 8.28. The figure reveals a certain shape (shown best by superimposing a sixth order least squares polynomial fit onto the graph) which at this level of accuracy, can only correspond to the actual topography of the mirror. In figure 8.28 the maximum PV deviation is approximately 80 nm.

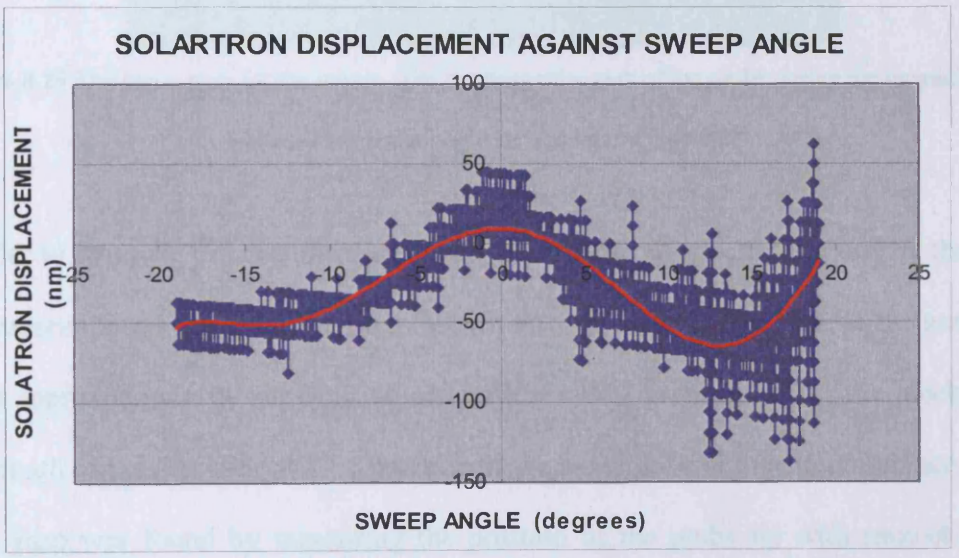

Figure 8.28 Graph of Solartron displacement against sweep angle after the SAP was re-aligned to correct residual tilt and roll errors. The red curve is a six order polynomial fit

In order to investigate the validity of the test the SAP measurement was compared to the measurement obtained by the WYKO interferometer. The phase map of figure 8.29 shows the interferometric measurement where it is obvious the mirror has a small astigmatic variation.

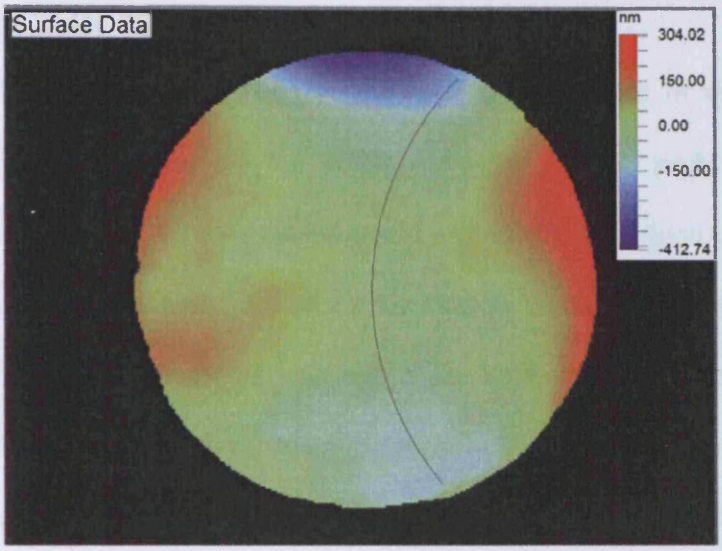

Figure 8.29 The phase map for the mirror. The arc shows the path of the probe during the measurement whose displacement data are shown in figure 8.28

In order to compare the two measurements, the arcuate scan path followed by the SAP was superimposed on the phase map (shown as a black arc). The path of the scan was found approximately by drawing an arc with a radius proportional to the mechanical arm length of the actual SAP. The position of the arc relative to the circumference of the phase map was found by measuring the position of the probe tip with respect to the circumference of the actual mirror.

The results from the SAP test replicate the features observed in the interferometric scan. As shown in figure 8.28, at the start of the scan the probe resides in one of the mirror troughs at approximately -50 nm. Consequently the probe traverses the central section of the mirror where it is progressively compressed and decompressed again. Towards the end of the scan the probe meets the edge of the second trough. A similar trend is observed in the trace of figure 8.28.

8.5.4 ACCURACY OF THE SAP MEASUREMENT

If the SAP was perfect, the deviation of the optic from the best fit sphere would be assessed by directly calculating the RMS deviation of the probe displacement. Nevertheless in reality, such a calculation would provide the combined error of the SAP plus the departure of the mirror from its nominal shape. In order to distinguish between the two types of error it is necessary to extract the SAP errors from the measurement data. Ideally this could be done by scanning a calibrated artefact, such as a large 1 m flat, since in that case any measurement errors would be attributed to the SAP. At the time when the current experiments were conducted there was no access to an appropriate calibrated artefact and it was attempted to approximate the SAP error by analysing the measurement data.

Throughout the measurements it was observed that the SAP can only exhibit errors that correspond to polynomials of even order. Hence subtracting a fourth order polynomial from the measured data should provide an approximation for the actual form error of the mirror. Doing this the RMS deviation of the mirror shape was found to be 13.7 nm. This represents the average deviation of the mirror profile from its nominal profile along the chosen scan path. The SAP error can then be found by subtracting 13.7 nm from the overall combined RMS error (26.8 nm). Subtraction in quadrature yields a SAP error of approximately 23 nm. It important to note that this method is only a crude approximation since errors corresponding to fourth order polynomials might be present on the actual optic. This approximation was only attempted due to the lack of a calibrated artefact that could be used to provide the real error of the SAP. 3

8.5.5 REPEATABILITY OF THE SAP MEASUREMENT

In order to assess the repeatability of the SAP measurement, ten scans were performed across the same scan path and under the same conditions. The ten traces are shown superimposed in figure 8.30. A ten point moving average fit was applied to the graph as a way to remove some of the noise. In order to calculate the repeatability of the measurement the RMS deviation of each scan from the best fit sphere was first calculated. Then the standard deviation of the ten calculated RMS values was estimated and found to be 3.5 nm. The calculated value represents the repeatability of the SAP measurement.

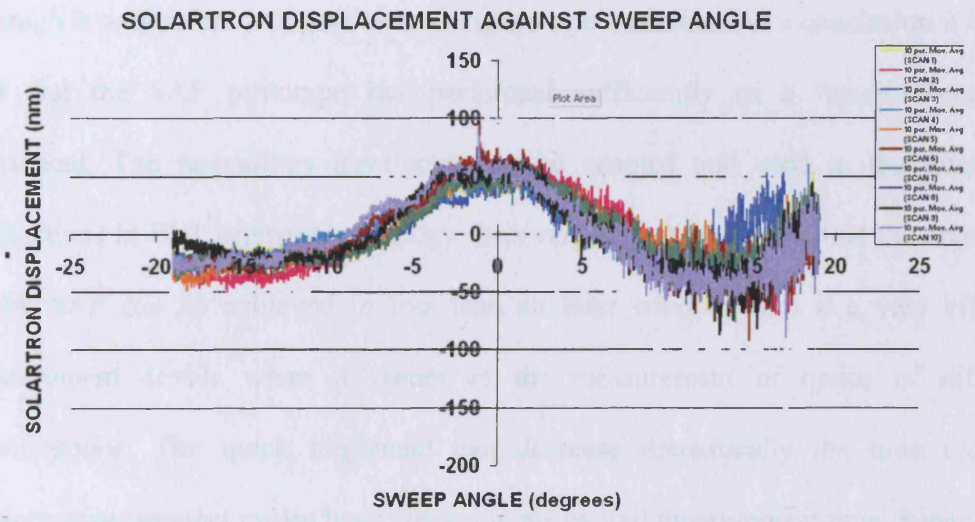

Figure 8.30 Ten repeat scans along the same scan path. A ten point moving average filter has been applied to the data

The repeatability of the SAP appears to be very good, however, it is important to note that the calculated value of 3.5 nm is only for scans along a single line profile. The repeatability for surface form measurement is expected to be significantly worse. Taking into account the poor performance of the Horstmann bearing a repeatability test

across different scan directions was postponed since it would not reflect the true SAP repeatability.

8.6 CONCLUSIONS

The operation of the SAP was verified through the measurement of the $f/9.5$ concave mirror. The alignment procedure followed is based on nulling the SAP axes with respect to the direction of gravity and consequently adjusting the tilt of the arm axis. Internal misalignments were corrected by trial and error. The accuracy of the SAP measurement was found to be 23 nm RMS, which is very close to specifications and confirms the advantage of using a single rotary motion axis as a way of reducing the overall instrument error. The estimated repeatability of the measurement is also very good although it only refers to repeat tests along a single scan line. As a conclusion it can be said that the SAP prototype has performed sufficiently as a "proof-of-concept" instrument. The technology developed can be adapted and used in the future for applications in ELT segment metrology. It is very important to note that the alignment of the SAP can be achieved in less than an hour which makes it a very efficient measurement device when it comes to the measurement of optics of different specifications. The quick alignment can decrease dramatically the time required between measurement cycles hence reducing the overall measurement time. Suggestions for future work, as well as the conclusions from the current work, are discussed in the following chapter.

Chapter 9

CONCLUSIONS

"This is not the end. It is not even the beginning of the end. But it is, perhaps, the end of the beginning."

Winston Churchill

9.1 SUMMARY

The work presented in this thesis contributed towards the design, construction and testing of a novel swing-arm profilometer (SAP) with the ability of carrying a hybrid, opto-mechanical probing system. The SAP is a profilometer capable of measuring the profile of a variety of optical surfaces including spherics, aspherics, convex and concaves. It can be used equally well for the measurement of steep surface slopes as well as for flat surfaces and it can be easily adapted to measure a range of optic diameters and radii of curvature. The potential of combining a contact displacement sensor with an optical wavefront sensor can result in a novel type of instrument that can measure both fast and accurately enough to provide the necessary metrology for mass production of ELT segments. Furthermore the quick alignment times can result to increased volume production since the overall measurement time is significantly reduced.

The result of the collaborative effort was the construction of a first SAP prototype which is currently located at NPL. The instrument is planned to be moved within 2007 to the UK National facility for research into the fabrication and metrology of ultra-precision surfaces at St Asaph in North Wales. The current SAP is capable of measuring spherical and aspherical optics up to 1 m in diameter.

The measurement range in terms of minimum measurable radii of curvature is 564 mm for concave optics and 1654 mm for convex optics. There is no upper limit in the measurable radii of curvature which means that the SAP can be employed for the measurement of flat surfaces. The measurable asphericity is only limited by the measurement range of the contact probe which is 13 mm.

9.2 EVALUATION AND FUTURE WORK

9.2.1 MEASUREMENT ACCURACY

The NPL/UCL is a prototype, "proof-of-concept" instrument and constitutes the first stage of development towards a solution for ELT segment metrology. The accuracy of the measurement was found to be better than 30 nm RMS although this included the errors from the test surface. In the future it will be necessary to perform measurements on calibrated artefacts in order to obtain the true accuracy of the instrument. It is suggested that this should be done in a way that covers the whole dynamic range of the SAP. At first it will be required to use a calibrated flat in order to obtain the SAP measurement error at its null position where the tilt of the PI bearing is zero. Ideally additional artefacts should be used in order to estimate the SAP's error at the

extremities of its range *i.e* at maximum tilt angles. This could be done by using a concave optic of approximate RoC of 564 mm and a convex optic of approximate RoC of 1654 mm.

9.2.2 REPEATABILITY AND REPLACEMENT OF HORSTMANN BEARING

The measurement repeatability was found to be very low at 3.5 nm. Nevertheless the repeatability test was performed using only one of the instrument's axes that is the PI bearing axis. A complete SAP measurement would require multiple scans on the test optic in several directions and this can only be achieved by rotating the optic. Currently, due to the low stiffness of the Horstmann bearing, the rotation of the optic results to random roll errors of several micrometres. For this reason it is suggested that a bearing of higher stiffness should be obtained in order to realise fully the capabilities of the SAP. The bearing should be chosen according to the future measurement requirements but it should have sufficient load capacity and stiffness for holding typical 1 m diameter optics. When the Horstmann bearing is replaced it will be possible to evaluate the repeatability of the SAP for complete measurement cycles.

9.3.3 MEASUREMENT OF ASPHERIC OPTICS

At the time when this thesis was completed it had not been possible, mainly due to time restrictions, to measure aspheric optics with the SAP. This will be part of future work. In the measurement of aspheric optics the same SAP principles apply as in the measurement of spherical optics. Thus it not expected that the measurement accuracy of the SAP will be significantly different.

9.4.4 COMPLETION OF THE HYBRID SENSOR

The design and evaluation of the hybrid sensor was the subject of a separate PhD project, although there was a significant overlap with the subject of the current thesis. In 2006 NPL and UCL decided to withdraw from the OMAM consortium due to delays in the delivery of the OMAM sensor. Consequently the Arden Photonics AWS-50 wavefront sensor was chosen for experimentation. As of January 2007 the implementation of the hybrid sensor was still under research. This work will be carried out by the end user when the instrument is commissioned.

9.5.5 ALIGNMENT OF THE SAP

As was mentioned in chapter 8, the alignment of the SAP was performed using the direction of gravity as an external reference. In this way all the instrument axes were nulled to zero tilt and roll and consequently the PI was tilted according to the RoC of the $f/9.5$ test optic. The necessary tilt angle was calculated using the knowledge of the effective arm length. Nevertheless the nature of the SAP geometry means that the value of the effective arm length used to calculate the tilt is only true when the arm axis is horizontal. As soon as the axis is tilted the value of the effective arm length changes. As a consequence the tilt of the SAP can only be set approximately. As discussed in chapter 8 the residual tilt can be identified and corrected by scanning the test optic and observing the shape of the resulting trace. Arched traces denote incorrect tilt angle. Nevertheless it is possible that the curvature of the trace is a result of combined SAP and SUT errors. Relying on the measurement traces to correct the residual tilt means that systematic errors are likely to be introduced into the measurement.

The true effective arm length can only be found if the distance between the probe tip and the PI centroid can be measured directly or indirectly. A direct measurement, to the required accuracy of ± 0.5 μm would be very difficult. In the first SAP prototype (chapter 5) such a measurement was achieved only because the instrument had small dimensions and the whole arm structure was removed and placed into a CMM. In the full scale prototype this is not feasible.

Another way of measuring the true effective arm length would be by tracing the motion of the arm whilst it is being tilted between its null position its final position. This could be done using distance measuring interferometers positioned appropriately around the SAP. The difference between the initial and final positions could then be used to provide the new value for the effective arm length and consequently to correct any tilt residuals. The tilt could be also monitored using interferometers or proximity sensors (for example capacitance sensors) placed appropriately in the SAP.

9.5.6 SCALING-UP

The initiative for the NPL/UCL SAP was the application of the emerging technology to ELT segment metrology. In order to do this it will be necessary to construct a SAP with sufficient measurement range. The main requirement for this would be the scaling up of the SAP sub-components according to the measurement requirements. The major components that will need replacing are the profilometer arm and two air bearings.

Coorstek offers the same type of beam used in the SAP in lengths of 1950 mm, 2825 mm and 3835 mm. The measurement of segments up to 2.4 m in diameter could

be achieved with the use of a 2825 mm beam. The main issue regarding the arm bearing has to do with the increased radial loading due to the heavier arm beam. PI offer bearings specifically designed for high radial load capacity. An example is the 10R-606 unit which offers a working radial load capacity of 1330 N and would be sufficient for holding a 2825 mm beam at a tilt angle of 33^0. For the component bearing a suggestion would be the 23R PI bearing that is commonly used in liquid mirrors and offers axial load capacities up to 33400 N. The quoted runout is lower than 25 nm. Further modifications will be required, such as the use of a larger translation stage with the same functionality as the FAG stage and a larger granite base. These could be made to order.

9.5.7 COMPARISON OF SAP AND OTHER TECHNIQUES

The advantages of a SAP system over other measurement techniques have been discussed in detail. Nevertheless the real value of such an instrument can be only be proven during real measurement conditions. At the current stage of development the SAP was operated using a contact probe and it was proven to measure with an accuracy better than 20 nm over a measurement range of 600 mm. This is significantly better compared to the accuracy of 50 nm quoted for similar instruments and for equivalent measurement ranges.

The higher measurement accuracy of the NPL/UCL SAP lies primarily on the use of very high quality bearings as well as the high stiffness alumina moving arm. These also contribute to the exceptional repeatability of the measurement which was found to be

under 5 nm. These results prove the efficacy of the NPL/UCL SAP prototype as an instrument that can be used to measure accurately large industrial optics.

Nevertheless the aim of the project was also to demonstrate fast measurements times in order to tackle the problems of mass metrology for ELT segments. This is expected to be fully addressed at the second phase of the prototype development with the introduction of the wavefront sensing capability. This is expected to reduce measurement times for large 2 m optics to just a few hours rather than days whilst increasing the overall surface coverage by orders of magnitude.

Is also very important to note that the alignment of the SAP can be achieved in less than an hour and following well defined procedures. This is really important when it comes to multiple element metrology since different types of segments can be prepared for measurement at a minimum time hence reducing the overall measurement time between grinding and polishing cycles.

As an epilogue, it is my belief that the construction of the NPL/UCL SAP will offer a practicable platform for experimentation into the measurement of large aspheric optics and the provision of the new generation of ELTs.

REFERENCES

Abbe E 1890 Messapparate für physiker, Zeits *Für Instrumenten-kundle* **10** 446-448

Andersen T, Ardeberg A and Owner-Petersen M (editors) 2003 *Euro50 - Design study of a 50 m adaptive optics telescope* (Lund Observatory)

Anderson D S and Burge J H 1995 Swing-arm profilometry of aspherics *Proc. SPIE* **2536** 169-179

Angel J R P and Parks R E 1982 Generation of off-axis aspherics *Proc. SPIE* **332** 316-326

Ashby M F 1999 *Materials selection in mechanical design* (Butterworth Heinemann, Oxford, UK)

Axelrad P, Park K C and Frew E 2006 Lecture notes on second order linear differential equations with modelling of vibration of cantilever beams ASEN 2003 Introduction to dynamics and systems
http://www.colorado.edu/ASEN/asen2003/ASEN2003_2ndOrderSys_06.pdf
(access date: 21/06/2007)

Bates W J 1946 A wavefront shearing interferometer *Proc. Phys. Soc.* **59**

Bensammar S 2003 "(POPSUD) MEELD – Metrology for the European Extremely Large Telescope"

Birch K P and Downs M J 1993 An updated Edlén equation for the refractive index of air *Metrologia* **30** 155-162

Blanchard P M, Fisher D J, Woods S C and Greenaway A H 2000 Phase-diversity wavefront sensing with a distorted diffraction grating *Appl. Opt.* **39** 6649-6655

Blanchard P M and Greenaway A H 1999 Simultaneous multiplane imaging with a distorted diffraction grating *Appl. Opt.* **38** 6692-6699

Bolton W 2003 *Mechatronics: electronic control systems in mechanical and electrical engineering* 3rd edition (Prentice Hall)

Born M and Wolf E 1999 *Principles of optics* (7th edition, Cambridge University Press)

Bosch J A (editor) 1995 *Coordinate measurement machines and systems* (Marcel Dekker, Inc)

Burge J H 1995 Application of computer-generated holograms for interferometric measurement of large aspheric optics *Proc. SPIE* **2567** 258-269

Burge J H 1996 Fizeau interferometry for large convex surfaces *Proc. SPIE* **2536** 127-138

Burge J H 1997 Measurement of large convex aspheres *Proc. SPIE* **2871** 362-373

Burge J H 1999 Efficient testing of off-axis aspheres with test plates and computer generated holograms *Proc. SPIE* **3782** 348-357

Carré P 1966 *Metrologia* **2** 13-23

Cebon D and Ashby M F 1994 Materials selection for precision instruments *Meas. Sci. Technol.* **5** 296-306

Cheng Y-Y and Wyant J C 1985 Multiple-wavelength phase-shifting interferometry *Appl. Opt.* **24** 804-807

Conely J I M, Railton R and Mackenzie A I 1981 Ventilator problems caused by humidity in the air supplied from simple compressors British *Journal of Anaesthesia* **53** 549

Creath K, Cheng Y-Y and Wyant J C 1985 Contouring aspheric surfaces using two-wavelength phase-shifting interferometry *Optica Acta* **32** 1455-146

Decker J E and Pedelsky J R 1997 Uncertainty evaluation for the measurement of gauge blocks by optical interferometry *Metrologia* **34** 479-493

Devaney N 2007 Review of astronomical adaptive optics systems and plans *Proc. SPIE* **6584** 10.1117/12.723350

Dierickx P, Delabre B and Noethe L 2000 OWL optical design, active optics and error budget *Proc. SPIE* **4003** 203-209 Dierickx P and Gilmozzzi R 2000 Progress of the OWL: 100 m telescope conceptual design *Proc. SPIE* **4004** 290-299

Downs M J and Nunn J W 1998 Verification of the sub-nanometric capability of an NPL differential plane mirror interferometer with a capacitance probe *Meas. Sci. Technol.* **9** 1437-1440

Edgall M and Breidenthal R S 1983 Large surface measuring machine, Applications of optical metrology-techniques and measurements II *Proc. SPIE* **416** 62-68

Edlén B 1966 The refractive index of air *Metrologia* **2** 71-80

Efstathiou A 2004 Profilometry to support large optical manufacturing and testing NPL report CBTLM (RES) 106

Ennos A E and Virdee M S 1982 High accuracy profile measurement of quasiconical mirror surfaces by laser autocollimation Prec. Eng. **4** 5-8

Ennos A E and Virdee M S 1986 Precision measurement of surface form by laser profilometry *Wear* **109** 275-286

Estler W T, Edmundson K L, Peggs G N and Parker D H 2002 Large-scale metrology - an update

Estler C, Gerhardt J, Schmidt P T, Schulz M and Weingärtner I 2002 Reconstructing surface profiles from curvature measurements *Optik* **113** 154-158

Euro50 website http://www.astro.lu.se/~torben/euro50/ (access date: 21/06/2007)

Ferreira P M and C R Liu Purdue 1986 A Contribution to the analysis and compensation of the geometric error of a machining center *Ann. CIRP* Vol. 35/1

Flack D 2001 CMM Probing *Measurement Good Practise Guide No. 43* (National Physical Laboratory)

Forbes A B and Harris P M 2000 Simulated instruments and uncertainty estimation NPL Report CMSC 01/00

Fried D L 1966 Optical resolution through a randomly inhomogeneous medium for very long and very short exposures *J. Opt. Soc. Am.* **56** 1372-1379

Gallaher J, Mountain M, Oschmann J and Strom S 1999 Report on the AURA MAXAT II workshop held on September 16 and 17, 1999 in Hyannis, Massachusetts.

Gåsvik K J 2002 *Optical Metrology* (3rd edition John Wiley and Sons Ltd)

Gillingham P R 1997 Operational performance of the Keck 10 m telescope *Proc. SPIE* **2871** 2-9

Glmozzi R 2004 Science and technology drivers for future giant telescopes *Proc. SPIE* **5489**

Glenn P and Hull-Allen G 2001 Self-referencing, motion-insensitive approach for absolute aspheric profiling of large optics to the nanometer level and beyond *Proc. SPIE* **4451** 313-324

Greenleaf A H 1983 Self-calibrating surface measuring machine *Opt. Eng.* **22** 276-280

Greivenkamp J E, Smith D G, Gappinger R O and Williby G A 2001 Optical testing using Shack-Hartmann wavefront sensors *Proc. SPIE* **4416** 260-263

Guide to Expression of Uncertainty in Measurement 1994 International Organization for Standardization (ISO) Switzerland

Hamid R, Sendogdu D and Erdogan C 2005 The temperature stabilisation and temperature measurement of a Kösters interferometer *Meas. Sci. Technol.* **16** 2201-2207

Harasaki A, Schmit J and Wyant J C 2000 Improved vertical-scanning interferometry **39** 2107-2115

Hariharan P, Oreb B F and Eiju T 1987 *Appl. Opt.* **26** 2504-5

Hartmann P and Morian H F 2004 100 years of mirror blanks from SCHOTT *Proc. SPIE* **5382** 331-336

Heather I C, Zhang S and Greenaway A H 2004 Generalised phase diversity for wave-front sensing *Opt. Lett.* **29** 2707-2709

Hecht E 2002 *Optics* (Addison-Wesley, fourth edition)

Heydemann P L M 1981 Determination and correction of quadrature fringe measurement errors in interferometers *Appl. Opt.* **20** 3382-3384

Hughes E B, Wilson A and Peggs G N 2000 Design of a high-accuracy CMM based on multi-lateration techniques *Ann. CIRP* **49** 391-394

Irick S C 1992 Determining surface profile from sequential interference patterns from a long trace profiler *Rev. Sci. Instrum.* **63** (1) 1432-1435

Jacob R 2001 Medical grade compressed air *Updates in anaesthesia* **13** Article 2

Johnson G and Jennings R 2001 *LabVIEW Graphical Programming* (3rd edition, McGraw-Hill)

Knoyle C H 1950 NPL Combination angle gauges Machinery **77** 275

Kumler J Designing and specifying aspheres for manufacturability 2005 *Proc. SPIE* **5874** 121-129

Leach R 2000 Nano-Surf IV: *Traceable measurement of surface texture at the nanometre level* PhD thesis (University of Warwick, Centre for Nanotechnology and Microengineering).

Lee Y, Shi Y and Du L Testing aspheric surfaces by TWHI *Proc. SPIE* **2536** 154-158

Liu H, Lu Z, Li F, Xie Y, Kan S and Wang S 2004 Using curved hologram to test large-aperture convex surface *Opt. Express* **12** 3251-3256

Lohmann A W and Paris D P 1967 Binary Fraunhofer holograms, generated by computer *Appl. Opt.* **6** 1739-1748

LSM 2003 Large Scale Metrology, 2 day workshop, NPL, June 2003, NPL-NIST-PTB

Malacara D 1992 *Optical shop testing* (John Wiley & Sons, Inc, Second edition) p732

Martin H M, Allen R G, Angel J R P, Burge J H,Davison W B, DeRigne S T, Dettmann L R, Ketelsen D A, Kittrell W C, Miller III S M, Strittmatter P A and West S C 1998 Fabrication and measured quality of the MMT primary mirror *Proc. SPIE* **3352** 194-204

May-Miller R 1985 *API gauge machine operator's manual* CUPE REF: UP1167/R149/D55

Melles Griot online technical literature libraries www.mellesgriot.com (access date: 21/06/2007)

Morrison E 1996 The development of a prototype high-speed stylus profilometer and its application to rapid 3D surface measurement *Nanotechnology* **7** 37-42

Nagy F and Siegler A 1987 *Engineering foundations of robotics* (Prentice-Hall International UK Ltd)

Novacek G 1999 Accurate linear measurement using LVDTs *Circuit Cellar* **106** 20-27

Oberg E, Jones F D, Horton H L and Ryffel H H 2000 *Machinery's handbook* (26th edition, Industrial Press Inc.-New York)

Otto W, Matthes A and Schiehle H 2000 Measuring large aspherics using a commercially available 3D-coordinate measuring machine *Proc. SPIE* **2536** 91-97

Pfeifer T, Evertz J, Tutsch R and Rothe H 1992 Testing aspherics without rotational symmetry using a Fizeau interferometer with computer generated holograms *Proc. SPIE* **1781** 216-223

Piekos E S and Breuer K S 1999 Pseudospectral orbit simulation of non-ideal gas-lubricated journal bearings for microfabricated turbomachines *J. Tribology* **121** 604-609

Powell J W 1970 *Design of aerostatic bearings* (The Machinery Publishing Co. Ltd)

Quandu W, Zhongyu Z and Xuejun Z 2000 Novel profilometer with dual digital length gauge for large aspherics measurement *Proc. SPIE* **4231** 39-46

Roper M 2003 General requirements and examples of optics for synchrotron radiation beamlines, Metrology for SR Optics Report, Daresbury internal requirements document

Roddier C and Roddier F 1993 Wavefront reconstruction from defocused images and the testing of ground based optical telescopes *Opt. Soc. Am. A* **10** 2277-2287

Sartori S and Zhang G X 1995 Geometric error measurement and compensation of machines *Ann. CIRP* Vol. 44/2/1995

Schmidt P T, Schulz M and Weingaertner I 2000 Facility for the curvature-based measurement of the nanotopography of complex surfaces *Proc. SPIE* **4098** 94-101

Schulz M, Schmidt P T and Weingärtner I 2000 A reliable curvature sensor for measuring the topography of complex surfaces *Proc. SPIE* **4098** 84-93

Schulz M 2001 Topography measurement by a reliable Large-area Curvature Sensor *Optik* **112** 86-90

Schwider J, Burrow R, Elssner K E, Grzanna J, Spolaczyk R and Merkel K 1983 Digital wavefront measuring interferometry: some systematic error sources *Appl. Opt.* **22** 3421-32

Schwieger V 2004 Variance-based sensitivity analysis for model evaluation in engineering surveys INGEO 2004 and FIG Regional Central and Eastern European confierence on Engineering Surveying, Bratislava, Slovakia, November 11-13, 2004

Sebring T A and Ramsey L W 1996 The Hobby-Eberly telescope: A progress report *Proc. SPIE* **2871** 32-37

Smith G M 1996 Keck II status report *Proc. SPIE* **2871** 10-14

Smith S T and Chetwynd D G 1992 *Foundations of ultraprecision mechanism design* (Gordon and Breach Science Publishers)

Sommargren G, Phillion D, Seppala L and Lerner S 2001 CELT report 20 University of California, Lawrence Livermore National Laboratory

Storz G E and Dow T A 1994 Cup Wheel grinding geometry *9th ASPE Meeting Ohio 2-7 October 1994*

Takacs P Z and Feng K S-C 1988 Long trace profile measurements on cylindrical aspheres *Proc. SPIE* **966** 354-363

Taylor B N and Kuyatt C E 1994 Guidelines for Evaluating and Expressing the uncertainty of NIST measurement results *NIST Tech. Note 1297*

Taylor-Hobson website www.taylor-hobson.com (accessible on 01/09/2007)

The expression of uncertainty and confidence in measurement 1997 United Kingdom Accreditation Service (UCAS)

Tong K E. Amine and L Joshi S 2003 Parametric error modelling and software error compensation for rapid prototyping *Rapid Prototyping Journal* **9** 301 - 313

Tong K 2005 *Parametric error modelling and software error compensation for rapid prototyping* (PhD thesis: Pennsylvania University)

Thomas T R 1999 *Rough surfaces* (2nd edition, Imperial College Press)

Thomsen-Schmidt P, Schulz M and Weingartner I 2000 A facility for the curvature-based measurement of the nanotopography of complex surfaces *Proc. SPIE* **4098** 94-101

Virdee M S 1986 High Accuracy measurement of specularly reflecting surfaces by laser autocollimation *Proc. SPIE* **676** 66-73

Walker D, Brooks D, Freeman R, King A, McCavana G, Morton R, Riley D and Simms J 2001 First aspheric form and texture results from a production machine embodying the precession process *Proc. SPIE* **4451** 267-276

Weimin Z and Tianning C 2000 Testing optical aspheric surfaces by aspherics characteristic interferogram *Proc. SPIE* **4221** 154-157

Weingärtner I, Schulz M, Elster C, Gerhardt J and Lucas A 2002 Simultaneous distance, slope, curvature and shape measurement with a multi-purpose interferometer *Proc. SPIE* **4778** 198-205

Whitehouse D J 1997 Surface Metrology *Meas. Sci. Technol.* **8** 955-972

Whiteley M R 1998 *Optimal atmospheric compensation for anisoplanatism in adaptive-optical systems* (PhD thesis: Air force Inst. of Tech. Wright-Patterson AFB OH)

William J, Wills-Moren and Peter B Leadbeater 1990 Stylus profilometry of large optics *Proc. SPIE* **1333** 183-194

Woods S C and Greenaway A H 2002 Wavefront sensing by the use of a Greens Function solution to the intensity transport equation *J. Opt. Soc. Am. A* **20** 508-512

Wyant J C 1971 Testing aspherics using Two-wavelength holography *Appl. Opt.* **10** 2113-

Wyant J C and Bennett V P 1972 Using computer generated holograms to test aspheric wavefronts *Appl. Opt.* **11** 2833

Wyant J C 1975 Use of an ac heterodyne lateral shear interferometer with real-time wavefront correction systems *Appl. Opt.* **14** 2622-2626

Irick S C 1992 Determining surface profile from sequential interference patterns from a long trace profiler *Rev. Sci. Instrum.* **63** 1432-1435

Yacoot A and Cross N 2003 Measurement of picometre non-linearity in an optical grating encoder using x-ray interferometry *Meas. Sci. Technol.* **14** 148-152

Yacoot A and Downs M J 2000 The use of x-ray interferometry to investigate the linearity of the NPL Differential Plane Mirror Optical Interferometer *Meas. Sci. Technol.* **11** 1126-1130

Yang H S 2000 *Developments in stylus profilometry* (PhD thesis: University College London, London)

Yang H S, Kim S W and Walker D 2003 Novel laser datum system for nanometric profilometry for large optical surfaces *Optics Express* **11** 624-631

APPENDIX A - RoC OF UNPERTURBED REFERENCE SPHERE

For zero positional and rotational error equation (4.21) should return $R' = R$, where

$$R' = \sqrt{(-l\cos\theta + l\cos\theta\cos\phi)^2 + (l\sin\phi)^2 + (R - l\sin\theta + l\sin\theta\cos\phi)^2}$$

$$= \sqrt{[l\cos\theta(\cos\phi - 1)]^2 + (l\sin\phi)^2 + [R + l\sin\theta(\cos\phi - 1)]^2}$$

$$= \sqrt{l^2\cos^2\theta(\cos\phi - 1)^2 + (l\sin\phi)^2 + R^2 + 2Rl\sin\theta(\cos\phi - 1) + l^2\sin^2\theta(\cos\phi - 1)^2}$$

$$= \sqrt{l^2(\cos\phi - 1)^2(\cos^2\theta + \sin^2\theta) + l^2\sin^2\phi + R^2 + 2Rl\sin\theta(\cos\phi - 1)}$$

$$= \sqrt{l^2(\cos\phi - 1)^2 + l^2\sin^2\phi + 2Rl\sin\theta(\cos\phi - 1) + R^2}$$

$$= \sqrt{l^2\cos^2\phi - 2l^2 + l^2 + l^2\sin^2\phi + 2Rl\sin\theta(\cos\phi - 1) + R^2}$$

$$= \sqrt{l^2(\cos^2\phi + \sin^2\phi) - 2l^2\cos\phi + l^2 + 2Rl\sin\theta(\cos\phi - 1) + R^2} \qquad \text{(A.1)}$$

Now substituting $\sin\theta = \frac{l}{R}$ gives

$$R' = \sqrt{l^2 - 2l\cos\phi + l^2 + \frac{2Rll}{R}(\cos\phi - 1) + R^2}$$

$$= \sqrt{2l^2(1 - \cos\phi) + 2l^2(\cos\phi - 1) + R^2}$$

$$= \sqrt{R^2} = R \qquad \text{(A.2)}$$

APPENDIX B – CALCULATION OF MODAL MASS

The static deflection of a cantilever beam, fixed at one end, is given by

$$y(x)=\frac{P}{6EI}(x^3-3Lx^2) \quad 0\le x\le L \tag{B.1}$$

where $y(x)$ is the deflection of the beam, P is the load at the end of the beam, E is the Young's modulus, I is the second moment of area, x is the distance from the fixed end and L is the overall length of the beam.

The deflection at the free end can be found using the equivalence from the spring-mass system where $F=k\varsigma$ and k is the spring constant and ς is the deflection at the free end. In the case of the cantilever beam the equivalent equation would be

$$P=\lambda\varsigma \tag{B.2}$$

where
$$\lambda=\frac{3EI}{L^3}. \tag{B.3}$$

The kinetic energy of the equivalent spring-mass system is

$$\varepsilon_{spring}=\frac{1}{2}m\dot{\varsigma}^2 \tag{B.4}$$

Also from equations (B.2) and (B.3)
$$\frac{P}{EI}=\frac{3\varsigma}{L^3} \tag{B.5}$$

Substituting equation (B.5) into equation (B.1) we obtain

$$y(x) = \frac{\varsigma}{2L^3}\left(x^3 - 3Lx^2\right) \tag{B.6}$$

The distributed velocity of the beam can be found by differentiating equation (B.5) with respect to time which gives

$$\dot{y} = \frac{\dot{\varsigma}}{2L^3}\left(x^3 - 3Lx^2\right) \tag{B.7}$$

In order to calculate modal mass it is necessary to use energy equivalence considerations. The kinetic energy of the beam would be

$$\varepsilon = \frac{1}{2}\int_0^V \dot{y}^2 \rho dV = \frac{1}{2}\int_0^L \dot{y}^2 \rho A dx = \frac{1}{2}\int_0^L \left(\frac{\dot{\varsigma}}{2L^3}\right)^2 \left(x^3 - 3Lx^2\right)^2 \rho A dx. \tag{B.8}$$

The integration yields

$$\varepsilon = \frac{1}{2}\left(\frac{33\rho AL}{140}\right)\dot{\varsigma}^2 \quad \text{or} \quad \varepsilon = \frac{1}{2}\left(\frac{33 m_{beam}}{140}\right)\dot{\varsigma}^2 \tag{B.9}$$

or

$$\varepsilon = \frac{1}{2} m_{\mathrm{mod}al}\, \dot{\varsigma}^2 \tag{B.10}$$

Hence the modal mass is given by $m_{\mathrm{mod}} = \frac{33}{140} m_{beam}$ or $m_{\mathrm{mod}} = 0.2357 m_{beam}$. (B.11)